Universiteit Gent
Faculteit Wetenschappen
Vakgroep Fysica en Sterrenkunde

Optimal use of the polychromaticity in X-ray microtomography for dual energy methods and contrast agent imaging

Elin Pauwels

Proefschrift ingediend tot het behalen van de graad van
Doctor in de wetenschappen:
fysica
Academiejaar 2016-2017

Universiteit Gent
Faculteit Wetenschappen
Vakgroep Fysica en Sterrenkunde

Promotor:	Prof. dr. Luc Van Hoorebeke
Examencommissie:	Prof. dr. Jan Ryckebusch (voorzitter) Dr. ir. Manuel Dierick (secretaris) Prof. dr. Luc Van Hoorebeke (promotor) Prof. dr. Koen Van Laere Prof. dr. ir. Klaus Bacher Prof. dr. ir. Jan Van den Bulcke

Universiteit Gent
Faculteit Wetenschappen

Vakgroep Fysica en Sterrenkunde
Proeftuinstraat 86, B-9000 Gent, België

Proefschrift ingediend tot het behalen van de graad van
Doctor in de wetenschappen: fysica
Academiejaar 2016-2017

Dankwoord

Als mensen mij vragen waarom ik fysica gestudeerd heb, kan ik nog altijd niet goed uitleggen wat mij precies gedreven heeft. Ik weet nog hoe ik thuiskwam na de infodag van de faculteit Wetenschappen, ondertussen al bijna twaalf jaar geleden, en het gevoel had dat dit de juiste beslissing was voor mij. Ik had toen echter nog helemaal geen idee wat ik verder met dat diploma ging doen en ik was al helemaal niet van plan om te doctoreren. Ik herinner mij nog hoe een prof in het tweede bachelor jaar tegen ons zei dat minstens één op twee van de studenten onder ons ging doctoreren. “Ik in elk geval niet”, dacht ik. Dat is dan toch behoorlijk anders uitgedraaid. Ik heb mij ondertussen wel nog op een “zijweg” begeven - die van de geneeskunde - maar ik ben gedurende mijn studies toch duidelijk gebeten geraakt door het wetenschappelijk onderzoek. Toen mijn promotor, Luc, mij tijdens mijn thesisjaar voorstelde om verder te doctoreren, moest ik dan ook niet lang twijfelen. En nu, na iets meer dan zes jaar is het eindelijk zover, mijn doctoraat is afgewerkt. Nu ja, “afgewerkt” is in het wetenschappelijk onderzoek altijd wel een beetje een relatief begrip.

Luc, bedankt om mij de kans te geven dit doctoraat te behalen en mij tegelijk ook de ruimte te geven voor en te steunen in mijn studies geneeskunde. Bedankt ook om steeds klaar te staan om mijn vele vragen te beantwoorden. Dit leidde vaak tot interessante discussies waarbij voor mij meer dan eens duidelijk werd dat fysica voor jou een echte passie is. En natuurlijk kon er regelmatig ook eens een grapje af (met als absoluut hoogtepunt de demonstratie van ballerina aan de waterkant). Tot slot bedankt om steeds alle teksten tot in de puntjes na te lezen. Het was voor mij altijd een geruststelling als ik een paper of abstract moest indienen dat dit eerst onder jouw goedkeurend oog gepasseerd was.

Daarnaast wil ik uiteraard ook mijn (ex-)collega’s bedanken. Manu, ook bij jou kon ik steeds terecht met al mijn vragen. De onuitputtelijke Manupedia-weetjes leidden ook tot vele interessante niet-fysische gesprekken, wat mijn kennis alleen maar heeft doen verruimen. Loes, de jaren met jou aan de tegenoverliggende bureau waren onvergetelijk. Bedankt om mee voor een ludieke sfeer te zorgen en mee het gezamenlijke middag-eetmoment in te voeren. Het wordt nu nog steeds verdergezet zonder ons. Denis, bedankt om mee de biomedische samples op het scanprogramma te zetten en het gebruik van contraststoffen te introduceren aan

UGCT. Amélie, het was fijn om samen te werken met jou. Ik ben heel blij dat ik de reumatologen en de vele muizenpootjes onder jouw hoede heb kunnen achterlaten. Jelle en Thomas, ik vond het geweldig dat jullie de projectiesimulator hebben kunnen ombouwen tot een snelle en handige software *tool*, iets wat mijn programmeercapaciteiten ver te boven ging. Matthieu, er was misschien iets minder overlap in ons onderzoekswerk, maar bedankt dat ik toch ook steeds met mijn (meestal praktische of organisatorische) vragen bij jou terecht kon. Pieter, het vele scanwerk dat jij hebt verricht - vooral de muizenpootjes waren vaak zeer talrijk - heeft mij enorm geholpen. Jelle V., Bert en Yoni, ik ben net na jullie bij UGCT terecht gekomen, maar jullie werk heeft voor de prachtige basis gezorgd waarop ik en vele anderen hebben kunnen verder bouwen.

Graag wil ik ook de UGCT'ers buiten de Stralingsfysica groep bedanken. Veerle, ik kan jou alleen maar bewonderen voor jouw gedrevenheid en enthousiasme in het wetenschappelijk onderzoek. Jan DW, Tim, Marijn, Wesley, Tom en Jeroen, jullie zorgden steeds voor een fantastische sfeer op de conferenties en daarbuiten. Jan VDB, ik vind het nog steeds jammer dat Nanowood naar jullie campus is verhuisd, maar ik vond het fijn dat ik daar toch steeds welkom was voor testjes. Bedankt ook om mijn doctoraat zo grondig en tot in de puntjes na te lezen. Hierbij aansluitend wil ik uiteraard ook de andere juryleden bedanken voor het nalezen van het werk en de waardevolle feedback.

Verder wil ik ook mijn vrienden bedanken voor de morele steun en de ontspanningsmomenten. Door mijn en jullie drukke leven hebben we mekaar de laatste tijd misschien wel wat minder gezien, maar uit het oog is zeker niet uit het hart.

Ook mijn familie wil ik graag bedanken en dan vooral mijn fantastische ouders. Jullie hebben mij steeds bij alle moeilijke en minder moeilijke momenten gesteund. Ik heb absoluut niet de gemakkelijkste weg gekozen, maar jullie stonden steeds achter mij en zonder jullie was ik nooit tot op dit punt geraakt. Dank je om er gewoonweg steeds te zijn voor mij! Ik kan niet omschrijven hoe belangrijk dat is voor mij. Ook Julie, bedankt om zo'n lieve zus te zijn en zo vaak te duimen voor mij.

En ten slotte, *last but not least*, mijn fantastische vriend Jelle, zonder jou was dit doctoraat nooit tot stand gekomen. Bedankt voor de vele hulp, niet alleen op fysica vlak, maar ook daarbuiten en vooral om er ook steeds te zijn voor mij. De laatste maanden zijn niet gemakkelijk geweest (en de komende maanden zien er ook nog steeds zeer druk uit), maar ik ben je gewoon zo dankbaar om zo geduldig te zijn en mij zo te ondersteunen. Je bent het beste wat mij de laatste jaren is overkomen.

Gent, 2017
Elin Pauwels

English summary

The discovery of X-rays in 1895 finally allowed to visualise the internal structure of objects in a non-destructive way. Especially in medical diagnostics, this property proved to be invaluable. In the 1970s, X-ray computed tomography (CT) was put into practice. This technique allows to produce a virtual three-dimensional (3D) representation of an object and to examine the inside from all possible directions in a non-destructive manner. CT was soon widely used, not only in medicine, but also in the industrial world. Of special importance is the amount of detail which can be visualised within the internal structure of objects. This led to the development of X-ray microtomography. For several of the current high resolution systems, the best achievable resolution is already below 1 micrometre.

The research presented in this work was performed within the Radiation Physics group of the Centre for X-ray tomography of the Ghent University (UGCT). UGCT is specialised in high resolution X-ray tomography, (almost) exclusively for *ex vivo* applications. This work focuses on optimalisation of X-ray imaging, mainly by investigating how scanning conditions can be adapted to optimally visualise a given sample, using the currently available hardware. In this context, the polychromatic behaviour of both X-ray source and detector will play a key role. Scan variables that will have a significant influence on the final CT image to a greater or lesser extent include tube voltage and power, beam filtration, exposure time and detector response characteristics. For an optimal image result, each type of sample will require a nearly unique combination of these parameters. The spectral behaviour of the different components will complicate such optimisation even further. This is especially true when the ideal scanning conditions have to be determined for a combination of two scans of the same object, as is the case in dual energy CT. This work elaborates further on this subject. Finally, this work also focuses more specifically on optimising soft tissue visualisation with X-ray CT. Mainly soft tissue contrast agents will be discussed.

The main contributions of the author of this work to the research on X-ray tomography, are predominantly situated around the following three aspects: predicting the final image result based on accurate simulations, optimising scanning conditions for dual energy CT and identifying adequate contrast agents for soft

tissue visualisation using high resolution X-ray CT. These topics are shortly discussed below.

The third chapter focuses entirely on simulations of the X-ray imaging process. To this purpose, two simulation tools were developed, the *Setup Optimiser* and *Arion*. The first allows for a fast and straightforward evaluation of various scan parameters by calculating the detected transmission through one or multiple material layers. This will already provide a rough indication of the effect of different variables on the final image result, but in order to obtain fully correct information, it is necessary to simulate a complete 3D CT scan. To this purpose, Arion was created. This program allows to simulate radiographic projections in an accurate and very fast way. It is of critical importance to fully understand and reproduce the entire polychromatic behaviour of X-ray source and detector. The experimental validation of the simulation tools presented in this work proves that we have a correct understanding of the physics behind the entire X-ray imaging process at UGCT. By comparing real and simulated CT scans, not only the qualitative, but also the quantitative correctness is demonstrated.

Chapter 4 is fully devoted to dual energy CT, where two scans of the same sample are made at different photon energies. Combining information from such scans can be useful when two or more materials with a different composition are difficult to distinguish in a single scan. For optimal results, a careful selection of these energies is of critical importance. The polychromatic behaviour of both X-ray source and detector, will complicate this choice. For instance, there is no unambiguous definition of the "energy" of a polychromatic X-ray spectrum. Therefore, in this work, first of all several definitions are proposed and studied. In the ideal case, a spectrum energy can be defined which corresponds to the grey values in the final CT image, regardless of the type of material and its thickness. One of the definitions introduced in this work, the "detected monochromatic energy", appears to largely meet these criteria, mainly when dealing with X-ray spectra with limited beam hardening. To quantify the degree of beam hardening, a measure was introduced as well, the "beam hardening factor". Combining this factor with the detected monochromatic energy allows for a fairly good selection of X-ray spectra for DECT. However, a major shortcoming of this approach is that the full shape of the spectrum is not completely taken into account. To overcome this, X-ray spectra can be selected based on full CT simulations. In this work, such technique is proposed, providing excellent results.

The fifth chapter elaborates on histology by means of high resolution X-ray tomography (HiXTom). A special challenge in this field is the visualisation of soft tissues. In a CT image, contrast is obtained when two adjacent types of materials give rise to a sufficiently different attenuation of X-rays. Soft tissues contain a lot of "cavities" filled with water. When this water is extracted and replaced by air, the contrast between soft tissue structures increases. To this purpose techniques such as freeze-drying and critical-point drying are used. Another important way

to improve soft tissue visualisation is to use contrast agents. In this work, a variety of possible candidates for X-ray contrast agents is studied. The focus lies on tissue samples larger than (1 cm)^3. Moreover, the staining procedure should be straightforward to apply and the substances should be sufficiently safe to handle. Excellent results were obtained mainly with $HgCl_2$, PMA and PTA. To conclude, a concrete example is given in this work of a biomedical application of HiXTom. This example clearly illustrates some of the important advantages as compared to conventional histology such as the non-destructive nature of CT and the fact that the inner structure of samples can be studied from every possible direction.

Nederlandse samenvatting

De ontdekking van X-stralen in 1895 maakte het voor het eerst mogelijk om de interne structuur van objecten in beeld te brengen op een niet-destructieve manier. Vooral in de wereld van de medische diagnostiek bleek deze eigenschap van onschatbare waarde. In de jaren 1970 werd X-stralen *computed tomography* (CT) in de praktijk gebracht. Deze techniek laat toe om een virtuele drie-dimensionele (3D) weergave te maken van een object en de binnenkant vanuit alle mogelijke richtingen te bestuderen op niet-destructieve wijze. Niet alleen in de medische wereld, maar ook in de industrie werd CT al snel veelvuldig gebruikt. Van belang is uiteraard ook de hoeveelheid detail die men kan in beeld brengen binnen de interne structuur. Dit leidde tot de ontwikkeling van X-stralen microtomografie waarbij verschillende van de huidige systemen resoluties halen tot minder dan 1 micrometer.

Het onderzoek voorgesteld in deze thesis werd verricht binnen de Stralingsfysica groep van het Centrum voor X-stralentomografie van de Universiteit Gent (UGCT). UGCT is gespecialiseerd in hoge resolutie X-stralentomografie, (nagenoeg) uitsluitend voor *ex vivo* toepassingen. Dit werk richt zich op optimalisatie van beeldvorming, waarbij voornamelijk onderzocht wordt hoe de scanomstandigheden aangepast kunnen worden om een object op de best mogelijke manier in beeld te brengen met de beschikbare apparatuur. Hierbij speelt voornamelijk het polychromatisch gedrag van zowel X-stralenbron als detector een belangrijke rol. Scanvariabelen die in meer of mindere mate een significante invloed zullen hebben op het uiteindelijke CT beeld omvatten onder andere de buisspanning en het vermogen, bundelfiltratie, belichtingstijd en de respons karakteristieken van de gebruikte detector. Ieder type object zal, afhankelijk van zijn samenstelling, vorm en grootte, een nagenoeg unieke combinatie van deze parameters vereisen voor een optimaal beeldresultaat. Het spectrale gedrag van de verschillende componenten maakt een dergelijke optimalisatie echter niet gemakkelijk. Dit is zeker zo wanneer men nog een stap verder gaat, en niet enkel de ideale scanomstandigheden wil bepalen voor één enkele scan, maar voor een combinatie van twee scans van een object zoals het geval is bij *dual energy* CT. In dit werk wordt vooral op dit laatste dieper ingegaan. Tot slot spitst dit werk zich ook meer specifiek toe op de optimalisatie van de beeldvorming van zachte weefsels. Hierbij wordt vooral

dieper ingegaan op het gebruik van contraststoffen.

De hoofdbijdragen van de auteur van dit werk aan het onderzoek naar de X-stralentomografie techniek situeren zich dan ook voornamelijk rond de volgende drie aspecten: het voorspellen van het uiteindelijke beeldresultaat aan de hand van accurate simulaties, het optimaliseren van de scan omstandigheden voor *dual energy* CT en onderzoek naar contrast stoffen voor de visualisatie van zachte weefsels met hoge resolutie X-stralen CT. Deze onderwerpen worden hieronder kort toegelicht.

Het derde hoofdstuk gaat integraal over simulaties van het X-stralen beeldvormingsproces. Hiervoor werden twee simulatieprogramma's ontwikkeld, de *Setup Optimiser* en *Arion*. Het eerste laat toe om op een snelle en eenvoudige manier verschillende scanparameters te gaan evalueren door de gedetecteerde transmissie te berekenen door één of meerdere lagen van een bepaald materiaal. Dit zal reeds een ruwe indicatie geven van de invloed van de verschillende variabelen op het eindresultaat, maar om volledig correcte informatie te verkrijgen, is het noodzakelijk om een volledige 3D CT scan te simuleren. Hiervoor werd Arion in het leven geroepen. Dit programma laat toe om op een accurate en vooral snelle manier simulaties uit te voeren van radiografische projecties. Hiervoor is het van belang om het volledige polychromatische gedrag van X-stralenbron en detector ten volle te begrijpen en te reproduceren. De experimentele validatie van de simulatieprogramma's voorgesteld in dit werk, toont aan dat we aan UGCT een correct begrip hebben van de fysica achter het volledige X-stralen beeldvormingsproces. Niet alleen kwalitatief, maar ook kwantitatief komen gesimuleerde en echte scans zeer goed overeen.

Hoofdstuk 4 is volledig gewijd aan *dual energy* CT. Hierbij worden twee scans van hetzelfde object verricht bij verschillende foton energieën. Het combineren van informatie van dergelijke scans kan nuttig zijn wanneer twee of meer materialen met een verschillende samenstelling moeilijk te onderscheiden zijn in één enkele scan. Van cruciaal belang voor een optimaal resultaat is uiteraard een zorgvuldige keuze van deze energieën. Het polychromatische gedrag van zowel X-stralenbron als detector, zal deze keuze er echter niet eenvoudiger op maken. Zo kan men de "energie" van een polychromatisch X-stralenspectrum niet eenduidig definiëren. In dit werk worden dan ook eerst en vooral verschillende definities hiervoor voorgesteld en onderzocht. In het ideale geval komt men tot een spectrumenergie die correspondeert met de grijswaarden in het uiteindelijke CT beeld, onafhankelijk van het type materiaal en de dikte ervan. Eén van de definities geïntroduceerd in dit werk, de "gedetecteerde monochromatische energie", blijkt in belangrijke mate aan deze criteria te voldoen, zij het dan vooral in het geval van X-stralenspectra met weinig bundelverharding (*beam hardening*). Om dit laatste in rekening te brengen werd een nieuwe grootheid geïntroduceerd; de *beam hardening* factor. Combinatie van de gedecteerde monochromatische energie met deze laatste factor laat toe om een redelijk goede selectie van X-stralenspectra te maken

voor *dual energy* CT. Een belangrijke tekortkoming van deze aanpak is echter dat de volledige vorm van het spectrum niet helemaal in rekening wordt gebracht. Dit is wel het geval wanneer men de X-stralenspectra gaat selecteren op basis van volledige CT simulaties. In dit werk wordt een dergelijke methode voorgesteld. Hiermee werden uitstekende resultaten verkregen.

In het vijfde hoofdstuk tenslotte, wordt dieper ingegaan op histologie met hoge resolutie X-stralen tomografie (HiXTom). Een speciale uitdaging binnen dit domein is de visualisatie van zachte weefsels. Contrast in een CT beeld wordt verkregen wanneer twee aaneengrenzende types materiaal aanleiding geven tot een voldoende verschillende attenuatie van X-stralen. Zachte weefsels bevatten veel "holtes" gevuld met water. Wanneer men dit water gaat extraheren en vervangen door lucht, kan men het contrast binnen zachte weefsels verhogen. Hiervoor gebruikt men technieken zoals vriesdrogen en kritisch-punt-drogen. Een andere belangrijke methode om de visualisatie van zachte weefsels te verbeteren is gebruik maken van contraststoffen. In dit werk wordt een uitgebreide lijst aan mogelijke kandidaten voor X-stralen contraststoffen onderzocht. Hierbij wordt er toegespitst op weefselstalen van meer dan $(1\text{ cm})^3$. Bovendien moet de procedure voor het contrasteren van de weefsels eenvoudig zijn en de stoffen moeten voldoende veilig zijn. Uitstekende resultaten werden voornamelijk verkregen met $HgCl_2$, PMA en PTA. Om af te sluiten, wordt in dit werk nog een concreet voorbeeld gegeven van een biomedische toepassing van HiXTom. Hiermee worden enkele belangrijke voordelen in vergelijking met klassieke histologie, met name het niet-destructieve karakter van CT en het feit dat men de objecten vanuit elke mogelijke richting kan bestuderen, duidelijk geïllustreerd.

List of symbols

Common abbreviations

- 3D: Three-dimensional
- aSi: Amorphous silicon
- BHF: Beam hardening factor
- CNR: Contrast-to-noise ratio
- CT: Computed tomography
- DECT: Dual energy computed tomography
- FBP: Filtered back projection
- GPU: Graphics processing unit
- HiXTom: Histology by means of high resolution X-ray tomography
- ICRU: International Commission on Radiation Units and measurements
- MRI: Magnetic resonance imaging
- NIST: National Institute of Standards and Technology
- PMA: Phosphomolybdic acid
- PTA: Phosphotungstic acid
- ROI: Region of interest
- SART: Simultaneous algebraic reconstruction algorithm
- SDD: Source-detector distance
- SOD: Source-object distance
- SpA: Spondyloarthritides
- UGCT: Centre for X-ray tomography of the Ghent University
- XRF: X-ray fluorescence

Common symbols

- $D_{d,i}$: Mean deposited energy per detected photon in energy bin i
- $D_{eff,i}$: Detector efficieny for energy bin i

- $D_{in,i}$: Mean deposited energy per incident photon in energy bin i
- E: Photon energy
- E_d: Total detected energy in a detector pixel
- $E_{av,d}$: Average detected energy
- E_{eff}: Effective energy
- $E_{eff,0}$: Effective energy for sample thicknesses approaching zero
- E_{mono}: Detected monochromatic energy
- I: X-ray beam intensity
- M: Magnification
- μ: Linear attenuation coefficient
- μ/ρ: Mass attenuation coefficient
- μ_{en}/ρ: Mass energy-absorption coefficient
- N: Amount of photons reaching a given detector pixel
- N_d: Amount of detected photons in a given detector pixel
- R: Resolving power - Resolution
- S_i': Filtered X-ray spectrum, expressed as the number of photons per simulated electron per keV per Sr
- σ: Total probability (atomic cross section) of Compton scattering
- τ: Total probability (atomic cross section) of photoelectric absorption
- T: Transmission
- Z: Atomic number

Table of Contents

List of Figures

List of Tables

1 Introduction

The discovery of X-rays in 1895 represented a giant leap forward in the world of imaging. From then on, it was possible to look at the internal structure of objects in a non-destructive way. Especially in medicine, this proved to be invaluable, but also in industry the newly discovered type of radiation was soon widely used. A second major leap forward was the development of X-ray computed tomography (CT) several decades later. This technique allows to reproduce a complete three-dimensional (3D), virtual reconstruction of the inner structure of an object in a non-destructive way, by combining the information of the regular two-dimensional radiographic projections taken from different points of view. The first CT-scanner was introduced in 1971.

In addition to visualising the internal structure of an object, researchers try to capture this structure into ever greater detail. This led to the development of high resolution X-ray computed tomography or micro-CT. Several current laboratory based micro-CT systems can provide an image resolution below 1 micrometre. At the "Centre for X-ray tomography of the Ghent University", UGCT, state-of-the-art high resolution CT scanners are developed and intensive research is performed, covering the complete CT workflow from data acquisition and processing to reconstruction, visualisation and 3D analysis. UGCT focuses (almost) exclusively on *ex vivo* CT applications.

X-ray tomography is a complex process involving many scan variables, such as tube voltage and power, beam filtration, exposure time and detector response

characteristics. Each of these parameters will to a greater or lesser extent, exert a significant influence on the final CT image. It is therefore often crucial to determine the ideal scanning conditions. An important inconvenient fact is that these optimal settings will largely depend on the object itself, in terms of its size, composition and density. At UGCT a wide variety of samples is imaged for a broad range of scientific applications, with each sample requiring its own nearly unique ideal scanning setup.

This work focuses on ways in which scanning conditions can be adjusted to obtain an optimal virtual representation of the sample, using the currently available hardware. The emphasis lies on the prediction of the final image result, so that based on this prediction scanner settings can be finetuned. Specific attention is paid to spectral characteristics resulting from the polychromatic nature of the X-ray beam. Furthermore, this work elaborates on biomedical samples where contrast agents are studied to optimise soft tissue visualisation.

1.1 Outline

In chapter 2, the fundamental concepts of X-ray physics and X-ray computed tomography are discussed. First, the mechanisms for the production of X-rays are explained. Then, the photon interaction processes for the photon energy range of interest in this work and the principles of attenuation of X-rays are thoroughly discussed. Next, the complete CT-workflow is briefly described. Further, a few important X-ray tomography concepts are discussed, such as flux, resolution, beam hardening and partial volume effect. Finally, an introduction to UGCT and the Radiation Physics group in which this work was performed is given, including an overview of the scanners and software packages currently available.

The third chapter is the first of the three main chapters in this work. This chapter focuses on the simulation of the X-ray imaging process. As previously mentioned, a careful selection of scanner settings is crucial for an optimal image result. It is however not practically feasible nor desirable to perform multiple experimental attempts to obtain the best scanning conditions. Therefore, at UGCT a simulation tool was developed, called the Setup Optimiser, to allow for a straightforward evaluation of various scanner settings by simulating the detected transmission of a specific X-ray beam through one or several layers of materials. Since this information is not easily extrapolated to a 3D CT scan for more complex samples, Arion, a program for fast and realistic simulations of radiographic projections was developed as well. The foundations of both simulation tools lie in a full understanding of the polychromatic hardware characteristics of the main components. Therefore, the chapter starts by discussing the simulation of the polychromatic behaviour of

the X-ray source and detector by means of Monte Carlo techniques. Next, the mathematical basis of the Setup Optimiser and Arion are described. Further, an overview of the different aspects and features of the simulation software is given. In the following part, a thorough experimental validation is presented by comparing simulated and real X-ray imaging data, proving the quantitative correctness of both tools. To conclude, some benchmarks are given and possible future improvements are suggested.

Chapter 4 is fully devoted to dual energy computed tomography (DECT). In a CT image, two or more materials with a different composition can have a very similar grey value, making it practically impossible to distinguish them from one another. This is due to the fact that the way in which X-ray photons interact with matter is dependent on several parameters, namely the local density of the material, the photon energy and the elements present. An unlucky combination of these parameters may lead to difficulties in discriminating the different materials in the final CT image. In these cases, DECT may be very useful. This implies that CT scans are performed at two (or more) different X-ray energies. The data of these scans is then combined to provide the necessary information to make a distinction between materials with otherwise very similar grey values. The chapter starts by giving a thorough background and literature overview on DECT techniques. Next, the dual energy image processing techniques applied at UGCT are described. The following part focuses on optimising the selection of dual energy X-ray spectra. First, the concept of the "energy" of a polychromatic spectrum is thoroughly elaborated and several definitions are proposed. Then two methods for selecting the X-ray spectra in practice are introduced, i.e. one based on spectrum parameters, the other based on complete CT simulations. In the last part, practical examples of dual energy CT are given, using both proposed methods for a self-made phantom and a real sample. To conclude, the obtained results are summarised and future improvements are suggested.

In chapter 5, the concept of virtual histology by means of high resolution X-ray tomography (HiXTom) is explored. Special attention is paid to soft tissue visualisation. X-ray image contrast is obtained when two adjacent types of materials give rise to a sufficiently different X-ray photon attenuation. The atomic composition of soft tissue is not so different from water. Since most "cavities" within tissue samples are filled with water, soft tissue contrast in CT images is rather limited. In this chapter, first some contrast enhancing techniques for HiXTom are discussed. In the second part, a substantial list of chemical substances is studied in order to identify useful X-ray contrast agents for soft tissue visualisation, suited for samples larger than $(1\ \mathrm{cm})^3$. In the final part, an important biomedical application of

HiXTom is extensively described.

To conclude this work, the obtained results are summarised in the final chapter. Moreover, an outlook is provided on possible future research.

1.2 Main contributions

The main contributions of the author to the field of high resolution X-ray computed tomography, which are presented in this work are:

- Further improvement and expansion of the Setup Optimiser into a versatile tool for straightforward evaluation of various CT scanner settings.
- Validation of the Setup Optimiser by quantitatively comparing simulated and real transmission values.
- Development of the first polychromatic projection simulator at UGCT, as a predecessor of Arion.
- Validation of the polychromatic projection simulator by quantitatively comparing simulated and real CT scans.
- Implementation of the decomposition in three basis materials dual energy technique at UGCT.
- Introduction of the different definitions for defining the "energy" of a polychromatic X-ray spectrum.
- Development of two selection methods for DECT X-ray spectra, i.e. based on spectrum parameters and based on complete CT simulations.
- Practical application of dual energy CT at UGCT.
- Identification of useful contrast agents for soft tissue visualisation by means of high resolution X-ray computed tomography.
- Biomedical application of HiXTom: study of the influence of biomechanical stress on bone formation in arthritis mouse models.

2

X-ray tomography

In 1895, while conducting experiments with a Crookes tube, Wilhelm Conrad Röntgen observed an unknown kind of penetrating radiation. He immediately started studying the basic properties of these rays, which he called X-rays [1]. The famous picture of his wife's hand, which he made during these initial experiments, proved that this new type of radiation made it possible to see through the human body. Soon after their discovery, X-rays were widely used not only in medicine but also for industrial applications, since it was now possible to look at the internal structure of objects in a non-destructive way.
Although the invention of the radiography caused a major revolution in medical diagnosis and it still represents a significant aspect of radiology, the technique has its limitations due to its two-dimensional nature. All information along a ray path is accumulated into a single 'pixel' on the detector medium. However, when combining a set of radiographs taken from different points of view, it is possible to reconstruct the object in a three-dimensional way. This led to the development of the first CT scanner, called the EMI Mark 1, in 1971. From that moment on, X-ray computed tomography has become an important and widely used imaging technique.

In this chapter, the fundamental concepts of X-ray physics and X-ray computed tomography will be briefly discussed and an introduction to UGCT will be given.

2.1 The production of X-rays

X-rays and γ-rays are a form of electromagnetic radiation at the high-energy end of the electromagnetic spectrum. They are characterised by their energy E, wavelength λ or frequency ν, which mutually relate as follows:

$$E = \frac{hc}{\lambda} = h\nu, \tag{2.1}$$

with h Planck's constant ($4.136 \cdot 10^{-15}$ eVs) and c the speed of light in vacuum. The difference between X-rays and γ-rays is not always clearly defined. The distinction between the two types of radiation was previously based on their wavelength. Nowadays, X-rays and γ-rays are rather distinguished based on their origin, i.e. X-rays are emitted by accelerated electrons while γ-rays are emitted by the nucleus as a result of radioactive decay or created in annihilation processes. The two definitions are however also often used interchangeably.

2.1.1 Sources

In this section, three different mechanisms for the production of X-rays (and γ-rays) are briefly discussed.

Radioactive decay

After decay, such as α- or β- decay, the nucleus often remains in an excited state. To return to a more stable energy level, the nucleus can emit the excess energy in the form of a high-energetic photon. Since the energy of the emitted photon equals the energy difference between the excited and stable state, this results in monoenergetic radiation for a certain decay process. Such γ-ray sources can be used in industrial tomography as an alternative to the more conventional X-ray tubes with the huge advantage that in this way a monochromatic beam can be produced. On the other hand, the disadvantages are numerous. A relatively low flux of photons is emitted uniformly in space by the radioactive isotopes. Therefore the source needs to be properly shielded and the beam needs to be collimated to a narrow beam making it difficult to obtain small focal spot sizes. Also the safety issues related to the use of radioactive isotopes limit the use of γ-ray sources as an alternative to X-ray tubes in computed tomography.

Synchrotron radiation

In a synchrotron installation, charged particles (usually electrons) are accelerated to a very high energy and subsequently injected into a large quasi-circular storage ring, composed of bending magnets and straight drift sections. Relativistic

charged particles will lose a fraction of their kinetic energy when they are deflected from their path by a magnetic field. This energy is emitted in the form of high energy photons, called *synchrotron radiation*. Initially this was considered as an annoying side effect resulting in unwanted energy loss. However, this radiation quickly proved to be very useful for various applications. The first generation of synchrotrons solely made use of bending magnets for the production of electromagnetic radiation. Using crystalline monochromators, monochromatic radiation could be extracted, however at the cost of a significant loss of radiation intensity. In the current (third) generation of synchrotrons periodic deflecting magnets of a few meters long are installed in the straight sections. The resulting magnetic field is static in time, but varies sinusoidally in space. The passing electrons will follow an oscillating trajectory and as such emit synchrotron radiation. The most commonly used types of these insertion devices are called *undulators* and *wigglers*. In a wiggler, a large number of bending magnets are placed in sequence, resulting in the accumulation and thus a large flux of polychromatic radiation. Undulators on the other hand have a smaller bending strength so that the deflection angle of the electrons is limited and all radiation is emitted in a forward cone with a small opening angle. Moreover, the produced radiation is quasi-monochromatic and the wavelength can be shifted by varying the magnetic field.

Synchrotron radiation offers some significant advantages for X-ray imaging purposes. A high intensity cone beam is produced with an extremely narrow opening angle, which allows imaging far from the source under quasi-parallel beam conditions. Moreover, the radiation is spatially coherent as it originates from a very small area making it highly suitable to use wave-related effects to enhance the detectability of certain features (see section 2.2.7). Finally, the possibility to create a quasi-monochromatic beam at tunable energies, opens doors for the application of dual energy techniques and K-edge imaging in particular. This will be further discussed in chapter 4. However, the construction and maintenance costs are enormous making the number of synchrotron facilities and thus the accessibility limited.

Note that there now exists a commercial system, the Lyncean Compact Light Source [2], that offers the possibility of a synchrotron beamline for home laboratory applications. However, there are several important limitations. First of all, the flux is lower than typically achieved at synchrotron facilities. Secondly, it is still a room size system. Furthermore, X-rays can only be focused to a spot of 45 µm, which is rather large for laboratory based micro-CT. Finally, the cone beam is only moderately diverging, which means that X-ray optics are necessary to accomplish a significant magnification.

X-ray tube

The majority of X-ray tubes are based on the design of the Coolidge tube, invented in 1913 by William David Coolidge. A schematic representation is shown in figure 2.1. Inside a vacuum glass tube, a filament (generally tungsten) is heated by an electric current. Due to thermionic emission electrons are produced from this filament and accelerated by an electric field towards a positively charged anode (target). In modern X-ray tubes the electrons are further focused using electromagnetic lenses to create a small focal spot. Upon hitting the target, the electrons produce X-ray photons due to interactions with the target material.

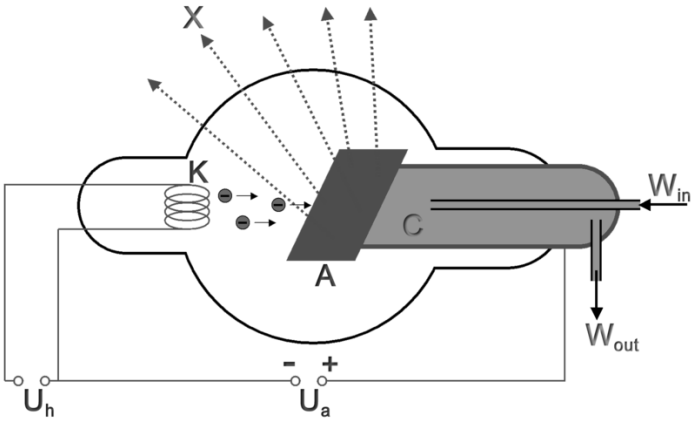

Figure 2.1: Design of the Coolidge tube [3]

X-ray tubes can have a closed or open design. An important advantage of the latter is that it can be opened to allow the user to replace the filament or change the target material. Furthermore, there are also two main types of target geometry for modern X-ray tubes as shown in figure 2.2. In a transmission tube the electron beam impinges perpendicular onto a thin target. The X-ray photons that leave the target on the opposite side are collimated into an X-ray beam. In a directional tube the target is positioned at a fixed angle relative to the incident direction of the electron beam. Due to a collimator the X-ray photons are emitted only at an angle of typically $60°$ to $90°$ with respect to the incident direction.
From this collimated beam, a small part of the produced X-ray photons are absorbed by the target material itself. As a result, the intensity of the X-ray beam emitted by a directional X-ray tube is higher on the cathode side and decreases towards the anode side, while the beam itself is harder on the latter side. This is called the *heel effect*. Of course this effect is not observed using a transmission type tube in conventional geometry, i.e. with the detector centered on the beam

axis.

Note that there exist also X-ray tubes with a jet of liquid metal as target material, instead of a solid anode (Excillum MetalJet [4]). The main advantage of these systems is that the maximum tube power is no longer limited by possible target melting (see also section 2.5.1). However, the minimal focal spot size achieved is around 5 µm, which does not allow very high resolution CT (i.e. order of 1 µm or below). Moreover, the cost of these liquid target X-ray sources is (still) rather high.

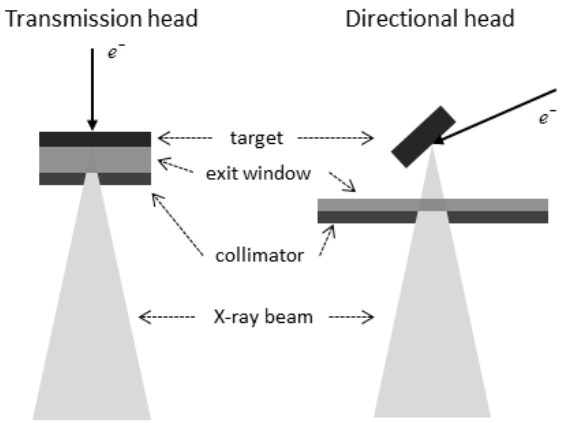

Figure 2.2: Schematic representation of a transmission (left) and directional head (right) of an X-ray tube

2.1.2 X-ray spectrum

The typical X-ray spectrum produced by conventional X-ray tubes for X-ray imaging is the result of two main interaction processes: *bremsstrahlung* and *characteristic radiation*.

Bremsstrahlung

The electrons striking the anode are deflected by the nuclei and electrons of the target material and thus lose energy which is emitted in the form of electromagnetic radiation, called *bremsstrahlung*. The energy of the produced photon depends on the energy fraction transferred from the electron to the photon, which in turn depends on the distance from the incident electron to the nucleus. The smaller the interaction distance, the higher the energy transfer. Impact with the nucleus results

in a complete transfer to the photon. Therefore, the bremsstrahlung spectrum is a continuum ranging from zero to the kinetic energy of the incident electrons. Since electrons with a higher energy are able to penetrate the electron cloud surrounding the atomic nucleus more easily than low energy electrons, they give rise to a higher photon yield. Furthermore, the bremsstrahlung yield is also dependent on the atomic number Z of the target material, with a higher Z corresponding to a stronger electromagnetic field surrounding the nuclei and thus resulting in a larger flux.

Characteristic X-rays

The impact of high energy electrons will also give rise to ionisation of the target material. A collision of an incident electron with a shell electron can result in the removal of the latter from its orbital shell. This is of course only possible if the energy from the incident electron is higher than the binding energy of the shell electron. The resulting vacancy in the shell is immediately filled by a higher-shell electron and the difference in binding energy can be released in the form of a photon with a well-defined energy. The photons created by this interaction process have energies with specific values characteristic for the Z-value of the ionised type of atom and are therefore referred to as *characteristic X-rays*.

The resulting X-ray spectrum consists of the continuous bremsstrahlung spectrum with characteristic X-ray peaks superimposed. An example is shown in figure 2.3.

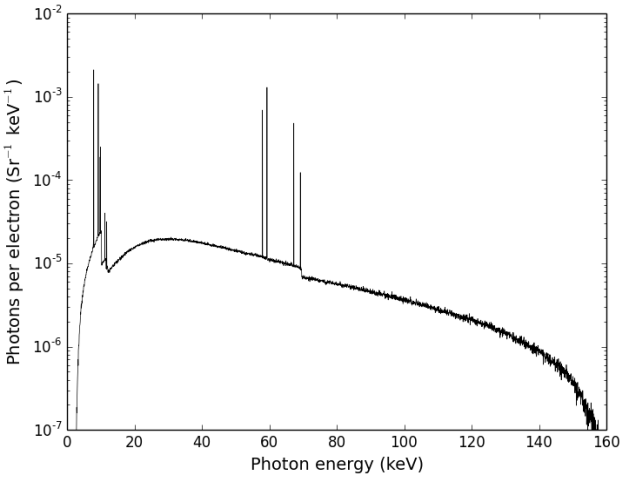

Figure 2.3: Example of a typical X-ray spectrum

2.2 Photon interaction processes

There are several possible interaction mechanisms X-rays in matter [5, 6]. For imaging purposes in the energy region of interest two types are predominant: *photoelectric absorption* and *Compton scattering*.

2.2.1 Photoelectric absorption

Photoelectric absorption leads to a complete transfer of the photon energy to an orbital electron from an atom. The incident photon will completely disappear and the electron, which is then called the photo-electron, is ejected from its shell due to the energy transfer. Of course, this process requires the photon energy to be higher than the binding energy of the shell electron. The resulting vacancy in the orbital shell will be immediately filled by a higher-shell electron or a free electron from the interaction medium. The energy that is released in this way is emitted as a secondary characteristic X-ray or in the form of an Auger-electron. Such an electron has a relatively low energy and will be stopped close to its origin. These secondary effects do not significantly influence the imaging process, but they represent an important contribution to the deposited dose in the sample. Photoelectric absorption occurs preferentially at the inner shell electrons. Therefore, the photoelectron will most likely originate from the K-shell of the atom for X-rays with a sufficiently high energy.

The probability of photoelectric absorption increases rapidly with increasing Z-value of the absorber material, but decreases towards higher photon energies. As a result, this is the predominant interaction process for low energy X-rays. The total probability (atomic cross section) of photoelectric absorption τ can be roughly approximated as follows:

$$\tau \cong constant \times \frac{Z^n}{E^{3.5}}, \tag{2.2}$$

where n varies between 4 and 5, and E represents the energy of the incident photon.

Figure 2.4 displays the total mass attenuation coefficient of tungsten and the contributions of the various photon interaction processes. This graph clearly shows that photoelectric absorption represents the predominant contribution in the lower energy range. Furthermore, the photoelectric curve contains a series of discontinuities, *absorption edges*, at photon energies corresponding to the binding energies of the orbital electrons from the absorber material. For instance, the discontinuity at the highest energy corresponds to the binding energy of the K-shell and is called the *K-edge*. Photons with an energy below this K-edge do not have enough energy

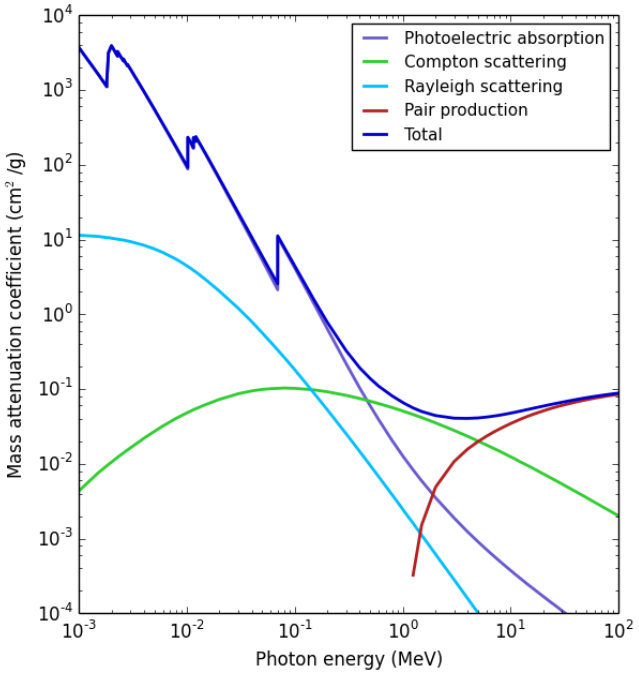

Figure 2.4: Mass attenuation coefficient of tungsten (data extracted from: [7])

for photoelectric absorption at the K-shell. Photons with an energy just above this edge do have the possibility to knock out a K-shell electron. Therefore, the attenuation coefficient shows a steep increase at this point. Evidently, the position of the absorption edges is unique for each absorber material, which is an important property.

2.2.2 Compton scattering

In *Compton scattering*, the photon behaves as a particle that performs a collision with an orbital electron from an atom of the absorber material. As a result, the photon is deflected at an angle θ with respect to its original direction. Part of the energy of the incident photon is transferred to this electron, which is then called the *recoil electron*. As such, the recoil electron (assumed to be initially at rest) acquires enough energy to leave the atom. Since the photon can be scattered in any direction, the transferred energy can vary from zero to a large fraction - but never all - of the initial photon energy. The angular distribution of the scattered photons

can be approximated by the *Klein-Nishina* differential cross section $d\sigma/d\Omega$:

$$\frac{d\sigma}{d\Omega} = Zr_e^2 \left(\frac{1}{1+\alpha(1-\cos\theta)} \right)^2 \left(\frac{1+\cos^2\theta}{2} \right) \left(1 + \frac{\alpha^2(1-\cos\theta)^2}{(1+\cos^2\theta)[1+\alpha(1-\cos\theta)]} \right), \tag{2.3}$$

with r_e the classical electron radius, $\alpha \equiv h\nu/m_e c^2$ and m_e the electron mass. In this approximation the electron is assumed to be *unbound* and *stationary*. Therefore, corrections have to be made for low incoming photon energies. On the other hand, in this energy range photoelectric absorption is predominant. A graphical representation of the distribution is shown in figure 2.5.

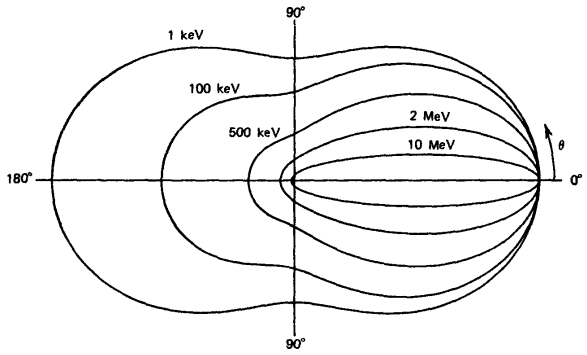

Figure 2.5: Angular distribution of Compton scattered photons with indicated initial energies [5]

Compton scattering can occur at Z electrons per atom. Therefore, the probability of this process increases linearly with Z. In addition, it increases slightly with the energy of the incident photon in the energy region of interest. By integrating equation 2.3, the total probability (atomic cross section) of Compton scattering can be approximated as follows:

$$\sigma \cong constant \times Zf(E), \tag{2.4}$$

with $f(E)$, the energy-dependent part.
In the typical energy range of X-rays produced by laboratory-based X-ray tubes, Compton scattering will be predominant for materials with a low atomic number. This is also clearly illustrated in figure 2.6, which shows the total mass attenuation coefficient of soft tissue as a function of energy and its different contributions.

The fact that the incident photons are deflected from their trajectory while still retaining part of their energy, may have an adverse effect on imaging since scattered X-rays could reach the detector. However, in micro-CT samples are positioned close to the source and thus far from the detector. The limited amount

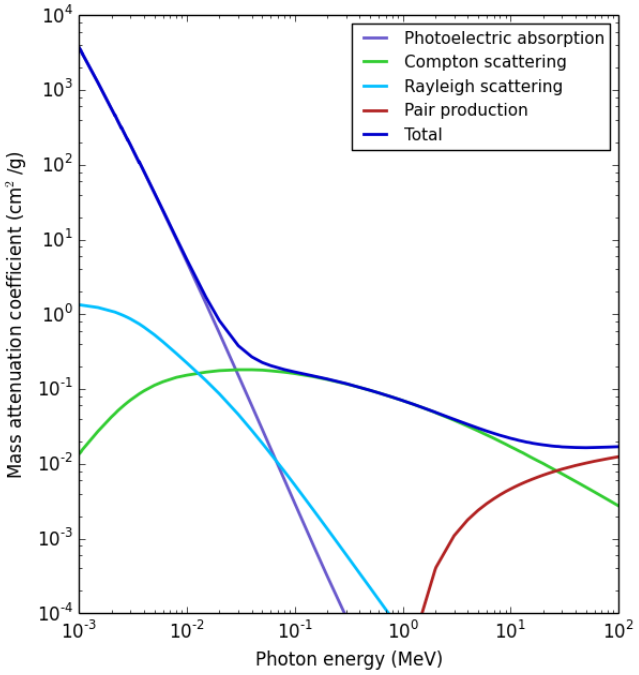

Figure 2.6: Mass attenuation coefficient of soft tissue (data extracted from: [7])

of scattered radiation that will reach the detector, will be almost homogeneously distributed and thus result in a small offset in the image.

2.2.3 Rayleigh scattering

In this second form of scattering, the incident photons interact coherently with all electrons from an atom of the absorber material. Therefore *Rayleigh scattering* is also known as *coherent scattering*. No energy is transferred in the process, so there is no ionisation or excitation. However, the photons can be deflected from their original trajectory and although this happens in a mainly forward direction, they can be removed from the primary X-ray beam. The probability for Rayleigh scattering decreases rapidly with increasing photon energy, but increases with increasing Z value of the absorber material. As a first approximation, this interaction process is negligible. However in the low energy range and for absorber materials with a high atomic number, this may be taken into account, especially when high accuracy is required.

2.2.4 Pair production

Pair production is a possible interaction process for photons with an energy above 1.022 MeV, which is twice the rest-mass energy of an electron. The photon disappears in the Coulomb field of an atomic nucleus from the absorber material and is replaced by an electron-positron pair with a kinetic energy equal to the excess energy, i.e. the initial photon energy minus the energy necessary for the creation of the pair (1.022 MeV). This interaction process is of course irrelevant for present purposes discussed in this work because of the high photon energies which are required.

2.2.5 Photonuclear absorption

At very high energies, photons can be absorbed by an atomic nucleus from the absorber material. This usually results in the emission of one or more neutrons and/or protons. This process is called *photonuclear absorption* and is again not relevant in this context.

2.2.6 Relative importance of photon interaction processes

Figure 2.7 illustrates the relative importance of the three principal photon interaction processes as a function of the incident photon energy and the absorber material. The line at the left represents Z as a function of energy for which photoelectric absorption and Compton scattering are equally probable. The line at the right connects the Z values at energies for which Compton scattering and pair production are equally probable. As explained above, the latter interaction process is irrelevant in this context. For heavy absorber materials and at apparently low X-ray energies, photoelectric absorption will be predominant. Note that for light materials, Compton scattering already takes over at relatively low photon energies. This is also evident when comparing figures 4.8(c) and 2.6.

2.2.7 Wave properties of X-rays

X-rays, being a form of electromagnetic radiation, are also subject to the wave-particle duality. In the previous sections, X-ray interactions were described from the "particle" point of view as interactions between photons and matter. On the other hand, X-rays can also manifest themselves as waves propagating through a medium. As such they can give rise to wave related effects. Like any form of wave, an X-ray wave can be defined by a frequency, amplitude and phase. While propagating through a medium, the wave is subject to attenuation resulting in a decrease of amplitude. Furthermore a phase shift will occur due to differences in propagation velocity depending on the medium. This causes a perturbation of the wavefront close to the edge of the absorber material. For features larger than the

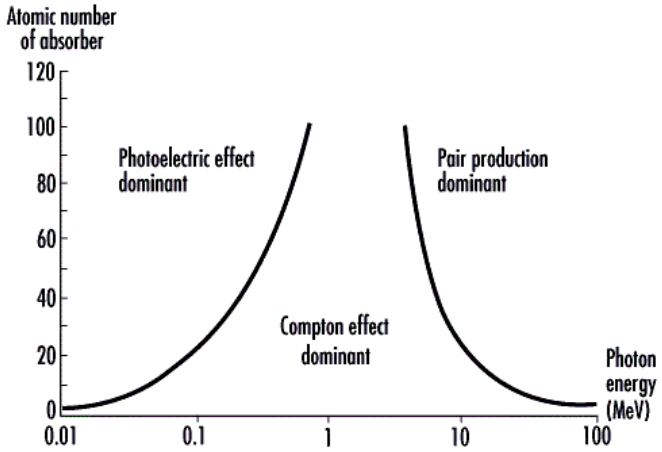

Figure 2.7: Relative importance of the three principal photon interaction processes [8]

wavelength of the X-rays, the ray optical approach, i.e. each part of the wavefront can be represented by a ray perpendicular to the front, is valid. Using this approach, the phase shift that occurs can be seen as a change of direction of the incident ray, which is then called *refraction*. As a result, X-rays close to material edges change their trajectory causing an apparently lower transmission here, while more X-rays arrive in the adjacent regions resulting in an enhancement of the edges. On the other hand, at distances further away from the object, interference occurs between the original and perturbed wavefront resulting in a complex pattern of intensity variations. This effect is called *diffraction*, for which the ray optical approach is no longer valid.
Such wave related effects may emerge in X-ray imaging and should thus be taken into account. This is extensively discussed in [9].

2.3 Attenuation of X-rays

In contrast to charged particles, photons are electrically neutral and therefore do not gradually lose energy while traveling through an absorber material. Instead, they are able to penetrate the material for some distance before an interaction takes place. This is a statistical process described by *attenuation coefficients* [5].

2.3.1 Linear attenuation coefficient

After passage through a medium, the X-ray beam will be attenuated due to individual interactions of the incident photons with atoms of the absorber, via photoelectric absorption, Compton scattering and to a limited extent Rayleigh scattering.

Note that pair production and photonuclear absorption are disregarded in the context of this work. Rayleigh scattering can also be neglected given the fact that the photons are hardly deflected from their trajectory and there is no energy loss. The probability per unit path length that a particular photon interacts in the medium and as such disappears from the original X-ray beam is called the *linear attenuation coefficient* μ. This is strongly dependent on the incident photon energy and the density of the medium. Furthermore its energy behaviour is also uniquely dependent on the atomic number of the absorber material. Note that not all photons that disappear from the original beam are completely absorbed by the medium. Some photons are merely deflected, with or without loss of energy.

Consider a narrow mono-energetic X-ray beam containing N_0 photons perpendicularly incident on a slab (Fig.2.8) [6]. As the beam penetrates the slab, it will be attenuated. Let $N(x)$ be the number of photons which are left after traveling a distance x inside the material. The number of photons that will interact in the next distance $\mathrm{d}x$ can be written as follows:

$$\mathrm{d}N = -\mu N \mathrm{d}x. \tag{2.5}$$

Integration of (2.5) results in the following equation:

$$N(x) = N_0 e^{-\mu x}. \tag{2.6}$$

From (2.6) it is evident that the attenuation of mono-energetic photons exhibits an exponential behaviour. Laboratory-based X-ray tubes produce polychromatic X-ray spectra. In this case equation 2.6 can be rewritten as follows:

$$N_d = \int_0^{E_{Max}} N_0(E) e^{-\mu(E)d}\, \mathrm{d}E \tag{2.7}$$

with N_d the number of photons which are left in the X-ray beam after a distance d.

The linear attenuation coefficient is composed of the contributions from the various photon interaction processes that can remove the photons from the original photon beam. Thus, μ can be written as the sum of the probabilities per unit path length (i.e. the linear attenuation coefficients) for photoelectric absorption (μ_τ) and Compton scattering (μ_σ):

$$\mu = \mu_\tau + \mu_\sigma. \tag{2.8}$$

The linear attenuation coefficient can also be related to the atomic cross sections for each process as follows:

$$\mu = \frac{N_A}{A}\rho(\tau + \sigma). \tag{2.9}$$

with N_A Avogadro's number, A the atomic weight and ρ the density of the material. Note that $\frac{N_A}{A}\rho$ equals the atomic density of the medium, expressed in $1/cm^3$.

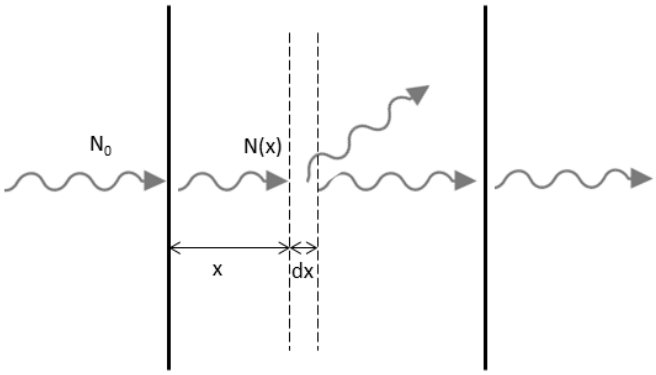

Figure 2.8: Narrow mono-energetic X-ray beam of N_0 photons perpendicularly incident on a slab. $N(x)$ is the number of photons that will reach a depth x without having an interaction.

2.3.2 Mass attenuation coefficient

Since the linear attenuation coefficient varies with the density of the medium even if the material remains the same, the *mass attenuation coefficient* μ/ρ is more widely used. As such the mass attenuation coefficient is also independent of the physical state of the material, e.g. for a given photon energy μ/ρ remains equal for a material in solid or in liquid state. Using (2.2) with n = 4, (2.4), (2.8) and (2.9), the mass attenuation coefficient can be written as follows:

$$\frac{\mu}{\rho} = \frac{\mu_\tau}{\rho} + \frac{\mu_\sigma}{\rho} = \frac{N_A}{A}(\tau + \sigma) \cong N_A \left(\frac{Z}{A}\right) \left(c_1 \times \frac{Z^3}{E^{3.5}} + c_2 \times f(E)\right), \quad (2.10)$$

with c_1 and c_2 two constants. Since Z/A is approximately 0.5, except for hydrogen and slight deviations towards heavier elements, (2.10) can be further simplified:

$$\frac{\mu}{\rho} = \frac{\mu_\tau}{\rho} + \frac{\mu_\sigma}{\rho} \cong \left(c_1' \times \frac{Z^3}{E^{3.5}} + c_2' \times f(E)\right). \quad (2.11)$$

As such, it is clear that the mass attenuation coefficient for Compton scattering is nearly independent of the atomic number of the medium. The mass attenuation coefficient for a compound or mixture of elements can be written as follows:

$$\left(\frac{\mu}{\rho}\right)_c = \sum_i w_i \left(\frac{\mu}{\rho}\right)_i \quad (2.12)$$

with w_i the weight fraction of element i.

2.3.3 Mass energy-absorption coefficient

As explained above, the linear attenuation coefficient describes the probability that a photon undergoes an interaction per unit path length. Therefore, in equation 2.6 every photon that interacts over a distance x is considered removed from the original beam. However, as also explained, the energy of the interacting photons is not always completely absorbed by the medium. This is especially important in dosimetry. Like the number of photons, the intensity of the X-ray beam decreases exponentially in a medium. Intensity I is defined as the energy that passes per second and per unit area perpendicular to the beam, expressed in W/m^2. The decrease in intensity however should be lower than expressed by the linear attenuation coefficient. It can instead be described by the *mass energy-absorption coefficient* μ_{en}/ρ, which is both energy- and material-dependent. Analogous to equation 2.6 the beam intensity $I(x)$ after a distance x can be written as follows:

$$I(x) = I_0 e^{-\mu_{en} x}, \tag{2.13}$$

with I_0 the original monochromatic beam intensity. $I(x)$ thus contains the energy of photons which have not interacted with the medium as well as scattered and secondary photons such as bremsstrahlung and fluorescence photons. Therefore, $I(x)$ is no longer monochromatic, but instead is a value integrated over the polychromatic spectrum at distance x.
Note that equation 2.6 is commonly written using intensities instead of photon numbers and is known in this form as the law of Lambert-Beer:

$$I(x) = I_0 e^{-\mu x}. \tag{2.14}$$

This is a valid approximation, but it should be kept in mind that it is only applicable for monochromatic radiation and that the intensity I contains only photons that did not interact. Equation 2.14 can also be written as follows:

$$I(x) = I_0 e^{-\left[\int_{\mathcal{L}} \frac{\mu(s)}{\rho(s)} \cdot \rho(s) \mathrm{d}s\right]}, \tag{2.15}$$

with $\mathcal{L}$ the radiation path from source to detector position and s the actual position along this radiation path.

2.4 CT-Workflow

The process of visualising an object using X-ray computed tomography takes place according to a typical workflow. First, radiographic projections of the sample are acquired in the *acquisition* phase. These projections are then reconstructed to obtain virtual cross sections through the object in the *reconstruction* phase. Finally, this virtual representation of the sample can be visualised and analysed using specific software packages (the *visualisation and analysis phase*).

2.4.1 Acquisition

Unlike medical scanners where the X-ray tube and detector revolve around the patient, micro-CT scanners are usually built with the tube and detector at a fixed position while the sample rotates. This is illustrated in figure 2.9. The X-ray source produces a conical, polychromatic X-ray beam. The sample is placed in the beam and undergoes a rotation about its axis by means of a rotation motor. By means of a three-axis motor system, the object can be precisely positioned in the centre of the field of view. Furthermore, it can be moved further away or closer to the source depending on the sample size or the required magnification. After passage through the sample, the remaining X-rays are registered by the detector.

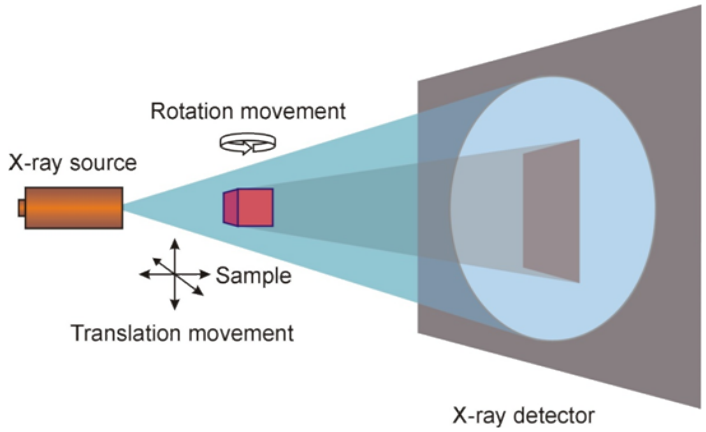

Figure 2.9: Schematic representation of a cone beam CT setup [10]

Each sample requires an optimal scanning setup according to its size, composition, density and the desired resolution. At the Centre for X-ray Tomography of the Ghent University (UGCT), several high resolution CT scanners are present, each home developed for different fields of application. Besides using the appropriate scanner, other scanning parameters such as tube voltage, beam filtration and exposure time per projection should be adequately chosen prior to acquisition.

During the actual acquisition phase, three sets of images are acquired:

- **Dark fields:** These images are recorded with the X-ray tube turned off. Dark fields capture the detector response in absence of X-rays, such as possible pixel offsets and dark current contributions. Due to the temporal nature of the latter, ideally the acquisition time of a dark image should be equal to that of a flat field. In practice, multiple dark fields are taken and averaged.

- **Flat fields:** Flat fields are acquired with the X-ray tube turned on, but the sample is removed from the field of view. In this way inhomogeneities in both the X-ray beam profile and the detector response are registered and can be corrected for in the actual projections images. Note that the heel effect is clearly visible in the flat fields in case of a directional tube and as such it can also be visually eliminated from the final images. Again, in practice, multiple flat fields are taken and averaged.
- **Projection images:** For the actual projection images, the sample is of course positioned in the field of view and the X-ray tube is turned on. As mentioned above, the sample undergoes a stepwise rotation with a fixed angular step. Projection images are recorded at each step. Usually the sample is rotated over 360 degrees, but a smaller angular range is also possible for short scans.

2.4.2 Reconstruction

After acquisition, the projection images need to be *normalised*, using the following formula:

$$T(i,j) = \frac{I(i,j) - D(i,j)}{F(i,j) - D(i,j)}, \tag{2.16}$$

with $T(i,j)$ the normalised intensity value of pixel (i,j). Similarly $I(i,j)$, $D(i,j)$ and $F(i,j)$ correspond to the intensity values of that pixel in the projection images, dark fields and flat fields, respectively. In this way transmission images are obtained with values between 0 and 100%. The normalised images may further be filtered by applying a spot filter and/or ring filter to avoid artefacts after reconstruction. For instance, fixed-pattern noise, such as an individual pixel that deviates systematically from its neighbours, can still be present after normalisation and will give rise to a ring artefact in the reconstructed image. By applying a ring filter such systematic pixel deviations can be removed.

Eventually, the normalised and filtered images can be reconstructed using the appropriate reconstruction algorithm to obtain a virtual 3D representation of the sample. This 3D representation is composed of small volume elements of a given size, called *voxels*. Each voxel contains a calculated value representing the linear attenuation coefficient for the materials present in that voxel. To obtain this value, the linear attenuation coefficient for each position (x,y,z) in the sample can be calculated by solving the line-integral, derived from equation 2.15:

$$\int_{\mathcal{L}} \mu(x,y,z)\mathrm{d}s = -ln\left(\frac{I}{I_0}\right). \tag{2.17}$$

There are several reconstruction algorithms based on analytical or iterative methods. The implementation of these methods will also depend on the scanner

geometry. Reconstruction algorithms are thoroughly discussed in [11] and [12]. To give a basic idea of how projection data can be transformed into a 3D representation of the sample composed of a stack of cross sections, consider a parallel X-ray beam and a single cross section of the sample resulting in one-dimensional projection data. In this case, the analytical *Filtered Back Projection* (FBP) algorithm can be used, which is illustrated in figure 2.10. Figure 2.10a shows a single attenuation line profile containing the sum of all the information about the sample along this radiation path. The information can be smeared out (*back-projected*) along this path. Doing this from multiple points of view will already bring forward the object in the reconstructed slice (Fig. 2.10b). However, also a starburst pattern and blurry edges are introduced by using a simple back-projection. This can be avoided by applying an additional filter first (Fig. 2.10c). The resulting negative values in the line profile will cancel out the starburst pattern and a clean representation of the sample is retrieved (Fig. 2.10d). For laboratory based high resolution

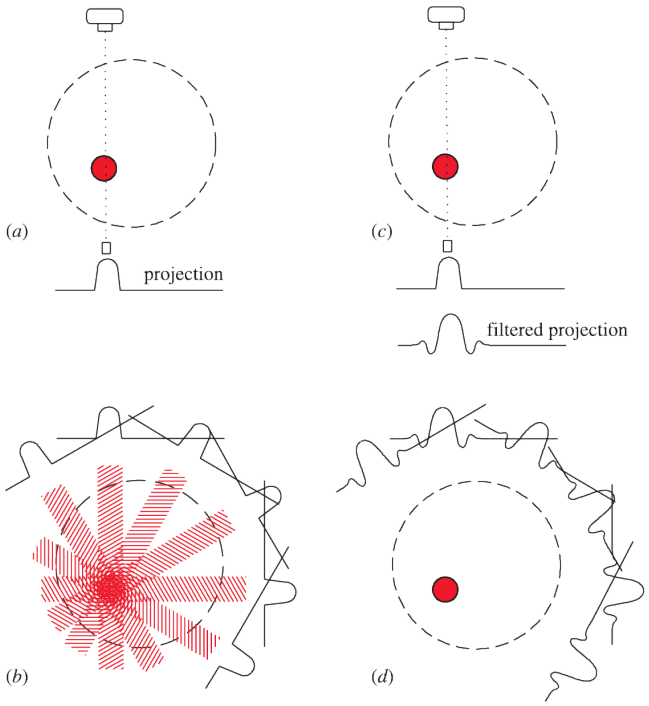

Figure 2.10: Principle of filtered back-projection for a parallel beam geometry [13]

X-ray tomography systems, typically a cone beam geometry is used. The previously described FBP reconstruction algorithm was adapted for cone beam geometry by Feldkamp, David and Kress [14]. The resulting FDK algorithm is the most commonly used reconstruction technique at present.

2.4.3 Visualisation and analysis

After acquisition and subsequent reconstruction a virtual 3D representation of the sample is available and can be visualised using 3D rendering software packages such as VGStudio MAX [15] and Avizo [16]. These programs also offer the possibility to obtain quantitative information about the object. Other 3D analysis software packages include Octopus analysis (see section 2.6.2), Mimics (Materialise, [17]), MAVI (Fraunhofer, [18]), Blob3D [19] and Pore3D [20].

2.5 A few important X-ray tomography concepts

In this section some other concepts are discussed that are highly relevant in high resolution X-ray computed tomography.

2.5.1 X-ray flux

The flux of the X-ray beam equals the number of photons that passes per second and per unit area perpendicular to the beam, and is proportional to the target current. The generated flux will largely determine how many photons may reach the detector after passage through the sample and as such it is an important parameter for the amount of statistical information in the images. If the flux is higher, more photons will be able to reach the detector so that a higher signal-to-noise ratio and thus a better image quality can be achieved. On the other hand, if the images already have the desired quality, a higher flux can allow for a shorter scanning time with the same amount of statistical information. The flux generated by laboratory based X-ray tubes for high resolution CT is typically rather low due to two important limitations. The first limiting factor is the focal spot size. This is the size of the spot created by the accelerated electrons inside the target and from which the produced X-rays are emitted. To obtain high resolutions, the spot size has to be kept as small as possible (see also section 2.5.2). However, the thermal load on the target becomes an important issue in this case. The electrons deposit most of their kinetic energy inside the target and this energy is largely converted into heat. This can lead to melting of the target material. To prevent this from happening, the electron beam needs to be slightly unfocussed on purpose once the target current reaches a certain level and this is of course at the expense of the achievable resolution. The second limiting factor is the filament, which can be damaged when the tube current exceeds its maximum value. At synchrotron installations, high resolution X-ray tomography is possible using a high generated flux.

Another important parameter is the source-to-detector distance. The flux of the X-ray beam will decrease quadratically as a function of distance. A large source-detector distance will result in a lower signal-to-noise ratio, since the amount of

photons that are able to reach the detector is smaller. On the other hand, a higher magnification can be obtained and cone beam artefacts can be reduced if the detector is positioned further away from the source.

2.5.2 Spatial resolution

Looking back at figure 2.9, it is clear that positioning a sample closer to the source will result in a larger magnification. This is however limited by the sample size, since large objects need to be moved further away from the source to be able to capture the whole object in a single projection image. The magnification M can be expressed as:

$$M = \frac{SDD}{SOD}, \tag{2.18}$$

with SDD and SOD the source-detector and source-object distance respectively.

For very small samples, the finite dimension of the focal spot size becomes the limiting factor for the achievable resolution. This is illustrated in figure 2.11. At large magnifications, a geometrical unsharpness U_G is created, given by:

$$U_G = d_s(M - 1), \tag{2.19}$$

with d_s the focal spot size. For a sharp image, the geometrical unsharpness needs to be smaller than the pixel size of the detector d.

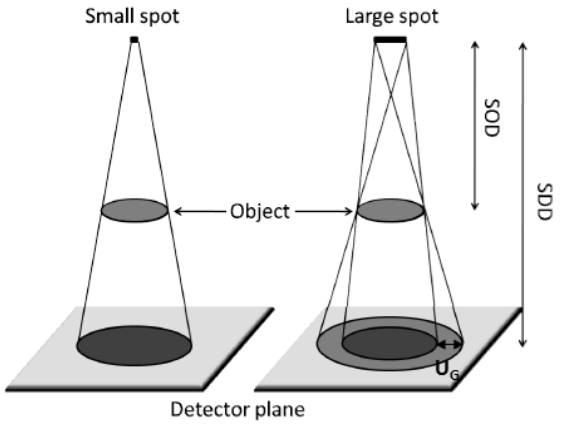

Figure 2.11: Influence of focal spot size on image sharpness [11]

The resolution or resolving power R of an imaging system is equal to the smallest distance between to features at which they can still be distinguished from

one another. For a point source, this can be expressed as:

$$R = \frac{d}{M}. \tag{2.20}$$

For a finite spot size, the geometrical unsharpness should be taken into account and the best achievable resolution becomes:

$$R = \frac{d}{M} + \left(1 - \frac{1}{M}\right) d_s \tag{2.21}$$

For large magnifications ($M \rightarrow \infty$) as is the case in very high resolution CT, $R \approx d_s$, which means that the resolution can never be smaller than the focal spot size.

2.5.3 Beam hardening

As mentioned earlier, the law of Lambert-Beer (2.15) is only valid in case of a monochromatic X-ray beam. On the other hand, laboratory-based X-ray tubes typically produce a polychromatic spectrum ($I(E)$). Not only the linear attenuation coefficient, but also the detector efficiency will depend on the photon energy. For a polychromatic X-ray beam, equation 2.15 should be rewritten as follows:

$$I = I_0 \frac{\int I(E) \exp(-\int_{\mathcal{L}} \mu(s, E) \mathrm{d}s) \gamma(E) \mathrm{d}E}{\int I(E) \gamma(E) \mathrm{d}E}, \tag{2.22}$$

with $\gamma(E)$ the energy-dependent detection efficiency. As demonstrated in section 2.2 and 2.3, the linear attenuation coefficient is larger at lower photon energies and as such low energy X-rays are more easily attenuated than high energy X-rays. As a result, the mean beam energy will shift to higher energies as the beam passes through the sample. This effect is called *beam hardening*. Figure 2.12 shows the detected energy as a function of energy without filter and for increasing thicknesses of aluminium filtration. This is simulated with the Setup Optimiser, which will be discussed in chapter 3. The directional X-ray tube of Nanowood operated at 100 kV in combination with the Varian flat-panel detector were used for the simulation, with a source-detector distance of 1 m. The graph clearly shows that the lower energy photons are preferentially stopped and the spectrum gradually shifts towards higher energies with increasing thickness of aluminium filtration. This can also be quantified by calculating the mean energy of the spectrum emitted by the source after filtration. These values are listed in table 2.1. Without filter material, the mean energy of the emitted spectrum is 26.9 keV. The addition of 1 mm aluminium makes it already increase to 43.6 keV. Thicker slices of aluminium lead to a further increase in mean energy, and thus further beam hardening.

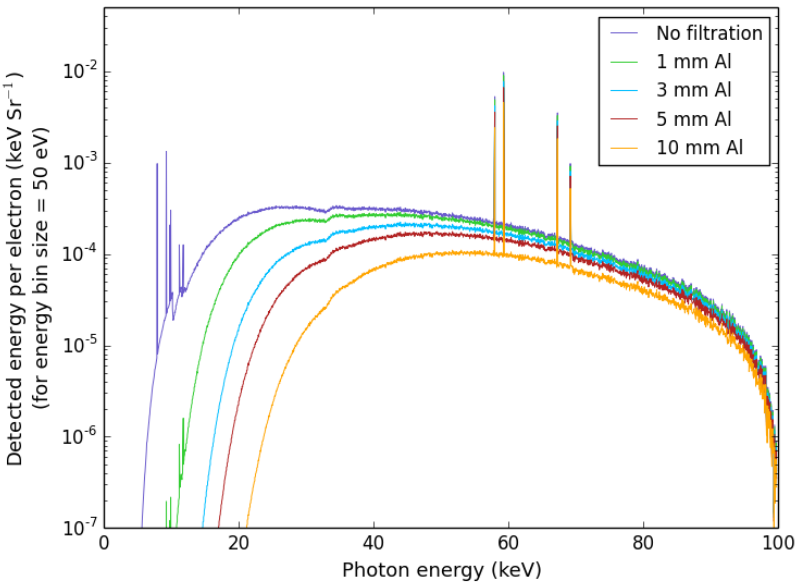

Figure 2.12: Detected energy as a function of energy for increasing thicknesses of aluminium filtration, illustrating the fact that low energy X-rays are more easily stopped than high energy X-rays.

Table 2.1: Mean energy of the spectrum emitted by the source after filtration

Filter	No filter	1 mm Al	3 mm Al	5 mm Al	10 mm Al
Mean energy (keV)	26.9	43.6	48.8	51.8	56.4

Most reconstruction algorithms ignore the energy dependency and simply use equation 2.15. This leads to the formation of typical artefacts in the reconstructed slices, called *beam hardening artefacts*. For example *cupping* is the result of the fact that relatively more photons will be absorbed in the outer layer of a mono-material and will as such show a higher attenuation coefficient compared to the inner part (see Fig. 2.13(a)). Furthermore, due to beam hardening also smearing and *streak artefacts* will arise in the reconstructions (see Fig. 2.13(b)). All these artefacts are of course unwanted. There are three ways to compensate for beam hardening: physical filtration, dual energy techniques and algorithmic corrections. By using filtration, the spectrum will be hardened in advance and the beam hardening that occurs inside the sample will be reduced. The application of dual energy techniques will also eliminate beam hardening. Dual energy CT will be discussed in chapter 4. Finally, algorithmic corrections will remove the influence of beam hardening computationally. This is discussed in [12]. At UGCT also

a beam hardening correction algorithm was developed which is incorporated in the forward projector of the simultaneous algebraic reconstruction technique (SART), available in Octopus Reconstruction [21].

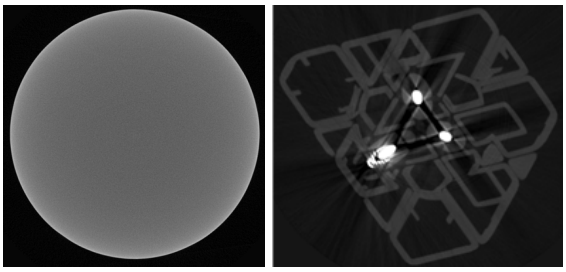

(a) (b)

Figure 2.13: Reconstructed slice of an aluminium sphere to illustrate cupping (a) and reconstructed cross-section of a toy containing metal with clear streak artefacts present (b)

2.5.4 Partial volume effect

As mentioned above, each voxel in the reconstructed image contains a calculated value which represents the weighted average of the linear attenuation coefficients of the materials present in that voxel. *Partial volume effect* can be intuitively understood looking at figure 2.14. Consider the straight edge of a copper plate. If this edge exactly coincides with the edge of the voxels in the reconstructed image, the transition between air and copper will be sharp with black voxels representing air and white voxels representing copper. However, in reality sample edges will not precisely coincide with voxel edges. The voxels through which the copper edge runs, will contain a mixture of both materials and as such become grey in the CT image. It is clear that the partial volume effect may complicate a quantitative analysis in which segmentation of the data is performed.

2.5.5 Radiation dose

In clinical and preclinical (small animal) CT another highly important concept is absorbed dose deposition by the radiation. Typical absorbed doses received by small animals in the current preclinical micro-CT systems vary from 6 mGy, for the shortest full-body scan [22], to as high as 0.5 Gy [23–25]. This large range is of course due to the many variations in scanner settings. Higher quality scans, using a larger target current and/or longer exposure time, will naturally lead to a higher absorbed dose. Absorbed doses will also increase as the resolution improves. As such, *in vivo* small animal micro-CT is limited to a resolution down to 50 µm.

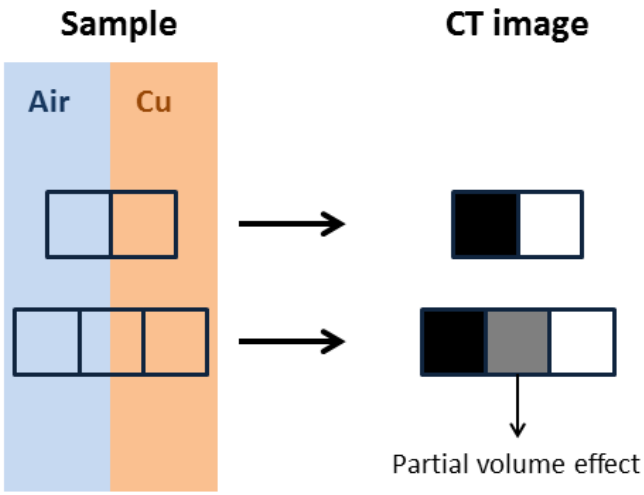

Figure 2.14: Schematic representation of the partial volume effect. Voxels containing exclusively air are black in the CT image and voxels solely copper are white. Voxels containing a mixture of both will become grey and are therefore difficult to classify.

As mentioned before, UGCT focuses (almost) exclusively on *ex vivo* CT applications. Therefore, absorbed dose deposition during a CT scan has only rather recently become a subject of research at the Radiation Physics group. In addition, due to the large variety of samples scanned at UGCT, requiring a wide range of scanner settings, dose calculations are not at all straightforward to perform. Therefore, it is up to now not possbile to provide accurate values of absorbed doses for different tissue samples, even for biomedical samples. However, based on Monte Carlo simulations that were performed for a cubic centimetre of water (data not shown here), a rough estimate can be given. For a typical biomedical sample as shown in this work, i.e. a stained mouse hind leg, the absorbed dose deposition in the sample will vary from 50 to 100 Gy.

2.6 UGCT

About thirteen years ago a collaboration arose between the research groups "Radiation Physics" (led by Prof. L. Van Hoorebeke, Department of Physics and Astronomy, Ghent University) and "Sedimentary Geology and Engineering Geology" (at that time led by Prof. P. Jacobs and now led by Prof. V. Cnudde, Department of Geology, Ghent University) around 3D computer tomography using X-rays and neutrons. In October 2006, this resulted in the foundation of the "Centre for X-ray tomography of the Ghent University", UGCT, which specialises in very high

resolution X-ray tomography. A few years later the "Laboratory of Wood Technology" (Woodlab, led by Prof. J. Van Acker, Department of Forest and Water Management, Ghent University) joined UGCT as well. In 2008, UGCT became the origin of a spin-off company *inCT*, currently known as *Inside Matters*, which offers X-ray services to companies and commercially distributes the reconstruction software package Octopus Reconstruction and the 3D analysis software package Octopus Analysis [26]. In 2011, *X-Ray Engineering*, XRE, a second spin-off company was founded. XRE provides state-of-the-art X-ray imaging solutions from conceptual design up to the development and delivery of a complete system [27]. The geology research group recently changed its name to "Pore-Scale Processes in Geomaterials Research group (PProGRess).

The main focus of the Radiation Physics group, in which this work was performed, involves the complete CT-workflow, including the development of state-of-the-art high resolution CT scanners and their applications. The scanners are characterised by a flexible, modular structure so that optimal scanning conditions can be created for a wide range of samples. Moreover, improvements and modifications can be made to meet the needs of the user. The software for the control of the scanners is in-house developed, which also allows for a greater flexibility in the use of these scanners. Furthermore simulation, reconstruction and 3D analysis methods and software is developed as well. As such, every step of the CT-workflow is covered and can be fully controlled and optimised. In the following subsections an overview of the scanners and software packages at UGCT is given.

2.6.1 Scanners

Nanowood

Nanowood (Fig. 2.15) is a versatile high resolution CT scanner primarily developed for research on wood and wood-related samples, but it can of course be used for many other applications [28]. It is equipped with two complementary X-ray sources. The closed-type Hamamatsu directional tube can generate high voltages up to 130 kV and allows for focal spot sizes down to 5 μm and a maximal power of 39 W, ideal for samples ranging from a few mm up to tens of centimeters in size. For smaller samples, the open-type Hamamatsu transmission tube is used. This tube has a 100 kV high voltage generator and a maximal power of 3 W. Focal spot sizes down to 400 nm can be generated with good stability. Nanowood is also equipped with two different detectors with a complementary spectral sensitivity. For larger samples, a 25 by 20 cm Varian amorphous Si flat-panel detector can be used. It consists of a CsI scintillator with a useful detection efficiency from about 20 to 130 keV and has 1920 by 1536 pixels with a pixel size of 127 μm. For the

smallest and lightest samples, the 30 by 25 mm Photonic Science VHR CCD detector is available. It has 4000 by 2667 pixels with a pixel size of 7.4 μm and is coupled to a Gadolinium oxysulfide (Gadox) scintillator layer. The detection efficiency for this camera is optimal at 10 keV, but does not exceed 20 keV. Further details can be found in [28].

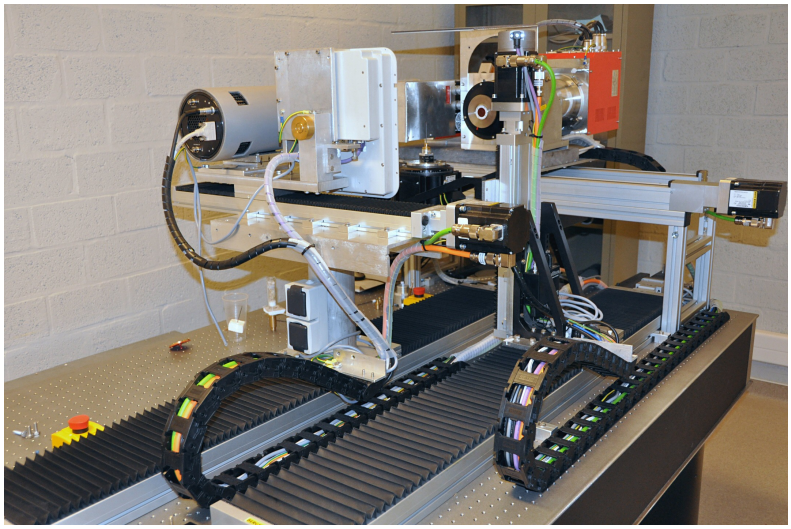

Figure 2.15: The Nanowood scanner located at the Woodlab

HECTOR

For Nanowood, the focus was mainly on achieving very high resolutions, which comes at a cost of limited tube voltages. For many samples, due to their size and/or composition, the transmission of X-rays through the object will be insufficient to obtain the desired image quality at these limited voltages. For these purposes a **High-Energy CT system Optimised for Research**, shortly HECTOR (Fig. 2.16), was developed in collaboration with XRE [29]. This scanner has a microfocus X-ray source from X-RAY WorX with a directional tube that can generate high voltages up to 240 kV. The tube has a maximum power of 280 W and a minimum focal spot size of 4 μm. HECTOR is equipped with a large Perkin Elmer flat-panel detector of 40 by 40 cm. The source-detector distance can be altered from 30 cm up to 200 cm. The high-precision rotation stage can carry a load of up to 80 kg. Samples up to 1 m long and 80 cm in diameter can be imaged. Further details are described in [29].

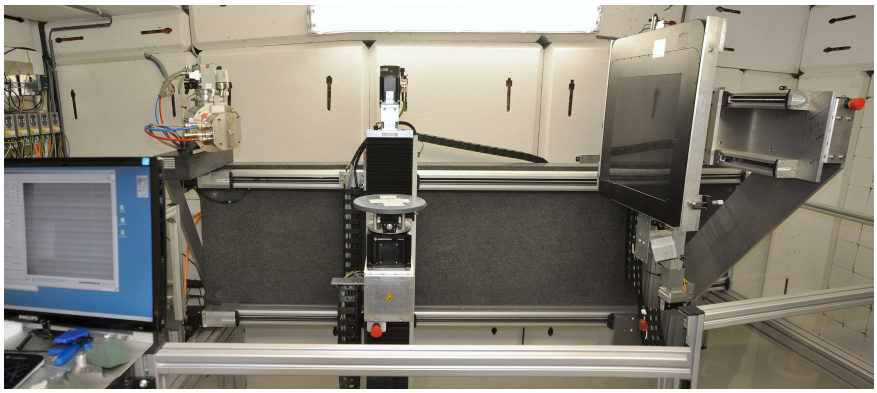

Figure 2.16: The High-Energy CT system Optimised for Research (HECTOR) at UGCT

Medusa

The first very high resolution CT scanner at UGCT, described in [30], has recently been re-designed and is now called Medusa. (Fig. 2.17) The system has a 160 kV FeinFocus transmission type X-ray source which can generate focal spot sizes down to 900 nm. Similar to Nanowood, Medusa is equipped with two different detectors with a complementary spectral sensitivity: a large-area Varian flat-panel detector for more absorbing objects and a Photonic Science VHR detector for light, low-density objects. These detectors are mounted on a linear motorised stage with additional available space so that also other detectors may be easily tested.

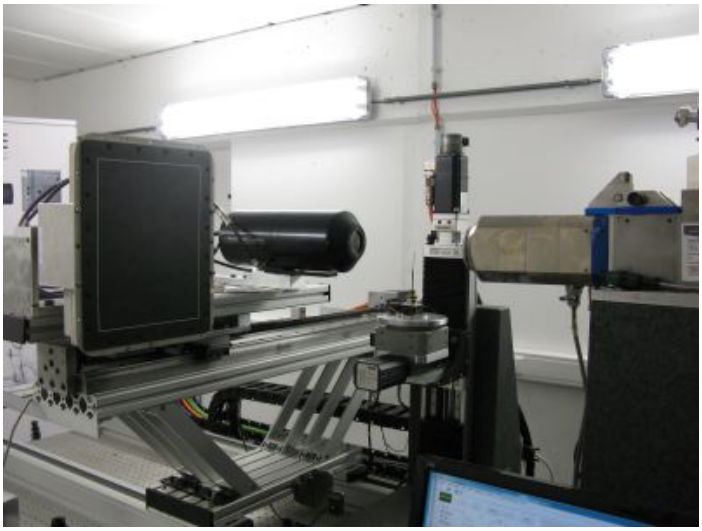

Figure 2.17: The Medusa scanner at UGCT

EMCT

The scanners described so far have a rotational stage for the sample, while source and detector remain spatially fixed during the scan. However, some samples cannot be easily mounted on a rotation stage, for instance when they are connected to additional experimental hardware for the application of external forces to the object such as pressure, or for controlling environmental parameters of the object such as temperature. For these purposes a gantry-based system was designed, the **Environmental Micro-CT** or EMCT (Fig. 2.18), where the source-detector assembly rotates around a fixed sample [28]. Unlike medical CT scanners, the source and detector are mounted horizontally on a linear motorised stage so that the magnification can be modified. This magnification stage is carried by a large goniometer, with a positional accuracy of less than 5 μm, on a firm granite base plate. A vertical stage with a 800 mm travel range is used to position the sample. This stage is mounted under the granite base. Furthermore, a custom-designed slip-ring system is embedded in the granite to transmit power and safety interlocks. The system allows for fast and continuous CT scanning at up to 5 full rotations per minute. A closed directional 130 kV X-ray source is used with a maximum power of 39 W and a minimum focal spot size of 5 μm. The detector is a CMOS flat panel of 1316 by 1312 pixels with a CsI-scintillator. Further details are explained in [28].

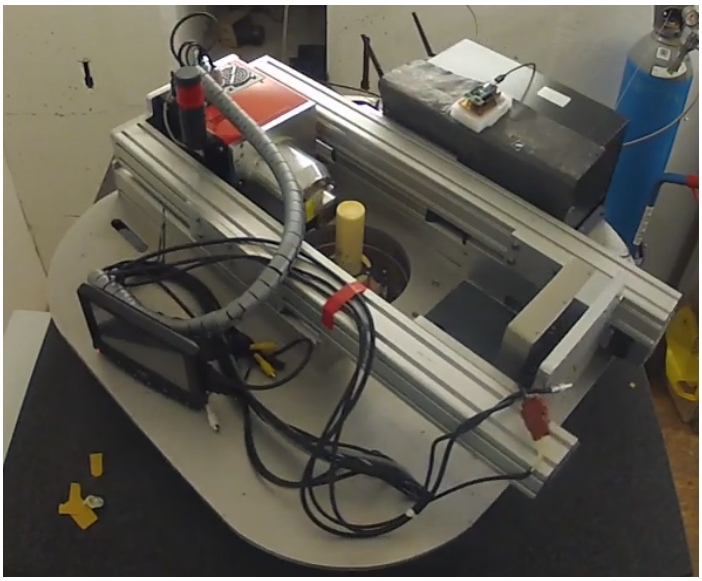

Figure 2.18: The Environmental micro-CT scanner (EMCT) at UGCT

Herakles (XMI-UGCT)

Herakles is a system designed for high-resolution visualisation, and subsequently actual characterisation and element identification of certain regions of interest in the sample under study. This is done by combining micro-CT and micro-X-ray fluorescence (XRF). Herakles contains three scanning stages: one high-resolution CT stage and two micro-XRF stages. These stages are linked via an air-beared positioning system, with a very high accuracy (10 μm) to ensure correct image correlation. Herakles is designed and constructed by the Radiation Physics group in collaboration with the X-ray Microscopy and Imaging group (XMI, led by Prof. L. Vincze). The system is currently in its final stages of construction.

2.6.2 Software

Acquila

As already mentioned above, the control software for the scanners is in-house developed. Since the scanners are each built for a specific purpose, their physical implementation can be quite different. However, their basic functionality is essentially identical. Therefore, a generic software platform was developed using LabVIEW® [31]. In this way, each scanner shares the same interface and functionality. The main advantages of the platform lie in the fact that it is generic, scalable, highly efficient, straightforward to develop and extend, and that it can easily be implemented for future scanners. The software was further developed and extended into the modular software platform, Acquila, which is also being used by XRE [27].

Octopus Reconstruction

Octopus Reconstruction is an in-house developed software package for the reconstruction of parallel, fan, cone and helical cone beam computed tomography [32, 33]. Advanced artefact reduction algorithms are implemented as well. The software package is characterised by a high performance which can be further optimised by distributing the calculations to multiple CPU cores or a graphics processing unit (GPU). Octopus Reconstruction is commercially distributed by Inside Matters [26]. The package also contains an iterative reconstruction add on module using the Simultaneous Algebraic Reconstruction Technique (SART).

Octopus Analysis

Octopus Analysis, formerly known as Morpho+, is an in-house developed software package for 3D analysis of reconstructed data [10, 33]. Originally, the main focus of the program was to be able to process very large data sets (up to 8 gigavoxel)

in a reasonable amount of time. The program has grown into a comprehensive 3D analysis software package, which provides several parameters and routines applicable in various research fields [12, 34]. It is still constantly being expanded with new parameters and algorithms. Octopus analysis is commercially distributed by Inside Matters as well [26].

Arion and Setup Optimiser

Arion is a GPU-based program for fast and realistic simulations of radiographic projections that has recently been developed at UGCT [35]. It also includes a simulation tool, called the Setup Optimiser, which is used to evaluate the influence of different scanner settings in a straightforward way. Arion and the Setup Optimiser will be discussed in great detail in chapter 3.

2.6.3 UGCT scanners versus commercial systems

Commercial micro-CT scanners are designed for specific purposes and are typically developed as a cabinet system that may only occupy a limited amount of space. They contain a specific source and detector, suited for the applications aimed at. There are for instance systems developed for very high resolution applications, while others focus on high energy CT. In the former case, the scanners are primarily limited in maximum object size, while the latter are limited in achievable resolution. The UGCT scanners on the other hand are characterised by an adaptable, modular structure, and some of them contain multiple X-ray sources and detectors. Moreover, they are constructed in a spacious bunker, allowing for a great experimental flexibility. As such, for instance auxiliary equipment can be easily mounted as well. Another important advantage is that UGCT controls the entire imaging chain, from construction of the scanners, including the control software, to the development of simulation, reconstruction and image analysis methods. As such, the systems can be optimised for many specific purposes and easily outperform typical commercial systems.

Another type of commercial systems are the preclinical, small animals scanners. These are both in terms of image quality and resolution limited by absorbed dose constraints, which are up to now (except for very few samples) not an issue at UGCT.

References

[1] W. C. Röntgen. *On a new kind of rays*. Science, 3(59):227–231, 1896.

[2] http://www.lynceantech.com.

[3] https://en.wikipedia.org/wiki/X-ray_tub.

[4] http://www.excillum.com/.

[5] G. F. Knoll. *Radiation detection and measurement*. J. Wiley & Sons, 3nd edition, 2000.

[6] J. E. Turner. *Atoms, radiation, and radiation protection*. J. Wiley & Sons, 2nd edition, 1995.

[7] *XCOM: Photon Cross Sections Database*. http://www.nist.gov/pml/data/xcom/.

[8] http://www.ilocis.org/documents/chpt48e.htm.

[9] M. N. Boone. *New imaging modalities in high resolution X-ray tomography*. Phd dissertation, Ghent University, 2013.

[10] J. Vlassenbroeck. *Advances in laboratory-based X-ray microtomography*. Phd dissertation, Ghent University, 2009.

[11] Y. De Witte. *Improved and practically feasible reconstruction methods for high resolution X-ray tomography*. Phd dissertation, Ghent University, 2010.

[12] L. Brabant. *Latest developments in the improvement and quantification of high resolution X-ray tomography data*. Phd dissertation, Ghent University, 2013.

[13] G. Michael. *X-ray computed tomography*. Physics Education, 36(6):442, 2001.

[14] L. Feldkamp, L. Davis, and J. Kress. *Practical cone-beam algorithm*. JOSA A, 1(6):612–619, 1984.

[15] http://www.volumegraphics.com.

[16] http://www.fei.com/software/avizo3d.

[17] http://biomedical.materialise.com/mimics.

[18] http://www.mavi-3d.de.

[19] R. A. Ketcham. *Computational methods for quantitative analysis of three-dimensional features in geologic specimens*. Geosphere, 1:32–41, 2005.

[20] F. Brun, L. Mancini, P. Kasae, S. Favretto, D. Dreossi, and G. Tromba. *Pore3D: A software library for quantitative analysis of porous media*. Nucl. Instrum. Methods Phys. Res., Sect. A, 615:326–332, 2010.

[21] L. Brabant, E. Pauwels, M. Dierick, D. Van Loo, M. A. Boone, and L. Van Hoorebeke. *A novel beam hardening correction method requiring no prior knowledge, incorporated in an iterative reconstruction algorithm*. NDT E Int., 51:68–73, 2012.

[22] *Bruker*. `https://www.bruker.com`.

[23] S. K. Carlson, K. L. Classic, C. E. Bender, and S. J. Russell. *Small animal absorbed radiation dose from serial micro-computed tomography imaging*. Mol. Imaging Biol., 9(2):78–82, 2007.

[24] H. Li, H. Zhang, Z. W. Tang, and G. S. Hu. *Micro-computed tomography for small animal imaging: Technological details*. Prog Nat Sci, 18(5):513–521, 2008.

[25] I. Willekens, N. Buls, T. Lahoutte, L. Baeyens, C. Vanhove, V. Caveliers, R. Deklerck, A. Bossuyt, and J. de Mey. *Evaluation of the radiation dose in micro-CT with optimization of the scan protocol*. Contrast Media Mol. Imaging, 5(4):201–7, 2010.

[26] *Inside Matters*. `https://insidematters.eu/`.

[27] *X-Ray Engineering*. `http://www.xre.be/`.

[28] M. Dierick, D. Van Loo, B. Masschaele, J. Van den Bulcke, J. Van Acker, V. Cnudde, and L. Van Hoorebeke. *Recent micro-CT scanner developments at UGCT*. Nuclear Instruments and Methods in Physics Research Section B: Beam Interactions with Materials and Atoms, 324(0):35–40, 2014.

[29] B. Masschaele, M. Dierick, D. Van Loo, M. N. Boone, L. Brabant, E. Pauwels, V. Cnudde, and L. Van Hoorebeke. *HECTOR: A 240kV micro-CT setup optimized for research*. J. Phys.: Conf. Ser., 463(1):012012, 2013.

[30] B. Masschaele, V. Cnudde, M. Dierick, P. Jacobs, L. Van Hoorebeke, and J. Vlassenbroeck. *UGCT: New x-ray radiography and tomography facility*. Nucl. Instrum. Methods Phys. Res., Sect. A, 580(1):266–269, 2007.

[31] M. Dierick, D. Van Loo, B. Masschaele, M. N. Boone, and L. Van Hoorebeke. *A LabVIEW® based generic CT scanner control software platform*. J. X-ray Sci. Technol., 18(4):451–461, 2010.

[32] M. Dierick, B. Masschaele, and L. Van Hoorebeke. *Octopus, a fast and user-friendly tomographic reconstruction package developed in LabView®*. Meas. Sci. Technol., 15(7):1366, 2004.

[33] J. Vlassenbroeck, M. Dierick, B. Masschaele, V. Cnudde, L. Van Hoorebeke, and P. Jacobs. *Software tools for quantification of X-ray microtomography*. Nucl. Instrum. Methods Phys. Res., Sect. A, 580(1):442–445, 2007.

[34] L. Brabant, J. Vlassenbroeck, Y. De Witte, V. Cnudde, M. N. Boone, J. Dewanckele, and L. Van Hoorebeke. *Three-dimensional analysis of high-resolution X-ray computed tomography data with Morpho+*. Microsc. Microanal., 17(2):252–263, 2011.

[35] J. Dhaene, E. Pauwels, T. De Schryver, A. De Muynck, M. Dierick, and L. Van Hoorebeke. *A realistic projection simulator for laboratory based X-ray micro-CT*. Nuclear Instruments and Methods in Physics Research Section B: Beam Interactions with Materials and Atoms, 342(0):170–178, 2015.

3
X-ray imaging simulations

This chapter is partly based on the publication: A realistic projection simulator for laboratory based X-ray micro-CT [1]

CT imaging is a complicated process which involves many different parameters, such as tube voltage, beam filtration, exposure time per projection and detector response characteristics. For an optimal scanning result a careful selection of these parameters is necessary. On the other hand, the optimal settings will largely depend on the sample itself. At UGCT a wide variety of samples in terms of composition, density and size, is scanned for a broad range of applications, with each sample requiring its own nearly unique ideal scanning setup. Due to factors such as scan duration and operating costs, multiple attempts to achieve the optimal scan settings are to be avoided. Therefore, a means to investigate the influence of the different variables without actually having to perform several CT scans can be very useful. Also it is often desirable to predict in advance whether certain features will be visible in the resulting CT image, or, when using contrast agents, to determine the concentration necessary to ensure detectability of the contrasted parts in the sample.

To meet some of the aforementioned needs, soon a basic simulation tool, the Setup Optimiser, was developed at UGCT which allowed to roughly predict the transmission of an X-ray beam through one or several layers of materials under different scanning conditions. As the Setup Optimiser was increasingly used for all kinds of applications such as DECT [2, 3], it was further expanded and im-

proved to a versatile tool for straightforward evaluation of various scanner settings. However, information is of course limited to one ray path and not easily extrapolated to an actual CT image. This led to the development of Arion, a program for fast and realistic simulations of radiographic projections [1]. Note that Arion is now the overarching program in which the Setup Optimiser was incorporated as a submodule, similar to the material creator and phantom creator (see further).

There exist multiple simulation programs for X-ray imaging developed by several research groups for different purposes, such as VXI [4–8], XRayImagingSimulator [9–11], ScorpiusXLab [12], XRSIM [13] and many others. Because of the wide range of possible samples and applications at UGCT, the aim was to realise a flexible, fast and accurate simulation tool to be used in a routine way for testing and defining ideal scanning parameters in all kinds of situations. Most importantly, and this is how Arion distinguished itself from other simulation programs, it should be quantitatively correct. The latter has been extensively verified by comparing real and simulated CT scans.

In this chapter both Arion and the Setup Optimiser will be presented. A more specific explanation on the actual implementation and functionality of the software is given in [18].

3.1 Simulation of source and detector

Both for Arion and the Setup Optimiser, a first important step is to fully understand the hardware characteristics of the main components, namely X-ray tube and detector. These are to be accurately simulated in order to reproduce their behaviour as correctly as possible. The best way to achieve this is to perform Monte Carlo simulations, taking into account all interaction processes. To this purpose, the BEAMnrc code was used from the simulation package EGSnrc. First, a short introduction to BEAMnrc will be given, then simulations of X-ray tubes and detectors will be discussed.

3.1.1 BEAMnrc

BEAMnrc is a Monte Carlo simulation system which was initially developed to calculate dose deposition of MeV electron beams as a part of treatment planning for radiotherapy [14], but its use can be extended to several other applications. As mentioned above, BEAMnrc is actually built on the EGSnrc (Electron-Gamma Showers) Code System. This package was developed for performing Monte Carlo simulations of electron and photon interactions and comprises a set of FORTRAN codes which can be adjusted to any geometry. To facilitate the implementation of

these codes, a macro language, called MORTRAN, was written. Originally the EGS package stems from high energy physics, but the development of EGS4 extended its scope towards lower energies (1 keV - 100 keV). With the introduction of the latest version, EGSnrc, especially the accuracy at lower energies was greatly improved [15].

With BEAMnrc, users can create their own specific model for performing Monte Carlo simulations. This is a two-step process. First, a new *accelerator* has to be specified. The accelerator is in fact a geometrical model which consists of several non-overlapping *component modules* centred around an optical axis. A component module can be considered as a structural unit. Several types of component modules are available in BEAMnrc such as a set of one or multiple slabs, cones, rings, a target configuration, a parallel-plate ion chamber... After the accelerator structure has been specified it is built and compiled into an executable file. In the second step, the user creates an input file containing all input/output and other necessary parameters for the simulation. Source type and configuration, the number of incident particles and their type and energy, and several parameters which influence the manner of simulating the physical interactions among others can be set. Output files can be generated at the back surface of each component module. The listing file contains a summary of the performed simulation. Furthermore, a phase space file is created in which all data is stored relating to particle position, direction, energy, particle type and optionally the last interaction site for every particle crossing a scoring plane.

Photon interaction cross sections used by BEAMnrc are imported from the XCOM Photon Cross Sections Database from NIST [16].

3.1.2 Source simulation

Simulation of sources is discussed in greater detail in [17] and especially in [18] where all X-ray tubes currently available at UGCT are accurately simulated. However, since this is a fundamental basis for Arion and the Setup Optimiser, a brief explanation with an example of a directional and a transmission type tube will be shown here.

It should be noted that simulation programs for X-ray imaging can also make use of tabulated semi-empirical data in order to determine the generated X-ray spectra [19–23]. However, Monte Carlo simulations are more accurate and the internal structure of the X-ray tube can be taken into account as well. The latter may be important for contributions such as secondary radiation (see further).

As mentioned above, using BEAMnrc the interactions of the incident electrons are simulated and the position, direction and energy of the produced photons are calculated. Subsequently, the paths of these photons are traced while they move through exit window and collimator towards a scoring plane. This plane is a square of 1 cm^2, placed at a distance of 5 cm. As such, the solid angle covered by this scoring plane $\Delta\Omega_{source}$ corresponds to a typical solid angle covered by a detector in high resolution CT. $\Delta\Omega_{source}$ can be written as follows:

$$\Delta\Omega_{source} = 4\ arccos\left(\sqrt{\frac{1+2\alpha^2}{(1+\alpha^2)^2}}\right) = 0.0396\ Sr, \tag{3.1}$$

with $\alpha = a/2d$ where a is the length of the side of the square scoring plane and d the distance of the plane to the source [24]. All photons in this solid angle are tallied per energy bin, resulting in an energy spectrum generated at a given tube voltage.

Directional head: 130 kV Hamamatsu X-ray tube

Figure 3.1 shows the design of the closed-type 130 kV Hamamatsu directional X-ray tube from the Nanowood scanner as specified in BEAMnrc. This type of source is also mounted on the EMCT scanner. It allows for focal spot sizes down to 5 µm and a maximal power of 39 W. The tungsten (W) target has an inclination angle of $20°$ with respect to the z-axis, while the angle between the positive x-axis and the incident electron beam is $150°$. The incident electrons therefore impinge on the target at a fixed angle of $40°$. Note that the axes in figure 3.1 are scaled differently. The X-ray tube further consists of an iron (Fe) structure and collimator and a beryllium (Be) exit window of 0.5 mm thickness. A scoring plane of 1 cm^2 is placed after a drift section of 5 cm starting from the outer surface of the collimator. For convenience, this drift section is vacuum instead of filled with air.

Figure 3.2 shows simulated X-ray spectra of the 130 kV Hamamatsu directional source generated at tube voltages of 40, 60, 80, 100 and 120 kV.

Transmission head: 160 kV FeinFocus X-ray tube

The 160 kV FeinFocus transmission tube (FXE 160.51) was originally mounted on the first UGCT scanner and is now part of the re-designed version, Medusa. The tube allows for targets of different materials, mainly tungsten and molybdenum (Mo), and different thicknesses (1, 3, 6 and 8 µm). Furthermore, an inner structure for the walls of the vacuum chamber and aperture made of Mo is present. Figure 3.3 shows the design of this X-ray tube with a 6 µm tungsten target as specified in BEAMnrc. Note that this thin tungsten target is not visible on the diamond backing.

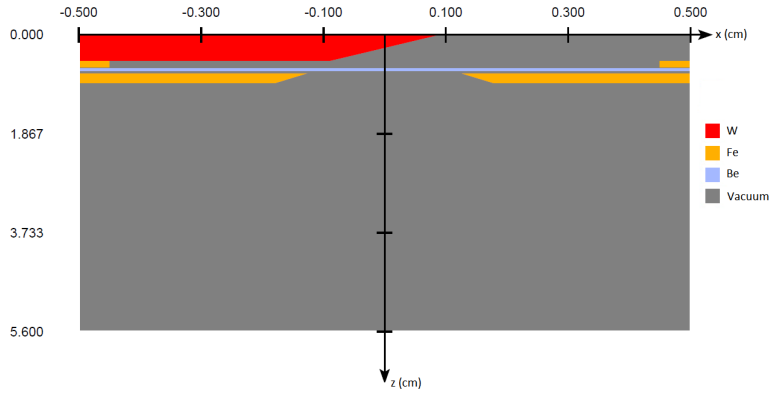

Figure 3.1: Design of the 130 kV Hamamatsu directional X-ray tube as specified in BEAMnrc

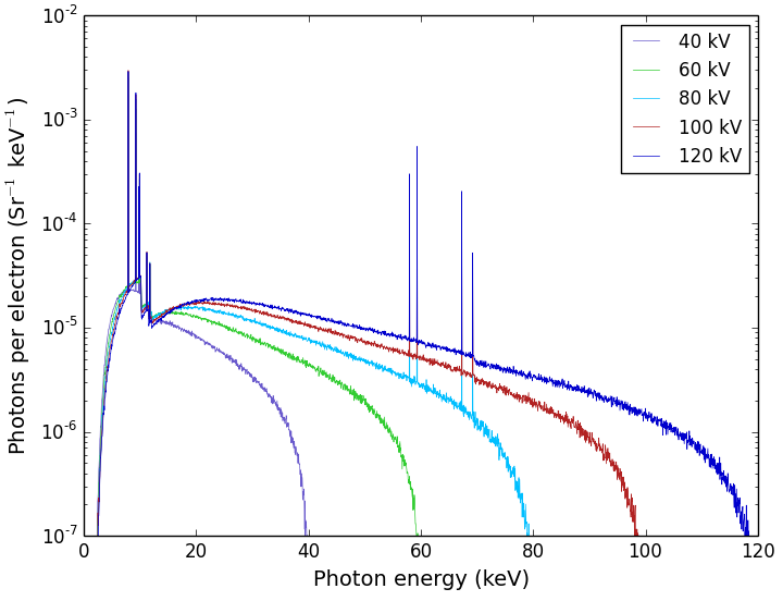

Figure 3.2: Simulated X-ray spectra of the 130 kV Hamamatsu directional source at tube voltages of 40, 60, 80, 100 and 120 kV

Figure 3.4 shows simulated X-ray spectra of the 160 kV FeinFocus transmission source generated at tube voltages of 40, 60, 80, 100, 120 and 160 kV.

In an X-ray tube, a number of secondary effects take place. On the one hand, electrons can be backscattered from the target and on the other hand X-ray photons

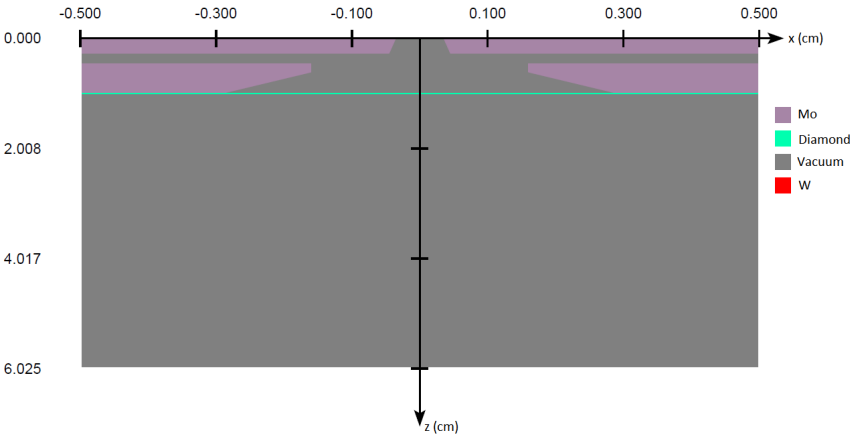

Figure 3.3: Design of the 160 kV FeinFocus transmission X-ray tube as specified in BEAMnrc

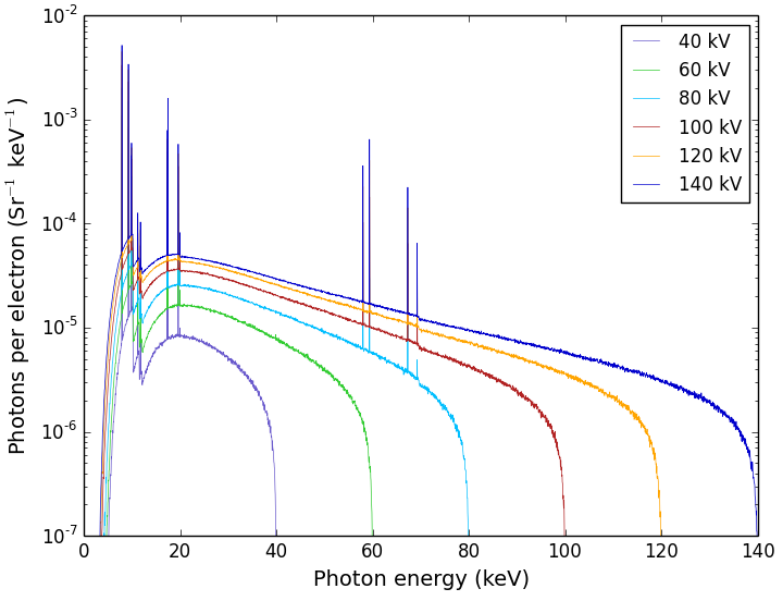

Figure 3.4: Simulated X-ray spectra of the 160 kV FeinFocus transmission source at tube voltages of 40, 60, 80, 100, 120 and 140 kV

can be emitted from the rear of the target. In both cases, these particles will hit the Mo structures and can as such give rise to bremsstrahlung and characteristic radiation, a phenomenon called secondary radiation [25]. To measure the extent

of this effect, additional simulations were performed using the same design after removal of the internal Mo structures as can be seen in figure 3.5.

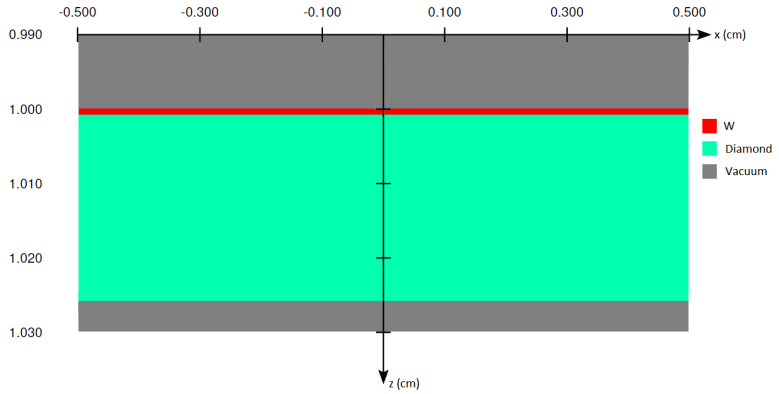

Figure 3.5: Design of the 160 kV FeinFocus transmission X-ray tube without internal molybdenum structures as specified in BEAMnrc

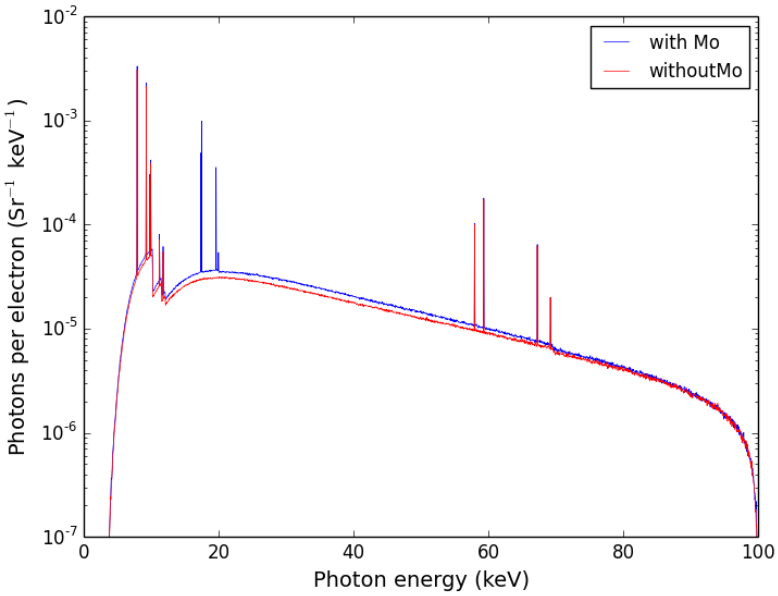

Figure 3.6: Simulated X-ray spectra of the 160 kV FeinFocus transmission source with and without internal molybdenum structures at 100 kV

Figure 3.6 shows the simulated spectra with and without internal structures at a tube voltage of 100 kV. The most striking feature in the first spectrum is the presence of additional characteristic peaks originating from Mo. In general, the yield of X-ray photons is slightly higher when the Mo structures are taken into account, especially in the 15 - 60 keV range. This is also illustrated in table 3.1, which shows the integrated number of photons of both spectra. The Mo structures give rise to an additional contribution of 17.5% X-ray photons at a tube voltage of 100 kV. Since these photons are originating from another location within the X-ray tube, the term secondary spot is often used as opposed to the primary spot inside the target where the majority of X-ray photons originate from. The secondary spot can be observed in X-ray transmission images of certain samples in the form of a *halo*. Detailed information on secondary radiation and how to correct for it can be found in [17, 25, 26]. In any case, it is important to take into account internal structures of an X-ray tube that can give rise to such a phenomenon when accurate X-ray imaging simulations are required.

Table 3.1: Integration of the simulated X-ray spectra of the 160 kV FeinFocus transmission source with and without internal molybdenum structures at 100 kV

Tube design	*Integrated spectrum (photons per electron per Sr)*
with Mo	1.9183×10^{-3}
without Mo	1.6276×10^{-3}

3.1.3 Detector simulation

The spectral sensitivity of detectors can be accurately simulated using BEAMnrc on the condition that their internal structure and composition are sufficiently well known. For each energy step a pencil beam of mono-energetic photons onto a specified detector geometry and its interactions are traced. From these data, the mean deposited energy per incident photon in the scintillator as a function of energy can be calculated as well as the absorption probability of a photon, derived from the actual number of interacting X-ray photons. The latter parameter is used for noise calculations on the assumption that the image noise depends on the amount of detected X-ray photons per pixel. On the other hand, the number of counts in a pixel of a projection image is proportional to the deposited energy in the scintillator in front of that pixel. Simulation of detectors and their properties is more thoroughly discussed in [17] and [18]. Simulations of the Varian flat panel detector will be shown here as an example.

Varian amorphous silicon flat-panel detector

A schematic cut-through of a typical flat-panel detector perpendicular to its surface is shown in figure 3.7(a). It consists of an entrance window which is usually made of carbon, a thin aluminium foil, a scintillator and an amorphous silicon (aSi) layer. The scintillator converts the incident X-rays into visible light. The Al foil acts as a reflector for all visible photons which are created and emitted in the direction of the entrance window and sends them towards the detector layer to increase the signal. The Varian detector is an example of an aSi flat-panel detector and is currently mounted on the Nanowood scanner and on Medusa at UGCT. Its scintillator is made of caesium iodide (CsI) which is grown in a columnar structure. The design of the Varian detector as specified in BEAMnrc is shown in figure 3.7(b).

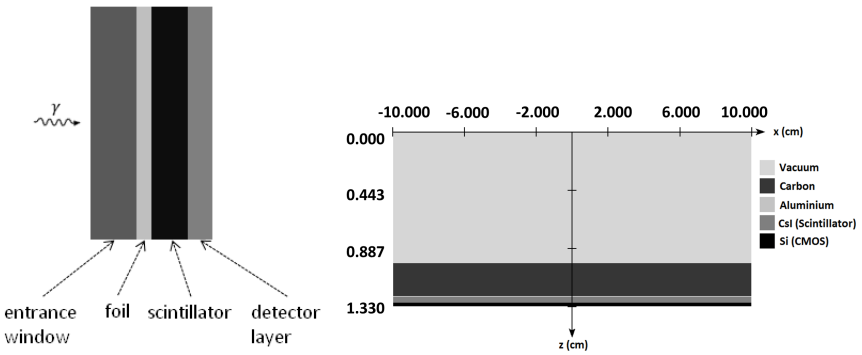

(a) (b)

Figure 3.7: (a) Schematic cut-through of a typical flat panel detector perpendicular to its surface. Note that the thicknesses of the different internal layers are not displayed in correct proportion. (b) Design of the Varian aSi flat-panel detector as specified in BEAMnrc.

Figure 3.8(a) shows the mean energy deposition per incident photon, while figure 3.8(b) shows the absorption probability as a function of photon energy simulated with BEAMnrc. In the latter graph a sharp increase can be observed just above the K-edges of I (33.2 keV) and Cs (36.0 keV). Note that the predominant photon interaction process in the CsI scintillator is photo-electric absorption at least up to 200 keV due to its high atomic number. The mean deposited energy per absorbed photon (Fig. 3.8(c)) can be calculated by dividing the mean deposited energy at a specific incident photon energy by the absorption probability at that energy. The theoretical limit is the situation where each absorbed photon deposits all its energy in the scintillator.

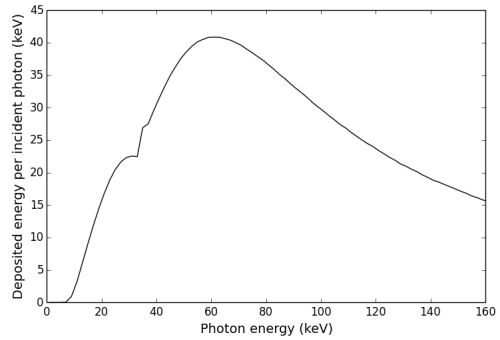

(a)

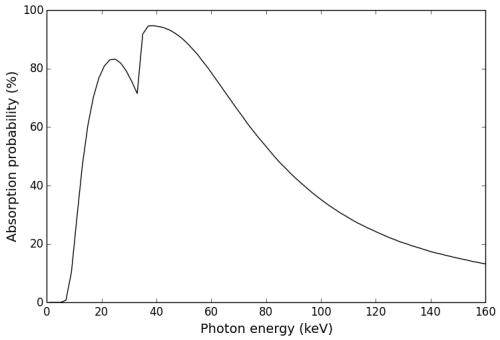

(b)

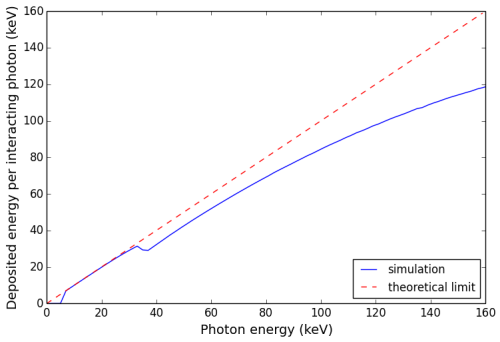

(c)

Figure 3.8: Simulated spectral sensitivity of the Varian aSi flat-panel detector: (a) mean deposited energy per incident photon, (b) absorption probability and (c) mean energy deposition per interacting photon as a function of incident photon energy

From figure 3.8(c) it is clear that this theoretical limit is only nearly reached in the lower energy range, except below 6 keV where a drop is observed due to the graphite entrance window. The mean energy deposition per interacting photon begins to deviate from its theoretical limit at the K-edges of I and Cs. Starting from these energies, fluorescence K-photons are created which are emitted in all directions and which can easily escape the thin scintillator layer without being re-absorbed. Towards higher photon energies the deviation between theory and reality is even larger since both photo-electrons and Compton photons will have a higher (kinetic) energy allowing an increasing fraction of them to escape the scintillator.

3.2 Mathematical basis of the simulation software

In this section, the mathematical foundations of both Arion and the Setup Optimiser are discussed. Simulations of X-ray imaging are essentialy based on the law of Lambert-Beer 2.14 or 2.15 which was introduced in chapter 2. However, because of the polychromatic character of X-ray spectra produced by conventional laboratory-based X-ray tubes, this law can no longer be straightforwardly used. Therefore, the spectra are divided into energy bins and in each of these bins, the law of Lambert-Beer is applied. Subsequently, the contribution of each bin is summed resulting in the beam intensity $I(x)$ after a distance x. The two parameters in equation 2.14 that are dependent on the photon energy are the intensity of the X-ray beam and the linear attenuation coefficient. As such, 2.14 can be rewritten as follows:

$$I(x) = \sum_{i=1}^{n} I_{0,i} exp(-\mu_i x), \tag{3.2}$$

with n the number of energy bins, $I_{0,i}$ the intensity of the original photon beam in energy bin i and μ_i the linear attenuation coefficient for energy bin i.

The main difference between Arion and the Setup Optimiser now lies in how x is determined. The Setup Optimiser was developed to predict the transmission through one or several planparallel layers of materials. The X-ray beam is considered perpendicularly incident on the material layers. As such, x_j is given by the thickness of material layer j. Since Arion is a simulator of actual radiographic projections, the full setup geometry has to be taken into account. Therefore, a ray tracing technique is applied connecting each detector pixel with the X-ray source. This is illustrated in figure 3.9. By tracing each ray path from source to detector and for each energy bin, the total attenuation and thus the resulting total beam intensity can be calculated.

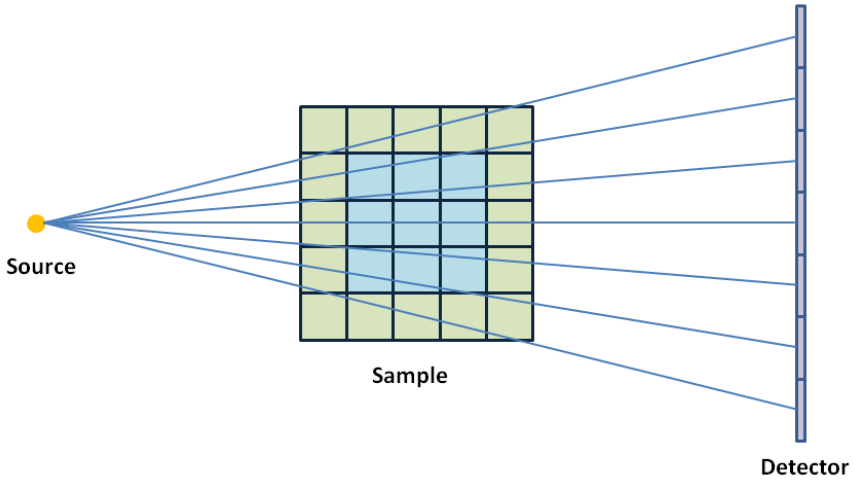

Figure 3.9: Schematical illustration of the ray tracing technique on a voxel based sample

As mentioned in chapter 2, equations 2.14 and 2.6 are often used interchangeably. Therefore, the resulting amount of photons N_i reaching a given detector pixel for energy bin i can be written as follows:

$$N_i = N_{0,i} exp(-\sum_{j=1}^{m} \mu_{i,j} x_j), \tag{3.3}$$

with $N_{0,i}$ the emitted amount of photons in energy bin i, m the number of materials in the sample crossed by the ray connecting the X-ray source and the given pixel, $\mu_{i,j}$ the linear attenuation coefficient of material j corresponding to energy bin i and x_j the thickness of material j crossed by the ray. To determine $N_{0,i}$, the solid angle of the given detector pixel $\Delta\Omega_{pixel}$ has to be taken into account, since only photons emitted in this solid angle will be able to reach that pixel (see section 3.2.2). As a result, $N_{0,i}$ is given by:

$$N_{0,i} = \left(\frac{P\Delta t}{UQ_{e^-}}\right)(\Delta\Omega_{pixel}\Delta E_i S_i'). \tag{3.4}$$

This expression consists of two main factors. The first, $\frac{P\Delta t}{UQ_{e^-}}$, represents the number of electrons accelerated in the X-ray tube during exposure. This can be calculated by multiplying the tube power P with the integration time Δt and dividing this by the product of the tube voltage U and the elementary charge Q_{e^-}. The second factor essentially expresses the yield of X-ray photons resulting from the accelerated electrons. It contains the filtered spectrum S_i' - for convenience, beam filtration is already taken into account (see section 3.2.3) - multiplied by the solid angle of the detector pixel $\Delta\Omega_{pixel}$ and the width of an energy bin ΔE_i. S_i' is

expressed as the number of photons per simulated electron per Sr per keV.

To obtain the amount of detected photons in a given detector pixel for energy bin i, $N_{d,i}$, the amount of photons reaching that pixel has to be multiplied by the detector efficiency for this energy bin $D_{eff,i}$ (Fig.3.8(b)):

$$N_{d,i} = D_{eff,i} \times N_i. \tag{3.5}$$

Using (3.4) and (3.3) this can be rewritten as follows:

$$N_{d,i} = \frac{P\Delta t}{UQ_{e^-}} \Delta\Omega_{pixel} \Delta E_i S_i' D_{eff,i} exp(-\sum_{j=1}^{m} \mu_{ij} x_j). \tag{3.6}$$

Since the number of counts per pixel in a projection image is proportional to the deposited energy in the scintillator in front of that pixel, $N_{d,i}$ has to be multiplied by the mean energy depostion per interacting photon in energy bin i, $D_{d,i}$ (Fig.3.8(c)). The total detected energy E_d per pixel is then given by:

$$E_d = \sum_{i=1}^{n} E_{d,i} = \sum_{i=1}^{n} D_{d,i} N_{d,i}, \tag{3.7}$$

with $E_{d,i}$ the detected energy per pixel for energy bin i.

3.2.1 Image noise and error calculation

As mentioned in the previous section, we assume that the image noise depends on the amount of detected X-ray photons per pixel and that Poisson statistics is valid. As such, the standard deviation on the number of detected photons in an energy bin, $\sigma_{N_{d,i}}$, can be calculated by taking the square root of (3.5).

$$\sigma_{N_{d,i}} = \sqrt{N_{d,i}}. \tag{3.8}$$

For the standard deviation on the total detected energy σ_{E_d}, gaussian error propagation is applied, since each energy bin contains a large number of photons, i.e. more than 20. Therefore, σ_{E_d} can be written as follows:

$$\sigma_{E_d} = \sqrt{\sum_{i=1}^{n} \left(\sigma_{E_{d,i}}\right)^2} = \sqrt{\sum_{i=1}^{n} \left(D_{d,i}\sigma_{N_{d,i}}\right)^2}, \tag{3.9}$$

with $\sigma_{E_{d,i}}$ the standard deviation on the detected energy per pixel for energy bin i.

3.2.2 Solid angle of a detector pixel

The solid angle of a detector pixel $\Delta\Omega_{pixel}$ can be derived from two parameters: the distance between that pixel and the source r and the orientation of the pixel. If **n** is defined as the normal vector on the plane of the pixel and **u** the normalised vector giving the direction from pixel to source, the solid angle can be written as follows:

$$\Delta\Omega_{pixel} \approx \frac{a^2 \mathbf{n} \cdot \mathbf{u}}{r^2} = \frac{a^2 cos(\theta)}{r^2}, \tag{3.10}$$

with a the pitch of the pixel and θ the angle between the two vectors. This is also illustrated in figure 3.10.

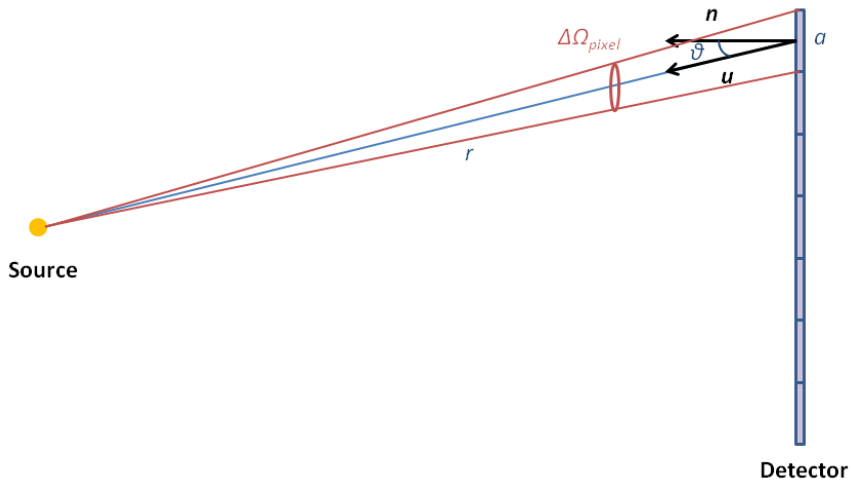

Figure 3.10: Schematical illustration of the solid angle of a detector pixel

3.2.3 Beam filtration

Beam filtration is an important aspect in X-ray imaging. Both simulation programs allow to add one or a combination of filters. As mentioned above, for convenience the beam filtration is taken into account prior to the actual simulation. The emitted X-ray spectrum is then modified as follows:

$$S_i' = S_i \prod_{j=1}^{l} exp(-\mu_{ij} d_j), \tag{3.11}$$

with S_i' and S_i representing the filtered and unfiltered spectrum, respectively, both expressed as the number of photons per simulated electron per Sr per keV, and l the number of filters added. The attenuation coefficient data is obtained from the XCOM Photon Cross Sections Database from NIST [16].

3.2.4 Binning of the X-ray spectra

The X-ray spectra shown in section 3.1.2 are subdivided into fine energy bins of 50 eV. This energy resolution allows to model the characteristic X-ray peaks present in the spectra with sufficient precision. On the other hand, for the continuum on which these peaks are superimposed, larger bin sizes can be selected for an accurate reproduction. The main advantage is that the number of energy bins can be reduced in the continuum part, leading to significantly shorter computation times, without loss of accuracy in the simulation results. For a projection simulator, such as Arion, where computation times are an important issue this can be very useful. Therefore, a rebinning procedure is incorporated in Arion. First, the characteristic peaks are identified so that these can be modeled using energy bins of 50 eV. Then, all K- and L- edges of target material, beam filtration, sample materials and scintillator are taken into account by ensuring that each of these coincides with the border of a bin. In this way it can be avoided that the abrupt behaviour due to an edge is averaged out over an entire energy bin. Due to the rebinning procedure not all energy bins will have an equal bin width. This has to be incorporated in equation 3.6. Figure 3.11 shows an example of a binned spectrum. Here the number of bins, and thus the computation time, is reduced by a factor of 20.

Note that no rebinning procedure is applied in the Setup Optimiser since computation times are no issue.

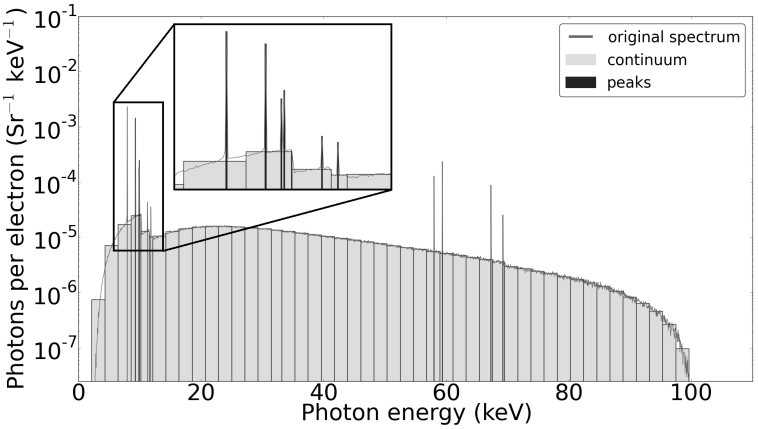

Figure 3.11: Example of a binned spectrum resulting in a reduction of the number of energy bins by a factor of 20 [1]

3.2.5 Focal spot size

Finally, a word about the focal spot size. As discussed in section 2.5.2, a finite spot size will give rise to a geometrical unsharpness and as such impose a limit on the best achievable resolution given by equation 2.21. For large magnifications as is the case in micro-CT, the best achievable resolution will be almost equal to the focal spot size, which implies that it can never be smaller. In practice, for realistic micro-CT scans, scanning conditions are normally carefully chosen to ensure that the geometrical unsharpness is negligible and that the X-ray source can be considered as a point source. Therefore, finite focal spot sizes have not yet been implemented in the simulation software so far.

3.3 Other aspects and features of the simulation software

In this section, a few other aspects and the remaining features of the simulation software will be discussed. The first section describes how samples are defined. Then the general flowchart will be explained and finally some general features will be discussed.

3.3.1 Sample definition

Just as for the filter materials, elemental tabulated attenuation data for the materials present in a sample are retrieved from the XCOM Photon Cross Sections Database from NIST [16].

The sample itself can be defined in two ways in Arion. For the first method, one or several image files can be loaded into the program. The files are interpreted as RGB format internally. For each image file, the user has to define how many copies have to be stacked onto each other. As such, the resulting sample is built up from a stacked sequence of image files, each representing a single slice in the 3D voxel based volume. This implies that existing segmented reconstructed data sets of real CT-scans can be loaded as well for testing under different scanning conditions. For the second method, the sample consists of a combination of one or several three dimensional geometrical shapes defined by the user.

The materials present in the sample are colour-coded, with each colour representing a specific material. Materials are assigned to a colour by the user during the sample building phase. They can include both single chemical elements and compounds and mixtures. Attenuation data for each element up to atomic number 100 (Fm) are incorporated in the software. Compounds and mixtures can be cre-

ated using the material creator (see section 3.3.3).

For the simulation of radiographic projections, the total linear attenuation coefficient is used. Note that now all parameters in equations 3.6 and 3.7 are available. On the other hand, the contributions to the total attenuation coefficient - photoelectric absorption and Compton scattering - are calculated as well. As such, these effects can also be studied separately.

3.3.2 Projection simulator flowchart

Figure 3.12 illustrates the flowchart of the different steps to setup a CT scan simulation using Arion. As a first step, the user creates the sample and defines the colour codes. The resulting 3D phantom can be saved as a *.phantom* file for repeated use in the future. Subsequently, the desired X-ray tube and detector are chosen and their parameters, such as tube voltage and power, binning and integration time are set. One or several filtration materials can also be added. Then the remaining scan settings are chosen, such as source-to-object and source-to-detector distance, the number of projections and the angular range. Further, the user has the possibility to add noise and choose the number of flatfields. Finally, prior to starting the full CT scan simulation, a single projection can be generated to allow the user to make a fast check of the chosen settings.

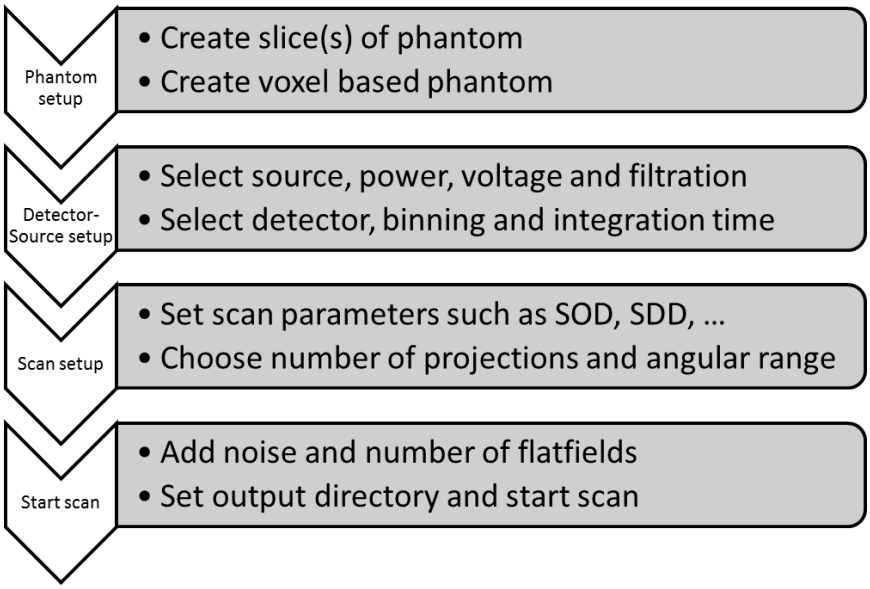

Figure 3.12: Flowchart of the different steps before starting the CT scan simulation [1]

3.3.3 Features

Scan geometry

An important feature of Arion is its flexibility in defining scan geometries. Apart from the conventional circular and helical CT scans, more exotic geometries can be implemented and simulated as well. This is of particular interest for testing industrial CT setups which often involve limitations with respect to angular range and number of projections. During the setup phase of a CT scan simulation, the user can define a position and rotation of the source, sample and detector for every projection. As such, every possible scan geometry can be created. The position is defined by means of three coordinates (x,y,z). The rotation component is composed of a skew, tilt and slant which represent rotations around the x-, y- and z-axis, respectively. Currently, there are three predefined CT setups: circular, helical and conveyer belt. Position and rotation coordinates are automatically calculated, based on a few input parameters which can be set by the user. The circular CT geometry for instance requires only a specific source-to-object and source-to-detector distance.

X-ray source geometry

Concerning X-ray source geometry, at the moment cone and fan beam geometry are available. Parallel beam is in development.

Material creator

Apart from the projection simulator itself, a few other useful tools are available as well in the software, such as a material creator. As mentioned earlier, elemental tabulated attenuation data are included up to atomic number 100. However, samples often contain non-elementary materials. Therefore, a material creator was developed, which allows the user to generate attenuation data for specific compounds and mixtures, such as polyethylene, concrete, soft tissue, cortical bone etc. Solutions can be made as well. After the user defines the solute, solvent and their respective quantities, attenuation data are calculated based on the mass fractions of the constituent elements. Also a mass density for the solution is generated which can be adapted by the user if necessary.

Phantom creator

Another tool incorporated in the simulation software is the phantom creator. Its function has already been described in section 3.3.1: samples are built up from a stacked sequence of image files, and a phantom sample file is produced which can be saved and accessed during scan setup.

Setup Optimiser features

As mentioned in the introduction to this chapter, the Setup Optimiser is incoporated in Arion as a submodule. This tool allows the user to evaluate the influence of different scanner settings in a fast and straightforward way. Most importantly it simulates the detected transmission of a polychromatic X-ray beam through one or several layers of material for the selected X-ray tube, tube voltage, beam filtration and detector. In addition, several other useful parameters concerning the emitted and detected spectrum, such as average energy, are computed and graphs of these spectra for visual interpretation are produced as well. Furthermore, a measure for the expected amount of beam hardening is given and a signal-to-noise ratio for a projection image is simulated. The Setup Optimiser can be easily extended to compute any other desired parameters.

3.4 Experimental validation of the simulation software

In this section an experimental validation for the simulation software will be presented by comparing real and simulated X-ray imaging data. First, transmission values through several filter materials, well known in terms of composition and thickness, will be compared with simulated values at two different UGCT scanners. Subsequently, differences between a real and simulated projection image of an aluminium sphere are examined. Then, reconstructed attenuation coefficients will be compared. Finally, an example will be shown which illustrates the capacity of Arion to correctly reproduce and model beam hardening. Note that for the first experiment, only the Setup Optimiser will be used. The other experiments require full projection simulations, which will be performed with Arion as a whole.

3.4.1 Comparison of transmission values

The signal of a detector pixel is given by the number of counts generated in that pixel. The latter is directly related to the amount of deposited energy in the given pixel. The conversion of this deposited energy to the number of counts is slightly dependent on the energy of the detected X-rays. This behaviour in turn depends on the scintillator thickness, electronics and detector gain factor, but will be treated here as a constant factor. Therefore, the transmission T through a sample can be calculated as follows:

$$T = \frac{E_d}{E_{d,0}}, \tag{3.12}$$

with E_d the total detected energy in a pixel given by 3.7 and $E_{d,0}$ the total detected energy with the sample removed from the X-ray beam. The standard deviation on

the transmission σ_T can be calculated using standard error propagation, which results in:

$$\sigma_T = \frac{1}{E_0}\sqrt{\sigma_E^2 + \frac{E^2}{E_0^2}\sigma_{E_0}^2}, \tag{3.13}$$

with σ_E and σ_{E_0} (3.9) the standard deviations on E and E_0, respectively. These formulas are implemented in the Setup Optimiser.

In table 3.2, 3.3 and 3.4 measured and simulated transmission values through various filters, well known in terms of composition and thickness, are compared for Nanowood, HECTOR and Medusa, respectively. For each of these scanners, the chosen tube head type and detector as well as the operating parameters are listed in table 3.5. Filters were placed immediately behind the exit window of the X-ray tube so as to cover the whole photon beam. Subsequently, projection images were obtained using each detector in binning two mode. In addition, flat field and dark field images were also recorded to correctly normalise the projection images. Transmission values T_M were measured in a sufficiently large central square of about 300 by 300 pixels in the normalised images using the Octopus Viewer. The standard deviations on these measurements σ_{T_M} are determined based on the inter-pixel variation. Simulated transmission values T_S and the corresponding standard deviations σ_{T_S} are calculated using the Setup Optimiser.

Table 3.2: Measured (T_M) and simulated (T_S) transmission values and corresponding standard deviations (σ_{T_M} and σ_{T_S}) at Nanowood, operated at 120 kV, with relative differences (R) between real and simulated data.

Filter	T_M(%)	T_S(%)	R(%)	σ_{T_M}(%)	σ_{T_S}(%)
50 μm W	42.5	43.6	-2.5	0.42	0.43
30 μm Mo	70.7	69.8	1.3	0.55	0.55
150 μm Al	95.6	95.9	-0.4	0.34	0.64
68 μm Cu	70.9	72.5	-2.2	0.74	0.57
136 μm Cu	58.1	59.9	-3.1	0.72	0.52
272 μm Cu	43.8	45.3	-3.3	0.61	0.45
544 μm Cu	28.9	29.8	-3.3	0.48	0.37
1.0 mm Cu	17.8	17.5	1.9	0.31	0.29

Real and simulated transmission values appear to be in good agreement with each other, with relative differences of only a few percent for all three scanners. Moreover, the data also indicates that Poisson statistics are a good approximation to model noise in projection images. Note however that there is a systematic positive bias of about 1 to 5 % for HECTOR, indicating that the simulated transmission

systematically underestimates the measured transmission. This may have several reasons. First of all, the exact detector construction (especially the composition and thickness of the entrance layer) of the Perkin Elmer detector is not known. Secondly, this detector suffers, more than the Varian detector, from ghosting. Finally, due to the high tube power typically used at HECTOR, some local melting of the anode material may occur, resulting in pitting of the target. X-rays originating from such a pit in the target, will generally cross more material before escaping the target, leading to a harder X-ray beam.

Table 3.3: Measured (T_M) and simulated (T_S) transmission values and corresponding standard deviations (σ_{T_M} and σ_{T_S}) at HECTOR, operated at 100 kV (upper part table) and 160 kV (lower part table), with relative differences (R) between real and simulated data.

Filter	$T_M(\%)$	$T_S(\%)$	*R(%)*	$\sigma_{T_M}(\%)$	$\sigma_{T_S}(\%)$
50 μm W	39.1	37.9	3.1	0.22	0.11
100 μm W	22.2	21.8	1.8	0.13	0.08
150 μm Al	94.3	94.1	0.3	0.13	0.16
68 μm Cu	66.9	66.1	1.2	0.25	0.14
136 μm Cu	53.9	52.5	2.6	0.23	0.13
272 μm Cu	39.3	37.6	4.3	0.16	0.11
408 μm Cu	30.5	29.9	2.0	0.16	0.10
50 μm W	50.9	49.5	2.8	0.25	0.12
100 μm W	31.7	31.0	2.4	0.17	0.09
150 μm Al	99.8	96.6	3.2	0.16	0.16
68 μm Cu	80.0	77.8	2.7	0.24	0.14
136 μm Cu	69.3	66.5	4.0	0.24	0.12
272 μm Cu	54.9	52.4	4.6	0.21	0.11
408 μm Cu	45.4	43.1	5.1	0.20	0.11

3.4.2 Comparison of a projection image

A projection image of an aluminium sphere with a 6 mm diameter was recorded at the Medusa scanner. The transmission source was operated at 100 kV with a tube power of 10 W and the Varian detector was used. SOD and SDD were 102.8 and 862.8 mm, respectively. Projection images of 910 by 725 pixels were obtained with a projection image resolution of 30 μm. Figure 3.13(a) shows a normalised image. As discussed in section 3.1.2, the internal Mo structures in the FeinFocus transmission tube can give rise to secondary radiation. By adjusting the grey value

Table 3.4: Measured (T_M) and simulated (T_S) transmission values and corresponding standard deviations (σ_{T_M} and σ_{T_S}) at Medusa, operated at 120 kV, with relative differences (R) between real and simulated data.

Filter	$T_M(\%)$	$T_S(\%)$	*R(%)*	$\sigma_{T_M}(\%)$	$\sigma_{T_S}(\%)$
50 μm W	39.6	39.6	0.0	0.17	0.15
100 μm W	24.3	23.0	5.3	0.15	0.11
30 μm Mo	70.3	68.0	3.3	0.15	0.19
150 μm Al	94.7	95.3	-0.6	0.14	0.22
68 μm Cu	65.2	68.4	-4.7	0.37	0.20
136 μm Cu	54.2	55.9	-3.0	0.32	0.18
272 μm Cu	41.0	42.0	-2.4	0.26	0.16
408 μm Cu	32.7	33.7	-2.8	0.21	0.14

Table 3.5: Chosen tube head type, detector and operating parameters for comparison of measured and simulated transmission values at three UGCT scanners. "Time" indicates the total integration time per projection.

Scanner	*Tube type*	*Detector*	*Voltage (kV)*	*Power (W)*	*SDD (mm)*	*Time (s)*
Nanowood	Directional	Varian	120	3.6	663.1	2
HECTOR	Directional	Perkin Elmer	100 160	20	1028.3	5
Medusa	Transmission	Varian	120	6	862.8	7.5

scaling, the *halo* resulting from this phenomenon can be made visible as illustrated in figure 3.13(b).

One of the options to correct for the secondary spot is a hardware correction method, which consists of a thin lead collimator that can be mounted on the X-ray tube [26]. The collimator opening has a diameter of approximately 1 mm and removes almost all secondary radiation. A similar projection of the Al sphere was made using this hardware correction. In addition, a simulation of the projection was performed with Arion. Note that the X-ray spectra used for this simulation were generated without taking the Mo inner structure into account as in figure 3.5. A line profile of the recorded projection is compared with the simulated projection in figure 3.14. It is clear that predicted and measured transmission values corre-

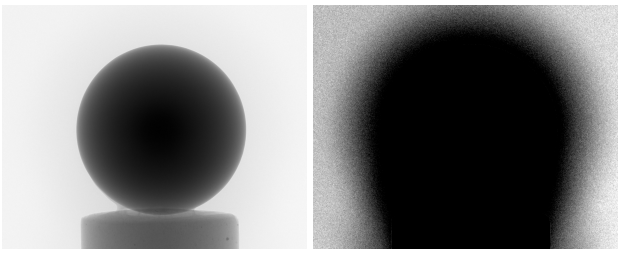

(a) (b)

Figure 3.13: A projection image of the Al sphere (a) and the halo resulting from secondary radiation (b). (Both images are generated using the same projection but use another grey value scaling.) [1]

spond quite well. Differences can be mainly attributed to the fact that secondary spot is not fully removed by the custom collimator.

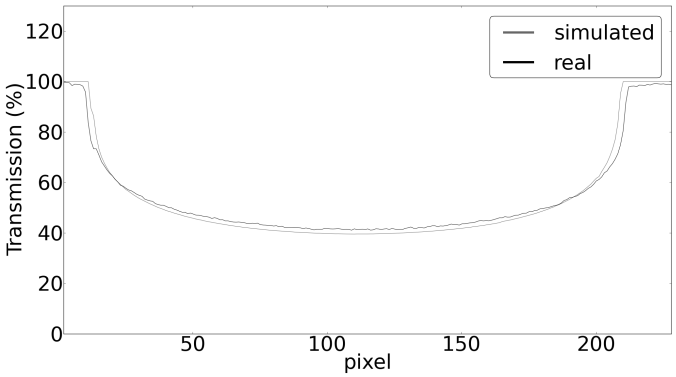

Figure 3.14: Line profile of a real and a simulated projection of the Al sphere [1].

3.4.3 Comparison of reconstructions

For comparison of reconstructed grey values, a cylindrical phantom of 34 mm diameter was made containing five tubes of 6.2 mm diameter with different aqueous solutions - lead nitrate, phosphotungstic acid (PTA), barium chlorate, potassium bromide and calcium bromide - each with a precisely known concentration (Table 3.6). The phantom itself was filled with water. Figure 3.15 shows the model of this phantom used for the simulations with Arion.

A scan of the sample was performed at Nanowood, using the directional X-ray source, operated at 100 kV with a tube power of 16 W, in combination with the

Table 3.6: Mass fractions of the solutes and water and the density for each solution contained in the cylindrical phantom

Material	*Mass fraction solute*	*Mass fraction H_2O*	*Density (g/cm^3)*
$Ba(ClO_3)_2$	0.103	0.897	1.12
KBr	0.115	0.885	1.13
$CaCl_2$	0.412	0.588	1.32
$Pb(NO_3)_2$	0.078	0.922	1.09
PTA	0.074	0.926	1.08

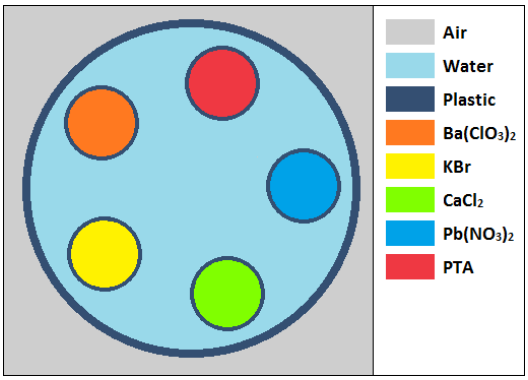

Figure 3.15: Model of the cylindrical phantom with colour legend used for the simulations

Varian detector. Additional beam filtration was provided by a 0.45 mm aluminium filter. SOD and SDD were 287.6 and 689.9 mm, respectively, with a voxel size of 105 µm. The exposure time per projection was 0.8 s. A reconstructed slice of both the real and the simulated CT scan of the sample are shown in figure 3.16. During reconstruction no beam hardening correction was applied to ensure a correct comparison of measured and simulated grey values. Note that the presence of beam hardening artefacts is very well reproduced in the simulated image.

Table 3.7 compares the reconstructed attenuation coefficients for the materials present in the cylindrical phantom for the recorded and the simulated CT scan. A maximum relative difference of 3.9% is observed for the $CaCl_2$ solution. However, uncertainty on the density of this solution is larger due to its high concentration. This may be a reason for the relatively large deviation observed for this material. Nevertheless, these data demonstrate the quantitative correctness of the simulations both in terms of reconstructed attenuation coefficients and image noise.

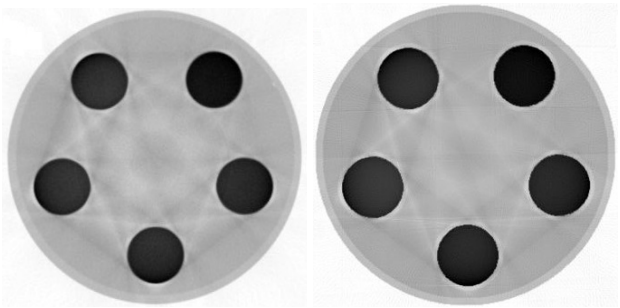

(a) (b)

Figure 3.16: Reconstructed slice of the real (a) and simulated (b) CT scan of the cylindrical phantom

A similar experiment performed at the Medusa scanner showed a maximum difference between real and simulated data of 6.5%. It should be noted that the effect of secondary spot can play a role in these results.

Table 3.7: Measured (M) and simulated (S) reconstructed attenuation values and corresponding standard deviations (σ_M and σ_S) at 100 kV for the different materials in the cylindrical phantom, with relative differences (R) between real and simulated data.

Material	*M(cm^{-1})*	*S(cm^{-1})*	*R(%)*	*σ_M(cm^{-1}))*	*σ_S(cm^{-1})*
$Ba(ClO_3)_2$	0.853	0.859	0.7	0.015	0.015
KBr	0.745	0.754	1.2	0.023	0.022
$CaCl_2$	0.748	0.720	3.9	0.021	0.023
$Pb(NO_3)_2$	0.769	0.776	0.9	0.022	0.022
PTA	0.776	0.777	0.1	0.021	0.020
H_2O	0.268	0.262	-2.2	0.026	0.022

3.4.4 Modeling beam hardening

It is of particular importance that the simulation software is able to correctly model the effects of beam hardening. The previous example already demonstrated that beam hardening artefacts are well reproduced, by means of a visual assessment. For a quantitative evaluation of beam hardening, the Al sphere from section 3.4.2 can be used. Relatively more photons will be absorbed in the outer layer of the sphere than in the middle resulting in a lower reconstructed attenuation coefficient in the centre of the sample. This phenomenon is called *cupping*. The sphere was scanned using the custom collimator and applying the same scanning parameters

as for the projections in section 3.4.2. The CT scan had a voxel size of 30 µm. A reconstructed slice of the scan is shown in figure 3.17(a) and a line profile of both the real and simulated scan are shown in figure 3.17(b). A deviation of 5% was observed, again demonstrating the quantitative correctness of the simulated CT images. Note that here as well, differences between the real and simulated data may be mainly attributed to the fact that secondary spot is not fully removed by the custom collimator.

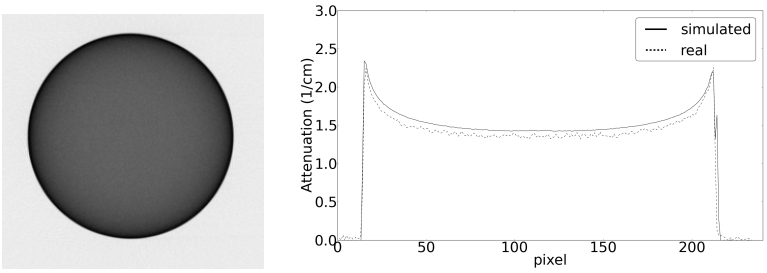

(a) (b)

Figure 3.17: Reconstructed slice of a real CT scan of the Al sphere (a) and line profiles of the real and simulated CT scan of the sphere (b) [1]

3.5 Benchmarks and outlook

Apart from its quantitative correctness, the speed of the simulation software is also of particular importance. Therefore, some benchmarks will be given here. To conclude, some future improvements will be mentioned briefly.

3.5.1 Benchmarks

All previous simulations were performed on an ASUS GTX780-DC2OC-3GD5 GPU. As described in section 3.2.4, the rebinning procedure which assigns a variable size to each energy bin in order to reduce the total number of bins without loosing accuracy, can drastically reduce the computation time. Other parameters which will exert an important influence on the computation time are the number of voxels in the phantom and the number of pixels of the detector. In table 3.8 the values for each of these parameters used in the previous simulations are given. In addition, the computation time for a single radiographic projection and the full CT scan are shown.

Table 3.8: Computation time for simulated projections and CT scans of the cylindrical phantom and Al sphere using a binned spectrum containing 50 bins.

Parameter	*Phantom*	*Al sphere*
Phantom dimensions (x,y,z)	(365,365,40)	(1024,1024,100)
Detector dimensions (x,z)	(500,500)	(500,500)
number of projections	501	501
time for 1 projection (ms)	33	37
total simulation time (s)	16.6	18.6

3.5.2 Future improvements

In this chapter it was demonstrated that the Setup Optimiser and Arion are versatile simulation tools allowing for quantitative correct and fast simulations in a flexible way. Since these tools are recently developed, they contain of course several areas for future improvements. For instance, the implementation of a finite spot size can be very useful, in particular for the simulation of secondary spot effects. Note that this is already covered to a great extent in [18], but not fully implemented in Arion at present. Other useful additions would be the implementation of scattering, since scattered photons may be able to reach the detector. This phenomenon is, for now, not taken into account in the simulation software. Wave properties of X-rays are neglected as well. Taking these into account would allow to simulate phase contrast effects as well. Furthermore, the implementation of detector "ghosting" would also be a useful addition. Ghosting is a type of detector lag, caused by delayed release of trapped charges from the detector resulting in a ghost image present long after its acquisition. Finally, research is currently being performed to incorporate an indication of absorbed dose in the simulation software. As mentioned in 2.5.5, this is not at all straightforward.

References

[1] J. Dhaene, E. Pauwels, T. De Schryver, A. De Muynck, M. Dierick, and L. Van Hoorebeke. *A realistic projection simulator for laboratory based X-ray micro-CT*. Nuclear Instruments and Methods in Physics Research Section B: Beam Interactions with Materials and Atoms, 342(0):170–178, 2015.

[2] E. Pauwels. *Optimalisatie van gebruik en detectie van contraststoffen in hoge resolutie X-stralentomografie op basis van de energieafhankelijkheid van hun attenuatie*. Master's thesis, Ghent University, 2010.

[3] E. Pauwels, L. Brabant, M. N. Boone, M. Dierick, D. Van Loo, and L. Van Hoorebeke. *The UGCT setup optimizer for developing DECT*. In CT Scan Workshop: Development on non-medical environment, Quebec City, Canada, 2012.

[4] P. Duvauchelle, N. Freud, V. Kaftandjian, and D. Babot. *A computer code to simulate X-ray imaging techniques*. Nucl. Instrum. Methods Phys. Res., Sect. B, 170(1-2):245–258, 2000.

[5] N. Freud, P. Duvauchelle, S. A. Pistrui-Maximean, J.-M. LÃ©tang, and D. Babot. *Deterministic simulation of first-order scattering in virtual X-ray imaging*. Nucl. Instrum. Methods Phys. Res., Sect. B, 222(1-2):285–300, 2004.

[6] N. Freud, J.-M. Létang, and D. Babot. *A hybrid approach to simulate multiple photon scattering in X-ray imaging*. Nucl. Instrum. Methods Phys. Res., Sect. B, 227(4):551–558, 2005.

[7] N. Freud, P. Duvauchelle, J.-M. Létang, and D. Babot. *Fast and robust ray casting algorithms for virtual X-ray imaging*. Nucl. Instrum. Methods Phys. Res., Sect. B, 248(1):175–180, 2006.

[8] A. Peterzol, J. Berthier, P. Duvauchelle, C. Ferrero, and D. Babot. *X-ray phase contrast image simulation*. Nucl. Instrum. Methods Phys. Res., Sect. B, 254(2):307–318, 2007.

[9] D. Lazos, K. Bliznakova, Z. Kolitsi, and N. Pallikarakis. *An integrated research tool for X-ray imaging simulation*. Comput. Methods Programs Biomed., 70(3):241–51, 2003.

[10] K. Bliznakova, Z. Kolitsi, and N. Pallikarakis. *Dual-energy mammography: simulation studies*. Phys. Med. Biol., 51(18):4497–4515, 2006.

[11] K. Bliznakova, R. Speller, J. Horrocks, P. Liaparinos, Z. Kolitsi, and N. Pallikarakis. *Experimental validation of a radiographic simulation code using breast phantom for X-ray imaging*. Comput. Biol. Med., 40(2):208–14, 2010.

[12] S. Kasperl, J. Hiller, and M. Krumm. *Computed tomography metrology in industrial research and development*. Mater. Test., 51(6):405–411, 2009.

[13] F. Inanc. *Scattering and its role in radiography simulations*. NDT E Int., 35(8):581–593, 2002.

[14] D. W. O. Rogers, B. A. Faddegon, G. X. Ding, C. M. Ma, J. We, and T. R. Mackie. *BEAM: A Monte Carlo code to simulate radiotherapy treatment units*. Med. Phys., 22(5):503–524, 1995.

[15] I. Kawrakow. *Accurate condensed history Monte Carlo simulation of electron transport. II. Application to ion chamber response simulations*. Med. Phys., 27(3):499–513, 2000.

[16] *XCOM: Photon Cross Sections Database*. `http://www.nist.gov/pml/data/xcom/`.

[17] J. Vlassenbroeck. *Advances in laboratory-based X-ray microtomography*. Phd dissertation, Ghent University, 2009.

[18] J. Dhaene. *Development and application of a highly accurate polychromatic X-ray microtomography simulator*. Phd dissertation, Ghent University, 2017.

[19] R. Birch and M. Marshall. *Computation of bremsstrahlung X-ray-spectra and comparison with spectra measured with a Ge(Li) detector*. Phys. Med. Biol., 24(3):505–517, 1979.

[20] D. M. Tucker, G. T. Barnes, and D. P. Chakraborty. *Semiempirical model for generating tungsten target X-ray-spectra*. Med. Phys., 18(2):211–218, 1991.

[21] D. M. Tucker, G. T. Barnes, and X. Z. Wu. *Molybdenum target X-ray-spectra: A semiempirical model*. Med. Phys., 18(3):402–407, 1991.

[22] J. M. Boone, T. R. Fewell, and R. J. Jennings. *Molybdenum, rhodium, and tungsten anode spectral models using interpolating polynomials with application to mammography*. Med. Phys., 24(12):1863–74, 1997.

[23] G. Tirao, C. Quintana, F. Malano, and M. Valente. *X-ray spectra by means of Monte Carlo simulations for imaging applications*. X-Ray Spectrom., 39(6):376–383, 2010.

[24] R. J. Mathar. *Solid angle of a rectangular plate*. `http://www.mpia-hd.mpg.de/~mathar/public/mathar20051002.pdf`, 2014.

[25] M. N. Boone, J. Vlassenbroeck, S. Peetermans, D. Van Loo, M. Dierick, and L. Van Hoorebeke. *Secondary radiation in transmission-type X-ray tubes: Simulation, practical issues and solution in the context of X-ray microtomography*. Nucl. Instrum. Methods Phys. Res., Sect. A, 661(1):7–12, 2012.

[26] M. N. Boone. *New imaging modalities in high resolution X-ray tomography*. Phd dissertation, Ghent University, 2013.

4

Dual Energy Computed Tomography

In an X-ray CT image it may occur that two or more materials with a different composition have a very similar grey value and as such become practically indistinguishable. This stems from the fact that the linear attenuation coefficient μ is the product of the local density of the material ρ and the local mass attenuation coefficient μ/ρ. The latter is in turn dependent on the X-ray energy and the element(s) present. To overcome this problem, **Dual Energy CT (DECT)** methods have been introduced. These methods rely on the fact that the mass attenuation coefficient of an element is uniquely dependent on the photon energy. Combining CT scans performed at two or more different X-ray energies can provide the necessary information to make a distinction between materials with otherwise very similar grey values. A more specific type of DECT is K-edge imaging, where the scanning energies are tuned around the K-edge of a selected element.

DECT can be quite easily applied if monochromatic X-ray sources are used, such as available at a synchrotron facility. However, for laboratory based CT scanners the combination of polychromatic X-ray sources with integrating detectors with an energy-dependent efficiency complicates matters to a great extent. Accurate simulations may prove to be particularly useful in these cases.

In this chapter, first a general background and brief literature overview on dual energy techniques will be given. K-edge imaging will also be discussed. Next, the dual energy image processing methods applied at UGCT will be described. In the following section, a thorough discussion on the fine tuning and selection of X-ray

spectra for DECT will be given. Finally, some practical examples of dual energy CT will be shown, applying the discussed principles for selecting the appropriate spectra.

4.1 DECT: background and literature overview

The first articles in which dual energy techniques for CT applications have been proposed already date back to 1976. This is remarkably early since the first CT scanner, the EMI Mark 1, was developed in 1971. However, experimental validation of these theories was not at all straightforward at that time due to the many shortcomings inherent to the first CT systems. Examples include a limited resolution, long scan times and tube currents which were insufficient to generate adequate output at low tube voltages. Moreover, the medical applications presented in several articles were in general not put into practice. It is therefore not at all surprising that publications on this subject seem to stall in the late eighties. A decade later, technical and computational evolutions have breathed new life into DECT techniques. In recent years, the first commercial dual energy CT scanners have even been emerging in hospitals [1].

The number of dual energy applications is growing rapidly and is becoming more varied, but the techniques themselves are still essentially extensions and refinements of the theories that have been proposed in 1976. In this section, these first theories will be discussed. Subsequently, a brief overview of some extensions and more recent DECT methods will be given. Furthermore, K-edge imaging will be more thoroughly discussed. Then, the different possible dual energy system setups will be explained and to conclude some DECT applications will be described.

4.1.1 Alvarez and Macovski's dual energy theory

In February 1976, an article written by Alvarez and Macovski [2] was published in which they proposed - probably - the first DECT technique. The reconstruction of CT images is based on measurements of the intensity of a polychromatic X-ray beam integrated over its whole energy spectrum. A general linear attenuation coefficient is then determined at a single average energy. As such, all information actually present in the energy behaviour of the attenuation coefficient $\mu(E)$ is lost. However, it is possible to write this attenuation coefficient $\mu(E)$ as a linear combination of a set of energy-dependent basis functions $\{f_i(E), i = 1, 2, ..., n\}$ with a small number of energy-independent coefficients $\{a_i, i = 1, 2, ..., n\}$:

$$\mu(E) = a_1 f_1(E) + a_2 f_2(E) + ... + a_n f_n(E). \tag{4.1}$$

The basis functions must be determined empirically, but it is of course useful that the basic set also carries a physical meaning. Alvarez and Macovski therefore chose the following form:

$$\mu(E) = a_1 \frac{1}{E^3} + a_2 f_{KN}(E), \tag{4.2}$$

with $f_{KN}(E)$ the Klein-Nishina function:

$$f_{KN}(\alpha) = \frac{1+\alpha}{\alpha^2}\left[\frac{2(1+\alpha)}{1+2\alpha} - \frac{1}{\alpha} ln(1+2\alpha)\right] + \frac{1}{2\alpha} ln(1+2\alpha) - \frac{1+3\alpha}{(1+2\alpha)^2} \tag{4.3}$$

and $\alpha = E/510.975$ keV. The basis function $1/E^3$ is a good approximation for the energy dependence of photoelectric absorption, while the Klein-Nishina function adequately describes the energy dependence of Compton scattering (see section 2.2). These are the two predominant photon interaction processes in the energy region of interest, making them a useful part of the basis set. a_1 and a_2 can then be written as follows:

$$\begin{aligned} a_1 &\approx K_1 \frac{\rho}{A} Z^n, n \approx 4 \\ a_2 &\approx K_2 \frac{\rho}{A} Z \end{aligned}, \tag{4.4}$$

using K_1 and K_2 as constants. The photoelectric coefficient a_1 is strongly dependent on the atomic number Z and will primarily provide information on the composition of the material, while the coefficient for Compton scattering a_2 depends on electron density, which is in turn proportional to the mass density for most materials. As such a_2 will give an indication on the local density. If the photoelectric and the Compton contribution to the attenuation coefficient can be separated, additional material information can be obtained.

In a CT scan, measurements are made of the line integral of the attenuation coefficient along the path of the X-rays through the object. The line integral of equation 4.2 then becomes:

$$\int \mu(x, y; E) \mathrm{d}s = A_1 \frac{1}{E^3} + A_2 f_{KN}(E), \tag{4.5}$$

with

$$\begin{aligned} A_1 &= \int a_1(x, y) \mathrm{d}s \\ A_2 &= \int a_2(x, y) \mathrm{d}s \end{aligned} \tag{4.6}$$

and (x, y) the position coordinate. The purpose is now to reconstruct $a_1(x, y)$ and $a_2(x, y)$. Therefore, A_1 and A_2 must be known at every point in the radiographic

projections. This requires that two independent sources of information are available for each of those points, such as intensity measurements (i.e. detected output) obtained with two different X-ray spectra. These can be expressed as follows [1]:

$$\begin{aligned} I_1(A_1, A_2) &= \Delta T \int S_1(E) exp\left[-\frac{A_1}{E^3} - A_2 f_{KN}(E)\right] \mathrm{d}E \\ I_2(A_1, A_2) &= \Delta T \int S_2(E) exp\left[-\frac{A_1}{E^3} - A_2 f_{KN}(E)\right] \mathrm{d}E \end{aligned}, \tag{4.7}$$

with ΔT the total measurement time and $S_1(E)$ and $S_2(E)$ the X-ray spectra. Solving these equations for all projections yields a known set of line integrals A_1 and A_2 for all projections. $a_1(x, y)$ and $a_2(x, y)$ can be derived from these line integrals and reconstructed, entirely analogous to a standard CT image reconstruction. Knowledge of the photoelectric and Compton coefficients can provide the necessary information to distinguish different materials with a similar grey value.

Extension to radiography

A specific challenge for dual energy techniques are single radiographic projections. Due to the superimposition of all materials along an X-ray trajectory in the final image, the method proposed by Alvarez and Macovski cannot readily be applied. A more comprehensive theoretical framework is needed. This was developed by Lehmann *et al.* [3] in 1981. Their method allows to remove a material from the image and "fill in" the resulting vacancy with a different specific material. Details can be found in [3], including an experimental verification of the theory.

4.1.2 Rutherford's dual energy theory

In May 1976, a second article was published by Rutherford *et al.* [4] presenting a different dual energy technique. This method allows to extract information on the electron density and the effective atomic number of the materials from two CT images obtained at two different X-ray beam energies. The main difference from Alvarez and Macovski's technique is that this is a postreconstruction method, since image operations are performed on the reconstructed data, and not on the radiographic projections. The disadvantage of such methods is the loss of accuracy due to image artefacts such as beam hardening [5].

The linear attenuation coefficient μ of a material may be related to its atomic composition as follows:

$$\mu = \sigma_{tot} N \tag{4.8}$$

[1] Note that since the total measurement time is taken into account in these expressions, they should be more correctly defined as detected energy instead of intensity.

with σ_{tot} the total microscopic cross section for photon interactions with the material and N the atomic density of the material. For X-ray photons, this total cross section can be approximated as follows:

$$\sigma_{tot}(Z,E) = \tau(Z,E) + \sigma(E) + \Delta(Z,E), \tag{4.9}$$

with τ and σ the atomic cross sections of photoelectric absorption and Compton scattering, respectively, and Δ a correction term to take Rayleigh scattering and binding energy effects into account. Note that σ is in fact the Klein-Nishina cross section. Rutherford *et al.* have shown that the linear attenuation coefficient for a particular material at a given photon energy can be written as follows:

$$\mu(E) = AE^{-B}Z^{C}N + \sigma(E)ZN + DE^{-F}Z^{G}N, \tag{4.10}$$

with constants A, B, C, D, F and G. Values for these constants were determined by Payne *et al.* [6] by fitting equations of the form $\sigma = const.E^{-m}Z^{n}$ to cross section values of several elements. Equation 4.10 then becomes:

$$\mu(E) = 21.7E^{-3.30}Z^{4.62}N + \sigma(E)ZN + 1.17E^{-1.86}Z^{2.92}N, \tag{4.11}$$

By performing CT scans at two different energies, E_1 and E_2, $\mu(E_1)$ and $\mu(E_2)$ can be measured. Moreover, the Klein-Nishina cross sections at these two energies are known. By means of an iterative method, the effective atomic number Z can then be obtained from the following equation:

$$\frac{\mu(E_1)}{\mu(E_2)} = \frac{AE_1^{-B}Z^{C} + \sigma(E_1)Z + DE_1^{-F}Z^{G}}{AE_2^{-B}Z^{C} + \sigma(E_2)Z + DE_2^{-F}Z^{G}} \tag{4.12}$$

Subsequently equation 4.10 can be used to determine N, and as such the electron density (NZ).

An important disadvantage of this dual energy algorithm is that the technique is highly sensitive to noise and variations in measured attenuation coefficients [4, 6, 7].

4.1.3 A raw data-based decomposition in basis materials

Alvarez and Macovski have shown that the linear attenuation coefficient can be expressed as a linear combination of a set of basis functions (4.1). They chose to use basis functions that represent the two dominant processes of X-ray interactions with matter (in the energy range of interest): photoelectric absorption and Compton scattering. Kalender *et al.* [5] proposed an alternative set of basis functions. The mass attenuation coefficient of any material can also be written as a linear combination of the mass attenuation coefficient of two basis materials (1 and 2):

$$\left(\frac{\mu}{\rho}\right)(E) = \alpha_1 \left(\frac{\mu}{\rho}\right)_1 (E) + \alpha_2 \left(\frac{\mu}{\rho}\right)_2 (E) \tag{4.13}$$

An important condition is that the two basis materials should have a sufficiently different atomic number Z and as such they should exhibit a sufficiently different behaviour in photoelectric absorption and Compton scattering. This decomposition is therefore highly suitable for K-edge imaging (see 4.1.5). The line integral of the attenuation coefficient - equivalent of (4.5) - can be written as follows:

$$\int \mu(\mathbf{r}, E)\mathrm{d}s = \left(\frac{\mu}{\rho}\right)_1 (E)\delta_1 + \left(\frac{\mu}{\rho}\right)_2 (E)\delta_2, \tag{4.14}$$

with:

$$\delta_i = \int \rho_i(\mathbf{r})\mathrm{d}s. \tag{4.15}$$

δ_i and $\rho_i(\mathbf{r})$ are the area density (in g/cm^2) and the local desity (in g/cm^3) of basis material i, respectively. Similar to equation 4.5 where the values for A_1 and A_2 were to be determined for each ray path, here values for the area densities δ_1 and δ_2 for the two basis materials should be obtained at each point in the projections. Again the solution lies in performing two scans with different X-ray spectra. The equivalent for equation set 4.7 can be written as follows [2]:

$$\begin{aligned} I_h &= \Delta T \int I_{0h}(E) exp\left[-\left(\frac{\mu}{\rho}\right)_1 (E)\delta_1 - \left(\frac{\mu}{\rho}\right)_2 (E)\delta_2\right] \mathrm{d}E \\ I_l &= \Delta T \int I_{0l}(E) exp\left[-\left(\frac{\mu}{\rho}\right)_1 (E)\delta_1 - \left(\frac{\mu}{\rho}\right)_2 (E)\delta_2\right] \mathrm{d}E \end{aligned}. \tag{4.16}$$

Indices h and l refer to the scan with the higher and lower energy spectrum, respectively. Solving this set of equations will allow to reconstruct the density distributions for the two basis materials. Materials with a different atomic number will contribute in a specific manner to both δ_1 and δ_2. An interesting possibility is to multiply the values δ_1 and δ_2 by the mass attenuation coefficients of the respective basis materials for a specific energy E_0:

$$\int \mu(\mathbf{r}, E_0)\mathrm{d}s = \left(\frac{\mu}{\rho}\right)_1 (E_0)\delta_1 + \left(\frac{\mu}{\rho}\right)_2 (E_0)\delta_2. \tag{4.17}$$

Reconstruction of the processed projection data will yield a mono-energetic CT image. An important advantage is that this allows to remove beam hardening artefacts.

Several methods have been proposed to solve the set of equations 4.16 (or 4.7). Alvarez and Macovski used second-order power series to fit the two equations and solved them numerically using a generalised Newton-Raphson method [2]. The disadvantage is that this is not only inefficient, but also unstable [8]. Other methods

[2] Again, this should be more correctly defined as detected energy instead of intensity.

are described in [3, 8, 9] and [5, 10]. In these last publications, a table look-up procedure is used. The construction of the look-up tables can be time consuming, but the actual decomposition procedure is fast, stable and straightforward.

4.1.4 An image-based decomposition in basis materials

A postreconstruction material decomposition method was developed by Vinegar and Wellington [11] and successfully applied by Granton *et al.* [12]. The attenuation coefficient in each voxel of a CT image can be expressed as a linear combination of the attenuation coefficients of the basis materials multiplied by their volume fraction. For a decomposition in two basis materials this becomes:

$$\mu(E) = \mu_1(E) \cdot f_1 + \mu_2(E) \cdot f_2, \tag{4.18}$$

with f_1 and f_2 the volume fractions of material 1 and 2, respectively. These parameters can be determined using DECT by solving the following set of equations:

$$\begin{aligned} \mu_{E_1} &= \mu_{1,E_1} \cdot f_1 + \mu_{2,E_1} \cdot f_2 \\ \mu_{E_2} &= \mu_{1,E_2} \cdot f_1 + \mu_{2,E_2} \cdot f_2 \end{aligned}, \tag{4.19}$$

with E_1 and E_2 the X-ray energies of the two recorded images. μ_1 and μ_2 for each image can be obtained by measuring the attenuation coefficient in voxels which contain solely material 1 and 2, respectively, with 100% certainty.

For many studies, especially when contrast agents are used, a three-material decomposition is often required. Although in principle, DECT only allows the quantification of a maximum of two basis materials, an extension towards three basis materials can be realised by adding a volume conservation constraint. In this case it is assumed that each voxel contains only basis materials. This can be expressed as follows:

$$f_1 + f_2 + f_3 = 1. \tag{4.20}$$

For three basis materials equation set 4.19 becomes:

$$\begin{aligned} \mu_{E_1} &= \mu_{1,E_1} \cdot f_1 + \mu_{2,E_1} \cdot f_2 + \mu_{3,E_1} \cdot f_3 \\ \mu_{E_2} &= \mu_{1,E_2} \cdot f_1 + \mu_{2,E_2} \cdot f_2 + \mu_{3,E_2} \cdot f_3 \end{aligned}. \tag{4.21}$$

Granton *et al.* used matrix factorisation for solving equation 4.20 and 4.21, with an added non-negative constraint. The latter serves to exclude negative volume fractions.

If a third CT scan is acquired at mean X-ray energy E_3, the decomposition may further be optimised. The system of equations is thus extended by a fourth equation:

$$\mu_{E_3} = \mu_{1,E_3} \cdot f_1 + \mu_{2,E_3} \cdot f_2 + \mu_{3,E_3} \cdot f_3. \tag{4.22}$$

The system is now over-determined, but may still be solved via the minimisation of the mean squared difference Δ between the measured attenuation coefficients at the three energies and the calculated attenuation coefficients for all possible combinations of volume fractions for the basis materials:

$$\Delta|_{f_1 f_2 f_3} = \sum_{i=1}^{3} (\mu_{Calculated,E_i} - \mu_{Observed,E_i})^2. \tag{4.23}$$

As mentioned in section 4.1.2, an important disadvantage of image-based DECT methods is that their accuracy is reduced by beam hardening effects, such as cupping and metal artefacts. Raw data-based techniques are more quantitative and generally result in better image quality [13]. Moreover, they allow to reconstruct monochromatic images and thus to remove all beam hardening (see section 4.1.3). On the other hand, raw data-based methods require that both scan sets have exactly the same scan geometry, which is often not the case, especially in clinical dual energy CT scanners. Maaß *et al.* [13] developed a new image-based method, based on the work of Coleman and Sinclair [14], which combines the mismatched raw data sets for dual energy information to reduce beam hardening effects. The technique proved to perform better than conventional image-based methods, but was inferior to raw data-based methods.

4.1.5 K-edge imaging

K-edge imaging, or K-edge digital subtraction technique (KES), is a specific type of the more general dual energy technique. The method can be applied when a sample contains a (contrast) material with a relatively high atomic number and thus a well-identifiable K-edge. The best way to selectively visualise this material is to take advantage of the marked behaviour of its attenuation coefficient around the K-edge. To this purpose, two CT scans are taken, one with an X-ray spectrum energy just below the K-edge and the other with an X-ray spectrum energy just above the edge. The attenuation coefficient of the given material will be significantly different at these two energies, which is not the case for the other materials present. As such, image processing, such as a a logarithmic subtraction of the projection images will enhance all structures containing the material, while the rest of the sample will virtually disappear [15]. How the X-ray spectrum energy is defined in case of a polychromatic spectrum, is thoroughly discussed in section 4.3.2.

All previously discussed DECT algorithms are directly applicable to K-edge imaging. K-edge imaging especially lends itself to tomography by means of monochromatic X-rays, such as synchrotron radiation. Not only does this allow for a much more accurate fine tuning of the two acquisition energies around the edge,

also the methods for processing the resulting images are a lot more straightforward. For purposes of illustration, a K-edge imaging algorithm using monochromatic X-ray spectra [15] will be briefly discussed below.

K-imaging using monochromatic X-ray spectra [15]

The logarithm of the attenuation caused by a sample at X-ray energy E_+ and E_- just above and below a specific material's K-edge, respectively, is given by:

$$ln\frac{I_0}{I}\Big|_{\pm} = C_{\pm} = \left[\frac{\mu_{\pm}}{\rho}\right]_X \cdot (\rho t)_X + \left[\frac{\mu_{\pm}}{\rho}\right]_W \cdot (\rho t)_W, \tag{4.24}$$

with the indices X and W referring to the chosen contrast material and a basis material (for instance water), respectively, and t the thickness of the material. In fact, this is equivalent to set of equations 4.16 for monochromatic X-ray spectra, since δ_i equals $(\rho t)_i$ according to equation 4.15. From the system of independent equations 4.24, $(\rho t)_X$ and $(\rho t)_W$ can be calculated as follows:

$$\begin{aligned}(\rho t)_X &= \frac{\left[\frac{\mu_-}{\rho}\right]_W C_+ - \left[\frac{\mu_+}{\rho}\right]_W C_-}{K_0} \\ (\rho t)_W &= \frac{\left[\frac{\mu_+}{\rho}\right]_X C_- - \left[\frac{\mu_-}{\rho}\right]_X C_+}{K_0}\end{aligned}, \tag{4.25}$$

with

$$K_0 = \left[\frac{\mu_-}{\rho}\right]_W \left[\frac{\mu_+}{\rho}\right]_X - \left[\frac{\mu_+}{\rho}\right]_W \left[\frac{\mu_-}{\rho}\right]_X \tag{4.26}$$

For a radiographic projection, the first equation of 4.25 corresponds to the "contrast" image with the chosen contrast material's contribution isolated from the background. In the image based on the second equation, the mass densities of all other materials crossed by the X-ray beam are expressed in terms of the density of the second basis material.

For CT scans, these algorithms can be applied on the projection data and subsequently reconstructed in a normal way. Apart from this raw data-based method, one can also opt for an image-based decomposition technique. For each voxel in the CT image, the linear attenuation coefficient can be expressed as a linear combination of the two basis materials:

$$\mu_{\pm} = \left[\frac{\mu_{\pm}}{\rho}\right]_X \cdot \rho_X + \left[\frac{\mu_{\pm}}{\rho}\right]_W \cdot \rho_W. \tag{4.27}$$

Analogously:

$$\begin{aligned} \rho_X &= \frac{\mu_- \left[\frac{\mu_+}{\rho}\right]_W - \mu_+ \left[\frac{\mu_-}{\rho}\right]_W}{K_0} \\ \rho_W &= \frac{\mu_+ \left[\frac{\mu_-}{\rho}\right]_X - \mu_- \left[\frac{\mu_+}{\rho}\right]_X}{K_0} \end{aligned} . \tag{4.28}$$

4.1.6 Dual energy system setups

There exist several technical approaches to dual energy CT systems [16]:

- **Temporally sequential scans:** Technically, the most straightforward approach to DECT is to perform two consecutive CT scans with each a different tube voltage and/or filtration. This requires no special hardware, but is of course prone to sample (or patient) movement and can be time-consuming.
- **Fast kV$_p$ switching:** A single X-ray source is used to alternately record the projection images at low and high energy by rapidly switching the peak tube voltage (kV$_p$). The near-simultaneous acquisition of the two data sets practically eliminates misregistration due to sample movement. Moreover, as there is no mismatch, both raw data-based and image-based DECT methods can be applied. On the other hand, there is a relatively large overlap between the two spectra since only one X-ray source is used. Furthermore, special hardware is required.
- **Dual source:** In this setup, two X-ray sources, operating at different tube voltages, and two detectors are mounted on the same gantry perpendicularly to one another. An important advantage is that tube current and beam filtration can be optimised for each tube independently, resulting in a limited overlap between the two generated spectra. On the other hand, scattered radiation of the beam originating from one tube, may be detected by the detector of the other X-ray source. Therefore, specialised scatter corrections are required. Moreover, the projection data of the two data sets are approximately 90° out of phase. As a result, only image-based DECT methods can be straightforwardly applied.
- **Dual-layer detector:** A single high energy X-ray exposure is used and the two data sets are created at the level of the detector. The low energy images are recorded at the top layer of the detector, while the high energy data are collected at the bottom layer. As a result both data sets are acquired simultaneously and there is no mismatch. However, the detector design is quite complicated and there exists a relatively high overlap between the detected spectra.

- **Photon-counting detector:** The advent of photon-counting detectors has opened up a new range of possibilities to implement DECT. This type of detector has several advantages over energy-integrating detectors. First of all, each detected photon is counted so the signal itself is digital in nature. As a result electronic noise can be minimised. Moreover, each photon is detected with the same energy weighting factor, regardless of its energy. This improves the signal-to-noise ratio even further, as compared to energy-integrating detectors, where high energy photons have a larger contribution to the output signal than low energy photons. Furthermore, rejection of scattered radiation would be possible. Finally, photon-detectors allow for energy-resolved imaging [17, 18]. Energy thresholds can be set so that the collected photons are divided in separate energy bins. This allows for "true" dual or even multi-energy imaging. Especially for K-edge imaging, photon-counting detectors can be highly useful. In this case, an energy threshold is chosen at the K-edge of a specific material. Specific processing methods of the spectral data have been developed [19–21].

Of the aforementioned dual energy approaches, mainly the middle three are used for clinical applications. Although photon-counting detectors offer many conceptual advantages over other approaches [22], they will not be commonly available in the near future due to existing limitations [16]. The critical issue in clinical CT is that detectors have to cope with high peak X-ray fluxes, up to 10^9 counts per s per mm^2, which is beyond the limits of current photon counting detectors [16, 19]. Therefore, up to now, experimental proof-of-concept studies have focused mainly on relatively low photon flux modalities, such as micro-CT [23, 24].

4.1.7 DECT: a growing research field with many practical applications

Through increasing technical and computational possibilities, DECT is a rapidly growing research field. In recent years, several new or more extensive reconstruction and decomposition methods were published [25–30], but above all the number of practical applications has shown a strong increase. Below, a non-exhaustive list of clinical DECT applications is briefly discussed [16]:

- **Characterisation of renal stone composition:** DECT allows for the characterisation of renal calculi [31]. It is of particular significance to differentiate uric acid stones from other stone types, since they can be dissolved by urinary alkalisation so that invasive interventional procedures may be avoided. Primak *et al.* [32] showed a 92% to 100% accuracy in discriminating uric acid stones from other types using DECT.

- **Automated bone removal in CT angiography:** Dual energy techniques are highly useful for CT angiography where intravascular iodine contrast is administered to the patient to visualise the blood vessels. Contrasted blood and bone structures can often be difficult to distinguish from one another. Dual energy techniques offer a solution by allowing for the automated removal of bone structures from the images [33, 34]. Especially in neuroradiology, visualisation of intracranial blood vessels can be greatly optimised in this way [35].
- **Virtual non-enhanced images:** It can also be interesting to remove the iodine contrast from the images, for instance to differentiate between hemorrhage and iodine after intra-arterial recanalisation in stroke patients [35]. These images are called virtual non-enhanced images or virtual non-contrast images. An important benefit is that in multiphase examinations the non-contrast scan may be omitted if the image quality is sufficient. This can be particularly useful in abdominal imaging [36].
- **Perfused blood volume (blood pool imaging):** On the other hand specific visualisation of the iodine content can provide important information as well. Iodine-density reconstructions will allow to visualise the perfused blood volume to detect perfusion defects resulting from pulmonary embolisms [37] or evaluate myocardial perfusion to assess for the hemodynamic significance of coronary disease [38, 39].
- **Virtual monochromatic images:** Dual energy techniques also allow to reconstruct mono-energetic images resulting in an important decrease or total removal of beam hardening artefacts. As such visualisation of the brain can be optimised by reduction of the artefacts resulting from dense skull structures. For patients with metal implants in the brain or spine, this can be highly useful as well [35]. Furthermore, monochromatic images improve the detection and characterisation of several hepatic, pancreatic and renal lesions [36].
- **Atherosclerotic plaque component analysis and removal:** DECT can be used to accurately detect and characterise coronary plaques [38, 39]. Moreover, DECT also allows to remove artherosclerotique plaques for grading of steno-occlusive lesions [33].

Despite these numerous clinical applications, it should be noted that the use of DECT is still very limited in routine clinical practice. DECT can also be applied in all kinds of other (research) domains. For instance in geology it can be used to quantify rock porosity [40] or to quantify density and atomic number of distributions of internal features of sedimentary rocks and as such obtain information on the mineralogical composition [41, 42]. Another example where DECT proves to

be useful is the visualisation of a vascular cast [12]. A vascular contrast-casting agent, such as Microfil (MV-122, Flow Tech, Carver, MA), is injected *ex vivo* in the vascular system of an animal specimen. The silicon-rubber compound contains a heavy element, such as lead, and quickly cures into a cast of the vascular system. However, in a CT image it is often difficult to distinguish the casting material from bone structures. Application of DECT can optimise the segmentation of these materials.

4.2 Dual energy image processing techniques applied at UGCT

Currently, there are two image processing techniques for DECT available at UGCT. The first is an image-based material decomposition method, originally from Vinegar and Wellington [11]. The second is an in-house developed technique for reconstructing the atomic value and mass densities of the sample materials. Both methods are postreconstruction methods.

4.2.1 Decomposition in three basis materials

The theoretical background of this image-based decomposition in basis materials method developed by Vinegar and Wellington [11] is described in section 4.1.4. For each voxel in the CT image, the following system of equations has to be solved (equations 4.20 and 4.21):

$$\begin{aligned} f_1 + f_2 + f_3 &= 1 \\ \mu_{E_1} &= \mu_{1,E_1} \cdot f_1 + \mu_{2,E_1} \cdot f_2 + \mu_{3,E_1} \cdot f_3. \\ \mu_{E_2} &= \mu_{1,E_2} \cdot f_1 + \mu_{2,E_2} \cdot f_2 + \mu_{3,E_2} \cdot f_3 \end{aligned} \tag{4.29}$$

Moreover, a non-negative constraint is added. As a result, it is no longer straightforward to solve this system of equations. Granton *et al.* [12] apply matrix factorisation with the added constraint, but gave no further explanation. Here, a different approach is chosen. The system can be solved by an iterative method introduced by Kacmarz [43] and further elucidated by Tanabe [44]. This technique allows to solve linear systems, even when they are over-determined. A full description of the Kacmarz method is given in [45].

First, a "starting solution" $\{f_{1,0}; f_{2,0}; f_{3,0}\}$ is chosen. In this specific case, the three volume fractions are given a realistic starting value of 0.33, thereby satisfying the first equation of the system. This initial solution is then adjusted for each new

iteration. The update step is performed by means of the following three equations:

$$\begin{aligned} f_{1,x+1} &= f_{1,x} + \lambda(p_{a,x}\mu_{1,E_1} + p_{b,x}\mu_{1,E_2} + p_{c,x}) \\ f_{2,x+1} &= f_{2,x} + \lambda(p_{a,x}\mu_{2,E_1} + p_{b,x}\mu_{2,E_2} + p_{c,x}), \\ f_{3,x+1} &= f_{3,x} + \lambda(p_{a,x}\mu_{3,E_1} + p_{b,x}\mu_{3,E_2} + p_{c,x}) \end{aligned} \tag{4.30}$$

with λ the relaxation parameter and $p_{a,x}$, $p_{b,x}$ and $p_{c,x}$ the correction factors. The latter are re-calculated for each iteration by using the following formulas:

$$\begin{aligned} p_{a,x} &= \frac{\mu_{E_1} - (\mu_{1,E_1} \cdot f_1 + \mu_{2,E_1} \cdot f_2 + \mu_{3,E_1} \cdot f_3)}{\mu_{1,E_1}^2 + \mu_{2,E_1}^2 + \mu_{3,E_1}^2} \\ p_{b,x} &= \frac{\mu_{E_2} - (\mu_{1,E_2} \cdot f_1 + \mu_{2,E_2} \cdot f_2 + \mu_{3,E_2} \cdot f_3)}{\mu_{1,E_2}^2 + \mu_{2,E_2}^2 + \mu_{3,E_2}^2}. \\ p_{c,x} &= \frac{1 - (f_{1,x} + f_{2,x} + f_{3,x})}{1+1+1} \end{aligned} \tag{4.31}$$

In order to add the condition that volume fractions cannot become negative, nor exceed a value of 1, a clipping procedure is performed for all new intermediate solutions. This means that after each iteration, negative preliminary volume fractions are set to zero, while those exceeding 1 are set to 1. As such, a realistic final solution will be obtained.

A small software tool was developed to calculate the volume fraction images for each pair of DECT images. The μ_1, μ_2 and μ_3 values are input parameters which should be measured in the DECT images. As the iterations may either converge or diverge, depending on the number or iterations and the value of the relaxation parameter, these two parameters can be manually selected.

4.2.2 Reconstruction of atomic value and mass density

A major drawback to the aforementioned basis material decomposition method is that the attenuation coefficient for the basis materials has to be measured in the DECT images in voxels which only contain one of these materials. It is often not possible to identify such voxels for each basis material with 100% certainty. Therefore, a new dual energy imaging processing technique was developed at UGCT which does not require such measurements. On the other hand, the technique relies on a full understanding of the polychromatic behaviour of each component of the used CT scanner. The method will be briefly presented here. A complete thorough explanation can be found in [46].

The recontructed attenuation coefficient of a material in a voxel can be written as follows:

$$\mu = \rho \frac{\sum S'_i D_{in,i} \frac{\mu}{\rho}(E_i, Z)}{\sum S'_i D_{in,i}}, \tag{4.32}$$

with $D_{in,i}$ the mean deposited energy per incident photon and $\frac{\mu_i}{\rho}(E_i, Z)$ the mass attenuation coefficient of the material, both in energy bin i . If the complete polychromatic behaviour of source and detector of a CT scanner are known, only two unkown parameters are present in this equation, i.e. the material composition represented by Z and its density ρ. Performing scans at two different energies E_1 and E_2, gives rise to the following system of equations:

$$\begin{aligned} \mu_{E_1} &= \rho \frac{\sum S'_{E_1,i} D_{in,E_1,i} \frac{\mu}{\rho}(E_i, Z)}{\sum S'_{E_1,i} D_{in,E_1,i}} \\ \mu_{E_2} &= \rho \frac{\sum S'_{E_2,i} D_{in,E_2,i} \frac{\mu}{\rho}(E_i, Z)}{\sum S'_{E_2,i} D_{in,E_2,i}} \end{aligned}. \tag{4.33}$$

Dividing these two equations by one another leads to:

$$\frac{\mu_{E_1}}{\mu_{E_2}} = \frac{\sum S'_{E_1,i} D_{in,E_1,i} \frac{\mu}{\rho}(E_i, Z)}{\sum S'_{E_1,i} D_{in,E_1,i}} \Big/ \frac{\sum S'_{E_2,i} D_{in,E_2,i} \frac{\mu}{\rho}(E_i, Z)}{\sum S'_{E_2,i} D_{in,E_2,i}}. \tag{4.34}$$

This equation is only dependent of Z, since the mass attenuation coefficient $\frac{\mu}{\rho}(E, Z)$ is only dependent on the photon energy E and the composition of the material, represented by Z.

For this dual energy processing technique, first a list of materials possibly present in the sample is given as user input. For each of these materials a look-up table is used, containing the mass attenuation coefficient as a function of photon energy. In this method Z refers to a specific look-up table corresponding to a material and therefore does not have to represent the actual atomic number corresponding to that material. It is therefore a user-defined arbitrary numerical value.

Minimising the following expression for all input materials:

$$\frac{\mu_{E_1}}{\mu_{E_2}} - \frac{\sum S'_{E_1,i} D_{in,E_1,i} \frac{\mu}{\rho}(E_i, Z)}{\sum S'_{E_1,i} D_{in,E_1,i}} \Big/ \frac{\sum S'_{E_2,i} D_{in,E_2,i} \frac{\mu}{\rho}(E_i, Z)}{\sum S'_{E_2,i} D_{in,E_2,i}} \tag{4.35}$$

allows to determine which material is present in each voxel. Implementing the Z value found in this way in equations 4.33 allows to calculate the density ρ.

If the following expressions are added to the minimisation process

$$\begin{matrix} \mu_{E_1} - \rho \dfrac{\sum S'_{E_1,i} D_{in,E_1,i} \dfrac{\mu}{\rho}(E_i, Z)}{\sum S'_{E_1,i} D_{in,E_1,i}} \\ \mu_{E_2} - \rho \dfrac{\sum S'_{E_2,i} D_{in,E_2,i} \dfrac{\mu}{\rho}(E_i, Z)}{\sum S'_{E_2,i} D_{in,E_2,i}} \end{matrix}, \tag{4.36}$$

it is possible to simultaneously determine ρ and Z. Note that ρ is in this case no longer an intrinsically free parameter, but linked to the input materials. This leads to better results, since non-physical solutions, for instance water with a density of 5 g/cm^3, are excluded in this way. Examples and applications of this dual energy image processing technique are presented in [46]. Note that, voxels may only contain a sole material which is not the case for the basis material decomposition method.

4.3 Selection of dual energy X-ray spectra

A crucial part of dual energy imaging is the selection of the X-ray spectra to be used for an optimal result. For clinical DECT some studies on spectral optimisation have been performed for general imaging [47, 48] as well as specific purposes, such as cardiac imaging [49, 50], chest imaging [51] and mammography [52, 53]. Spectra were evaluated based on image contrast-to-noise ratio (CNR) and patient dose. Variables for optimisation included tube voltage, filtration material and filter thickness. In some studies patient thickness was taken into account as well [50, 51]. However, for non-clinical applications, very few authors clearly describe how their spectra were chosen. Granton *et al.* [12] make use of simulations to calculate a figure of merit based on ratio's of CT number differences between the chosen basis materials, for a range of tube voltages and two filter types.

There are a few essential differences between clinical CT and CT performed at UGCT or similar institutes or research groups, besides the resolution aspect. First of all, dose considerations are often not necessary for non-clinical application, so the focus for optimisation may exclusively lie on CNR. Secondly, samples at UGCT can vary a lot in size, shape and composition. Adequate dual energy X-ray spectra will greatly depend on these three parameters. As a result, spectral optimisation has to be performed for each individual case. Therefore, a fast, straightforward and preferably automated optimisation algorithm should be developed.

In this section, first some approaches to tune X-ray spectra for DECT will be described. Subsequently, the concept of the "energy" of a polychromatic X-ray

spectrum and how to define it will be discussed. Finally, some practical ways to select X-ray spectra for DECT will be presented.

4.3.1 Approaches to tune X-ray spectra

There are essentially three parameters which can be adjusted to tune X-ray spectra:

- **Tube voltage:** The most straightforward way to create different X-ray spectra is to change the tube voltage. A higher tube voltage will lead to a spectrum with a higher average energy, and vice versa. The influence of varying tube voltages is clearly shown in figures 3.2 and 3.4.
- **Beam filtration:** The use of a beam filter will allow to tune the X-ray spectra even further. There are two different options. In conventional filtration, mainly the low energy component of the spectrum is removed. As a result, the average energy of the X-ray spectrum will increase. To this purpose, elements with a relatively low atomic number, i.e. at least $Z < 40$, are used. Some typical examples are aluminium and copper. Figure 4.1 shows the effect of a 1 mm aluminium and a 0.5 mm copper filter on the emitted spectrum of the Hamamatsu directional tube operated at 100 kV.

  The second option is to make use of filter materials with a prominent K-edge in the energy range of interest. These are typically elements with a high atomic number, such as tungsten. Similar to conventional filtration, the lower energy photons will be filtered most strongly. As the photon energy increases, more photons will get through the filter. However, when the K-edge of the filter material is reached, X-ray attenuation will show a sudden strong increase, which is followed by a further slow decrease with energy. As a result, filtration will take place both at the low and the high energy side of the spectrum, while the middle part is relatively spared. As such a somewhat more monochromatic profile is obtained. This is illustrated in figure 4.2, which again shows the emitted spectrum of the Hamamatsu directional tube operated at 100 kV, with a 0.1 mm tungsten and a 0.1 mm lead filter. K-edge filtration is ideally suited to tune the average energy of a spectrum just below the K-edge of a specific material, as required in K-edge imaging. A filter element with an atomic number close or equal to that of the material should be chosen.
- **Changing the target material:** A more complex way to create different X-ray spectra is to change the anode material itself. Each target material will give rise to a unique set of fluorescence lines in terms of photon energy. Since these characteristic X-rays may represent a significant part of an X-ray spectrum, changing this material can introduce an important change in the

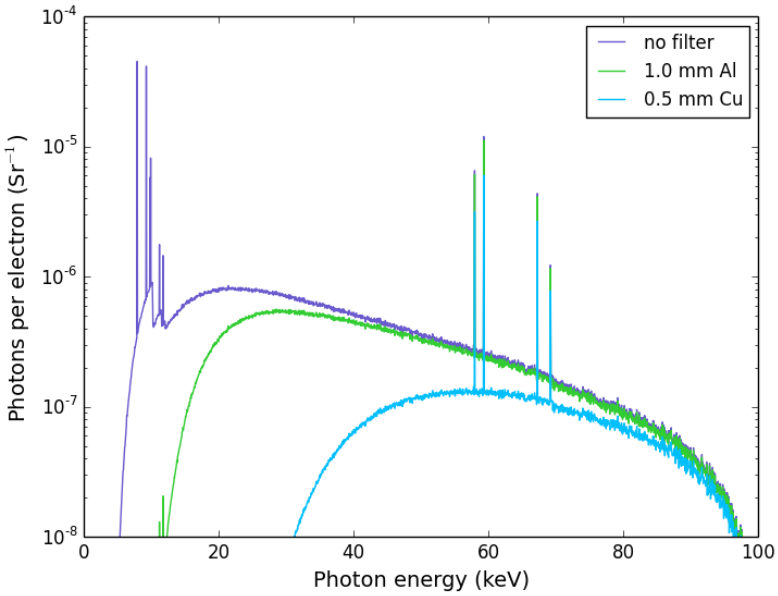

Figure 4.1: Influence of 1 mm aluminium and a 0.5 mm copper filter on the emitted spectrum of the 130 kV Hamamatsu directional X-ray tube operated at 100 kV: conventional filtration

spectrum. Figure 4.3 shows the spectra of the FeinFocus transmission tube at 100 kV with a 6 μm molybdenum and a 6 μm tungsten target. Note that for a clearer illustration of the principle, the internal molybdenum structures of the tube are not taken into account. In the tungsten spectrum, both K- and L-lines are visible. The L-lines, with the Lα1 line at 8.396 keV, are easily removed by a relatively thin filter. The K-lines, with the Kα1 line at 58.864 keV, are not so easily attenuated and as such may significantly influence the X-ray spectrum, as is for instance the case in figure 4.1 using the 0.5 mm copper filter. In the molybdenum spectrum, the L-lines (Lα1 at 2.293 keV) have already been removed by the tube exit window. The K-lines (Kα1 at 17.443 keV) are not as easily filtered as the tungsten L-lines, but heavy filtration will be able to completely remove them from the spectrum if necessary.

It should be noted that to accurately tune X-ray spectra for DECT, the energy-dependent efficiency of the detector should always be taken into account. In figure 4.4 the emitted spectrum of the Hamamatsu directional tube operated at 100 kV is shown in combination with the same spectrum as detected by the Varian and the Perkin Elmer flat-panel detector. The sensitivity of the Perkin Elmer detector

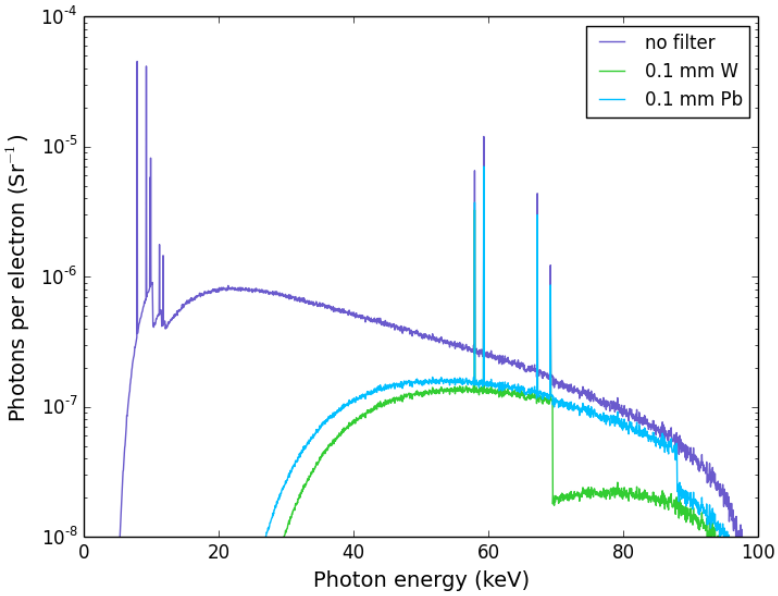

Figure 4.2: Influence of 0.1 mm tungsten and a 0.1 mm lead filter on the emitted spectrum of the 130 kV Hamamatsu directional X-ray tube operated at 100 kV: K-edge filtration

is higher for low energy photons than that of the Varian detector. In principle, a detector change can also be considered as an approach to tune X-ray spectra.

In practice, mainly the tube voltage and beam filtration are adjusted.

4.3.2 Defining the "energy" of a polychromatic X-ray spectrum

In the context of DECT, often the "energy" of an X-ray spectrum is mentioned. Based on the attenuation coefficients of the materials present in a sample, photon energies can be selected where the relative differences between these coefficients are greatest. Scans performed using X-ray spectra with these selected energies will lead to optimal DECT results. In K-edge imaging for instance, a spectrum with an energy just below and one just above the K-edge of a specific material have to be created. It is however not quite clear how this spectrum energy should be defined in case of a polychromatic X-ray beam. Often the spectrum energy is intuitively equated with the average energy of that spectrum. However, practical problems will arise when using this definition (see further). Below several definitions for the "energy" of an X-ray spectrum will be discussed. It is hereby important to keep in mind that ideally the spectrum energy should correlate with the resulting attenua-

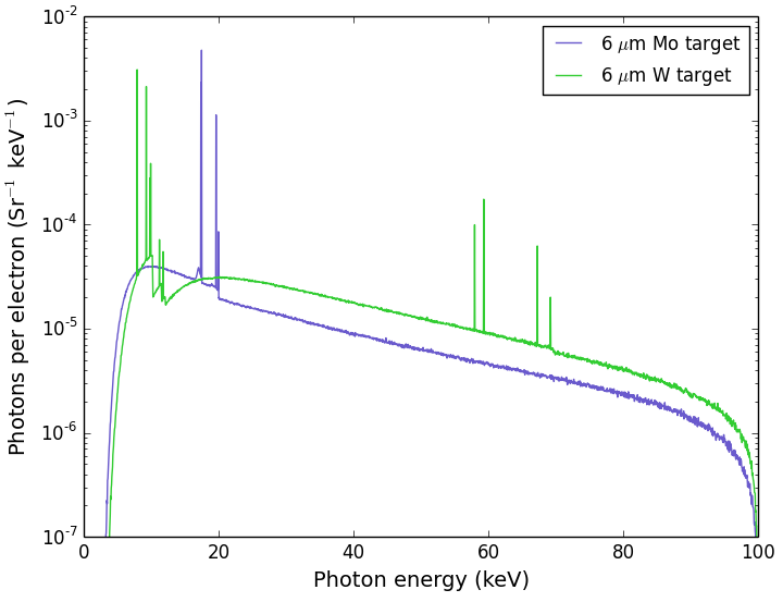

Figure 4.3: Simulated spectrum of the 160 kV FeinFocus transmission X-ray tube operated at 100 kV with a 6 μm molybdenum and a 6 μm tungsten target. Note that for illustrative purposes the internal molybdenum structures are not taken into account.

tion coefficients, and thus grey values, in the CT image for each material. Further, note that since the energy-dependent efficiency of the detector should be taken into account, all of the following definitions are based on detected spectrum energies. Moreover, the detector efficiency is expressed in terms of detected energy, and not in terms of detected photons, since the actual detector signal is proportional to the deposited energy. All calculations and simulations in this section are performed with the Setup Optimiser.

Average detected energy

The **average detected energy**, $E_{av,d}$, can be defined as follows:

$$E_{av,d} = \frac{\sum_{i=1}^{n} D_{d,i} N_{d,i} E_i}{\sum_{i=1}^{n} D_{d,i} N_{d,i}}, \tag{4.37}$$

with $D_{d,i}$ the mean deposited energy per detected photon in energy bin i, $N_{d,i}$ the number of detected photons in that same energy bin and E_i the energy of bin i (see

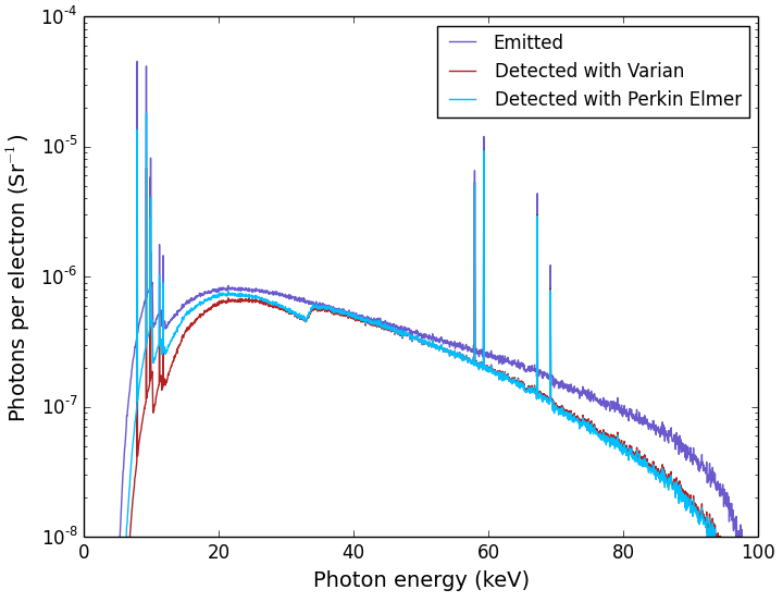

Figure 4.4: Emitted and detected spectrum with the Varian and Perkin Elmer flat-panel detector of the 130 kV Hamamatsu direction X-ray tube operated at 100 kV and 10 W

section 3.2). Using (3.5) this becomes:

$$E_{av,d} = \frac{\sum_{i=1}^{n} D_{d,i} D_{eff,i} N_i E_i}{\sum_{i=1}^{n} D_{d,i} D_{eff,i} N_i}. \tag{4.38}$$

Multiplying the detector efficiency or absorption probability $D_{eff,i}$ in energy bin i by $D_{d,i}$ equals the mean deposited energy per incident photon $D_{in,i}$ in that bin. Furthermore, given that the definitions for the energy of a spectrum should be independent of the sample, N_i equals $N_{0,i}$ which is the number of emitted photons in energy bin i after beam filtration. The latter also includes the filtration due to the air between source and detector. So (4.38) can be rewritten as follows:

$$E_{av,d} = \frac{\sum_{i=1}^{n} D_{in,i} N_{0,i} E_i}{\sum_{i=1}^{n} D_{in,i} N_{0,i}}. \tag{4.39}$$

Using (3.4) with the width of an energy bin ΔE_i considered as a constant (rebinning of a spectrum is only necessary for full CT scan simulations), the average

detected energy of an X-ray spectrum is defined as:

$$E_{av,d} = \frac{\sum_{i=1}^{n} S'_i D_{in,i} E_i}{\sum_{i=1}^{n} S'_i D_{in,i}}. \tag{4.40}$$

Table 4.1 shows the average detected energies of the X-ray spectra from figures 3.2, 4.1 and 4.2 using the Varian flat-panel detector at a distance of 1 m from the source. As expected, the average detected energies increases with increasing tube voltage. Also heavier filtration will lead to higher average energies. Nevertheless, this definition for the X-ray spectrum energy is not ideally suited for DECT. This can already be easily understood looking at figure 4.5. Two detected X-ray spectra using the Hamamatsu directional tube in combination with the Varian detector at a distance of 1 m are shown, one with the tube operated at 100 kV and no filtration, the other with the tube operated at 60 kV and a 0.35 mm copper filter. Although these spectra are clearly different, they have approximately the same average detected energy: 44.5 keV and 44.6 keV, respectively. Of course, they will lead to different imaging results. For instance, the detected transmission through 1 cm water is 73.1% for the 100 kV spectrum and 79.5% for the 60 kV spectrum.

Table 4.1: Average detected energy $E_{av,d}$ of the X-ray spectra from figures 3.2, 4.1 and 4.2 using the Hamamatsu directional tube and the Varian detector with an SDD of 1 m

Tube voltage (kV)	*Filter*	$E_{av,d}$ *(keV)*	*XX*
40 kV	no filter	20.5	
60 kV	no filter	30.5	
80 kV	no filter	38.0	
100 kV	no filter	44.5	
120 kV	no filter	49.4	
100 kV	1 mm Al	48.4	
100 kV	0.5 mm Cu	61.9	
100 kV	0.1 mm W	57.7	
100 kV	0.1 mm Pb	59.4	

Effective energy

Ideally, the spectrum energy should be that energy corresponding to the resulting attenuation coefficients, and thus CT image grey values. It is clear that this is not

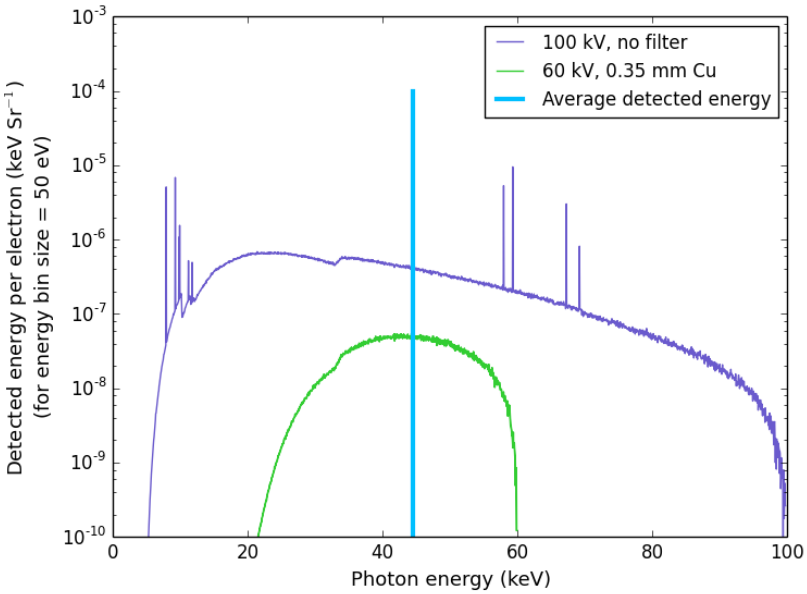

Figure 4.5: X-ray spectra detected with the Varian detector using the Hamamatsu direction tube operated at 100 kV without filter and 60 kV with a 0.35 mm Cu filter, both with an SDD of 1 m. Furthermore the average detected energy of the spectra (same value for both) is shown.

the case for the average detected energy $E_{av,d}$. Therefore, it can be interesting to invert the problem and start by looking at these resulting attenuation coefficients and check to what photon energy they should correspond. This photon energy will be called the **effective energy** E_{eff}. Six spectra with varying tube voltages and beam filtration were chosen from table 4.1 together with the 60 kV spectrum with a 0.35 mm copper filter, which has the same average detected energy as the 100 kV spectrum without filtration. Furthermore, five different sample materials were selected. Tests were performed using the Setup Optimiser. In principle, this tool only allows for simulation of detected transmission values through one or several layers of material and thus along one fixed ray path. Therefore, it is not possible to straightforwardly calculate attenuation coefficients. However, if a cylindrical sample is considered, the grey value in its centre can be calculated using the information of only one ray path through this centre, since this will be exactly the same for every projection angle. Each of the five selected sample materials has its own specific thickness d. Subsequently the transmission T through these sample layers for the seven different X-ray spectra was simulated. The transmission values were then converted to the attenuation coefficient of the centre of a cylindrical sample

as follows:

$$\mu = -\frac{lnT}{d}. \tag{4.41}$$

Finally, the approximate photon energy corresponding to this calculated attenuation coefficient value was determined using the attenuation data as a function of energy from NIST as a look-up table. As such the effective energy "seen" by a voxel can be obtained. In this case, E_{eff} at the centre of a mono-material cylinder was determined. All these values are listed in table 4.2.

It is immediately clear that the effective energy values can vary greatly within a single spectrum, depending on the sample. The strongest variations are observed in the broad, non-filtered spectra, while the differences in effective energy decrease for increasing filtration and thus narrowing spectra. These results also show that finding a spectrum energy definition that is independent of sample material or thickness is not at all straightforward. To further explore the problem, the behaviour of the linear attenuation coefficient as a function of the cylinder diameter was studied. This is shown in figure 4.6 for the water sample. As the diameter approaches zero, the attenuation coefficient approaches a constant value μ_0. These μ_0 values and their corresponding effective energy values $E_{eff,0}$ were simulated for the five samples and are listed in table 4.2 as well.

The variation of $E_{eff,0}$ within the same spectrum is a lot smaller and reaches a maximum of 5 keV. The strongest variations are observed within the non-filtered spectra where $E_{eff,0}$ increases slightly with increasing Z value of the sample. As soon as some beam filtration is used, variations are smaller. Moreover, for the heavily filtered spectra (60 kV, 0.35 mm Cu; 100 kV, 0.5 mm Cu and 100 kV, 0.1 mm W) the E_{eff_0} values correspond a lot better with the E_{eff} values, especially for the samples with small atomic numbers.

Detected monochromatic energy

The limited variations in $E_{eff,0}$ per spectrum indicate that a spectrum energy can be defined which is practically independent of the sample. In order to derive a formula for such a spectrum energy, the sample thickness is assumed to approach zero. Using (3.12) and (3.7), equation 4.41 becomes:

$$\mu = -\frac{1}{d} ln \frac{E_d}{E_{d,0}} = -\frac{1}{d} ln \frac{\sum_{i=1}^{n} D_{d,i} N_{d,i}}{\sum_{i=1}^{n} D_{d,i} N_{0,d,i}}, \tag{4.42}$$

with $N_{0,d,i}$ the number of detected photons without a sample present in energy bin i. Since the mean deposited energy per incident photon $D_{in,i}$ in energy bin i is the

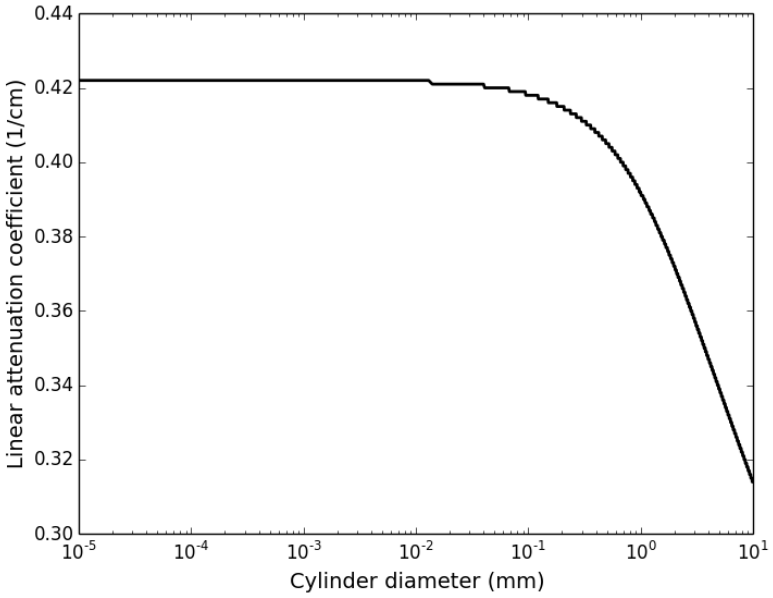

Figure 4.6: Simulated linear attenuation coefficient of the central point of a cylindrical water sample as a function of the cylinder diameter using the Hamamatsu directional tube operated at 100 kV (no beam filtration) in combination with the Varian detector (SDD of 1 m)

product of the absorption probability $D_{eff,i}$ and the mean deposited energy per detected photon $D_{d,i}$ in that bin, equation 4.42 can be rewritten by means of (3.5):

$$\mu = -\frac{1}{d} ln \frac{\sum_{i=1}^{n} D_{in,i} N_i}{\sum_{i=1}^{n} D_{in,i} N_{0,i}}. \tag{4.43}$$

Using (3.3) and the fact that the linear attenuation coefficient is determined for a single sample material with thickness d this becomes:

$$\mu = -\frac{1}{d} ln \frac{\sum_{i=1}^{n} D_{in,i} N_{0,i} exp(-\mu_i d)}{\sum_{i=1}^{n} D_{in,i} N_{0,i}}. \tag{4.44}$$

Table 4.2: Simulated transmission values (T) through the centre of five different cylindrical samples and the resulting attenuation coefficient (μ) and corresponding effective energy E_{eff} using the Hamamatsu directional tube and Varian detector (SDD = 1 m). Similar simulations were performed for cylinder diameters approaching zero to determine μ_0 and $E_{eff,0}$.

Cylindrical sample	*T (%)*	*μ (1/cm)*	*E_{eff} (keV)*	*μ_0 (1/cm)*	*$E_{eff,0}$ (keV)*
***Spectrum:* 100 kV, no filter**					
10 mm H_2O	73.1	0.314	31	0.422	26
10 mm polyethylene	79.4	0.230	29	0.253	26
3 mm Al	59.5	1.73	36	4.00	26
1 mm Cu	13.1	20.3	52	108	29
0.1 mm Pb	31.6	115	44	289	31
***Spectrum:* 60 kV, 0.35 mm Cu**					
10 mm H_2O	79.5	0.230	42	0.230	42
10 mm polyethylene	82.6	0.191	43	0.191	43
3 mm Al	70.3	1.18	43	1.21	42
1 mm Cu	6.88	26.8	47	35.8	42
0.1 mm Pb	31.8	115	44	131	42
***Spectrum:* 60 kV, no filter**					
10 mm H_2O	62.7	0.467	24	0.720	20
10 mm polyethylene	74.1	0.300	22	0.353	20
3 mm Al	39.5	3.09	29	8.27	20
1 mm Cu	1.90	39.6	41	219	22
0.1 mm Pb	11.5	216	35	537	25
***Spectrum:* 120 kV, no filter**					
10 mm H_2O	75.4	0.283	34	0.361	28
10 mm polyethylene	80.6	0.216	32	0.232	28
3 mm Al	64.4	1.47	39	3.12	29
1 mm Cu	17.6	17.4	54	84.2	31
0.1 mm Pb	36.7	100	47	235	34
***Spectrum:* 100 kV, 1 mm Al**					
10 mm H_2O	77.4	0.256	37	0.265	36
10 mm polyethylene	81.9	0.200	38	0.201	37
3 mm Al	66.4	1.37	40	1.77	36
1 mm Cu	15.4	18.7	53	54.5	36
0.1 mm Pb	36.7	100	47	187	37
***Spectrum:* 100 kV, 0.5 mm Cu**					
10 mm H_2O	82.3	0.195	58	0.195	58
10 mm polyethylene	83.9	0.176	59	0.176	59
3 mm Al	80.8	0.713	56	0.724	56
1 mm Cu	29.0	12.4	62	16.0	56
0.1 mm Pb	57.1	56.1	58	62.4	56
***Spectrum:* 100 kV, 0.1 mm W**					
10 mm H_2O	81.8	0.201	54	0.201	54
10 mm polyethylene	83.7	0.179	55	0.179	55
3 mm Al	79.1	0.780	53	0.795	53
1 mm Cu	23.3	14.6	58	18.9	53
0.1 mm Pb	52.6	64.3	55	72.0	53

This can be rewritten with (3.4), where ΔE_i is considered constant:

$$\mu = -\frac{1}{d} ln \frac{\sum_{i=1}^{n} D_{in,i} S'_i exp(-\mu_i d)}{\sum_{i=1}^{n} D_{in,i} S'_i}. \tag{4.45}$$

Following series expansion about zero (Maclaurin series) and in the limit $x \to 0$ the following is valid:

$$\begin{aligned} exp(x) &= 1 + x \qquad (x \to 0) \\ ln(1+x) &= x \qquad (x \to 0) \end{aligned} \tag{4.46}$$

Therefore, equation 4.45 can be written as follows:

$$\begin{aligned} \mu &= -\frac{1}{d} ln \frac{\sum_{i=1}^{n} D_{in,i} S'_i (1 - \mu_i d)}{\sum_{i=1}^{n} D_{in,i} S'_i} \\ &= -\frac{1}{d} ln \left(1 - \frac{\sum_{i=1}^{n} D_{in,i} S'_i \mu_i d}{\sum_{i=1}^{n} D_{in,i} S'_i} \right) \\ &= \frac{1}{d} \frac{\sum_{i=1}^{n} D_{in,i} S'_i \mu_i d}{\sum_{i=1}^{n} D_{in,i} S'_i} \\ &= \frac{\sum_{i=1}^{n} D_{in,i} S'_i \mu_i}{\sum_{i=1}^{n} D_{in,i} S'_i}. \end{aligned} \tag{4.47}$$

From tables 4.1 and 4.2 it is clear that $E_{eff,0}$ is significantly smaller than $E_{av,d}$. This indicates that low energy photons are relatively more important. At low X-ray energies, photoelectric absorption is the dominant photon interaction process (see figure 2.7). As a rough approximation, the linear attenuation coefficient at these energies can be considered equal to the total probability of photoelectric absorption τ alone, given by equation 2.2:

$$\mu \cong constant \times \frac{Z^n}{E^{3.5}}, \tag{4.48}$$

where n varies between 4 and 5. The photon energy E in this equation equals the monochromatic energy as seen by a voxel with a grey value equal to the linear

attenuation coefficient μ. Based on the results in table 4.2, for sample thicknesses approaching zero, this **detected monochromatic energy** E_{mono} should be practically independent of the sample material. E_{mono} can be derived by implementing (4.48) in (4.47):

$$constant \cdot \frac{Z^n}{E_{mono}^{3.5}} = \frac{\sum_{i=1}^{n} D_{in,i} S'_i \cdot constant \cdot Z^n / E_i^{3.5}}{\sum_{i=1}^{n} D_{in,i} S'_i}, \tag{4.49}$$

which results in:

$$E_{mono} = \left(\frac{\sum_{i=1}^{n} D_{in,i} S'_i E_i^{-3.5}}{\sum_{i=1}^{n} D_{in,i} S'_i} \right)^{-2/7}. \tag{4.50}$$

4.3.3 Selection of DECT X-ray spectra based on the detected monochromatic energy

In table 4.3 the detected monochromatic energies of the seven X-ray spectra from table 4.2 are shown together with their average detected energies and their effective energies for sample thicknesses approaching zero. For the latter, the most frequently occurring value in table 4.2 was selected for each spectrum. First of all, it is clear that E_{mono}, although based on the concept of $E_{eff,0}$, is slightly smaller than $E_{eff,0}$. This is due to the fact that the contribution of Compton scattering is completely neglected in formula 4.50, but also due to the fact that the total probability of photoelectric absorption given by equation 2.2 is an approximation in which K-edges are not taken into account. Nevertheless, E_{mono}, which can be easily calculated for each X-ray spectrum, appears to be a successful reproduction of $E_{eff,0}$.

Furthermore, this table proves once more that the average detected energy is not a good parameter for tuning and selecting X-ray spectra. The first two spectra in table 4.3 have an almost identical average detected energy, but as already shown by figure 4.5, their shape - and thus photon composition - is quite different. This is correctly reflected by $E_{eff,0}$ and E_{mono}. The latter thus appears to be a better and at the same time easy to determine spectrum parameter. However, a major disadvantage of this parameter is that it is only valid in the case of extremely thin samples, in the order of 1 μm for low Z materials and 1 nm for high Z materials. Once a sample has substantial dimensions E_{mono} should be used with caution.

Finally, it is clear that as soon as some beam filtration is applied $E_{av,d}$ corresponds a lot better with E_{mono} and this further improves with heavier filtration.

Table 4.3: Average detected energy $E_{av,d}$, effective energy for sample thicknesses approaching zero $E_{eff,0}$ and detected monochromatic energy E_{mono} for the seven X-ray spectra from table 4.2

Tube voltage (kV)	*Filter*	$E_{av,d}$ *(keV)*	$E_{eff,0}$ *(keV)*	E_{mono} *(keV)*
100 kV	no filter	44.5	26	24.4
60 kV	0.35 mm Cu	44.6	42	41.7
60 kV	no filter	30.5	20	19.3
120 kV	no filter	49.4	28	26.6
100 kV	1 mm Al	48.4	36	34.6
100 kV	0.5 mm Cu	61.9	56	55.3
100 kV	0.1 mm W	57.7	53	52.2

This is of course a reflection of the fact that beam hardening will play a less significant role when the low energy X-ray photons are filtered out. It is this beam hardening which causes the fine tuning of spectra to be a difficult task. As previously mentioned the E_{eff_0} values correspond a lot better with the E_{eff} values in table 4.2, especially for thin samples with low atomic numbers. For X-ray spectra where beam hardening has been removed to a large extent by beam filtration, attenuation coefficients will be easier to predict, particularly for light sample materials.

In order to quantify the degree of beam hardening for a given sample under specific scanning conditions, a **beam hardening factor** BHF was introduced which is defined as follows:

$$BHF = 1 - \frac{\mu}{\mu_0}. \tag{4.51}$$

This factor indicates how much the grey values will vary within a sample (outer edge relative to central point) due to beam hardening. This can of course only be calculated for a mono-material. The beam hardening factors for the five samples from table 4.2 are shown in table 4.4 for the seven X-ray spectra. The lower this factor, the better E_{eff_0} and E_{eff} correspond and the more reliable E_{mono} can be used as a spectrum parameter. The detected monochromatic energy could therefore be used, in combination with the beam hardening factor, for selecting DECT spectra. In section 4.4 some practical examples will be given. Logically, a relatively large degree of inaccuracy is associated with this method, especially when complex samples are considered.

Table 4.4: Beam hardening factor for the five samples and seven X-ray spectra from table 4.2

Spectrum	*10 mm H_2O*	*10 mm polyethylene*	*3 mm Al*	*1 mm Cu*	*0.1 mm Pb*
100 kV, no filter	25.6%	9.02%	56.7%	81.1%	60.2%
60 kV, 0.35 mm Cu	0.25%	0.04%	3.06%	25.3%	12.6%
60 kV, no filter	35.2%	15.1%	62.6%	81.9%	59.8%
120 kV, no filter	21.6%	7.10%	53.0%	79.4%	57.4%
100 kV, 1 mm Al	3.43%	0.57%	22.7%	65.7%	46.3%
100 kV, 0.5 mm Cu	0.11%	0.03%	1.56%	22.3%	10.1%
100 kV, 0.1 mm W	0.13%	0.03%	1.87%	22.8%	10.8%

4.3.4 Selection of DECT X-ray spectra based on complete CT simulations

Dual energy spectra can be most accurately selected based on complete CT simulations. This is the only way to take into account the complete sample geometry and composition, which is especially useful for complex samples. Furthermore, the influence of image noise can be included. This is necessary information to calculate the contrast-to-noise ratio (CNR), which is in fact the most useful parameter to optimise for obtaining the best results (see further). The main disadvantage is of course that this can be a lot more time-consuming than an assessment based on instantly calculable spectrum parameters. Moreover, a virtual phantom of the sample should also be created. It may not always be possible to make an exact virtual copy, especially when full knowledge of the sample composition is lacking, but a rough approximation is in most cases sufficient. In this section it will be shown by means of a virtual example how optimal X-ray spectra can be selected based on full CT simulations (using Arion).

A simple cylindrical virtual phantom was created, consisting of three aqueous solutions (KBr, PTA and $Pb(NO_3)_2$) (Fig. 4.7). The composition of the three solutions can be found in table 4.5. Subsequently, short (1 minute) simulations were performed for different X-ray spectra, using three beam filters (1 mm Al, 1 mm Cu and 0.1 mm W), covering a broad range of tube voltages (80, 100, 120 and 160 kV). Tube power and exposure time were kept constant to allow a fair comparison between the different settings. The source and detector of HECTOR were chosen with an SDD of 800 mm. After reconstruction, the attenuation coefficients of the three solutions and their corresponding standard deviations σ, i.e. the image noise, in the simulated CT images were measured. These are graphically presented in

figure 4.8. It is clear that most scanner settings allow to distinguish no more than one solution from the others. Only at 120 kV and 160 kV using 1 mm aluminium filtration there is no significant overlap between the simulated attenuation coefficients within one standard deviation.

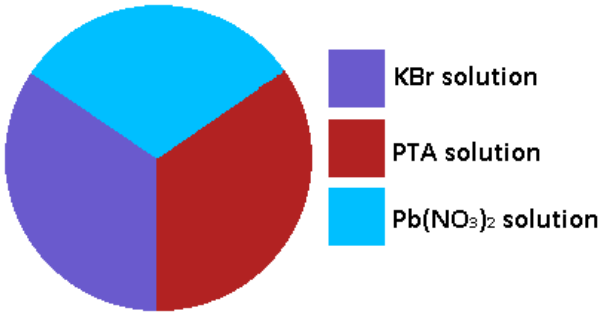

Figure 4.7: Virtual phantom consisting of three aqueous solutions

Table 4.5: Mass fractions of the components of the aqueous solutions in the virtual phantom

Material	*Mass fraction solute*	*Mass fraction H_2O*	*Density (g/cm^3)*
KBr	0.115	0.885	1.13
$Pb(NO_3)_2$	0.099	0.901	1.11
PTA	0.074	0.926	1.08

How to determine the optimal spectra based on these data will be illustrated first for a single (energy) scan and then for the dual energy case.

Single energy

As previously mentioned, it is important to take into account image noise. If it is too large, even a prominent image signal may disappear in the background noise. The parameter which includes both the image signal and the noise is the signal-to-noise ratio (SNR) given by:

$$SNR = \frac{\mu}{\sigma}. \tag{4.52}$$

The signal-to-noise ratios of the phantom solutions for each simulated scan setting are shown in table 4.6. The best combination of SNR values is observed for the 160 kV scan with 1 mm Al filtration, while the worst combination is seen at 80 kV with 1 mm Cu filtration. A reconstructed CT slice and corresponding histogram

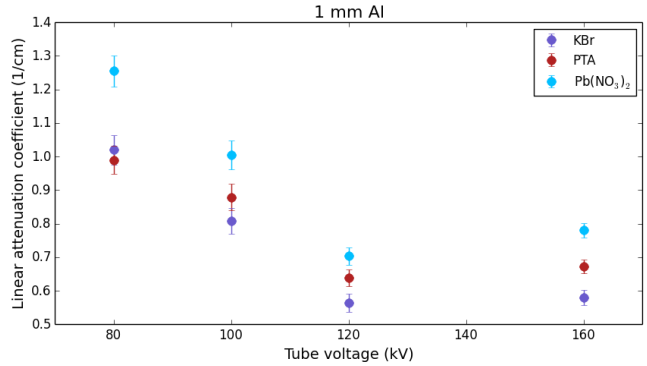

(a)

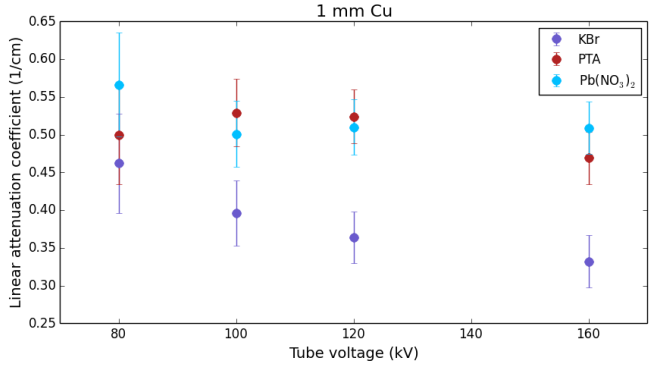

(b)

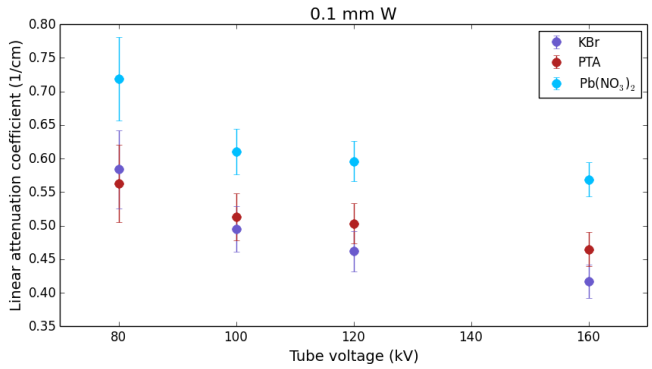

(c)

Figure 4.8: Attenuation coefficients of the three solutions and their corresponding errors (errorbar = 1 σ) in terms of tube voltage and beam filtration

are shown for both situations in figure 4.9. Using the worst scan setting, the three different components of the sample cannot be individually identified in the histogram. As such, in a realistic sample where different materials are often mixed throughout the whole object, they will no longer be visually distinguishable. At 160 kV using 1 mm aluminium filtration, three peaks can be clearly identified in the histogram. However, there is a significant overlap at the base, mainly between the KBr and PTA peak. As such, in a realistic sample, segmentation of the three materials will not always be straightforward, especially when fine structures are present.

Table 4.6: Signal-to-noise of the phantom solutions and contrast-to-noise ratios for each combination of solutions for all simulated scan settings. Index 1, 2 and 3 refer to KBr, PTA and $Pb(NO_3)_2$, respectively. As such, $CNR_{1,2}$ is the contrast-to-noise ratio between KBr and PTA.

Voltage (kV)	SNR_1	SNR_2	SNR_3	$CNR_{1,2}$	$CNR_{1,3}$	$CNR_{2,3}$
***Filter:* 1 mm Al**						
80	23.2	24.1	27.3	0.50	3.69	4.30
100	20.7	22.0	23.9	1.27	3.44	2.17
120	20.1	25.6	27.0	2.00	3.64	1.77
160	25.2	32.0	35.5	2.95	6.28	3.55
Filter: 1 mm Cu						
80	7.0	7.7	8.2	0.40	1.09	0.71
100	9.2	11.8	11.4	2.14	1.71	0.44
120	10.7	14.6	13.8	3.23	2.91	0.27
160	9.5	13.4	14.5	2.77	3.58	0.81
***Filter:* 0.1 mm W**						
80	10.1	9.7	11.6	0.26	1.59	1.84
100	14.6	14.7	17.9	0.37	2.39	1.99
120	15.4	16.8	19.9	0.97	3.16	2.19
160	16.7	18.6	22.8	1.36	4.30	2.94

In fact, to distinguish different materials from one another, it is not the signal-to-noise ratio, but the contrast-to-noise ratio that needs to be optimised. The SNR expresses how narrow the histogram peaks are. However, to discriminate different components, the peaks should not only be sufficiently narrow, but more importantly they should be spatially separated. The contrast-to-noise ratio (CNR), as

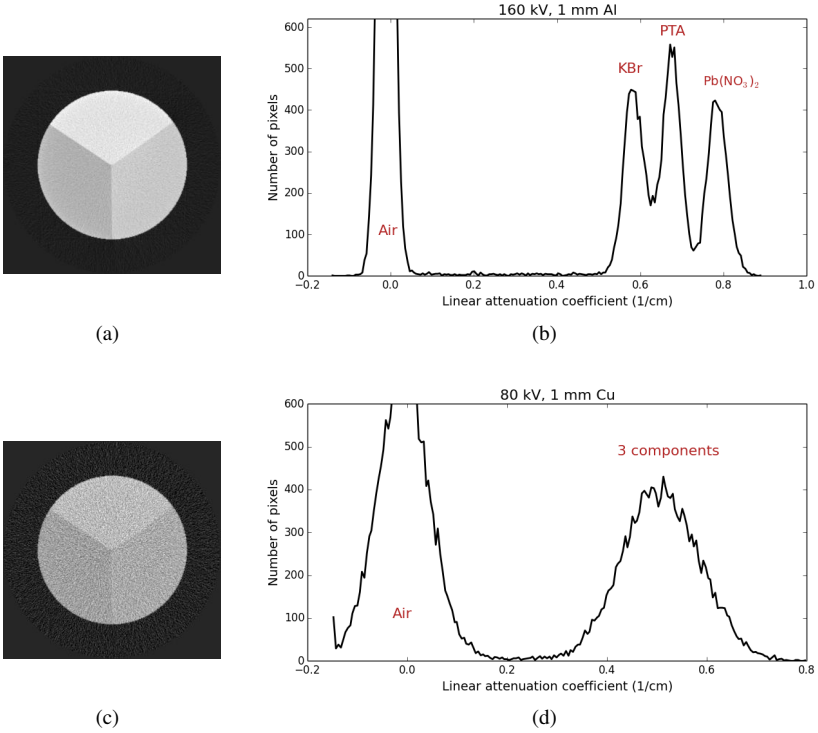

Figure 4.9: Reconstructed CT slice and corresponding histogram at 160 kV with 1 mm Al filtration, providing the best combination of SNR values (a & b) and at 80 kV with 1 mm Cu filtration, providing the worst combination of SNR values (c & d)

given by the following definition:

$$CNR = \frac{|\mu_1 - \mu_2|}{\sqrt{\sigma_1^2 + \sigma_2^2}}, \tag{4.53}$$

contains both the separation of the peaks (numerator), i.e. image contrast, and their width (denominator), i.e. image noise. The CNR values for each combination of phantom solutions for all simulated scan settings are shown in table 4.6 as well. The most suitable setting can be found by selecting the smallest CNR for each setting and subsequently determine the highest CNR of this list of minima. The scan parameters corresponding to this best "worst CNR" will allow to optimally distinguish the three materials. As such, for the given virtual example, the best results will be obtained at 160 kV with 1 mm aluminium filtration. If only two materials are present the X-ray spectra resulting in the highest CNR should be chosen.

Dual energy

As previously mentioned, even using the most appropriate scan settings, there is often significant overlap between the grey values of different materials (see Fig.4.9(b)). In such cases, DECT may offer a solution. Selection of the two X-ray spectra is again preferably based on optimising contrast-to-noise ratios. How this should be done can be intuitively understood by looking at the virtual example. For most scanner settings, the linear attenuation coefficient of KBr is significantly lower than that of $Pb(NO_3)_2$ so that these solutions can be relatively easily separated from one another (see Fig. 4.8). The PTA solution however, exhibits a quite different behaviour. When the copper filter is used, its grey value mainly overlaps with that of $Pb(NO_3)_2$, while it behaves more similar to KBr using the aluminium and tungsten filter. In order to realise as much as possible difference between the three materials, the scan settings should be chosen were PTA differs most from KBr (at 120 kV with 1 mm Cu) and from $Pb(NO_3)_2$ (at 80 kV with 1 mm Al). Figure 4.10 shows the volume fractions of the three solutions, calculated by applying the three material decomposition method. It is clear that they can now be easily and correctly distinguished. To automatically determine these two optimal settings, first a list is made of all pairwise combinations of the simulated settings, where for each of these pairs the largest CNR values are saved. For instance, for the combination of the 120 kV with 1 mm Cu and the 80 kV with 1 mm Al parameters, $CNR_{1,2}$, $CNR_{1,3}$ and $CNR_{2,3}$ are 3.23, 3.69 and 4.30, respectively. Subsequently, for this new list the same strategy is applied as for determining the optimal single energy scan settings, i.e. selecting the smallest CNR value for each combination and then determining the highest value from this final list.

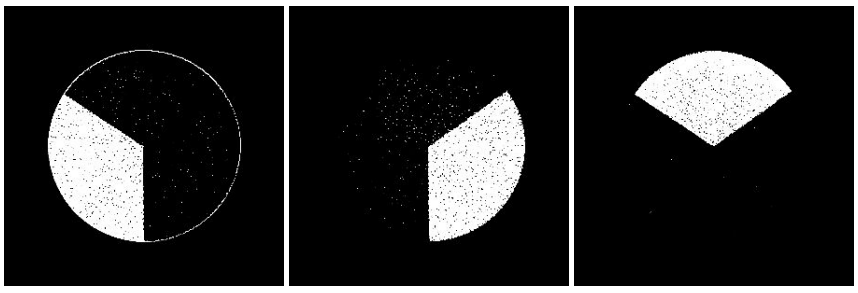

(a) (b) (c)

Figure 4.10: Volume fractions of the KBr (a), PTA (b) and $Pb(NO_3)_2$ (c) solution obtained by applying the three material decomposition method on the simulated CT images recorded at 80 kV with 1 mm Al and 120 kV with 1 mm Cu

It is striking that in the single energy case, the best results are achieved with the scan parameters leading to the best combination of signal-to-noise ratios, while this is no longer the case for dual energy. This indicates that it can be useful to sacrifice some image quality to obtain better DECT results.

As previously mentioned, this complete CT simulation based method to select dual energy spectra is a lot more time-consuming than a strategy based on instantly calculable spectrum parameters. However, many of the steps can be automised. For example, the user must configure the CT simulation only once. After specifying a range of tube voltages and beam filters, the simulations can run fully automatically. Also, reconstruction of the simulations can be done in batch mode. Finally, measuring the linear attenuation coefficients and their corresponding standard deviations can be done almost automatically, as the measurement region is the same for all images.

4.4 Practical examples of dual energy CT

In this section some real examples of dual energy CT are given. X-ray spectra are selected based on spectrum parameters and on complete CT simulations, so that both methods can be compared. First, a series of experiments is performed on a self-made sample in which the different materials are spatially separated, to determine the optimal method for selecting scan settings. Then, the optimal technique will be applied on a real sample as well. All experiments in this section were performed on HECTOR using the 240 kV X-RAY WorX directional tube with the Perkin Elmer flat-panel detector. Moreover, the SDD for all scans was 1167 mm.

4.4.1 Self-made phantom for DECT application

A cylindrical phantom of 34 mm diameter was made containing five Eppendorf tubes. These tubes were filled with different aqueous solutions with strongly varying atomic numbers: calcium chloride, potassium bromide, barium chlorate, phosphotungstic acid and lead nitrate. The concentrations of these solutions are precisely known (Table 4.7) and are chosen so that their linear attenuation coefficients more or less coincide in the photon energy range from 20 to 70 keV (Fig. 4.11). In this way they will all have similar grey values for most standard scan settings and dual energy techniques will be necessary to distinguish them from one another. Note that due to the K-edge of barium at 37.414 keV, the linear attenuation coefficient of the barium chlorate solutions is lower than that of the other solutions below this edge and higher above this edge. To reduce metal artefacts between the different tubes, the cylindrical phantom itself is filled with water. A model,

which was also used for the simulations (see further), is shown in figure 4.12. The diameter of the Eppendorf tubes in this model is 6.2 mm. Note that this is a slightly different phantom as presented in 3.4.3, since it was newly made for these experiments, which were performed a few years later.

Table 4.7: Mass fractions of the solutes and water and the measured density for each solution of the cylindrical phantom

Material	*Mass fraction solute*	*Mass fraction H_2O*	*Density (g/cm^3)*
$CaCl_2$	0.410	0.590	1.37
KBr	0.115	0.885	1.11
$Ba(ClO_3)_2$	0.103	0.897	1.11
PTA	0.074	0.926	1.07
$Pb(NO_3)_2$	0.077	0.923	1.10

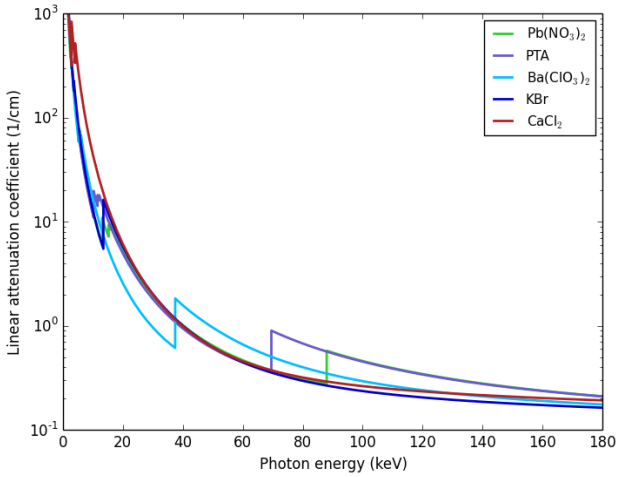

Figure 4.11: Linear attenuation coefficient of the five solutions from the phantom

4.4.2 Self-made phantom: DECT with X-ray spectra based on spectrum parameters

The first step is to look at the behaviour of the linear attenuation coefficient of the different materials that have to be distinguished (see figure 4.11). Based on this behaviour photon energies have to be identified where the largest changes in grey

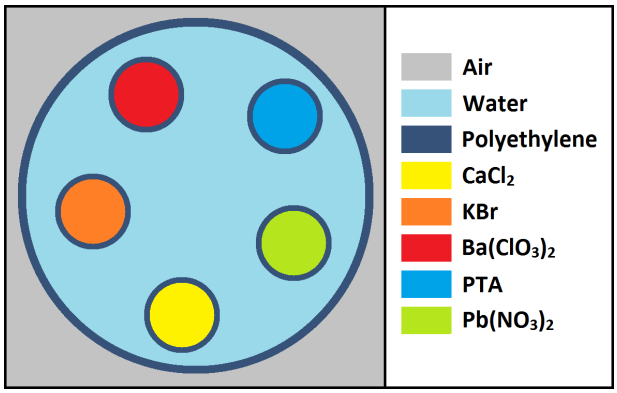

Figure 4.12: Model of the cylindrical phantom with colour legend indicating each component

values for these materials relative to one another are to be expected. For the given sample, the largest changes are observed at the K-edges of the three solutions with the highest atomic number. Therefore, on this sample, the principle of K-edge imaging can be applied for the $Ba(ClO_3)_2$, PTA and $Pb(NO_3)_2$ solution. Note that the K-edge of Br (at 13.483 keV) and especially of Ca (at 4.034 keV) are at photon energies which are too low to be useful in the current experimental setup. Below, K-edge imaging based on spectrum parameters will be illustrated for the $Ba(ClO_3)_2$ and PTA solution.

K-edge imaging for the $Ba(ClO_3)_2$ solution

The K-edge of barium is located at a photon energy of 37.414 keV. X-ray spectra with a detected monochromatic energy just above and below this edge have to be selected. Since this is a relatively low X-ray energy, the main challenge is to filter out enough low energy photons to avoid beam hardening artefacts as much as possible, but still maintain a sufficient total beam intensity within a reasonable exposure time to have an appropriate signal-to-noise ratio in the resulting CT image and keep the monochromatic spectrum energy beneath this edge. Using a tube voltage of 50 kV and 3 mm Al filtration, an X-ray spectrum can be created which more or less fulfills all of these conditions. The detected monochromatic energy of this "low energy" spectrum is 32.5 keV. Note that the water cylinder was taken into account by adding an extra 30 mm H_2O filter. By increasing the tube voltage using the same beam filter, a "high energy" spectrum with monochromatic energy above the barium K-edge can easily be selected. For instance at 100 kV, the detected monochromatic energy is 43.8 keV. To ascertain the extent to which beam hardening will have an influence for these two spectra, the beam hardening factor for each solution was calculated and listed in table 4.8 (first two rows). This factor

indicates that, especially for $Ba(ClO_3)_2$, the degree of beam hardening is quite low, so that E_{mono} should be close to the actual photon energy as seen by the barium tube.

Table 4.8: Detected monochromatic energy (E_{mono}) and beam hardening factors (BHF) of the five solutions for four different X-ray spectra

Spectrum	E_{mono}	*BHF* $CaCl_2$	*BHF KBr*	*BHF* $Ba(ClO_3)_2$	*BHF PTA*	*BHF* $Pb(NO_3)_2$
50 kV, 3 mm Al	32.5	11.75%	11.16%	4.16%	8.99%	9.93%
100 kV, 3 mm Al	43.8	10.39%	10.68%	4.39%	7.13%	9.52%
100 kV, 0.1 mm W	52.8	2.51%	2.83%	3.14%	2.02%	2.55%
180 kV, 1 mm Cu	69.4	1.02%	1.35%	2.85%	1.37%	0.81%

For the two selected spectra, CT scans of the phantom were made, both at a tube power of 30 W, with an exposure time of 2 s per projection. 1500 projections per scan were recorded in total. A reconstructed CT slice of the two scans is shown in figure 4.13. Comparing both images, the $Ba(ClO_3)_2$ solution seems to attenuate less X-ray photons than the other solutions at 50 kV, while at 100 kV it seems to be the other way round. In order to make this different behaviour more clear, a DECT image processing technique should be applied. Here, the decomposition in three basis materials is performed (4.2.1), with the $Ba(ClO_3)_2$ solution as the first basis material, the KBr solution as the second - representing the other "background" solutions in the sample - and water as the third. The calculated volume fractions of these three basis materials are shown in figure 4.14. Note that a threshold of 0.5 was applied. The $Ba(ClO_3)_2$ can be clearly identified, indicating that the choice of the two X-ray spectra was very succesful. The Eppendorf tube with the KBr solution is also correctly allocated to the second basis material. The $CaCl_2$ and $Pb(NO_3)_2$ solutions are mostly classified as KBr as well, which was to be expected. The PTA solution however, was partly classified as the first basis material, with a volume fraction of approximately 0.4, and partly as the second basis material, with a volume fraction of approximately 0.5. This can be logically explained looking at figure 4.11. The "high energy" spectrum in this example contains a significant amount of X-ray photons with an energy above the tungsten K-edge at 69.5 keV. Therefore the behaviour of the linear attenuation coefficient of PTA will be somewhat different compared to the other "background" solutions. At 88 keV the K-edge of lead is reached, but the amount of X-ray photons with an energy exceeding this edge is limited, causing no significant difference in the behaviour of the $Pb(NO_3)_2$ solution. Obviously, water is correctly identified as the third basis material. Note that the air surrounding the sample is mostly classified as water as well.

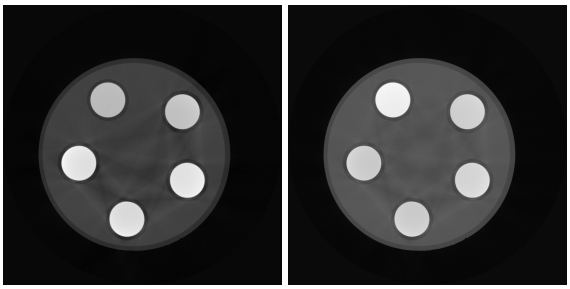

(a) (b)

Figure 4.13: Reconstructed CT slice of the scans performed at 50 kV using 3 mm Al (a) and at 100 kV using 3 mm Al (b)

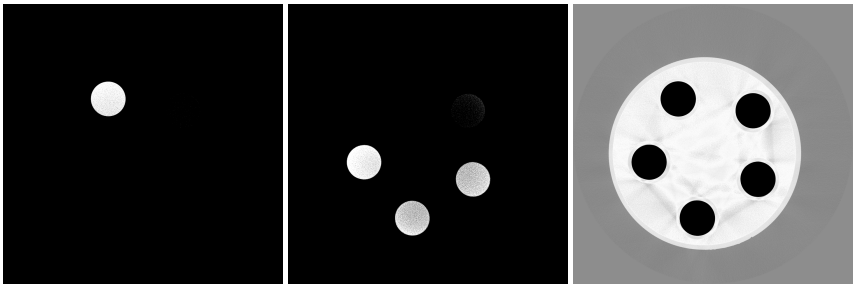

(a) (b) (c)

Figure 4.14: Decomposition in three basis materials of the CT slices from figure 4.13 showing the calculated volume fractions of the $Ba(ClO_3)_2$ solution (a), the KBr solution (b) and water (c). A threshold of 0.5 was applied for each image.

K-edge imaging for the PTA solution

The K-edge of tungsten is located at a photon energy of 69.517 keV. To create the "low energy" X-ray spectrum with as much photons as possible with an energy just below this edge and only a limited amount with an energy above the edge, the principle of K-edge filtration can be applied by using a tungsten filter (see figure 4.2). A suitable choice is a tube voltage of 100 kV with a 0.1 mm tungsten filter. This spectrum has a detected monochromatic energy of 52.8 keV. This is somewhat below the K-edge of tungsten, but increasing the tube voltage will predominantly lead to an increase of photons with an energy above the edge, which is undesirable, while adding more tungsten filtration will decrease the total beam intensity too much for adequate imaging. For the "high energy" spectrum, conventional filtration should be used in combination with high tube voltages. For instance, at 180 kV using a 1 mm copper filter, an X-ray spectrum with a detected monochromatic energy of 69.4 keV can be created. Since E_{mono} is slightly smaller than

$E_{eff,0}$ (see section 4.3.3), the actual energy as seen by the sample will be above 69.5 keV. Table 4.8 (last two rows) shows the beam hardening factor for each solution for these two spectra as well. Since both spectra are heavily filtered, it is not surprising that the degree of beam hardening is very low. Therefore, the detected monochromatic energies should be an adequate measure for the actual photon energy as seen by the PTA tube.

For these two selected spectra, CT scans of the phantom were again made, both using a tube voltage of 30 W, with an exposure time of 2 s per projection, for a total of 1500 projections per scan. Reconstructed slices of these scans are shown in figure 4.15. In the lower energy image, PTA seems to be equal to the other solutions, except for $Ba(ClO_3)_2$, while in the higher energy image its attenuation coefficient is higher than that of the others. This different behaviour is confirmed by applying the three basis material decomposition technique, with the PTA solution as the first basis material, the KBR solution as the second - again representing the other "background" solutions - and water as the third (Fig. 4.16). The PTA solution can be clearly identified in the first basis material image (volume fraction of approximately 0.96). On the other hand, the $Pb(NO_3)_2$ solution is also for a large part classified as the first material, with a volume fraction of approximately 0.65, and for a smaller part classified as the second material, with a volume fraction of approximately 0.35. This is not surprising since the "high energy" spectrum contains a significant amount of photons with an energy above the K-edge of lead at 88.0 keV. For these photons, the PTA and $Pb(NO_3)_2$ solution will have a similar behaviour. Therefore, if these materials have to be clearly separated in a specific sample, a lower tube voltage should be used for the "high energy" spectrum to limit the amount of photons with an energy exceeding 88 keV. The other "background" solutions are all quite clearly classified as the second basis material. Also water is correctly identified. Note that again the air surrounding the sample is mostly classified as water as well.

Beyond (one material) K-edge imaging

The previous examples show that K-edge imaging can be successfully applied using X-ray spectra based on spectrum parameters. Of course, K-edge imaging aims at distinguishing (or even identifying) only one specific material, while the other materials present are hardly taken into consideration. Dual energy techniques, however, are particularly useful for separating three materials from one another. For distinguishing two materials, a single scan with carefully chosen scan parameters will often be sufficient, except when highly accurate segmentation of the materials must be done. Selecting two spectra for discriminating three materials, solely based on their linear attenuation coefficient requires a more complex rea-

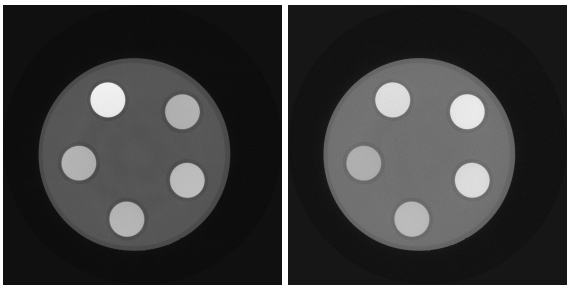

(a) (b)

Figure 4.15: Reconstructed CT slice of the scans performed at 100 kV using 0.1 mm W (a) and at 180 kV using 1 mm Cu (b)

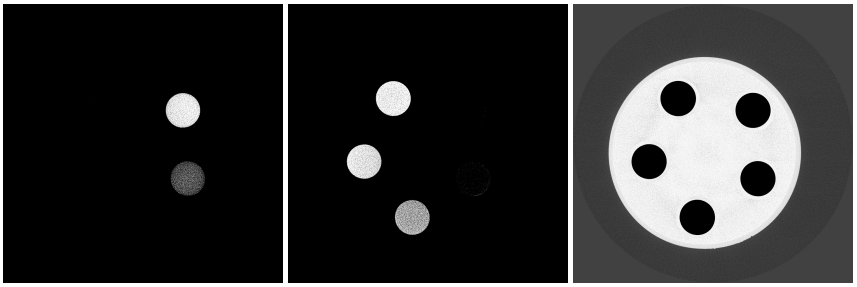

(a) (b) (c)

Figure 4.16: Decomposition in three basis materials of the CT slices from figure 4.15 showing the calculated volume fractions of the PTA solution (a), the KBr solution (b) and water (c). A threshold of 0.5 was applied for each image.

soning. For instance, to separate the KBr (or $CaCl_2$), $Ba(ClO_3)_2$ and PTA solution from one another, a spectrum at a photon energy below the K-edge of Ba in combination with a spectrum at a photon energy above the edge of tungsten would be a good choice, i.e. the first and the fourth spectrum from table 4.8. The resulting decomposition in three basis materials (KBr, $Ba(ClO_3)_2$ and PTA solution) is shown in figure 4.17. The KBr solution can be clearly and correctly identified (volume fraction of 0.96, σ 0.044). The $Ba(ClO_3)_2$ and PTA solutions, with a volume fraction of 0.7 and 0.8, respectively, are mostly correctly classified. However the standard deviations on these volume fractions, 0.15 and 0.16, respectively, are quite large. For samples where these materials are scattered throughout the entire sample, these deviations are too large to allow adequate image segmentation. Note that some cupping in the volume fraction images is visible as well. A better choice of X-ray spectra is necessary, preferably based on complete CT simulations.

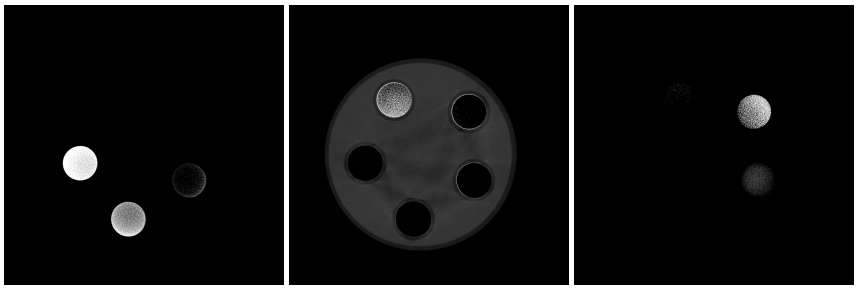

(a) (b) (c)

Figure 4.17: Decomposition in three basis materials of CT slices 4.13(a) and 4.15(b) showing the calculated volume fractions of the KBr solution (a), the $Ba(ClO_3)_2$ solution (b) and the PTA solution (c). A threshold of 0.5 was applied for each image.

Discriminating KBr (or $CaCl_2$), PTA and $Pb(NO_3)_2$ is an even more difficult task. Ideally a spectrum at an energy between the edges of tungsten and lead in combination with a spectrum at an energy above the lead edge is chosen, but this is practically not quite feasible. For instance, at 180 kV 3 mm copper filtration is needed to reach a detected monochromatic energy of 88 keV. Using this much filtration, long exposure times will be necessary to compensate for the low beam intensities. Even at 240 kV, the maximum tube voltage at HECTOR, still 2.5 mm copper is required. On the other hand, the previous examples demonstrated that as soon as there is a significant amount of photons with an energy above the K-edge of a material, the influence of this edge becomes detectable. However, it is difficult to determine when this is the case based solely on spectrum parameters. Therefore, complete CT simulations are necessary.

4.4.3 Self-made phantom: DECT with X-ray spectra based on complete CT simulations

As in section 4.3.4, simulations were performed for different X-ray spectra using the model of the self-made phantom (Fig. 4.12). Four beam filters were applied (1 mm Al, 3 mm Al, 1 mm Cu and 0.1 mm W) and a broad range of tube voltages (50, 60, 70, 80, 90, 100, 120, 140, 160 and 180 kV) was chosen with a tube power of 30 W. 1000 projections were simulated, each with an exposure time of 1 s per projection, for all settings. After reconstruction, the attenuation coefficients of the five solutions and their corresponding standard deviations in the simulated CT images were measured. These are graphically represented in figures 4.18 and 4.19. It is clear that for most of the settings, there is a significant overlap between the different solutions, except for $Ba(ClO_3)_2$. For three different combinations of

solutions, the ideal X-ray spectra can be determined based on the simulated CNR values and the DECT results will be shown.

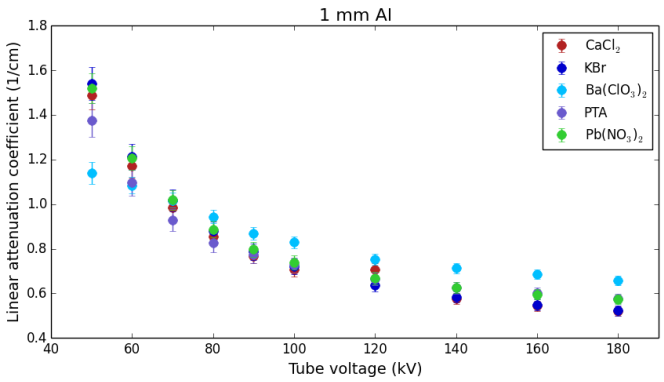

(a)

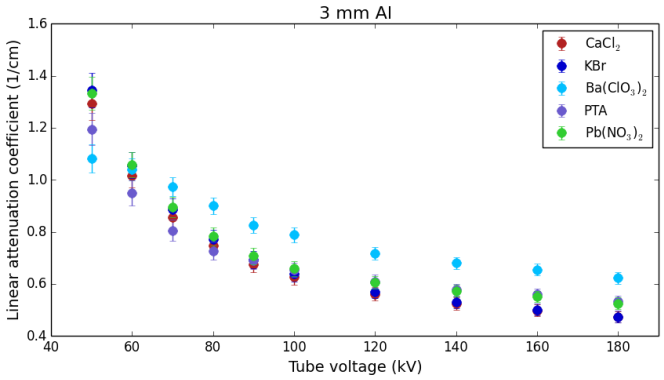

(b)

Figure 4.18: Attenuation coefficients of the five solutions and their corresponding errors (errorbar = 1 σ) in terms of tube voltage for 1 and 3 mm Al beam filtration

Distinguishing the KBr, $Ba(ClO_3)_2$ and PTA solution from one another

The results in the previous section, where two spectra were selected based on spectrum parameters to try to identify the KBr, $Ba(ClO_3)_2$ and PTA solution using DECT were already promising. However, for more complex samples or actual segmentation purposes, a better choice of X-ray spectra is necessary. As explained in section 4.3.4, the optimal spectra can be automatically selected using the simulated CNR values. For the given combination of materials, the two spectra chosen in this way are the one at 90 kV with a 3 mm aluminium filter and the one at 160

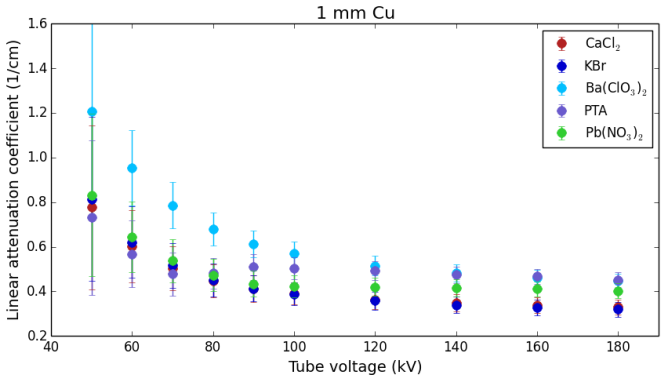

(a)

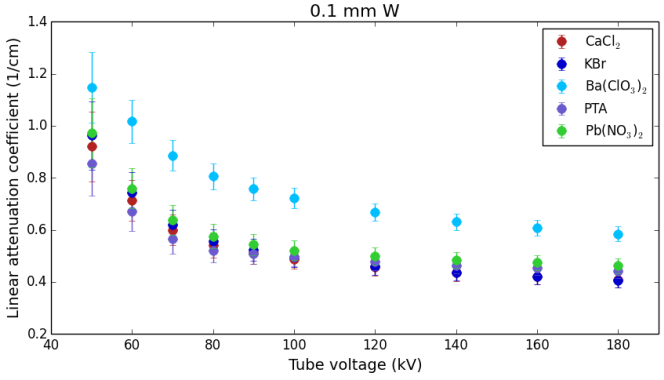

(b)

Figure 4.19: Attenuation coefficients of the five solutions and their corresponding errors (errorbar = 1 σ) in terms of tube voltage for 1 mm Cu and 0.1 mm W beam filtration

kV using a 1 mm copper filter. In figure 4.18(b) it can be seen that in the first case the attenuation coefficient of the $Ba(ClO_3)_2$ solution is significantly larger than that of the other two, while in the second case the KBr solution distinguishes itself from the other two solution by means of a significantly smaller attenuation coefficient. The resulting basis materials decomposition is shown in figure 4.20. Compared to figure 4.17, this is clearly a much better result. The three solutions are correctly identified with calculated volume fractions of 0.94, 0.88 and 0.93 for the KBr, $Ba(ClO_3)_2$ and PTA solution, respectively. The standard deviations on these values are acceptable as wel: 0.077, 0.092 and 0.085, respectively.

Although it requires some extra work, it is clearly worthwhile to carry out simulations for an optimal selection of dual energy X-ray spectra. Note that the

(a) (b) (c)

Figure 4.20: Decomposition in three basis materials of the same CT slice recorded at 90 kV using a 3 mm Al filter and at 160 kV with a 1 mm Cu filter, showing the calculated volume fractions of the KBr solution (a), the $Ba(ClO_3)_2$ solution (b) and the PTA solution (c). A threshold of 0.5 was applied for each image.

90 kV with 3 mm Al spectrum and the 160 kV with 1 mm Cu spectrum have a detected monochromatic energy of 65.9 keV and 68.3 keV, respectively. These spectra would therefore never have been chosen based on these values alone. In figure 4.21 the detected energy as a function of photon energy is shown for the two scanner settings without a sample present. The spectra are clearly significantly different, but this is not reflected by the detected monochromatic energy. This example therefore illustrates the shortcomings of a choice of X-ray spectra based on the "spectrum energy". Only by means of simulations, their full shape can be taken into account allowing for an optimal DECT result.

Distinguishing the KBr, PTA and $Pb(NO_3)_2$ solution from one another

In the previous section, the question also rose on how to determine X-ray spectra to discriminate the KBr, PTA and $Pb(NO_3)_2$ solution based solely on spectrum parameters. An automatic selection based on simulations for the given combination of materials results in the following spectra: 60 kV with 3 mm aluminium filtration and 180 kV also with 3 mm aluminium filtration. From figure 4.18(b) it is clear that at 60 kV the attenuation coefficients of the KBr and $Pb(NO_3)_2$ solution largely overlap, while that of the PTA solution is significantly lower. At 180 kV the attenuation coefficients of the PTA and $Pb(NO_3)_2$ solution mainly overlap, while the KBr solution is less attenuating. The decomposition in three basis materials (KBr, PTA and $Pb(NO_3)_2$ solution) for the two selected X-ray spectra is shown in figure 4.22. Again, the results are quite good, since the three solutions are correctly classified. However, the accuracy is slightly less than in the previous example, mainly for the $Pb(NO_3)_2$ solution. The calculated volume fractions are 0.91, 0.92 and 0.78 for the the KBr, PTA and $Pb(NO_3)_2$ solution, with a standard deviation of 0.105, 0.107 and 0.159, respectively.

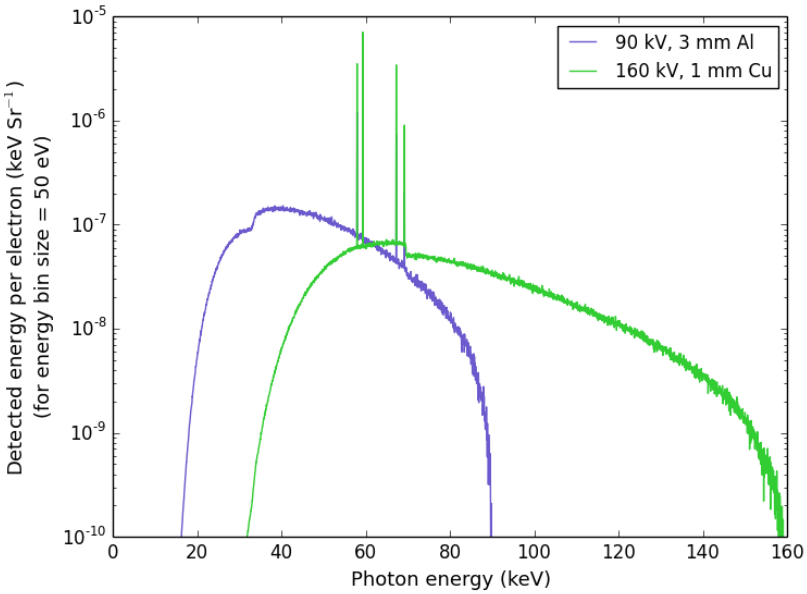

Figure 4.21: Comparison of the two automatically selected spectra for identifying the the KBr, $Ba(ClO_3)_2$ and PTA solution

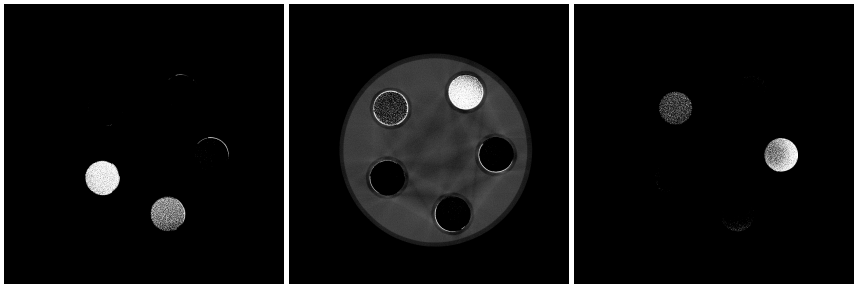

(a) (b) (c)

Figure 4.22: Decomposition in three basis materials of the same CT slice recorded at 60 kV and at 180 kV, both using a 3 mm Al filter, showing the calculated volume fractions of the KBr solution (a), the PTA solution (b) and the $Pb(NO_3)_2$ solution (c). A threshold of 0.5 was applied for each image.

Distinguishing the $CaCl_2$, KBr and $Pb(NO_3)_2$ solution from one another

As a final example, a more challenging combination of solutions is chosen: $CaCl_2$, KBr and $Pb(NO_3)_2$. In figure 4.11 it is shown that the $CaCl_2$ and KBr solution have an overlapping linear attenuation coefficient across the photon energy range of in-

terest. Only at the lower energy side, i.e. below 13.48 keV being the K-edge of Br, they start deviating from one another. This part is however mainly filtered out by the exit window of the tube alone, let alone when the slightest beam filtration is used. Therefore, the chances of being able to distinguish the $CaCl_2$ from the KBr solution are minimal. The automatically selected X-ray spectra for this combination of materials is obtained with a tube voltage of 120 kV using 1 mm aluminium filtration and with a tube voltage of 180 kV using a 3 mm aluminium filter. The three basis material decomposition is shown in figure 4.23. As expected, the $CaCl_2$ and KBr solution are incorrectly classified. They are represented as a mixture of the first and second basis material. For instance, the $CaCl_2$ solution has a volume fraction of 0.72 (σ 0.331) and 0.20 (σ 0.251), for the first en second basis material respectively. For the KBr solution, the decomposition is even worse with volume fractions of 0.63 (σ 0.326) and 0.35 (σ 0.319), respectively. Only the $Pb(NO_3)_2$ solution is correctly identified as the third basis material, with a volume fraction of 0.91 with a standard deviation of 0.120. Note that the decomposition suffers from cupping artefacts, due to the significant degree of beam hardening present in the 120 kV with 1 mm Al spectrum.

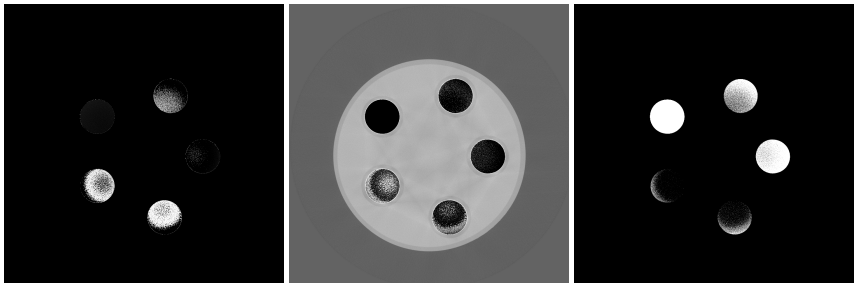

(a) (b) (c)

Figure 4.23: Decomposition in three basis materials of the same CT slice recorded at 120 kV using a 1 mm Al filter and at 180 kV with a 3 mm Al filter, showing the calculated volume fractions of the $CaCl_2$ solution (a), the KBr solution (b) and the $Pb(NO_3)_2$ solution (c). No threshold was applied.

This example clearly demonstrates that DECT is only useful when the linear attenuation coefficients of the materials that have to be distinguished are significantly different in at least a part of the photon energy range useful for X-ray imaging, i.e. at least above 25 keV and preferrably below an estimated energy of 140 keV.

4.4.4 DECT applied on a real sample

As a step towards the next chapter on histology by means of high resolution X-ray tomography, a stained mouse hind leg is chosen as a real example for DECT. Section 5.2 focuses on contrast agents for soft tissue visualisation using micro-CT. Useful contrast agents typically contain an element with a high atomic number. A new, promising staining agent identified in the next chapter is mercury(II) chloride ($HgCl_2$), used in the form of an aqueous solution. $HgCl_2$ allows to reveal a lot of details within soft tissue structures, such as different muscle fascicles. As such, visualisation of biomedical samples containing sof tissue can be greatly improved. However, when a sample contains bone as well, it is not always straightforward to distinguish the $HgCl_2$ stained soft tissue from the bone structures, since their grey values will start to overlap. If the materials have to be segmented, DECT may come in useful.

From the previous section it was clear that the best results were achieved when the X-ray spectra were selected based on complete CT simulations. Moreover, the K-edge of mercury is located at an inconveniently high energy (83.19 keV) so that realistic sanner settings leading to a detected monochromatic energy above this edge are difficult to find and the method based on spectrum parameters cannot be straightforwardly applied. However, this real example is more cumbersome in several areas compared to the self-made phantom for the simulations approach. First of all, it is not possible to construct an exact replication of the sample as a basis for the CT simulations. Therefore, a simplified model has to be made which of course entails some inaccuracies. Figure 4.24 shows a simplified model of a mouse hind leg, containing muscle tissue, adipose tissue and bone. Two bones are present in this model, the tibia and the smaller fibula at the centre of the sample. Secondly, the exact elemental composition of the materials is not known. Therefore, a good approximation should be used. In report 44 of the International Commission on Radiation Units and Measurements (ICRU) [54], the general composition of several materials of dosimetric interest were determined, such as muscle, adipose tissue and cortical bone. These data were used for the mouse sample model. Note that the tibia should actually be filled with bone marrow, but since the composition of bone marrow was not determined in the ICRU-44 report, adipose tissue was used instead. The grey values of the different materials in a CT simulation of this model are in very good agreement with the grey values in a real CT scan of an unstained mouse hind leg (data not shown here). However, in the current example the mouse hind leg was stained with an aqueous 1% $HgCl_2$ solution for 6 hours. For the simulations, it is assumed that only the muscle tissue is stained by the contrast agent. Moreover, from experience with this substance, it is assumed that the $HgCl_2$ concentration in the muscle tissue is higher than that of the original contrast solution. Therefore, the muscle tissue is simulated as a “solution” of 5% $HgCl_2$ in

muscle, defined by the ICRU-44 composition, as a rough approximation.

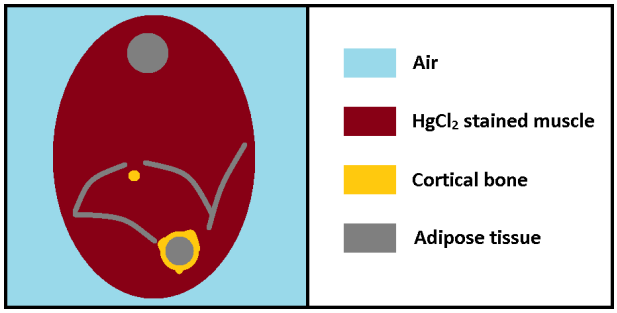

Figure 4.24: Simplified model of the mouse hind leg sample used for the CT simulations with colour legend indicating each material

Simulations were performed for three beam filters (1 mm Al, 3 mm Al and 1 mm Cu) and five different tube voltages, two in the low energy range (50 and 60 kV), one in the middle energy range (100 kV) and two in the high energy range (160 and 180 kV). A tube power of 15 W was chosen. 500 projections were simulated, each with an exposure time of 1 s per projection. Figure 4.25 shows the measured attenuation coefficients and their corresponding standard deviations of stained muscle, adipose tissue and bone in a reconstructed slice of each simulation. From these graphs it is clear that at 50 kV using 1 mm Al these three materials should easily be distinguished from one another. Indeed, when applying the automatic selection of spectra based on the simulated CNR values, this spectrum is selected twice. Therefore, a single scan at these settings with double exposure time should be ideal, i.e. a high quality scan. However, it may nevertheless be of interest to perform a second scan with a different X-ray spectrum to make use of the additional spectral information. As such, it is for instance possible to calculate volume fractions for the different materials, which is particularly useful for samples with a lot of partial volume effect present. For the current sample, segmentation of a high quality scan performed at a single energy will be compared with the results of a dual energy based material decomposition. A second spectrum for this specific sample should be selected based on the behaviour of the two materials that are hardest to distinguish, i.e. stained muscle and bone. Table 4.9 lists the simulated attenuation coefficients and corresponding standard deviations for these materials. In the last column, the attenuation coefficient of muscle is divided by the attenuation coefficient of bone. This number reflects the relative behaviour of these two materials. At 50 kV with 1 mm aluminium filtration, the smallest value for this number is obtained (0.61). For the second scan settings, the relative behaviour of muscle and bone should differ as much as possible from the behaviour at the first settings. Therefore, the spectrum leading to the largest value

of $\frac{\mu_{Muscle}}{\mu_{Bone}}$ should be selected, i.e. 50 kV using 1 mm copper. However, looking at the standard deviations, at these settings image quality will be very poor. A better option is to use a tube voltage of 180 kV with 1 mm Cu resulting in the second largest value for $\frac{\mu_{Muscle}}{\mu_{Bone}}$ with acceptable image quality.

Table 4.9: Attenuation coefficients and corresponding standard deviations of the stained muscle tissue and and bone for all simulated scan settings. In the last column, the attenuation coefficient of muscle is divided by the attenuation coefficient of bone.

Voltage (kV)	μ_{Muscle}	σ_{Muscle}	μ_{Bone}	σ_{Bone}	$\frac{\mu_{Muscle}}{\mu_{Bone}}$
***Filter:* 1 mm Al**					
50	1.35	0.16	2.21	0.16	0.61
70	0.93	0.11	1.49	0.12	0.63
100	0.67	0.09	1.02	0.10	0.66
160	0.53	0.08	0.80	0.08	0.66
180	0.50	0.08	0.75	0.08	0.67
Filter: 3 mm Al					
50	1.10	0.20	1.80	0.20	0.61
70	0.76	0.13	1.22	0.12	0.62
100	0.57	0.10	0.88	0.10	0.65
160	0.47	0.09	0.67	0.08	0.71
180	0.46	0.08	0.66	0.10	0.69
***Filter:* 1 mm Cu**					
50	0.92	1.09	1.19	1.15	0.77
70	0.45	0.39	0.60	0.47	0.75
100	0.36	0.22	0.53	0.22	0.68
160	0.34	0.16	0.48	0.17	0.72
180	0.34	0.15	0.45	0.14	0.75

Figure 4.26 shows the same reconstructed CT slice of the scans performed at 50 kV with 1 mm aluminium filtration and at 180 kV with 1 mm copper filtration. In figure 4.27 the decomposition in stained muscle tissue, cortical bone and adipose tissue of these slices is shown. The classification appears to be quite succesful, especially for cortical bone and secondarily for adipose tissue, taking into account the several shortcomings of this real sample. First of all, the muscle tissue is far from uniformly stained. A gradient in grey values is clearly visible from the edge of the sample to its centre. A such, in the centre of the sample, part of the muscle tissue is incorrectly identified as adipose tissue. Secondly, not only the

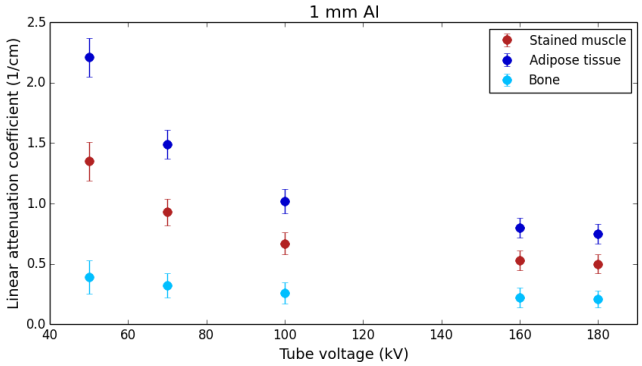

(a)

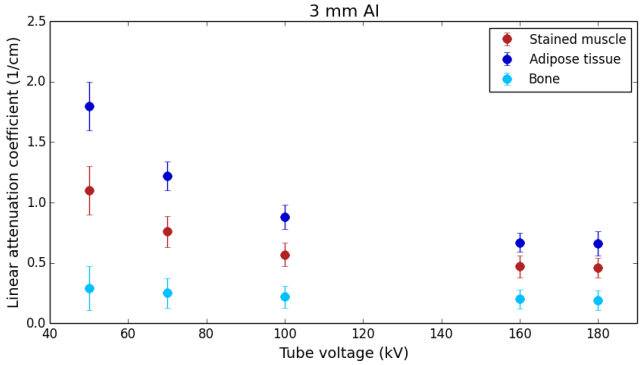

(b)

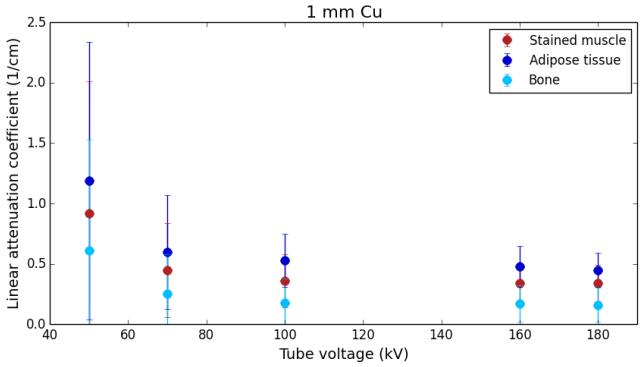

(c)

Figure 4.25: Attenuation coefficients of the three materials and their corresponding errors (errorbar = 1 σ) in terms of tube voltage and beam filtration

muscle tissue is stained, but the adipose tissue is stained to a lesser extent as well. Moreover, some of the contrast solution managed to penetrate the outer edge of the bone. Finally, some $HgCl_2$ molecules precipitated inside the muscle tissue. Some of these precipitations are incorrectly classified as bone.

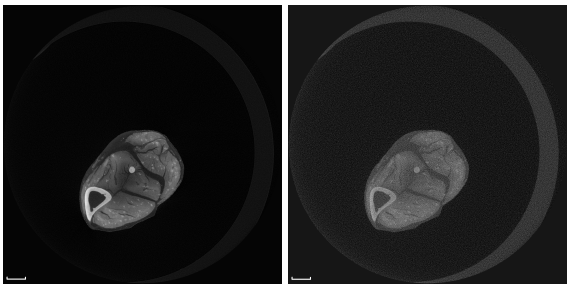

(a) (b)

Figure 4.26: Reconstructed CT slice of the scans performed at 50 kV using 1 mm Al (a) and at 180 kV using 1 mm Cu (b). Scale bar = 1 mm.

(a) (b) (c)

Figure 4.27: Decomposition in three basis materials of the CT slices from figure 4.26 showing the calculated volume fractions of adipose tissue (a), $HgCl_2$ stained muscle tissue (b) and cortical bone (c). A threshold of 0.7 was applied for each image. Scale bar = 1 mm.

Figure 4.28 shows the segmentation in adipose tissue, stained muscle tissue and cortical bone of the same recontructed CT slice of a high quality scan performed at 50 kV with 1 mm aluminium filtration. Compared to the dual energy material decomposition, the muscle tissue is more clearly identified, except for the central part of the sample. The classifications of adipose tissue and cortical bone seem to be somewhat better in the dual energy case. However, based on these images it is not possible to state that either a single high quality scan or dual energy

scans lead to significantly better results. Both techniques have their own advantages. A single high quality scan is easier to practically realise. On the other hand, DECT leads to more nuanced information, for instance in the form of volume fractions for the different materials.

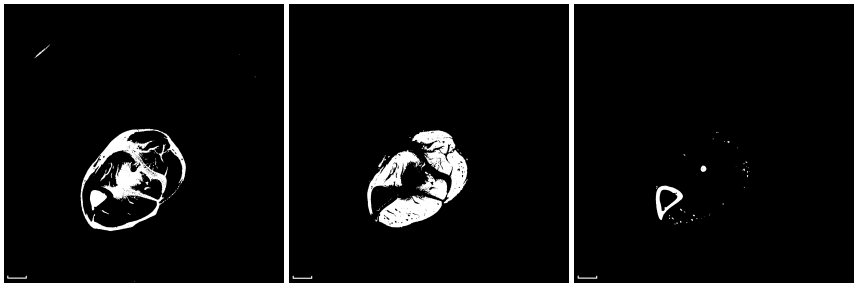

(a) (b) (c)

Figure 4.28: Segmentation of the same CT slice as in figure 4.26 from a high quality scan obtained at 50 kV using 1 mm Al showing adipose tissue (a), $HgCl_2$ stained muscle tissue (b) and cortical bone (c). Scale bar = 1 mm.

References

[1] T. G. Flohr, C. H. McCollough, H. Bruder, M. Petersilka, K. Gruber, C. Suss, M. Grasruck, K. Stierstorfer, B. Krauss, R. Raupach, A. N. Primak, A. Kuttner, S. Achenbach, C. Becker, A. Kopp, and B. M. Ohnesorge. *First performance evaluation of a dual-source CT (DSCT) system*. Eur. Radiol., 16(2):256–268, 2006.

[2] R. E. Alvarez and A. Macovski. *Energy-selective reconstructions in X-ray computerized tomography*. Phys. Med. Biol., 21(5):733–744, 1976.

[3] L. A. Lehmann, R. E. Alvarez, A. Macovski, W. R. Brody, N. J. Pelc, S. J. Riederer, and A. L. Hall. *Generalized image combinations in dual KVP digital radiography*. Med. Phys., 8(5):659–67, 1981.

[4] R. A. Rutherford, B. R. Pullan, and I. Isherwood. *Measurement of Effective Atomic Number and Electron-Density Using an Emi Scanner*. Neuroradiology, 11(1):15–21, 1976.

[5] W. A. Kalender, W. H. Perman, J. R. Vetter, and E. Klotz. *Evaluation of a prototype dual-energy computed tomographic apparatus. I. Phantom studies*. Med. Phys., 13(3):334–9, 1986.

[6] W. H. Payne, W. D. McDavid, R. G. Waggener, M. J. Dennis, and V. J. Sank. *Extrapolation of linear attenuation coefficients of biological materials from diagnostic-energy x-ray levels to the megavoltage range*. Med. Phys., 4(6):505–7, 1977.

[7] M. R. Millner, W. D. McDavid, R. G. Waggener, M. J. Dennis, W. H. Payne, and V. J. Sank. *Extraction of information from CT scans at different energies*. Med. Phys., 6(1):70–1, 1979.

[8] K. S. Chuang and H. K. Huang. *Comparison of four dual energy image decomposition methods*. Phys. Med. Biol., 33(4):455–466, 1988.

[9] W. R. Brody, G. Butt, A. Hall, and A. Macovski. *A method for selective tissue and bone visualization using dual energy scanned projection radiography*. Med. Phys., 8(3):353–7, 1981.

[10] K. S. Chuang and H. K. Huang. *A fast dual-energy computational method using isotransmission lines and table lookup*. Med. Phys., 14(2):186–92, 1987.

[11] H. J. Vinegar and S. L. Wellington. *Tomographic imaging of three-phase flow experiments*. Rev. Sci. Instrum., 58(1):96–107, 1987.

[12] P. V. Granton, S. I. Pollmann, N. L. Ford, M. Drangova, and D. W. Holdsworth. *Implementation of dual- and triple-energy cone-beam micro-CT for postreconstruction material decomposition*. Med. Phys., 35(11):5030–42, 2008.

[13] C. Maass, M. Baer, and M. Kachelriess. *Image-based dual energy CT using optimized precorrection functions: A practical new approach of material decomposition in image domain*. Med. Phys., 36(8):3818–3829, 2009.

[14] A. J. Coleman and M. Sinclair. *A beam-hardening correction using dual-energy computed-tomography*. Phys. Med. Biol., 30(11):1251–1256, 1985.

[15] A. Sarnelli, H. Elleaume, A. Taibi, M. Gambaccini, and A. Bravin. *K-edge digital subtraction imaging with dichromatic x-ray sources: SNR and dose studies*. Phys. Med. Biol., 51(17):4311–28, 2006.

[16] C. H. McCollough, S. Leng, L. Yu, and J. G. Fletcher. *Dual- and Multi-Energy CT: Principles, Technical Approaches, and Clinical Applications*. Radiology, 276(3):637–53, 2015.

[17] P. M. Shikhaliev, T. Xu, and S. Molloi. *Photon counting computed tomography: concept and initial results*. Med. Phys., 32(2):427–36, 2005.

[18] P. M. Shikhaliev. *Computed tomography with energy-resolved detection: a feasibility study*. Phys. Med. Biol., 53(5):1475–95, 2008.

[19] E. Roessl and R. Proksa. *K-edge imaging in x-ray computed tomography using multi-bin photon counting detectors*. Phys. Med. Biol., 52(15):4679–96, 2007.

[20] J. P. Schlomka, E. Roessl, R. Dorscheid, S. Dill, G. Martens, T. Istel, C. Baumer, C. Herrmann, R. Steadman, G. Zeitler, A. Livne, and R. Proksa. *Experimental feasibility of multi-energy photon-counting K-edge imaging in pre-clinical computed tomography*. Phys. Med. Biol., 53(15):4031–47, 2008.

[21] E. Roessl, B. Brendel, K. J. Engel, J. P. Schlomka, A. Thran, and R. Proksa. *Sensitivity of photon-counting based K-edge imaging in X-ray computed tomography*. IEEE Trans. Med. Imaging, 30(9):1678–90, 2011.

[22] H. Atak and P. M. Shikhaliev. *Dual energy CT with photon counting and dual source systems: comparative evaluation*. Phys. Med. Biol., 60(23):8949–75, 2015.

[23] S. Feuerlein, E. Roessl, R. Proksa, G. Martens, O. Klass, M. Jeltsch, V. Rasche, H. J. Brambs, M. H. Hoffmann, and J. P. Schlomka. *Multienergy photon-counting K-edge imaging: potential for improved luminal depiction in vascular imaging*. Radiology, 249(3):1010–6, 2008.

[24] A. de Vries, E. Roessl, E. Kneepkens, A. Thran, B. Brendel, G. Martens, R. Proska, K. Nicolay, and H. Grull. *Quantitative spectral K-edge imaging in preclinical photon-counting x-ray computed tomography*. Invest. Radiol., 50(4):297–304, 2015.

[25] P. Sukovic and N. H. Clinthorne. *Penalized weighted least-squares image reconstruction for dual energy X-ray transmission tomography*. IEEE Trans. Med. Imaging, 19(11):1075–1081, 2000.

[26] P. Stenner, T. Berkus, and M. Kachelriess. *Empirical dual energy calibration (EDEC) for cone-beam computed tomography*. Med. Phys., 34(9):3630–41, 2007.

[27] X. Liu, L. F. Yu, A. N. Primak, and C. H. McCollough. *Quantitative imaging of element composition and mass fraction using dual-energy CT: Three-material decomposition*. Med. Phys., 36(5):1602–1609, 2009.

[28] T. G. Schmidt. *Optimal "image-based" weighting for energy-resolved CT*. Med. Phys., 36(7):3018–3027, 2009.

[29] T. Y. Niu, X. Dong, M. Petrongolo, and L. Zhu. *Iterative image-domain decomposition for dual-energy CT*. Med. Phys., 41(4), 2014.

[30] Y. S. Zhao, X. Zhao, and P. Zhang. *An extended algebraic reconstruction technique (E-ART) for dual spectral CT*. IEEE Trans. Med. Imaging, 34(3):761–768, 2015.

[31] M. Mansouri, S. Aran, A. Singh, A. R. Kambadakone, D. V. Sahani, M. H. Lev, and H. H. Abujudeh. *Dual-energy computed tomography characterization of urinary calculi: basic principles, applications and concerns*. Curr. Probl. Diagn. Radiol., 44(6):496–500, 2015.

[32] A. N. Primak, J. G. Fletcher, T. J. Vrtiska, O. P. Dzyubak, J. C. Lieske, M. E. Jackson, Jr. Williams, J. C., and C. H. McCollough. *Noninvasive differentiation of uric acid versus non-uric acid kidney stones using dual-energy CT*. Acad. Radiol., 14(12):1441–7, 2007.

[33] B. C. Meyer, T. Werncke, W. Hopfenmuller, H. J. Raatschen, K. J. Wolf, and T. Albrecht. *Dual energy CT of peripheral arteries: effect of automatic bone and plaque removal on image quality and grading of stenoses*. Eur. J. Radiol., 68(3):414–22, 2008.

[34] B. Schulz, K. Kuehling, W. Kromen, P. Siebenhandl, M. J. Kerl, T. J. Vogl, and R. Bauer. *Automatic bone removal technique in whole-body dual-energy CT angiography: performance and image quality*. AJR Am. J. Roentgenol., 199(5):W646–50, 2012.

[35] A. A. Postma, M. Das, A. A. Stadler, and J. E. Wildberger. *Dual-Energy CT: What the Neuroradiologist Should Know*. Curr. Radiol. Rep., 3(5):16, 2015.

[36] T. Lestra, S. Mule, I. Millet, A. Carsin-Vu, P. Taourel, and C. Hoeffel. *Applications of dual energy computed tomography in abdominal imaging*. Diagn Interv Imaging, 97(6):593–603, 2016.

[37] M. Ohana, M. Y. Jeung, A. Labani, S. El Ghannudi, and C. Roy. *Thoracic dual energy CT: acquisition protocols, current applications and future developments*. Diagn Interv Imaging, 95(11):1017–26, 2014.

[38] I. Danad, O. H. B, and J. K. Min. *Dual-energy computed tomography for detection of coronary artery disease*. Expert Rev. Cardiovasc. Ther., 13(12):1345–56, 2015.

[39] H. Machida, I. Tanaka, R. Fukui, Y. Shen, T. Ishikawa, E. Tate, and E. Ueno. *Current and Novel Imaging Techniques in Coronary CT*. Radiographics, 35(4):991–1010, 2015.

[40] A. P. Teles, I. Lima, and R. T. Topes. *Rock porosity quantification by dual-energy X-ray computed microtomography*. Micron, 83:72–78, 2016.

[41] M. Van Geet, R. Swennen, and M. Wevers. *Quantitative analysis of reservoir rocks by microfocus X-ray computerised tomography*. Sediment Geol, 132(1-2):25–36, 2000.

[42] H. Alves, I. Lima, J. T. de Assis, A. A. Neves, and R. T. Lopes. *Mineralogy evaluation and segmentation using dual-energy microtomography*. X-Ray Spectrom., 44(3):99–104, 2015.

[43] S. Kacmarz. *Angenäherte auflösung von systemen linearer gleichungen*. Bulletin International de l'Académie Polonaise des Sciences et des Lettres, 35:355–357, 1937.

[44] K. Tanabe. *Projection method for solving a singular system of linear equations and its applications*. Numer. Math., 17(3):203–214, 1971.

[45] Y. De Witte. *Improved and practically feasible reconstruction methods for high resolution X-ray tomography*. Phd dissertation, Ghent University, 2010.

[46] J. Dhaene. *Development and application of a highly accurate polychromatic X-ray microtomography simulator*. Phd dissertation, Ghent University, 2017.

[47] A. N. Primak, J. C. Ramirez Giraldo, X. Liu, L. Yu, and C. H. McCollough. *Improved dual-energy material discrimination for dual-source CT by means of additional spectral filtration*. Med. Phys., 36(4):1359–69, 2009.

[48] Y. Jin. *Implementation and optimization of dual energy computed tomography*. Phd dissertation, Friedrich-Alexander University, 2011.

[49] J. L. Ducote, T. Xu, and S. Molloi. *Optimization of a flat-panel based real time dual-energy system for cardiac imaging*. Med. Phys., 33(6):1562–8, 2006.

[50] T. Xu, J. L. Ducote, J. T. Wong, and S. Molloi. *Feasibility of real time dual-energy imaging based on a flat panel detector for coronary artery calcium quantification*. Med. Phys., 33(6):1612–22, 2006.

[51] N. A. Shkumat, J. H. Siewerdsen, A. C. Dhanantwari, D. B. Williams, S. Richard, N. S. Paul, J. Yorkston, and R. Van Metter. *Optimization of image acquisition techniques for dual-energy imaging of the chest*. Med. Phys., 34(10):3904–15, 2007.

[52] J. M. Boone, G. S. Shaber, and M. Tecotzky. *Dual-energy mammography: a detector analysis*. Med. Phys., 17(4):665–75, 1990.

[53] M. Saito. *Dual-energy approach to contrast-enhanced mammography using the balanced filter method: spectral optimization and preliminary phantom measurement*. Med. Phys., 34(11):4236–46, 2007.

[54] International Commission on Radiation Units and Measurements. *Tissue substitutes in radiation dosimetry and measurement (ICRU Report 44)*. International Commission on Radiation Units and Measurements, 1989.

5

HiXTom: Histology by means of high resolution X-ray Tomography

This chapter is based on the publication: An exploratory study of contrast agents for soft tissue visualization by means of high resolution X-ray computed tomography imaging [1]

Curiosity and the urge to understand has driven mankind ever further in the exploration of the universe, even beyond the possibilities of the naked eye. Researchers are trying to visualize in detail both the large world at ever greater distances from the earth and the microscopic world nearby. In both areas, scientists have surpassed the limitations of visible light in terms of penetrating power and resolution by making use of other radiation probes from the electromagnetic spectrum as well, such as radio waves in astronomy. In microscopy, the smallest features that can be distinguished are determined by the wavelength of the microscope's illumination source. Features smaller than half this wavelength, will be indiscernible. Optical microscopy uses visible light (0.4 - 0.7 μm) and therefore the best achievable resolution will be 0.2 μm. For visualising smaller features, the illumination source should be changed to a probe with a smaller wavelength. An overview of the electromagnetic spectrum is given in figure 5.1. For each type of electromagnetic radiation the corresponding wavelengths and examples of real

world objects of similar size are given.

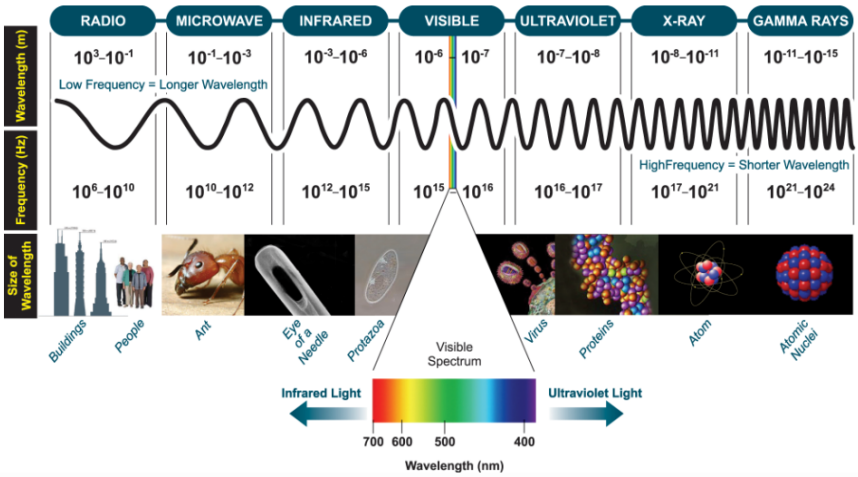

Figure 5.1: The electromagnetic spectrum according to the wavelength and corresponding real world objects of similar sizes [2]

According to the wave-particle duality, each particle can behave as a wave and vice-versa. In particular, electrons can act as waves and as such be used as an alternative radiation probe in microscopy. Using the de Broglie-hypothesis, the wavelength of an electron can be written as follows:

$$\lambda = \frac{h}{p} = \frac{h}{mv} = \frac{h}{m_0 v}\sqrt{1 - \frac{v^2}{c^2}}, \tag{5.1}$$

with h Planck's constant, p the momentum of the electron, m the relativistic mass of the electron, v the velocity of the electron, m_0 the electron's rest mass and c the speed of light. Electrons can be accelerated to velocities approaching the speed of light. In this way, electrons can be created with wavelengths below 0.1 nm allowing for resolutions smaller than one-twentieth of a nanometre for the most powerful electron microscopes, which is down to the atomic and molecular scale of matter.

Traditionally, microscopy has been frequently applied in the field of biology and biomedical sciences. As the knowledge of the anatomy, morphology and physiology of human beings and animals is evolving, research is expanding towards ever smaller structures even below the sub-cellular level. Furthermore, the need for three-dimensional imaging is increasing, especially in the field of functional morphological studies, but also for general histological purposes. Optical and electron microscopy offer an excellent resolution within this context. However,

the disadvantage of these techniques is that the studied tissues must be of a limited thickness since visible light or electrons have to be able to penetrate through them. As a result, when a sample needs to be visualised over its complete volume, there is no choice but to physically slice the whole sample and study each slice individually. Virtually aligning all slices will eventually result in a 3D data set of the sample, but possibly important information on the cutting surfaces may be missing. Moreover, the whole process is extremely time-consuming and the sample is destroyed in the end, which can be a major disadvantage.

Within the field of medical imaging, techniques have been developed which allow to make 3D reconstructions in a non-destructive manner, including X-ray computed tomography (CT) and magnetic resonance imaging (MRI). However, for histological purposes the typical resolution of clinical CT and MRI scanners is inadequate. In the case of both imaging techniques, scanners have been developed intended for the visualisation of smaller objects, for instance small-animal scanners, which achieve a resolution in the order of 10 μm. Other high resolution scanners for non-living applications even go down to a few micrometers and below.

Micro-MRI has proven to be a valuable imaging method in histology [3–6]. A further improvement in tissue contrast can be obtained by making use of MRI contrast agents such as gadopentetic acid (Gd-DTPA), which is a gadolinium-based contrast agent. An additional advantage is that magnetic fields and radio waves are non-ionising radiation and are therefore considered harmless for tissues so that also living organisms can be imaged without inducing biological radiation damage.

Micro-CT systems on the other hand are cheaper than micro-MRI systems, are easier to install in laboratories and have maintenance costs that are significantly lower. As a result, they provide easier access than their MRI counterpart. When studying bone structures and other mineralised tissues, micro-CT has proven to be a valuable imaging method and should be preferred over micro-MRI [7–12]. On the other hand, adequate visualisation of soft tissues is more challenging. Samples containing only soft tissue components can be reasonably well imaged in some cases [13]. However, when strong X-ray attenuating tissue, such as bone, is present as well, it is far more difficult. For these situations, contrast enhancing techniques quickly become indispensable.

This chapter provides a comprehensive introduction to Histology by means of high resolution X-ray Tomography (HiXTom), and especially soft tissue visualisation. First, some general contrast enhancing techniques will be discussed. Then, a study will be presented which explores several chemical substances for their potential to serve as a contrast agent for soft tissue visualisation using micro-CT [1].

In the last section a practical application will be shown, clearly illustrating the potential added value of HiXTom in biomedical studies with a histological focus.

5.1 Contrast enhancing techniques for HiXTom

In X-ray imaging, contrast is obtained when two adjacent types of materials give rise to a sufficiently different X-ray photon attenuation. Tissue drying and the use of tissue contrast agents are two methods to increase this attenuation differential in order to improve soft tissue visualisation.

5.1.1 Tissue drying

Soft tissues usually contain a lot of "cavities" filled with water. As a result, relatively few soft tissue details can be discerned in CT images. This can be easily explained by looking at the atomic composition of soft tissue. Table 5.1 shows the general composition of soft tissue as it was determined in report 44 of the International Commission on Radiation Units and Measurements (ICRU) [14]. The most abundant elements are oxygen and to a lesser extent carbon, hydrogen and nitrogen. The density of soft tissue determined by the ICRU is 1.060 g/cm^3. Carbon, nitrogen and oxygen will result in a very similar X-ray attenuation since their atomic numbers are nearly equal. Therefore, removing the water from the soft tissue "cavities" en replacing it by a gas - thus drying of the sample - will give rise to an overall contrast enhancement.

Table 5.1: Atomic composition of soft tissue (ICRU-44) (data extracted from: [15])

Element	*Atomic number (Z)*	*Weight fraction*
H	1	0.102
C	6	0.143
N	7	0.034
O	8	0.708
Na	11	0.002
P	15	0.003
S	16	0.003
Cl	17	0.002
K	19	0.003

When tissues dry in a normal manner, i.e. through evaporation, deformations can arise or certain structures may even collapse. This is caused by the very high

surface tensions arising in small cavities where a fluid/vapour interface is present. As the tissue dries, this fluid/vapour interface gradually moves through the sample and cavities may collapse, resulting in structural damage of the sample. Two drying techniques have been developed with which these unwanted effects are greatly limited or can even be avoided altogether: *freeze drying* and *critical-point drying*.

Freeze drying

Freeze drying or lyophilisation is a three stage process [16]. First, the sample is frozen (usually between -50 °C and -80 °C). Subsequently, the pressure is reduced during the primary drying process and sufficient heat is gradually supplied to make sure the water in the sample can sublimate. About 98% of the water present will eventually be sublimated. The process must be carried out slowly, since the administration of an excessive amount of heat can lead to unwanted structural changes in the material. The third stage comprises a secondary drying process to ensure that all water molecules that have been adsorbed by the material during the previous drying process, are sublimated. This is accomplished by increasing the temperature even further to break all physical and chemical interactions that have formed between the water molecules and the frozen material. The pressure is again reduced to promote sublimation.

Using this method of drying, there is an immediate transition from the solid to the vapour state. As a result the high surface tensions at fluid/vapour interfaces can be avoided. However, this method is not optimal since freezing of the sample will still lead to some structural changes.

Critical-point drying

Critical-point drying makes it possible to bypass the fluid/vapour interface in a very elegant way during the drying process [16]. Each pure substance has a critical point to which a critical temperature T_C is associated. Once above this critical temperature, the substance is always gaseous and cannot be condensed by an increase in pressure. The transition from fluid to gas at this critical point occurs without fluid/vapour interface an thus in absence of surface tension. This is clarified in figure 5.2 which represents the phase diagram of CO_2. In critical-point drying, the liquid present in a tissue is brought from below the critical point (point A) to a temperature and pressure above the critical point (point B). As a result, the liquid in the tissue will be automatically converted to gas and the sample is thus dried in the absence of surface tension.

The critical point of water lies at a temperature of 374 °C which is very high. Warming of tissues above this temperature would inevitably lead to thermal dam-

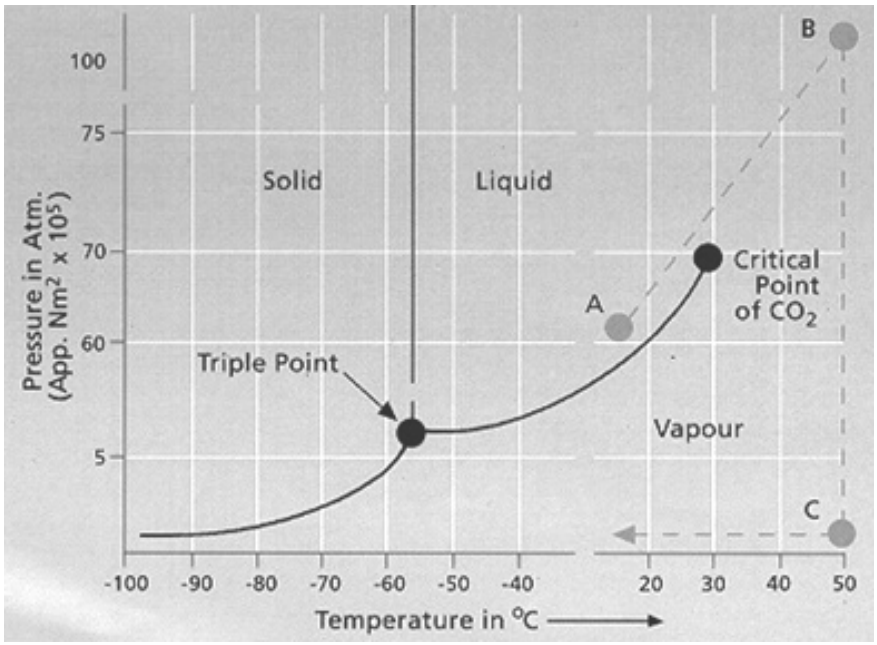

Figure 5.2: Phase diagram of CO_2 [17]

age. On the other hand, the critical temperature of CO_2 lies considerably lower at 31.1 °C which is perfect for the drying process. However, liquid CO_2 is not miscible with water. Therefore, all water inside the tissue has to be replaced first with another liquid which is miscible with CO_2. For this intermediate fluid usually acetone is used. In summary, first all water is replaced by acetone and subsequently the acetone is replaced by CO_2 prior to the actual critical-point drying process [17].

Figure 5.3 shows a CT slice of a micro-CT scan of a chicken embryo performed at UGCT using the Nanowood scanner (tube voltage 70 kV, tube current 115 μA and exposure time 200 ms). The chicken embryo is approximately six days old and has been critical-point dried. This image clearly illustrates that by merely drying a sample good contrast can be achieved. Several other authors have reported good results using critical-point drying as well [18, 19].

5.1.2 Tissue contrast agents

As shown in the previous subsection, tissue drying, especially critical-point drying can yield very good results in terms of contrast enhancement. However, the drying techniques are quite labour-intensive and require special devices for temperature and pressure control. It is often far more straightforward to make use of contrast

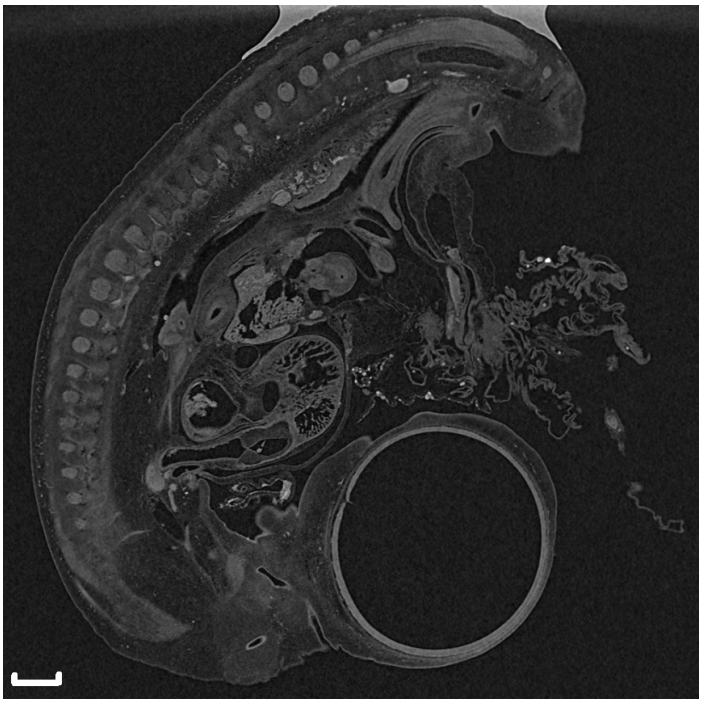

Figure 5.3: CT slice of a chicken embryo after critical-point drying [16]. Scale bar = 0.5 mm.

agents instead [20, 21]. A study of de Crespigny *et al.* [22] compared imaging of postmortem rabbit brains using micro-MRI and micro-CT. All rabbit brains were treated with a contrast agent: those in the MRI group with Gd-DTPA and those in the CT group with an iodinated contrast agent. The authors concluded that both imaging techniques are comparable in terms of spatial resolution and contrast when using an adequate contrast agent.

For optical and electron microscopy a comprehensive knowledge of optimal tissue preparation techniques, contrast enhancing substances and staining procedures has been acquired. X-ray imaging on the other hand, has been introduced more recently in the field of histology. As a result, literature is rather limited and mainly focused on well-defined applications or specific research domains such as embryology [23, 24]. Furthermore, the number of used X-ray contrast agents for histological purposes so far is also quite limited. In section 5.2, an exploratory study will be presented in which 28 chemical substances have been investigated for their potential to serve as a contrast agent for soft tissue visualisation using micro-CT [1].

5.1.3 High quality micro-CT scans

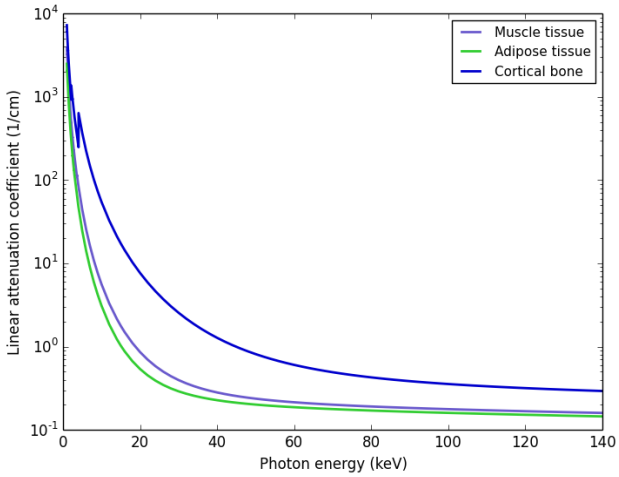

Figure 5.4: Linear attenuation coefficient of muscle, adipose tissue and cortical bone

Figure 5.4 shows the linear attenuation coefficient of two soft tissue types - muscle and adipose tissue - and cortical bone. From this graph it is clear that the largest differences in X-ray attenuation and thus the highest soft tissue contrast can be achieved in the lower energy range, using a tube voltage of about 40 kV. This is a valid option for relatively small samples containing only materials that cause limited X-ray attenuation. If for instance calcified structures such as bone are present as well, these materials will give rise to beam hardening artefacts. To reduce these artefacts, higher tube voltages in combination with adequate beam filtration are required. As a result, the average energy of the X-ray spectrum shifts towards higher energies and soft tissue contrast decreases. On the other hand, due to its polychromaticity, a high energy spectrum still contains a large fraction of lower energy photons. This is illustrated in figure 5.5 which shows the detected energy as a function of incident photon energy for an X-ray spectrum generated at a tube voltage of 110 kV, with and without 1 mm aluminium beam filtration. As such, information from the lower energy range is contained in the images as well. Therefore, a higher signal-to-noise ratio will lead to an increasing soft tissue contrast.

An example of such a high quality scan is shown in figure 5.6. A mouse hind leg was scanned at Hector with a tube voltage of 110 kV and a beam filtration of 1 mm Al (see Fig. 5.5). To obtain a high signal-to-noise ratio the tube power was set at 13 W and 4000 projections were recorded with an exposure time of 2 s per

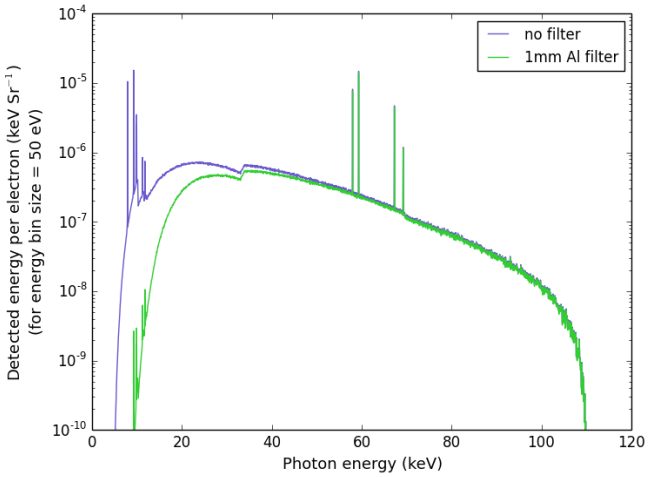

Figure 5.5: Detected energy as a function of incident photon energy for an X-ray spectrum generated at 110 kV, with and without 1 mm Al beam filtration

(a) (b)

Figure 5.6: Micro-CT sections of a high quality scan of a mouse hind leg

projection. The CT images illustrate that a reasonably good soft tissue contrast can be achieved in this way, although some beam hardening artefacts are still present.

On the other hand, high quality scans are time consuming and as such not always practically feasible, especially when a large series of scans have to be performed.

5.2 Contrast agents for soft tissue visualisation using micro-CT

As mentioned above, contrast is achieved if two adjacent types of tissue result in a sufficiently different X-ray photon attenuation. Therefore, to give rise to a clear difference in attenuation between stained and non-stained tissue, suitable X-ray contrast agents should consist of molecules containing atoms with a high atomic number. Since this condition is also valid for electron microscopy, most known X-ray contrast agents originate from electron microscopy applications. Furthermore, it is also essential that the various types of soft tissue exhibit a different binding affinity for the contrast agent in order to create a clear gradient in attenuation. Several parameters such as pH and concentration of the contrast solution and the solvent itself will affect the binding affinity. Pretreatment or fixation of the sample can also change the binding affinity. If the binding affinity of a certain type of tissue is very high for a particular contrast agent/solution compared to the other tissues present in the sample, this tissue type will be selectively stained. This can be a very interesting and useful property. A classical example from electron microscopy is osmium tetroxide. Osmium tetroxide preferentially binds to lipid-rich structures, such as cell membranes and nerve tissue.

Apart from atomic number and binding affinity, another important characteristic of a contrast agent is the degree to which it can penetrate a sample. Contrary to light or electron microscopy, micro-CT visualises samples as a whole. Many contrast agents have a limited penetration depth, which is generally sufficient for fine slices but often inadequate for larger volume tissue samples. Therefore, not only the present tissue types, but also the dimensions of the sample itself will impose restrictions on the suitable contrast agents. Osmium tetroxide for instance exhibits a slow penetration that may even be limited and is therefore not suitable for samples larger than mid-gestation mouse embryos [25].

In this section, several chemical substances will be investigated in order to identify useful X-ray contrast agents for soft tissue visualisation, suited for samples larger than (1 cm)^3. Furthermore, the products have to be relatively safe and staining of the samples must be straightforward without the need for a highly equipped chemical laboratory.

5.2.1 Selection and preparation of the contrast solutions

First of all, various chemical substances that are potential candidate X-ray contrast agents were listed. It was decided to only use aqueous contrast solutions. Therefore, each selected substance has to be soluble in water. Several contrast agents were added to the list based on scientific literature, for instance phosphotungstic acid (PTA) [26], phosphomolybdic acid (PMA) [27, 28], silver nitrate ($AgNO_3$) [29, 30], lead citrate [31] and potassium iodide (KI) [32–34]. It should be noted that in the last three cited papers actually I_2KI, also known as Lugol's solution, is used. This is a mixture of both KI and iodine (I_2) dissolved in water. For practical reasons and since I_2 is almost insoluble in water, only KI was added to the list, although the aforecited references demonstrated the usefulness of Lugol's solution as a contrast agent for micro-CT.

The classical electron microscopy staining agent, osmium tetroxide (OsO_4) has also proven to be a valuable contrast agent for micro-CT [26, 31, 35]. For this study however, it was not selected since the product combines a high toxicity with a volatile character, making it hazardous to work with and expensive to dispose of. A well-equipped laboratory is needed and particular safety measures have to be taken to handle this substance. Other disadvantages include its slow, possibly limited, penetration rate and the fact that staining of tissues preserved in alcohol is suboptimal [26].

The list was further supplemented with other potential candidates selected from electron and even light microscopy [36–42]. In total 28 chemical substances were chosen.

As mentioned above, only water was used as solvent. This is not just a simple and practical choice, but it also ensures comparability between the results. Each chemical substance was dissolved at room temperature in 20.0 mL distilled and de-ionised water until saturation was reached. The amount was limited to 10 g for those chemicals with a very high solubility. In table 5.2 all substances are listed with exact concentration and molarity of the resulting contrast solutions. Several of these solutions probably have a concentration which is too high to achieve an optimal staining result, in particular those with a very high atomic number. However, in this heavily concentrated form, a significant change in X-ray attenuation is most likely to be obtained. If the first experiments with these solutions show that precipitation occurs in the sample or if the CT images contain too many artefacts due to excessive attenuation, the solutions can be further diluted.

*Table 5.2: The list of the 28 selected chemical substances and the reference (distilled and de-ionised water) with the highest atomic number (Z) of the elements present in each chemical. Furthermore, the concentration - **(S)** indicates whether saturation was reached - and the molarity of the contrast solutions are shown. The contrast numbers for Bacon (C_B) after 24 h staining and after subsequent water immersion ($C_{B,water}$) are also given. The seventh column indicates whether the chemicals remained fixed in the tissue. The last column denotes the 12 substances used for experiment 2 [1]*

Chemical	*Z*	*Amount (g) dissolved in 20 mL water*	*Molarity(mol/L)*	C_B	$C_{B,water}$	*Fixed?*	*Exp.2*
Reference	8	-		0.03	0.03	-	
$VOSO_4$	23	10	3.07	0.08	0.04	No	
$KMnO_4$	25	2 **(S)**	0.63	0.00	0.00	-	
$FeCl_3$	26	10	3.08	0.07 (0.29)[1]	0.05	No	*
$FeSO_4$	26	7 **(S)**	2.30	0.08	0.04	No	
$CuSO_4$	29	10 **(S)**	3.13	0.15	0.07	No	
$Cu(NO_3)_2$	29	10	2.67	0.17	0.04	No	
$ZnCl_2$	30	10	3.67	0.23	0.09	No	*
$ZnSO_4$	30	6 **(S)**	1.86	0.11	0.04	No	
KBr	35	10	4.20	0.36	0.09	No	
PMA	42	10 **(S)**	0.27	0.44	0.41	Yes	*
Na_2MoO_4	42	10	2.43	0.34	0.05	No	
$(NH_4)_2MoO_4$	42	1 **(S)**	0.26	0.16	0.13	Yes	*
$AgNO_3$	47	10	2.94	0.44	0.18	No	
KI	53	10	3.01	0.51	0.22	No	*
KIO_3	53	3 **(S)**	0.70	0.16	0.06	No	
Cs_2CO_3	55	10	1.53	0.44	0.16	No	
CsCl	55	10	2.97	0.46	0.14	No	
$CsNO_3$	55	5 **(S)**	1.28	0.24	0.08	No	
$BaCl_2$	56	10 **(S)**	2.40	0.41	0.09	No	*
$Ba(ClO_3)_2$	56	8 **(S)**	1.31	0.39	0.14	No	*
$Ba(NO_3)_2$	56	4 **(S)**	0.77	0.23	0.06	No	
$La(NO_3)_3$	57	10	1.54	0.37	0.16	No	
PTA	74	10	0.17	0.57	0.54	Yes	*
Na_2WO_4	74	10	1.70	0.34 (0.44)[1]	0.05	No	*
$HgCl_2$	80	3 **(S)**	0.55	0.27	0.28	Yes	*
$Pb(NO_3)_2$	82	10 **(S)**	1.51	0.46	0.24	No	*
Pbacetate	82	10 **(S)**	1.54	0.40	0.25	No	*
Pbcitrate	82	$<$1 **(S)**	0.05	0.03	0.03	-	

[1] C_B number calculated with the grey value of connective tissue instead of muscle tissue

5.2.2 Sample preparation

Two experiments were performed. The first was designed to serve as a straightforward screening of all the chemicals to be able to discard all substances without potential for X-ray contrast agent. To this purpose, strips of green Bacon (cured with salt) of about 2.5 $\times$ 0.5 $\times$ 0.5 cm were used, since these samples are readily available and contain two types of tissue: adipose and muscle tissue. The Bacon strips were immersed in the contrast solutions for approximately 24 hours. After they were removed from the liquid, they were scanned in two groups using exactly the same scanning parameters. Both groups were scanned with the same unstained Bacon strip, which served as a reference tissue. Immediately following the scan, the strips were immersed in water for 4 days. They were scanned again afterwards. This gives a first idea whether the contrast agents remain fixed in the tissue or dissolve again in the water and by extension in other hydrophilic solutions. This can be an important characteristic of a contrast agent, especially when staining samples that have to be preserved in liquid.

From the first experiment, 12 solutions were selected which showed some potential to serve as an X-ray contrast agent (last column in table 5.2). The other chemicals were discarded. For the second experiment, postmortem mice hind legs were chosen since they are composed of various tissue types such as muscle, fat, tendons, cartilage and bone. The mice cadavers were provided by the Department of Morphology, Faculty of Veterinary Medicine, and were obtained from the end-stage of other experiments. The research focus in these experiments was not related to musculoskeletal disorders and thus the mice may be regarded as normal. Prior to immersion in the contrast solutions, the skin was removed from the legs except for the paws. Skin is for many substances practically impermeable and as such forms an important barrier for the penetration of the solutions. The paws were cut off the legs just proximal of the ankle joint. Since the paws are not flayed and only the cutting edge is free from skin, they can be used to get an idea of the penetration depth and rate of each solution. Similar to the first experiment, the samples - both legs and paws - were immersed for 24 hours in the 12 remaining contrast solutions. After 24 hours, they were taken out of the fluid and scanned. Immediately after the scan they were re-immersed in their solution for another 7 days and subsequently scanned a second time using the same scanning parameters.

Finally, a few mice hind legs were stained using the best contrast agents according to the second experiment. High resolution CT scans were performed and for comparison also an unstained mice hind leg was scanned under the same scanning conditions.

5.2.3 CT scans: acquisition and interpretation

All micro-CT scans in this study were performed on the first high resolution CT scanner at UGCT [43], before it was re-designed. The FeinFocus FXE 160.51 transmission type X-ray tube with tungsten target in combination with the Perkin-Elmer flat-panel detector were chosen. The X-ray tube was operated at the relatively high voltage of 120 kV, because of two reasons. First, for most scans several samples were scanned at the same time resulting in a fairly large scanning volume of a few cubic centimetres. Second, the presence of staining materials and bone in the mice hind legs will give rise to a relatively high attenuation of X-rays. Therefore, to ensure adequate beam transmission for all scans a high tube voltage was necessary. Furthermore, since both the bone tissue and the staining materials can introduce beam hardening artefacts, appropriate aluminium beam filtration was used for each scan to keep this to a minimum. It should be mentioned that the visualisation of pure and nonstained soft tissue CT scans should be performed at lower tube voltages for optimal results. Therefore, reference tissues and weakly stained samples have not been scanned under ideal scanning conditions in this study. This should however not significantly alter the final conclusions since the contrast enhancement resulting from the use of contrast agents is larger than what would be achieved by fine tuning scanning parameters.

The parameters for each scan are summarised in table 5.3. Note that the mice hind legs and paws were scanned in one volume.

Table 5.3: Scanning parameters for each scan performed in the context of this study.

Sample	*Tube voltage (kV)*	*Exposure time per proj. (ms)*	*Number of projections*	*Voxel size (μm)*	*Filtration (mm Al)*
Bacon strips	120	1000	1800	38	0.15
Bacon strips post[1]	120	1000	1500	40	0.15
Mice legs (24 h[2])	120	2000	1800	40	3.0
Mice legs (1 week[2])	120	2000	1800	42	3.0
High resolution scans	120	1500	1200	23	1.0

[1] Bacon strips after immersion in water for 4 days.
[2] Total staining duration

In order to compare the various contrast agents in a kind of quantitative manner, a measure for the CT image contrast was introduced, called the contrast number C. This quantity represents the relative contrast difference between two material/tissue types present in a sample. The contrast number is defined as follows:

$$C = \frac{G_{T1} - G_{T2}}{G_{T1}}, \tag{5.2}$$

with G_{T1} and G_{T2} the mean grey values of the first and the second tissue type respectively.

In this study, the contrast number is mainly an interesting parameter for the evaluation of the Bacon samples. These samples only contain two distinct tissue types, muscle and adipose tissue, which must be clearly distinguished from each other. The contrast number for Bacon C_B can be written as follows:

$$C_B = \frac{G_M - G_{AT}}{G_M}, \tag{5.3}$$

with G_M representing the mean grey value of muscle and G_{AT} the mean grey value of adipose tissue. These values were measured using the Octopus Viewer [44]. For each tissue type, the largest possible region of interest (ROI) was selected in the CT images. Subsequently, the grey values of all included pixels were averaged. The uncertainty on the calculated C_B values σ_C was determined using standard error propagation:

$$\sigma_C = \frac{1}{G_M}\sqrt{\frac{G_{AT}^2}{G_M^2}\sigma_{G_M}^2 + \sigma_{G_{AT}}^2}, \tag{5.4}$$

This resulted in an absolute uncertainty of about 0.02.

In order to select the correct ROI, adipose tissue was identified in the CT images based on its smaller grey value compared to the surrounding muscle tissue. This has proven to be a reliable method for determining intramuscular fat distribution in meat [45]. As such, a simple thresholding operation allows for the separate visualisation of adipose and muscle tissue.

A second quantitative measurement was carried out on the CT images of the mice paws to evaluate the penetrating power of the different contrast solutions. The paws were rendered in 3D using VGStudio MAX [46]. The penetration depth was then obtained by measuring the distance each contrast agent actually penetrated in the paw, starting from the point where the skin is still attached. For this purpose the measuring tool in VGStudio was used. The uncertainty on the obtained penetration depth values is about 0.2 mm, which is calculated using standard error calculation.

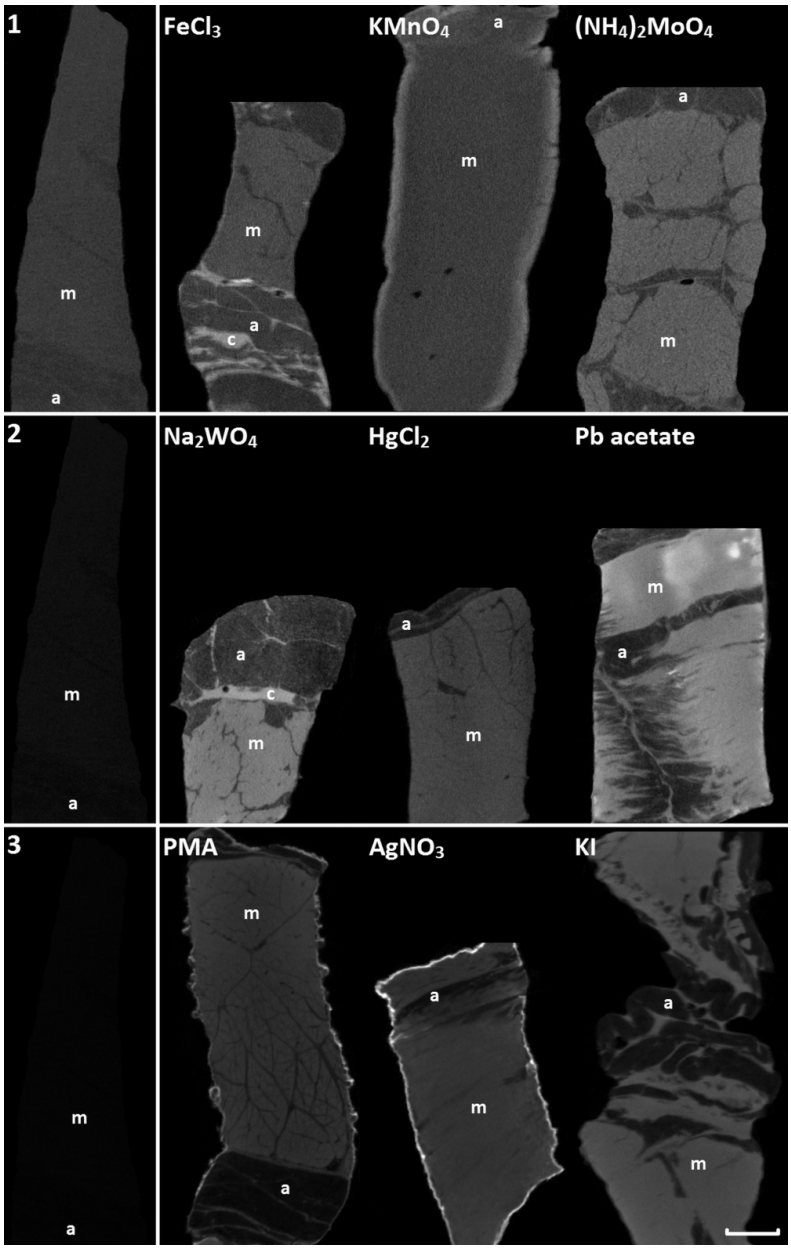

Figure 5.7: CT sections through some of the stained Bacon strips visualised according to a most suitable grey scale range together with the unstained reference. The three rows represent the three sets of fixed grey scale ranges (1-3) with the reference sample in the first column. The contrast agents are indicated on the figure. (a), (m) and (c) are adipose, muscle and connective tissue respectively. Scale bar = 2.5 mm [1].

5.2.4 Results and discussion

Experiment 1: Bacon strips

Figure 5.7 shows a selection of several of the stained Bacon strips together with the unstained reference sample as comparison. Since some samples are heavily stained resulting in a high maximum grey value in the CT image, while others are rather weakly stained and thus give rise to lower maximum grey values, the grey scale range can vary strongly for each Bacon strip. For a correct comparison of the absolute contrast enhancement however, each sample needs to be visualised according to a uniform grey scale range. As a result, the reference tissue and the weakly stained Bacon strips will become invisible. To avoid this, three standard sets of fixed grey scale ranges were chosen (the three rows in figure 5.7), encompassing low (Fig. 5.7(1)), moderate (Fig. 5.7(2)) and high grey values (Fig. 5.7(3)). As such, each sample can be visualised according to the most suitable range. In the left column of figure 5.7, the reference material is shown for each grey scale range. As expected, it becomes already nearly invisible in the second and third row.

Looking at the CT images, it is immediately clear that most contrast agents give rise to contrast enhancement as compared to the unstained reference tissue. The two exceptions are potassium permanganate ($KMnO_4$) and lead citrate. As can be seen in figure 5.7(1), only the edges of the sample stained with $KMnoO_4$ exhibit an increased X-ray attenuation suggesting that the contrast solution did not penetrate further than a distance of 1 mm into the sample. This limited penetrability is a likely explanation for the fact that this substance did not lead to a contrast improvement. The lead citration solution on the other hand has a very low concentration (see table 5.2). This was confirmed by taking a radiograph of two small tubes, the one filled with this solution, the other with water. No significant difference in X-ray attenuation could be observed between these two tubes. Therefore, no contrast enhancement can be expected with the lead citrate solution.

When looking at the distribution of the contrast agent in each sample, it is clear that mainly the muscle tissue is stained while the adipose tissue is only stained to a lesser extent. For most samples, the grey value of the latter is only slightly increased. The fact that these two tissue types are stained in different ways is of course the cause of the contrast enhancement. Since all contrast agents in this study are water-based, and therefore hydrophilic, they are less likely to penetrate the hydrophobic adipose tissue. This is probably the explanation for the selective staining of muscle tissue.

Through a purely visual assessment of the CT images, especially PMA seems to be a very effective contrast agent, but also KI, PTA and lead nitrate show promis-

ing results. To allow for a more objective and at the same time a more or less quantitative evaluation, contrast numbers were introduced in the previous section. For each sample, the contrast number for Bacon C_B (equation 5.3), was determined. The values are listed in the fifth column of table 5.2. The C_B numbers are in fairly good agreement with the visual assessment of the CT images. KI, lead nitrate, PTA and PMA for instance show high C_B values. $KMnO_4$ and lead citrate have numbers close to zero, similar to the reference sample, and as such indicating no contrast enhancement.

Furthermore, there appears to be a trend present with higher C_B values in the lower part of table 5.2. The substances are arranged according to the highest atomic number of all elements contained in each chemical (which is listed in the second column). Since X-ray photon attenuation increases with a higher atomic number, this partly explains the trend present in table 5.2. The main exceptions are mercury(II) chloride $HgCl_2$, barium nitrate ($Ba(NO_3)_2$), cesium nitrate ($CsNO_3$), potassium iodate (KIO_3) and ammonium orthomolybdate ($(NH_4)_2MoO_4$) which all show somewhat lower C_B numbers. However, all these contrast solutions have a lower concentration (as compared to the others) in common.

Finally, some specific comments should also be given:

- The samples stained with PMA and PTA show some precipitation at their surface, which is probably due to the high concentration of these contrast solutions. Simply diluting the solutions should solve this problem. The $AgNO_3$ sample has a strongly stained surface as well, which could also be the result of precipitation.
- In the the iron(III)chloride ($FeCl_3$) sample the connective tissue present inside the adipose tissue is heavier stained than the muscle tissue. This effect is also visible in the sodium tungstate (Na_2WO_4) sample. These results indicate that the connective tissue is selectively stained in these cases, but this should be investigated further. Contrast numbers can also be calculated using the mean grey value of connective tissue instead of muscle. This results in a C_B value of 0.29 (instead of 0.07) for $FeCl_3$ and 0.44 (instead of 0.34) for Na_2WO_4.
- Some contrast solutions, especially PMA, also reveal structures within the muscle tissue.

After the first scan, the Bacon strips were immersed in water for four days and scanned again. A first visual assessment of the CT images immediately indicates that most chemicals diluted in the water. Still, some substances, such as PMA and PTA, remained fixed in the tissue. For this second scan, C_B numbers were

determined as well and are listed in the sixth column of table 5.2. The last but one column indicates which chemicals remain fixed in their sample. No conclusions could be made for the lead citrate sample. The $KMnO_4$ sample showed significantly stained edges even after water immersion, suggesting that the chemical also remains more or less fixed in the tissue. However, its low penetrability makes it only useful for very small samples which are not considered in this paper.

In summary, only four chemicals ($HgCl_2$, PTA, PMA and $(NH_4)_2MoO_4$) remained fixed in the tissue after four days of water immersion. This can be an important characteristic when staining samples which have to be preserved in liquid.

Experiment 2: mice hind legs

For the second experiment 12 contrast agents were selected based on the previous results. Firstly, the four substances that remained fixed in their sample were chosen. Secondly, Na_2WO_4 and $FeCl_3$ were selected to further investigate the possibility of selective staining of certain tissue types such as connective tissue. Finally, the list was further complemented with six contrast solutions based on a visual assessment of the CT images of the Bacon strips. Moreover, these six substances had high C_B values. In the last column of table 5.2 the 12 selected contrast agents are marked.

In figure 5.8 sagittal CT slices of the mice paws after a 24 hour staining period are shown. Note that in this figure a uniform grey scale range is used for all mice paws. As such, the range is a lot broader than in figure 5.7 and some contrast agents, e.g. KI, may appear to stain more heavily in this experiment. This is however merely perception. Most samples are not fully stained and show a clear demarcation line between the stained and unstained tissue. As such, the penetration depth of each contrast agent could be easily measured. All values are listed in the second column of table 5.4. Only KI and Na_2WO_4 were able to completely stain the paws in 24 hours.

Figure 5.9 shows similar sagittal CT slices of the same mice paws after 1 week staining. The penetration depth of each contrast agents was again measured and the values are listed in the third column of table 5.4. By extending the staining period, the penetration depth significantly increased for most contrast agents. $BaCl_2$, $Ba(ClO_3)_2$ and $Pb(NO_3)_2$ now managed to fully penetrate the paws. $FeCl_3$ and $(NH_4)_2MoO_4$ on the other hand appear to have a very slow penetration rate (or their penetration can even be limited).

Figure 5.8: Sagittal CT slices of the mice paws illustrating the penetration depth after 24 hours staining. The contrast agents are indicated on the figure. Scale bar = 2.5 mm [1].

These results indicate that KI and Na_2WO_4 are most useful for larger samples of the order of several tens of cm^3. $Ba(ClO_3)_2$ and $Pb(NO_3)_2$ are also suited, but a longer staining period is necessary for these substances. On the other hand $FeCl_3$ and $(NH_4)_2MoO_4$ can only be efficiently used for smaller samples of a few mm^3 in size. The remaining chemicals, $ZnCl_2$, PMA, PTA, $HgCl_2$ and Pb acetate have relatively slow penetration rates. Therefore sample sizes should be limited to a few cm^3. It is important to note that penetration depth and rate not only depend on the chemical substance itself, but also on the concentration of the contrast solution and the used solvent. Moreover, tissue composition and potential pretreatment of the samples will also constitute a significant influence on these parameters.

Table 5.4: The penetration depth in the mice paws of the contrast agents after 24 h (1) and 1 week (2) staining. The uncertainty on these values is about 0.2 mm. F = fully stained [1].

Contrast agents	*Penetration depth 1 (mm)*	*Penetration depth 2 (mm)*
$FeCl_3$	1.49	2.37
$ZnCl_2$	1.99	4.57
PMA	3.19	7.21
$(NH_4)_2MoO_4$	1.29	2.33
KI	F	F
$BaCl_2$	4.38	F
$Ba(ClO_3)_2$	2.77	F
PTA	2.08	8.88
Na_2WO_4	F	F
$HgCl_2$	4.74	9.61
$Pb(NO_3)_2$	7.24	F
Pb acetate	4.48	8.34

In figure 5.10, the 12 mice hind legs are shown. Since the skin was removed prior to staining, most contrast solutions were able to fully penetrate the samples over a period of approximately 24 hours. Only in the PMA, $(NH_4)_2MoO_4$ and PTA samples there are still some unstained regions present.

As could be expected from the first experiment, each contrast agent enables to clearly differentiate muscle from adipose tissue. The visibility of other soft tissue structures on the other hand varies greatly. For example, different muscle fascicles can be clearly distinguished using PMA, PTA and $HgCl_2$. Also Na_2WO_4 and $(NH_4)_2MoO_4$ allow for this, albeit to a lesser extent, whereas the other contrast agents scarcely reveal any structures inside the muscle tissue. An important remark however is that most used contrast solutions have a high osmolarity as compared to biological tissues. This could induce tissue shrinkage and as such enhance tissue contrast. This process, and the extent to which this takes place should be further investigated for each contrast agent.

In the knee joint, the patellar tendon could be clearly visualised with $HgCl_2$, $(NH_4)_2MoO_4$, $Ba(ClO_3)_2$, Na_2WO_4, lead nitrate and lead acetate, and to a lesser extent with PMA, PTA and $BaCl_2$. The ligaments of the knee joint on the other hand could not be identified in any of the samples. This is however probably due to the limited resolution of the CT images.

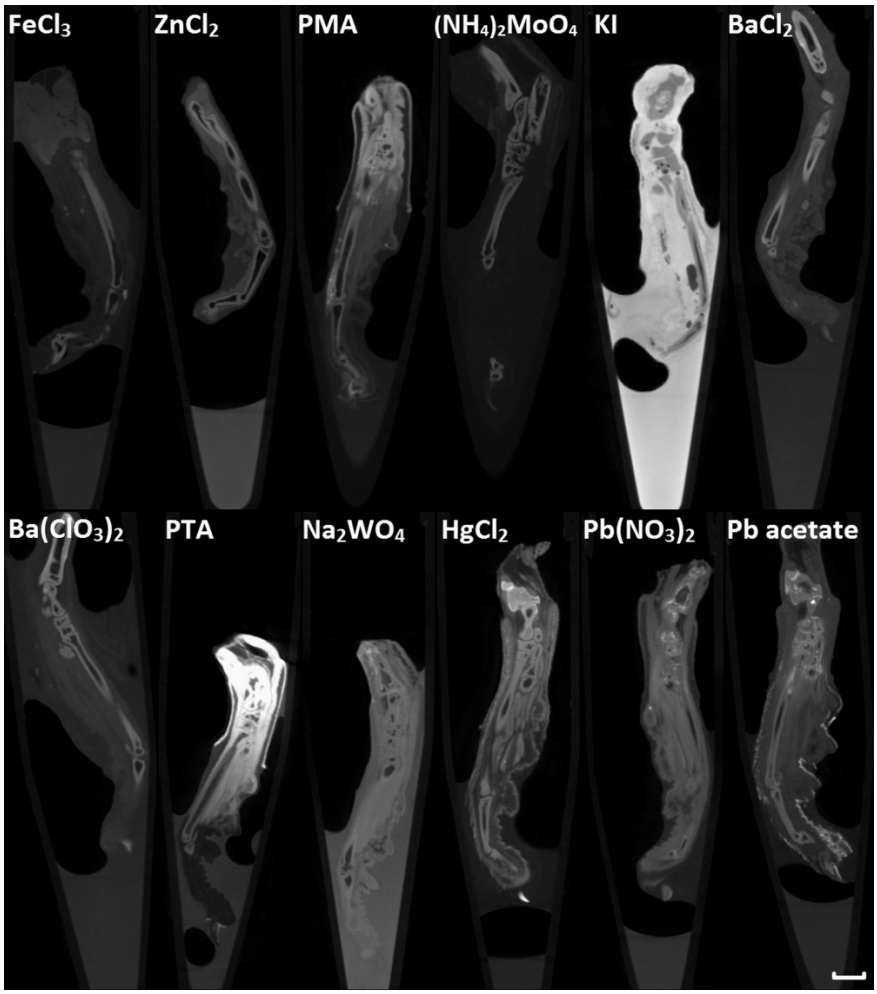

Figure 5.9: Sagittal CT slices of the mice paws illustrating the penetration depth after 1 week staining. The contrast agents are indicated on the figure. Scale bar = 2.5 mm [1].

A more striking observation is that the bone structures in the mice leg stained with $FeCl_3$ seem to be dissolved. $FeCl_3$ hydrolyses in water, eventually leading to the formation of hydrochloric acid, which is a very strong acid. This probably also explains why the knee joint is not properly imaged. As a result, $FeCl_3$ is not a suitable contrast agent when important bone structures are present in the sample. A similar effect has been observed previously at UGCT for PMA and PTA, which are also strong acids, in other experiments with samples containing porous bone structures, for instance an auditory organ (images not shown here). This seemed to be mainly related to the use of highly concentrated contrast solutions. In the

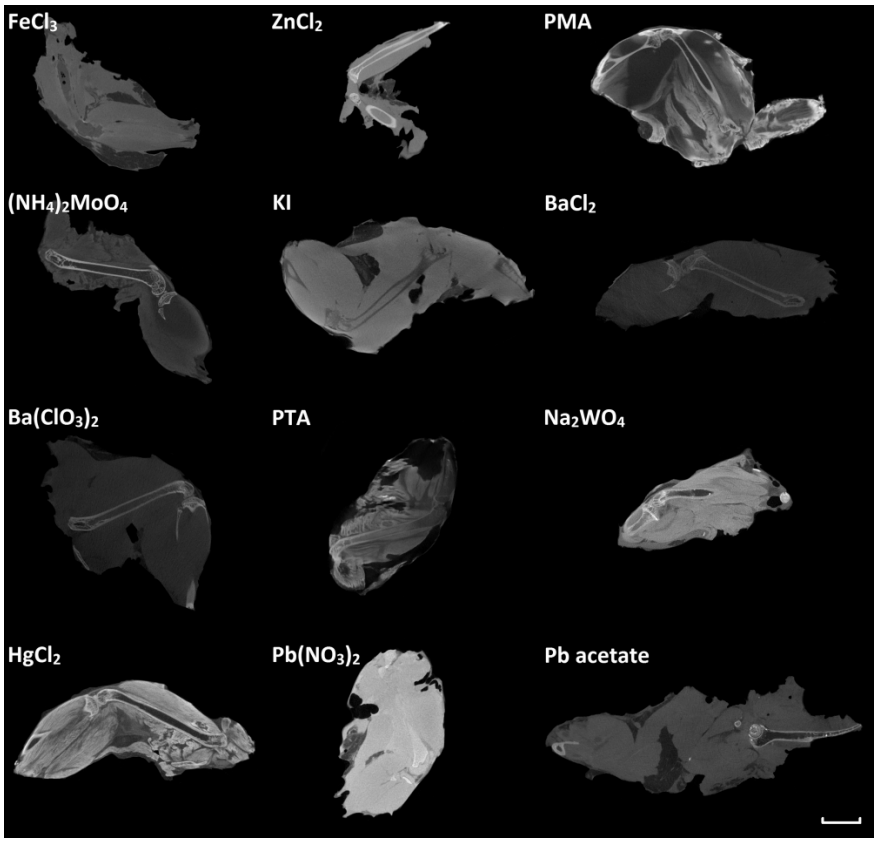

Figure 5.10: CT slices of the mice hind legs stained for a period of 24 h. The contrast agents are indicated on the figure. Scale bar = 5 mm [1].

mice hind legs in this experiment no immediate damage was observed to the bone structures presumably because they are sufficiently solid. Nonetheless, PMA and PTA should be used with caution in the presence of calcified structures.

A final remark for this first scan is that several dense dots are visible within the bone of the lead acetate sample. Since both femur and tibia are cut through at one end, some contrast solution could possibly have infiltrated the bone here and subsequently precipitated.

After the first scan, the mice hind legs were re-immersed in their contrast solution for another six days to a total staining period of 1 week. The results of the second scan (not shown here) are generally quite similar to the results shown in figure 5.10. Most importantly, due to the longer staining duration PMA, $(NH_4)_2MoO_4$ and PTA were now able to fully penetrate the samples which is of course an im-

provement. In the PTA sample, some artefacts are visible, probably caused by the high concentration of the contrast solution. For optimal results it should therefore be somewhat diluted. Another result of the longer staining period is that precipitations in and around the bone structures are now also present in the $BaCl_2$, $Ba(ClO_3)_2$ and lead nitrate sample. Therefore, a limited staining duration in addition to a reduction of the concentration is preferable for these contrast agents. For future research it would be very interesting and highly useful to evaluate the influence of different concentrations of the same contrast agent.

Optimal high resolution scans

The previous experiments demonstrate that several of the tested contrast substances can be efficiently used to enhance soft tissue contrast. The best results were achieved with $HgCl_2$ which allowed to clearly visualise the different muscle fascicles as well as the patellar tendon. The second best results were obtained using PMA and PTA. For these three chemical substances new aqueous contrast solutions were made with a lower, more practical, concentration, i.e. 5%. In each contrast solution a mice hind leg was immersed for 48 hours. Subsequently, each hind leg was scanned seperately at a high resolution. An unstained mice hind leg was scanned for comparison. Figure 5.11 shows CT slices at a similar position of the reference and the $HgCl_2$ sample. Without the use of a contrast agent it is very difficult, if not impossible, to discern different soft tissue structures. The $HgCl_2$ stain on the other hand allows to visualise muscle fascicles, tendons, ligaments, including the cruciate ligaments of the knee joint, and large blood vessels.

Figure 5.12 shows CT slices of the mice hind legs stained with PMA and PTA. Both contrast agents show soft tissue contrast enhancement similar to that achieved with $HgCl_2$. However, the penetration rate of PMA and PTA is lower as is again confirmed in these images since both samples, and especially the somewhat large PTA sample, are not fully stained. An important advantage of these chemicals compared to $HgCl_2$ is that they are less toxic and therefore safer to work with and easier to dispose of.

5.2.5 Conclusions

In this exploratory study, 28 chemicals have been investigated for their potential to serve as an X-ray contrast agent for soft tissue visualisation. All substances were used in the form of aqueous contrast solutions. The assessment of the quality of each contrast agent candidate was based on several parameters such as penetration depth and rate (and thus largest appropriate sample size), fixation of the contrast

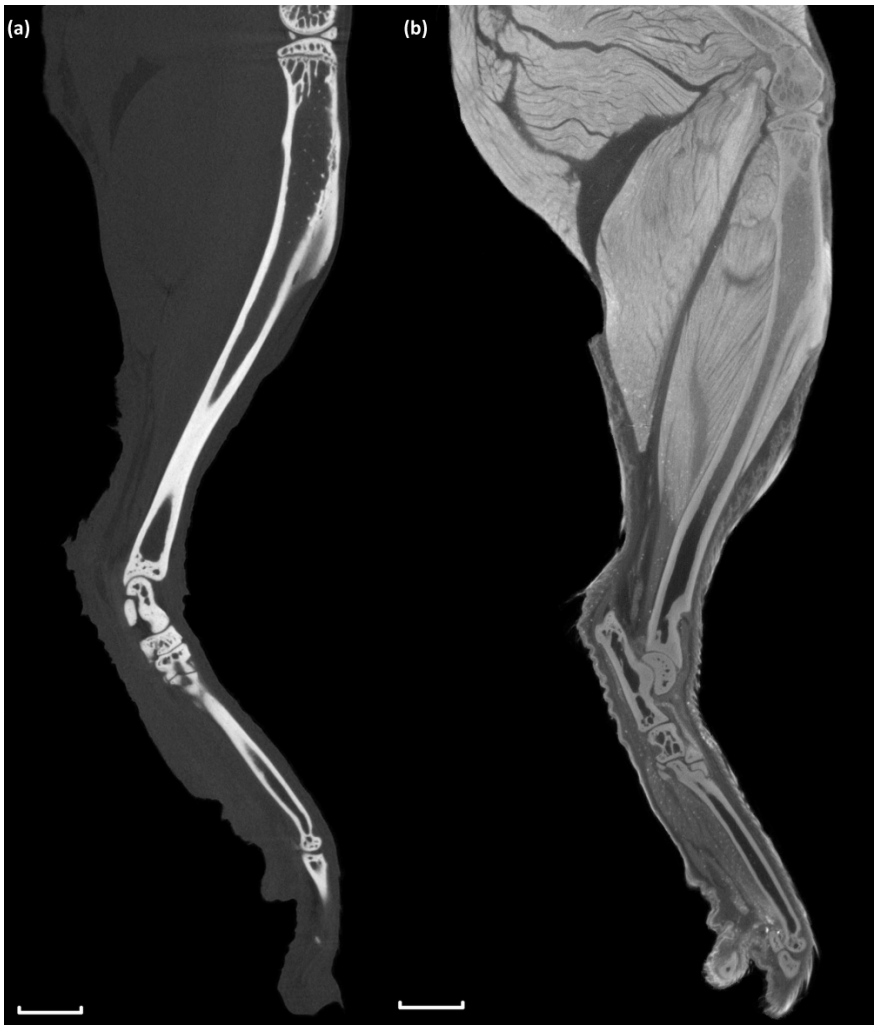

Figure 5.11: CT slices at a similar position of an unstained mice hind leg (a) and a mice hind leg stained with $HgCl_2$ (b). Scale bar = 2 mm [1].

agent in the tissue and actual contrast enhancement.

From the first experiment it was clear that most contrast agents give rise to a clear contrast enhancement between muscle and adipose tissue, except for $KMnO_4$ and lead citrate. For the first, this was mainly due to a low penetrability in the tissue. The latter has a low solubility in water resulting in a very low concentration of the contrast solution and therefore limited to no staining. A general trend was present with a better contrast enhancement for contrast agents containing elements

Figure 5.12: CT slices of a mice hind leg stained with PMA (a) and PTA (b). Scale bar = 2 mm.

with high atomic numbers. Finally, it was also demonstrated that $HgCl_2$, PTA, PMA and $(NH_4)_2MoO_4$ remain fixed in the tissue. This can be a very useful characteristic for samples which have to be preserved in liquid.

In the second experiment, penetration depth and rate were investigated showing that KI and Na_2WO_4 can be most efficiently used for large samples of the order of several tens of cm^3. Taking into account a longer staining period, $BaCl_2$, $Ba(ClO_3)_2$ and $Pb(NO_3)_2$ can also be suitable for larger samples. $ZnCl_2$, PMA,

PTA, $HgCl_2$ and Pb acetate have slower penetration rates. Therefore, samples should be limited to a few cm^3 in size and/or a longer staining duration is necessary. Penetration rates were lowest for $FeCl_3$ and $(NH_4)_2MoO_4$

The second experiment further allowed to assess the ability to discern different soft tissue structures for each contrast agent. Different muscle fascicles could be visualised using PMA, PTA and $HgCl_2$ and to a lesser extent Na_2WO_4 and $(NH_4)_2MoO_4$. The patellar tendon could be distinguished with $(NH_4)_2MoO_4$, PMA, $BaCl_2$, $Ba(ClO_3)_2$, $HgCl_2$, Na_2WO_4, PTA, lead nitrate and acetate. Note that the resolution of the scans was too low to visualise other anatomical structures.

For the type of samples used in this study, the best results were obtained with $HgCl_2$ and secondly with PMA and PTA. Other contrast agents can be preferred depending on the application and other parameters such as sample size and type.

To conclude, a 3D rendering of the high resolution scan of the mice hind leg stained with $HgCl_2$ is shown in figure 5.13.

5.2.6 Recent publications

As a final remark, it should be mentioned that after the publication of this research paper several other authors have investigated different aspects of soft tissue staining. Buytaert *et al.* [47] for instance studied volume shrinkage of different tissue types due to staining with PTA, iodine with potassium iodide (I2KI) and iodine in absolute ethanol (I2E). For muscle tissue they observed 10% shrinkage with PTA, 42% with I2KI and 56% with I2E. In brain tissue a volume shrinkage of 27%, 39% and 66% was reported using PTA, I2KI and I2E, respectively. The authors concluded that PTA applied in an aqueous solution appeared to be the best performing stain in terms of minimal tissue shrinkage.

Descamps *et al.* [48] investigated the contrasting potential of OsO_4, PTA and PMA for soft tissue discrimination. Good results were achieved with PTA and especially PMA, proving that they are a suitable and less toxic alternative to OsO_4. Organs and tissues that were particularly well stained included lungs, liver, blood, cell-dense brain regions and epithelial structures. A similar analysis of the contrasting potential of I2KI by Gignac and Kley [49] showed excellent results as well.

Another study demonstrated the usefulness of PTA for staining articular cartilage. Sufficient contrast enhancement was even achieved to allow for automatic

Figure 5.13: 3D rendering of a mice hind leg stained with $HgCl_2$. The upper part was virtually sliced to view the internal structure. Scale bar = 2 mm [1].

segmentation and analysis [50].

Nierenberger *et al.* [51] studied the imaging of the collagenous network of vascular tissues using I2KI, PTA and PMA. They concluded that PTA and PMA provided the best contrast results. These three contrast agents were also evaluated by Balint *et al.* [52] for their potential to stain ligaments and tendons. Both contrast enhancement as a function of time and tissue deformation were assessed. The fastest penetration rates were observed using I2KI. Tissue shrinkage occurred mainly in the first day of staining and was greatest for PTA, followed by PMA and eventually I2KI. Note that this observation is different from [47]. However, 3D deformation of the tissue was most pronounced in tendons stained with I2KI.

5.3 Biomedical application of HiXTom

In this section the results of an *in vitro* micro-CT study investigating the influence of biomechanical stress on bone formation in arthritis mouse models will be briefly discussed to illustrate the added value of HiXTom. This study is fully presented in a thesis for master of medicine in medicine [53].

5.3.1 Introduction: Spodyloarthritides

Spondyloarthritides (SpA) are a group of chronic inflammatory disorders, including ankylosing spondylitis, reactive arthritis, arthritis/spondylitis associated with inflammatory bowel disease (IBD), psoriatic arthritis and undifferentiated SpA. These diseases are characterised by (asymmetrical) peripheral arthritis and axial inflammation. In addition, often extra-articular manifestations are present, such as uveitis, IBD and psoriasis. Within the European Caucasian population, the prevalence of SpA is estimated between 0.5% and 1.9% [54, 55]. An important hallmark of SpA is enthesitis, which is an inflammation of the insertion of ligaments and tendons to the bone. Another key feature of SpA is new bone formation eventually evolving into ankylosis or into enthesophytes. This new bone formation usually occurs in close relationship with entheses [12]. Entheses are subject to repetitive biomechanical stress caused by the normal forces exerted by muscles, ligaments and tendons. In response to such stress, entheses and nearby areas of the articular capsule, tendons and ligaments can increase in mass. Also the adjacent bone may respond to biomechanical stress by means of bone formation [56–58]. Currently, the relationship between inflammation (enthesitis), new bone formation and biomechanical stress has not yet been elucidated [12].

There are several existing mouse models to study the pathophysiology of arthritis. For SpA, the *Collagen Antibody-Induced Arthritis* (CAIA) mouse model is

very suitable since this model not only gives rise to a destructive polyarthritis, but also to repair phenomena leading to osteophyte formation (i.e. new bone formation) [12, 59].

The purpose of the study briefly presented here, is to examine the role of biomechanical stress on new bone formation in the CAIA mouse model by means of high resolution X-ray tomography.

5.3.2 Experimental design

CAIA was induced in a group of 20 DBA/1 mice using the ArthritoMab™Antibody Cocktail from MD Biosciences. Approximately 7 days after immunisation, the mice develop an enthesitis which progressively evolves into a destructive arthritis [60]. New bone formation only occurs as a result of repair phenomena after resolution of the inflammation. Clinical signs for arthritis were assessed on a regular basis by two independent persons who assigned a clinical score per paw, ranging from 0 to 3 (i.e. 0 = no swelling; 1 = minimal swelling of the ankle or wrist; 2 = swollen carpus/tarsus; 3 = swelling of the complete paw). The total clinical score then equals the sum of the clinical scores of the four paws.

To investigate the influence of biomechanical stress, a hind limb unloading model was applied [61]. In this model, the mice are suspended by their tails in order to lift their hind legs from the ground by means of an unloading device which allows free movement throughout the cage. Ten days after immunisation half of the mice were tail suspended (TS) to avoid the exertion of mechanical forces on their hind legs for a total period of 28 days, while the control group was kept under normal conditions. Randomisation of the TS group and non-tail suspended (NTS) group was done using the total clinical score. Figure 5.14 shows an overview of the timing protocol with an example of the evolution of clinical arthritis as a function of time.

After termination of the clinical phase of the experiment, the mice were sacrificed and the mice legs were preserved in 4% formaldehyde. Note that the mice were bred, housed and sacrificed according to the Ethical Committee of Animal Welfare. Micro-CT scans of the mice hind legs were performed to study the new bone formation. For practical reasons, the scans were split into two sets. For the first set, the first high resolution CT scanner at UGCT was used [43] with the FXE 160.51 transmission tube head in combination with the Varian flat-panel detector. The X-ray tube was operated at 120 kV and a beam filtration of 1 mm aluminium was applied. The number of projections was 1800 with an exposure time of 1 s per projection. The resulting voxel size ranged from 6.5 to 10.0 μm. The second set

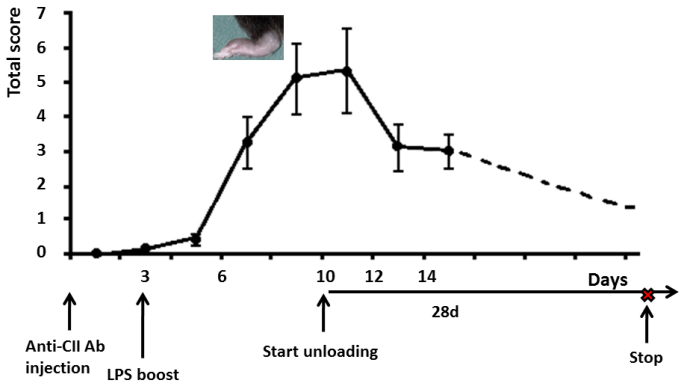

Figure 5.14: Timing protocol and example of the evolution of clinical arthritis as a function of time

of scans was performed at Hector [62] with the X-ray tube operated at 130 kV and a beam filtration of 1 mm aluminium. 2400 projections were taken, each with an exposure time of 1 s. The resulting voxel size was 5 μm.

Figure 5.15 shows the top view of a 3D rendering of one of the hind legs illustrating the basic skeletal anatomy of a mouse paw.

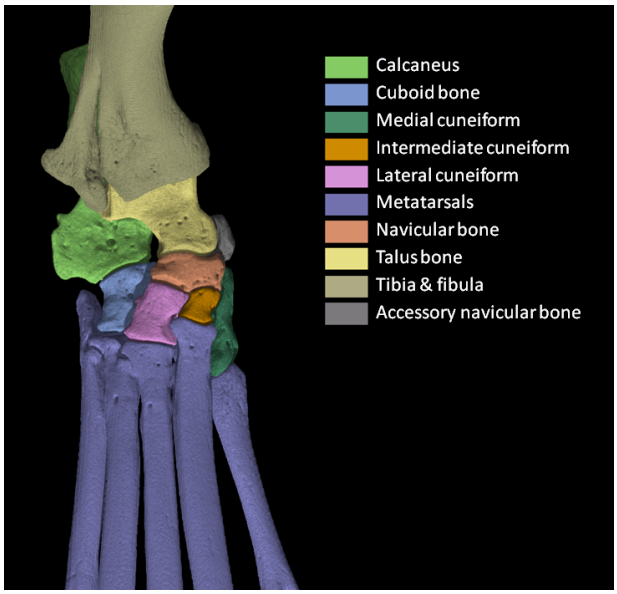

Figure 5.15: Top view of a 3D rendering of one of the hind legs illustrating the basic skeletal anatomy.

5.3.3 New bone formation assessed with micro-CT

As illustrated in figure 5.16 new bone formation can be clearly visualised by means of high resolution X-ray tomography.

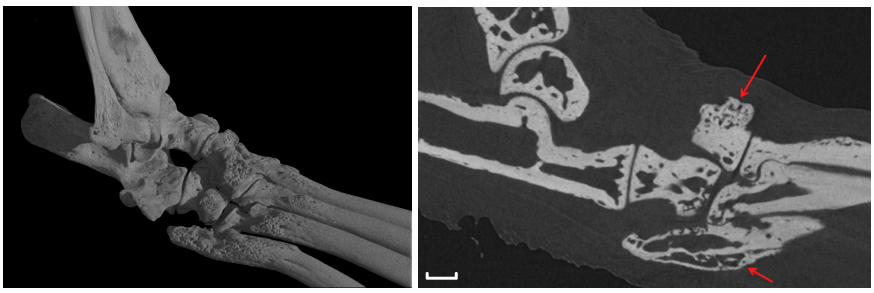

(a) (b)

Figure 5.16: (a) 3D rendering of a paw with clear bone erosion and new bone formation. (b) Sagittal section through the same paw with visible osteophytes at the fifth metatarsal and lateral cuneiform (see arrows). Scale bar = 0.5 mm.

The micro-CT images were analysed using VGStudio MAX [46]. Similarly to the clinical score, a qualitative new bone formation score, ranging from 0 to 3 (i.e. 0 = no new bone formation; 1 = small osteophytes at a limited number of locations; 2 = osteophytes at many locations; 3 = large osteophytes at many locations), was independently assigned to each hind leg by two persons. Furthermore, osteophyte volumes at two distinct standard locations, i.e. the dorsal surface of the lateral cuneiform and the plantar surface of the navicular bone, were measured by carefully drawing a ROI for each osteophyte as shown in figure 5.17.

The actual numerical data and statistical analysis, including an extensive discussion can be found in [53]. Here only a short summary of the key results will be provided:

- There was a significant correlation between the degree of inflammation and new bone formation. Both the qualitative new bone formation score and the measured osteophyte volumes showed a significantly linear relation with the clinical arthritis score. As the inflammation was more pronounced, more new bone formation occurred with formation of larger osteophytes.
- Both in terms of the degree of inflammation and new bone formation, there was no significant correlation between the left and right hind leg. It is therefore incorrect to assume that the joint damage is bilaterally equal, despite the fact that arthritis was induced by systemic administration of an antibody

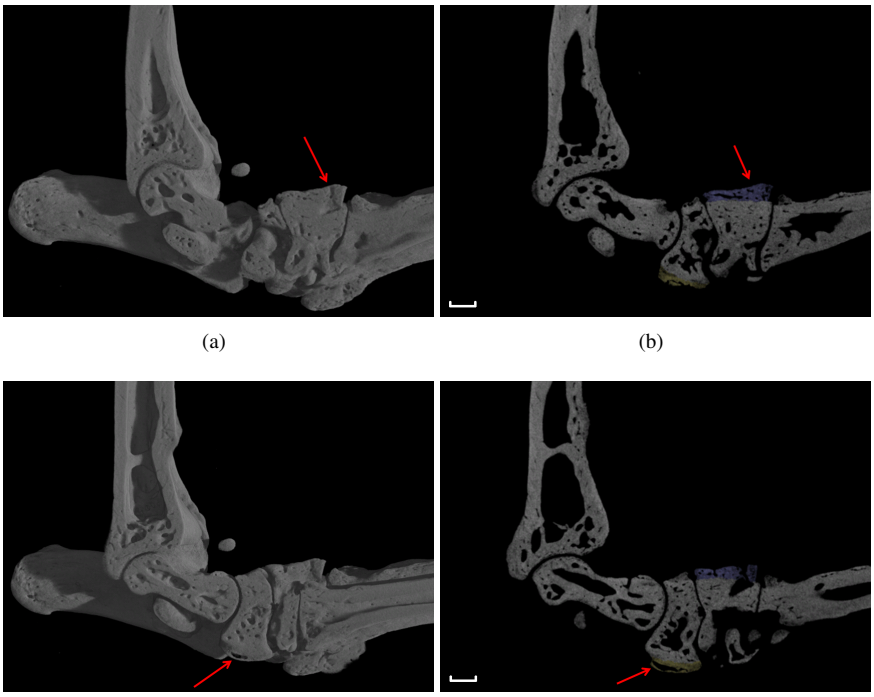

(a) (b)

(c) (d)

Figure 5.17: Osteophyte at the dorsal surface of the lateral cuneiform: (a) sagittal section through a 3D rendering and (b) sagittal CT image with the selected ROI in purple; Osteophyte at the plantar surface of the navicular bone: (c) sagittal section through a 3D rendering and (d) sagittal CT image with the selected ROI in yellow. Scale bar = 0.5 mm.

cocktail. This also implies that randomisation of the mice based on the total clinical score was not an optimal choice since large differences in clinical score between the four different legs will be leveled out in the total score. This can introduce a bias. Indeed, the clinical arthritis scores for the right hind leg were somewhat higher in the TS group compared to the NTS group. A fully correct randomisation can therefore only be carried out by considering only one hind leg.

- The influence of biomechanical stress on new bone formation was less clear. There was no significant difference between the TS and NTS group for the various parameters of new bone formation. However, the data seemed to globally indicate that biomechanical stress will give rise to more bone formation and larger osteophytes, but due to a combination of a limited sample size and a non-optimal randomisation significance could not be achieved.

5.3.4 Visualisation of entheses by means of micro-CT

Given the importance of the entheses in the pathophysiology of SpA, the purpose of this study was also to visualise the entheses to determine whether new bone formation occurs primarily at these sites of increased biomechanical stress. Therefore, the hind legs from the first series were scanned a second time after staining with an aqueous 4% solution of $HgCl_2$.

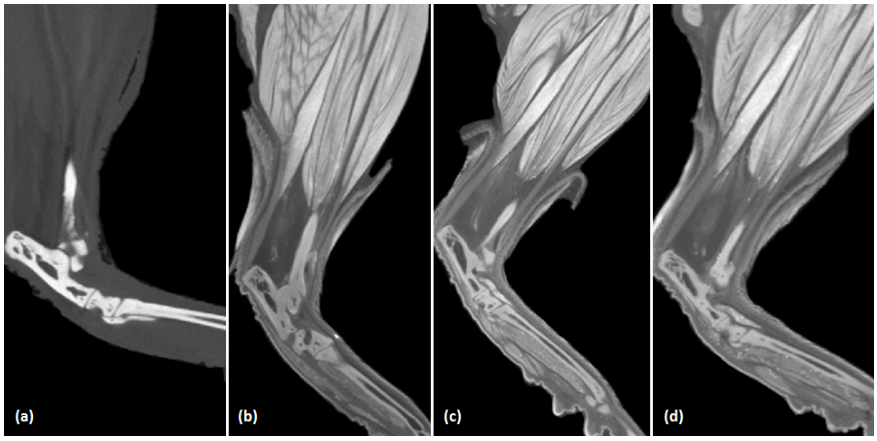

Figure 5.18: CT sections of mice hind legs for comparison of different staining durations: (a) non-stained reference, (b) 2 days, (c) 3 days and (d) 4 days of staining

Since tendons and ligaments are dense structures and as such not easily penetrated by the contrast solution, first some tests were performed on hind legs of wild-type mice in order to determine the ideal staining duration. Figure 5.18 shows the results after 2, 3 and 4 days of immersion in the $HgCl_2$ solution together with a non-stained reference for comparison. Staining gives a clear advantage for the visualisation of different soft tissue structures, but the effect of an increasing staining duration is less evident. Ligaments and tendons in the paw seem to be slightly more visible after 3 days as compared to 2 days. Four days, however, appears to give no further improvement. On the contrary, there seems to be slightly more precipitation of contrast agent present. Therefore, a staining duration of 3 days was considered optimal, although the differences are minimal.

Furthermore, it was also verified whether direct injection of contrast solution into the paws is useful. A few millilitres of contrast solution was injected into two locations in the paw using a fine needle. After injection, the paws were immersed in the staining solution for 3 days before scanning. Figure 5.19 shows that there is no visible effect resulting from direct injection of contrast solution. As such, this

was not applied on the CAIA mice.

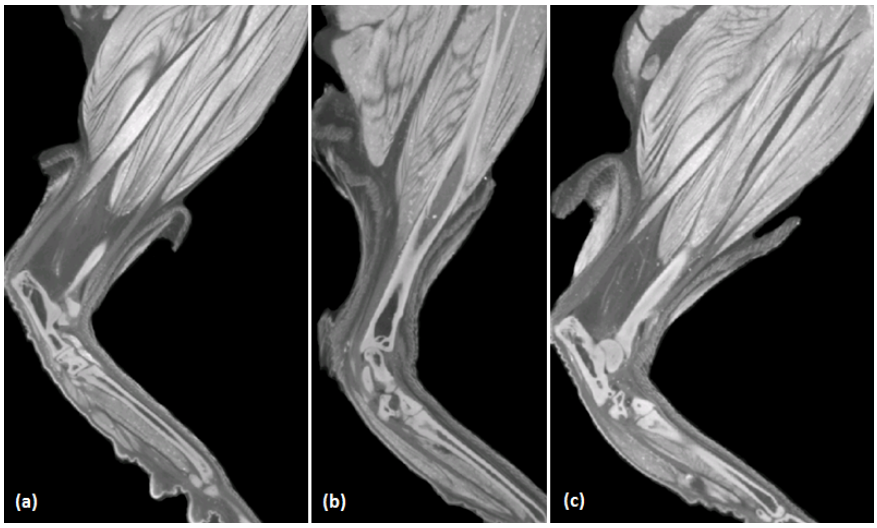

Figure 5.19: CT sections of mice hind legs after 3 days immersion in contrast solution without (a) and with (b) & (c) direct injection of contrast solution in the paws

Through the use of contrast agents, it is more or less possible to locate (functional) entheses in the CAIA mice. The CT images show that the osteophytes are indeed mainly formed at the level of these locations of increased biomechanical stress. Figure 5.20 shows a section through a 3D rendering of a highly affected mouse (both in terms of arthritis and new bone formation) from the TS group. The osteophytes at the lateral cuneiform and navicular bone are marked together with the surrounding tendon structures that seem to insert there at the bone and a such form an enthesis.

Conclusion

This study clearly illustrates the usefulness of HiXTom in biomedical studies with a histological focus. Important advantages with respect to classical histology, include the non-destructive character of the technique and the fact that samples can be virtually sliced in any direction. Moreover, micro-CT not only proves to be a valuable imaging method for bone structures or other mineralised tissues, but also for the visualisation of soft tissues when a suitable contrast enhancing technique is applied.

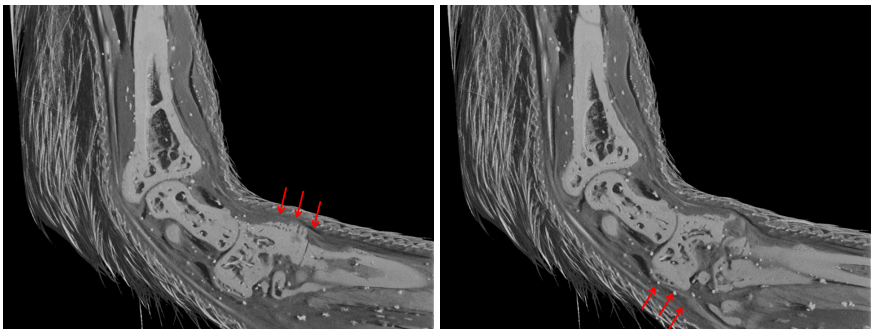

(a) (b)

Figure 5.20: Section through a 3D rendering of highly affected mouse from the TS group with indication of the osteophytes (red arrows) and the corresponding entheses at the lateral cuneiform (a) and navicular bone (b)

References

[1] E. Pauwels, D. Van Loo, P. Cornillie, L. Brabant, and L. Van Hoorebeke. *An exploratory study of contrast agents for soft tissue visualization by means of high resolution X-ray computed tomography imaging*. J. Microsc., 250(1):21–31, 2013.

[2] `http://www.andor.com/learning-academy/what-is-light-an-overview-of-the-properties-of-light`.

[3] G. A. Johnson, H. Benveniste, R. D. Black, L. W. Hedlund, R. R. Maronpot, and B. R. Smith. *Histology by magnetic resonance microscopy*. Magn. Reson. Q., 9(1):1–30, 1993.

[4] G. A. Johnson, G. P. Cofer, B. Fubara, S. L. Gewalt, L. W. Hedlund, and R. R. Maronpot. *Magnetic resonance histology for morphologic phenotyping*. J. Magn. Reson. Imaging, 16(4):423–429, 2002.

[5] J. M. Tyszka, S. E. Fraser, and R. E. Jacobs. *Magnetic resonance microscopy: recent advances and applications*. Curr. Opin. Biotechnol., 16(1):93–99, 2005.

[6] B. Driehuys, J. Nouls, A. Badea, E. Bucholz, K. Ghaghada, A. Petiet, and L. W. Hedlund. *Small animal imaging with magnetic resonance microscopy*. ILAR J., 49(1):35–53, 2008.

[7] J. S. Thomsen, A. Laib, B. Koller, S. Prohaska, L. Mosekilde, and W. Gowin. *Stereological measures of trabecular bone structure: comparison of 3D micro computed tomography with 2D histological sections in human proximal tibial bone biopsies*. J. Microsc., 218(Pt 2):171–179, 2005.

[8] F. Neues and M. Epple. *X-ray microcomputer tomography for the study of biomineralized endo- and exoskeletons of animals*. Chem. Rev., 108(11):4734–41, 2008.

[9] H. M. Britz, J. Jokihaara, O. V. Leppanen, T. Jarvinen, and D. M. L. Cooper. *3D visualization and quantification of rat cortical bone porosity using a desktop micro-CT system: a case study in the tibia*. J. Microsc., 240(1):32–37, 2010.

[10] F. Particelli, L. Mecozzi, A. Beraudi, M. Montesi, F. Baruffaldi, and M. Viceconti. *A comparison between micro-CT and histology for the evaluation of cortical bone: effect of polymethylmethacrylate embedding on structural parameters*. J. Microsc., 245(3):302–310, 2012.

[11] O. Cros, M. Borga, E. Pauwels, J. J. Dirckx, and M. Gaihede. *Micro-channels in the mastoid anatomy. Indications of a separate blood supply of the air cell system mucosa by micro-CT scanning*. Hear. Res., 301:60–5, 2013.

[12] P. Jacques, S. Lambrecht, E. Verheugen, E. Pauwels, G. Kollias, M. Armaka, M. Verhoye, A. Van der Linden, R. Achten, R. J. Lories, and D. Elewaut. *Proof of concept: enthesitis and new bone formation in spondyloarthritis are driven by mechanical strain and stromal cells*. Ann. Rheum. Dis., 73(2):437–45, 2014.

[13] J. Dinley, L. Hawkins, G. Paterson, A. D. Ball, I. Sinclair, P. Sinnett-Jones, and S. Lanham. *Micro-computed X-ray tomography: a new non-destructive method of assessing sectional, fly-through and 3D imaging of a soft-bodied marine worm*. J. Microsc., 238(2):123–133, 2010.

[14] International Commission on Radiation Units and Measurements. *Tissue substitutes in radiation dosimetry and measurement (ICRU Report 44)*. International Commission on Radiation Units and Measurements, 1989.

[15] `http://physics.nist.gov/PhysRefData/XrayMassCoef/tab2.html`.

[16] E. Pauwels. *Optimalisatie van gebruik en detectie van contraststoffen in hoge resolutie X-stralentomografie op basis van de energieafhankelijkheid van hun attenuatie*. Master's thesis, Ghent University, 2010.

[17] `https://www.emsdiasum.com/microscopy/technical/datasheet/critical_drying.aspx`.

[18] O. Leroux, F. Leroux, E. Bellefroid, M. Claeys, M. Couvreur, G. Borgonie, L. Van Hoorebeke, B. Masschaele, and R. Viane. *A new preparation method to study fresh plant structures with X-ray computed tomography*. J. Microsc., 233(1):1–4, 2009.

[19] A. M. Zysk, A. B. Garson III, Q. Xu, E. M. Brey, W. Zhou, J. G. Brankov, M. N. Wernick, J. R. Kuszak, and M. A. Anastasio. *Nondestructive volumetric imaging of tissue microstructure with benchtop x-ray phase-contrast tomography and critical point drying*. Biomed. Opt. Express, 3(8):1924–1932, 2012.

[20] V. Cnudde, B. Masschaele, H. E. V. De Cock, K. Olstad, L. Vlaminck, J. Vlassenbroeck, M. Dierick, Y. De Witte, L. Van Hoorebeke, and P. Jacobs. *Virtual histology by means of high-resolution X-ray CT*. J. Microsc., 232(3):476–485, 2008.

[21] R. Mizutani and Y. Suzuki. *X-ray microtomography in biology*. Micron, 43(2-3):104–115, 2012.

[22] A. de Crespigny, H. Bou-Reslan, M. C. Nishimura, H. Phillips, R. A. D. Carano, and H. E. D'Arceuil. *3D micro-CT imaging of the postmortem brain*. J. Neurosci. Methods, 171(2):207–13, 2008.

[23] B. D. Metscher. *MicroCT for developmental biology: a versatile tool for high-contrast 3D imaging at histological resolutions*. Dev. Dyn., 238(3):632–640, 2009.

[24] B. D. Metscher. *X-ray microtomographic imaging of intact vertebrate embryos*. Cold Spring Harb. Protoc., (12):1462–71, 2011.

[25] J. T. Johnson, M. S. Hansen, I. Wu, L. J. Healy, C. R. Johnson, G. M. Jones, M. R. Capecchi, and C. Keller. *Virtual histology of transgenic mouse embryos for high-throughput phenotyping*. PLoS Genet., 2(4):471–477, 2006.

[26] B. D. Metscher. *MicroCT for comparative morphology: simple staining methods allow high-contrast 3D imaging of diverse non-mineralized animal tissues*. BMC Physiol., 9:11, 2009.

[27] R. E. Golding and A. S. Jones. *Micro-CT as a novel technique for 3D reconstruction of molluscan anatomy*. Molluscan Res, 27(3):123–128, 2007.

[28] R. E. Golding, W. F. Ponder, and M. Byrne. *Three-dimensional reconstruction of the odontophoral cartilages of caenogastropoda (mollusca: gastropoda) using micro-CT: morphology and phylogenetic significance*. J. Morphol., 270(5):558–587, 2009.

[29] H. Watz, A. Breithecker, W. S. Rau, and A. Kriete. *Micro-CT of the human lung: imaging of alveoli and virtual endoscopy of an alveolar duct in a normal lung and in a lung with centrilobular emphysema–initial observations*. Radiology, 236(3):1053–1058, 2005.

[30] R. Mizutani, A. Takeuchi, T. Hara, K. Uesugi, and Y. Suzuki. *Computed tomography imaging of the neuronal structure of Drosophila brain*. J. Synchrotron Rad., 14(Pt 3):282–287, 2007.

[31] K. A. Faraj, V. M. J. I. Cuijpers, R. G. Wismans, X. F. Walboomers, J. A. Jansen, T. H. van Kuppevelt, and W. F. Daamen. *Micro-computed tomographical imaging of soft biological materials using contrast techniques*. Tissue Eng. Part C, 15(3):493–9, 2009.

[32] K. Degenhardt, A. C. Wright, D. Horng, A. Padmanabhan, and J. A. Epstein. *Rapid 3D phenotyping of cardiovascular development in mouse embryos by*

micro-CT with iodine staining. Circ. Cardiovasc. Imaging, 3(3):314–322, 2010.

[33] N. S. Jeffery, R. S. Stephenson, J. A. Gallagher, J. C. Jarvis, and P. G. Cox. *Micro-computed tomography with iodine staining resolves the arrangement of muscle fibres*. J. Biomech., 44(1):189–92, 2011.

[34] P. G. Cox and N. S. Jeffery. *Reviewing the morphology of the jaw-closing musculature in squirrels, rats, and guinea pigs with contrast-enhanced microCT*. Anat. Rec., 294(6):915–928, 2011.

[35] W. Ribi, T. J. Senden, A. Sakellariou, A. Limaye, and S. Zhang. *Imaging honey bee brain anatomy with micro-X-ray-computed tomography*. J. Neurosci. Methods, 171(1):93–7, 2008.

[36] A. C. Lendrum, D. S. Fraser, W. Slidders, and R. Henderson. *Studies on character and staining of fibrin*. J. Clin. Pathol., 15(5):401–413, 1962.

[37] J. C. Stockert. *Sodium tungstate as a stain in electron-microscopy*. Biol. Cell., 29(2-3):211–214, 1977.

[38] T. Hanaichi, T. Sato, T. Iwamoto, J. Malavasi-Yamashiro, M. Hoshino, and N. Mizuno. *A stable lead by modification of Sato's method*. J. Electron Microsc. (Tokyo), 35(3):304–306, 1986.

[39] R. A. Horowitz and C. L. Woodcock. *Alternative staining methods for Lowicryl sections*. J. Histochem. Cytochem., 40(1):123–133, 1992.

[40] C. J. Churukian. *Improved methods for staining fibrin*. J. Histotechnol., 26(2):127–129, 2003.

[41] S. De Carlo and J. R. Harris. *Negative staining and cryo-negative staining of macromolecules and viruses for TEM*. Micron, 42(2):117–131, 2011.

[42] D. P. Harland, J. A. Vernon, R. J. Walls, and J. L. Woods. *Transmission electron microscopy staining methods for the cortex of human hair: a modified osmium method and comparison with other stains*. J. Microsc., 243(2):184–196, 2011.

[43] B. Masschaele, V. Cnudde, M. Dierick, P. Jacobs, L. Van Hoorebeke, and J. Vlassenbroeck. *UGCT: New x-ray radiography and tomography facility*. Nucl. Instrum. Methods Phys. Res., Sect. A, 580(1):266–269, 2007.

[44] *Inside Matters*. `https://insidematters.eu/`.

[45] P. Frisullo, R. Marino, J. Laverse, M. Albenzio, and M. A. Del Nobile. *Assessment of intramuscular fat level and distribution in beef muscles using X-ray microcomputed tomography*. Meat Sci., 85(2):250–255, 2010.

[46] `http://www.volumegraphics.com`.

[47] J. Buytaert, J. Goyens, D. De Greef, P. Aerts, and J. Dirckx. *Volume shrinkage of bone, brain and muscle tissue in sample preparation for micro-CT and light sheet fluorescence microscopy (LSFM)*. Microsc. Microanal., 20(4):1208–17, 2014.

[48] E. Descamps, A. Sochacka, B. De Kegel, D. Van Loo, L. Van Hoorebeke, and D. Adriaens. *Soft tissue discrimination with contrast agents using micro-CT scanning*. Belg. J. Zool., 144(1):20–40, 2014.

[49] P. M. Gignac and N. J. Kley. *Iodine-enhanced micro-CT imaging: methodological refinements for the study of the soft-tissue anatomy of post-embryonic vertebrates*. J. Exp. Zool. Part B, 322(3):166–76, 2014.

[50] P. Das Neves Borges, A. E. Forte, T. L. Vincent, D. Dini, and M. Marenzana. *Rapid, automated imaging of mouse articular cartilage by microCT for early detection of osteoarthritis and finite element modelling of joint mechanics*. Osteoarthritis Cartilage, 22(10):1419–28, 2014.

[51] M. Nierenberger, Y. Remond, S. Ahzi, and P. Choquet. *Assessing the three-dimensional collagen network in soft tissues using contrast agents and high resolution micro-CT: Application to porcine iliac veins*. C. R. Biol., 338(7):425–33, 2015.

[52] R. Balint, T. Lowe, and T. Shearer. *Optimal Contrast Agent Staining of Ligaments and Tendons for X-Ray Computed Tomography*. PLoS ONE, 11(4):e0153552, 2016.

[53] E. Pauwels. *In vitro micro-CT studie van de invloed van biomechanische stress op botnieuwvorming in muismodellen voor artritis*. Master's thesis, Ghent University, 2014.

[54] J. Sieper, M. Rudwaleit, M. A. Khan, and J. Braun. *Concepts and epidemiology of spondyloarthritis*. Best Pract. Res. Clin. Rheumatol., 20(3):401–17, 2006.

[55] J. Sieper, M. Rudwaleit, X. Baraliakos, J. Brandt, J. Braun, R. Burgos-Vargas, M. Dougados, K. G. Hermann, R. Landewe, W. Maksymowych, and D. van der Heijde. *The Assessment of SpondyloArthritis international Society (ASAS) handbook: a guide to assess spondyloarthritis*. Ann. Rheum. Dis., 68 (Suppl II):ii1–44, 2009.

[56] D. McGonagle, W. Gibbon, and P. Emery. *Classification of inflammatory arthritis by enthesitis*. Lancet, 352(9134):1137–40, 1998.

[57] M. Benjamin and D. McGonagle. *The anatomical basis for disease localisation in seronegative spondyloarthropathy at entheses and related sites*. J. Anat., 199:503–26, 2001.

[58] D. McGonagle, L. Stockwin, J. Isaacs, and P. Emery. *An enthesitis based model for the pathogenesis of spondyloarthropathy. additive effects of microbial adjuvant and biomechanical factors at disease sites*. J. Rheumatol., 28(10):2155–9, 2001.

[59] K. S. Nandakumar and R. Holmdahl. *Efficient promotion of collagen antibody induced arthritis (CAIA) using four monoclonal antibodies specific for the major epitopes recognized in both collagen induced arthritis and rheumatoid arthritis*. J. Immunol. Methods, 304(1-2):126–36, 2005.

[60] J. P. Sherlock, B. Joyce-Shaikh, S. P. Turner, C. C. Chao, M. Sathe, J. Grein, D. M. Gorman, E. P. Bowman, T. K. McClanahan, J. H. Yearley, G. Eberl, C. D. Buckley, R. A. Kastelein, R. H. Pierce, D. M. Laface, and D. J. Cua. *IL-23 induces spondyloarthropathy by acting on ROR-gammat+ CD3+CD4-CD8- entheseal resident T cells*. Nat. Med., 18(7):1069–76, 2012.

[61] E. R. Morey-Holton and R. K. Globus. *Hindlimb unloading rodent model: technical aspects*. J. Appl. Physiol., 92(4):1367–77, 2002.

[62] B. Masschaele, M. Dierick, D. Van Loo, M. N. Boone, L. Brabant, E. Pauwels, V. Cnudde, and L. Van Hoorebeke. *HECTOR: A 240kV micro-CT setup optimized for research*. J. Phys.: Conf. Ser., 463(1):012012, 2013.

6
Conclusions and outlook

This work focuses on image optimisation in high resolution X-ray tomography, mainly by exploring how scanning conditions can be adjusted to obtain an optimal virtual representation of the sample, using the currently availabe hardware. In this context, the polychromatic behaviour of both source and detector plays an important role. On the one hand, it represents a challenge in the prediction of the final image result. On the other hand, a full understanding of this behaviour allows to exploit this polychromatic nature for image optimisation, especially in the context of dual energy computed tomography. Furthermore, this work also elaborates more specifically on the use of contrast agents for soft tissue visualisation.

Chapter 3 was fully devoted to X-ray imaging simulations. For an optimal image result several different scanning variables, such as tube voltage, tube power, beam filtration and exposure time per projection, need to be carefully chosen. Moreover, the ideal combination of these parameters will depend on the sample itself in terms of size, composition and density. Two simulation tools developed at UGCT, the Setup Optimiser and Arion, were presented in this work. The first tool allows a fast and straightforward evaluation of various scanner setting by simulating the detected transmission of a specific X-ray beam through one or several layers of materials. However, to take into account the full geometry and nature of the sample it is necessary to simulate complete radiographic projections. To this purpose Arion was developed. The experimental validation of the simulation software, presented in section 3.4, proves not only the qualitative but more importantly also the quantitative correctness of the simulations as compared to real

X-ray imaging data. Moreover, these results imply that we have a correct understanding of the physics behind the whole imaging process and more specifically of the polychromatic behaviour of the X-ray sources and detectors available at UGCT. An important practical aspect of the simulation software is its computing speed. A lot of effort has been made to keep the calculation time to a minimum, first of all by performing the calculation on a GPU and secondly by introducing a rebinning procedure, described in section 3.2.4. The benchmarks shown in section 3.5.1 illustrate the excellent computation speed of Arion. Future improvements of the simulation software may consist of implementing photon scattering, detector ghosting and X-ray wave properties to simulate phase contrast effects.

Chapter 4 elaborated on dual energy computed tomography. Combining information from CT scans perfomed at two (or more) X-ray energies may be very useful in cases where two or more materials with a different composition are difficult to distinguish in a single scan. The key for an optimal result, is a careful selection of these energies. However, in laboratory based CT, the combination of polychromatic X-ray sources with integrating detectors with an energy-dependent efficiency complicates matters to a great extent. First of all, the "energy" of a polychromatic X-ray spectrum is not easily defined. In section 4.3.2, several definitions were proposed and explored. Ideally, the spectrum energy should be that energy corresponding to the resulting attenuation coefficients in the CT image. Moreover, it should be independent of the sample. The "detected monochromatic energy", which was introduced in this work, proved to largely meet these criteria. An important disadvantage is that its formula is derived for sample thicknesses approaching zero. It was shown however, that for X-ray spectra with limited beam hardening, i.e. sufficiently hard spectra, the detected monochromatic energy corresponds quite well to the actual attenuation coefficients for finite sample sizes. To quantify the degree of beam hardening for a specific X-ray spectrum and sample, a measure was introduced, called the beam hardening factor. As shown in sections 4.3.3 and 4.4.2, combining the detected monochromatic energy and the beam hardening factor allows to make a fairly good selection of dual energy scanner settings. However, in some cases it is not possible to choose ideal scan energies based on the attenuation profile of the sample or they may be too high to be practically feasible. Moreover, as illustrated in section 4.4.3, significantly different X-ray spectra may have a (nearly) identical detected monochromatic energy. For an optimal selection of scanner settings, the full shape of the spectrum has to be taken into account. This can be done by means of complete CT simulations, as shown in sections 4.3.4 and 4.4.3. A method was presented to automatically select the optimal X-ray spectra for dual energy CT based on the performed simulations. Excellent results were obtained in this way. However, application of this method on the real sample presented in section 4.4.4, proved that in some cases a single

high quality CT scan may lead to equally good results. Crucial is an optimal selection of scanning conditions, taking the full polychromatic behaviour of the image process into account. As demonstrated in this chapter, accurate simulations play a key role. Future work may lie in the automisation of the whole process from performing CT simulations leading to the selection of the optimal X-ray spectra. Up to now, this is quite time consuming, since the purpose of this work was to provide a proof of principle. Therefore, some efforts still have to be made to turn it into a practical, fast and easily applicable spectrum selection method/tool.

Chapter 5 focused more specifically on histology by means of high resolution X-ray tomography (HiXTom). A special challenge in this topic is optimisation of soft tissue visualisation. X-ray image contrast is obtained when two adjacent types of materials give rise to a suffciently different X-ray photon attenuation. Soft tissues contain a lot of "cavities" filled with water. Therefore, one way to enhance soft tissue contrast is to remove this water from the cavities and replace it with air, i.e. tissue drying. This was shown in section 5.1.1. Another way to improve soft tissue contrast is to make use of contrast agents. Typically, these agents consist of molecules containing atoms with a high atomic number. In this chapter, a substantial list of chemical substances is studied to identify useful X-ray contrast agents for soft tissue visualisation, suited for samples larger than $(1\ \mathrm{cm})^3$. An important criterion was that the staining procedure was straightforward to realise. Moreover, the products had to be relatively safe to handle and dispose of. As shown in section 5.2, excellent results were obtained with $HgCl_2$, PMA and PTA. However, depending on the application, sample size and soft tissue type, other contrast agents may be preferred. Future work may consist of developing a concrete staining protocol, especially for $HgCl_2$, which is a newly identified staining agent. To this purpose, the influence of different contrast agent concentrations and staining durations have to be adequately studied. It would also be very useful to test the potential of these products on a large variety of different soft tissue types. In section 5.3, a concrete example of a biomedical application of HiXTom is shown, clearly illustrating its usefulness. Important advantages with respect to classical histology, include the non-destructive character of the technique and the fact that samples can be virtually sliced in any direction. Moreover, micro-CT not only proves to be a valuable imaging method for bone structures or other mineralised tissues, but also for the visualisation of soft tissues when a suitable contrast enhancing technique is applied.

7
Bibliography

A1 Publications

[1] J. Dhaene, E. Pauwels, T. De Schryver, A. De Muynck, M. Dierick, and L. Van Hoorebeke. *A realistic projection simulator for laboratory based X-ray micro-CT*. Nuclear Instruments and Methods in Physics Research Section B: Beam Interactions with Materials and Atoms, 342(0):170–178, 2015.

[2] E. H. Hendrickson, K. Olstad, A. Nodtvedt, E. Pauwels, L. van Hoorebeke, and N. I. Dolvik. *Comparison of the blood supply to the articular-epiphyseal growth complex in horse vs. pony foals*. Equine Vet. J., 47(3):326–32, 2015.

[3] S. Poppe, E. P. Holohan, E. Pauwels, V. Cnudde, and M. Kervyn. *Sinkholes, pit craters, and small calderas: Analog models of depletioninduced collapse analyzed by computed X-ray microtomography*. Geol Soc Am Bull, 127(1-2):281–296, 2015.

[4] C. D. Byron, A. Herrel, E. Pauwels, A. De Muynck, and B. A. Patel. *Mouse hallucal metatarsal cross-sectional geometry in a simulated fine branch niche*. J. Morphol., 276(7):759–65, 2015.

[5] M. N. Boone, J. Garrevoet, P. Tack, O. Scharf, D. P. Cormode, D. Van Loo, E. Pauwels, M. Dierick, L. Vincze, and L. Van Hoorebeke. *High spectral and spatial resolution X-ray transmission radiography and tomography using a Color X-ray Camera*. Nucl Instrum Meth A, 735:644–648, 2014.

[6] L. Brabant, M. Dierick, E. Pauwels, M. N. Boone, and L. Van Hoorebeke. *EDART, a discrete algebraic reconstructing technique for experimental data obtained with high resolution computed tomography*. J. X-ray Sci. Technol., 22(1):47–61, 2014.

[7] D. Van Loo, L. Bouckaert, O. Leroux, E. Pauwels, M. Dierick, L. Van Hoorebeke, V. Cnudde, S. De Neve, and S. Sleutel. *Contrast agents for soil investigation with X-ray computed tomography*. Geoderma, 213:485–491, 2014.

[8] P. Jacques, S. Lambrecht, E. Verheugen, E. Pauwels, G. Kollias, M. Armaka, M. Verhoye, A. Van der Linden, R. Achten, R. J. Lories, and D. Elewaut. *Proof of concept: enthesitis and new bone formation in spondyloarthritis are driven by mechanical strain and stromal cells*. Annals of the rheumatic diseases, 73(2):437–45, 2014.

[9] O. Cros, M. Borga, E. Pauwels, J. J. Dirckx, and M. Gaihede. *Micro-channels in the mastoid anatomy. Indications of a separate blood supply of the air cell system mucosa by micro-CT scanning*. Hearing research, 301:60–5, 2013.

[10] W. De Crop, E. Pauwels, L. Van Hoorebeke, and T. Geerinckx. *Functional morphology of the Andean climbing catfishes (Astroblepidae, Siluriformes): Alternative ways of respiration, adhesion, and locomotion using the mouth*. J. Morphol., 274(10):1164–1179, 2013.

[11] Z. T. Nagy, D. Adriaens, E. Pauwels, L. Van Hoorebeke, J. Kielgast, C. Kusamba, and K. Jackson. *3D reconstruction of fang replacement in the venomous snakes Dendroaspis jamesoni (Elapidae) and Bitis arietans (Viperidae)*. Salamandra, 49(2):109–113, 2013.

[12] H. Henderickx, J. Bosselaers, E. Pauwels, L. Van Hoorebeke, and M. N. Boone. *X-ray micro-CT reconstruction reveals eight antennomeres in a new fossil taxon that constitutes a sister clade to Dundoxenos and Triozocera (Strepsiptera: Corioxenidae)*. Palaeontol Electron, 16(3), 2013.

[13] B. Willaert, F. Bossuyt, S. Janssenswillen, D. Adriaens, G. Baggerman, S. Matthijs, E. Pauwels, P. Proost, A. Raepsaet, L. Schoofs, G. Stegen, D. Treer, L. Van Hoorebeke, W. Vandebergh, and I. Van Bocxlaer. *Frog nuptial pads secrete mating season-specific proteins related to salamander pheromones*. J. Exp. Biol., 216(Pt 22):4139–43, 2013.

[14] E. Pauwels, D. Van Loo, P. Cornillie, L. Brabant, and L. Van Hoorebeke. *An exploratory study of contrast agents for soft tissue visualization by means of high resolution X-ray computed tomography imaging*. Journal of microscopy, 250(1):21–31, 2013.

[15] M. N. Boone, W. Devulder, M. Dierick, L. Brabant, E. Pauwels, and L. Van Hoorebeke. *Comparison of two single-image phase-retrieval algorithms for in-line x-ray phase-contrast imaging*. Journal of the Optical Society of America A, 29(12):2667–2672, 2012.

[16] L. Brabant, E. Pauwels, M. Dierick, D. Van Loo, M. A. Boone, and L. Van Hoorebeke. *A novel beam hardening correction method requiring no prior knowledge, incorporated in an iterative reconstruction algorithm*. NDT & E International, 51:68–73, 2012.

[17] R. Wagner, D. Van Loo, F. Hossler, K. Czymmek, E. Pauwels, and L. Van Hoorebeke. *High-resolution imaging of kidney vascular corrosion casts with nano-CT*. Microscopy and Microanalysis, 17(2):215–219, 2011.

Conference contributions

[1] Elin Pauwels, Stijn Bonte, Andre Dobbeleir, Stijn Verleden, Kurt Audenaert, Roel Van Holen, and Ingeborg Goethals. *18F-FDG uptake in the healthy brain as a function of age and start of acquisition*. In European Journal of Nuclear Medicine and Molecular Imaging, volume 43, pages S253–S253, 2016.

[2] Elin Pauwels, Jelle Dhaene, Amélie De Muynck, Manuel Dierick, and Luc Van Hoorebeke. *Optimization of scanner parameters for dual energy micro-CT*. In Bernard Long, editor, Tomography of Materials and Structures, 2nd International conference, Proceedings, pages 87–91, 2015.

[3] Jelle Dhaene, Elin Pauwels, Thomas De Schryver, Amélie De Muynck, Manuel Dierick, and Luc Van Hoorebeke. *Arion: a realistic projection simulator for optimizing laboratory and industrial micro-CT*. In Bernard Long, editor, Tomography of Materials and Structures, 2nd International conference, Proceedings, pages 60–64, 2015.

[4] Matthieu Boone, Bert Masschaele, Manuel Dierick, Denis Van Loo, Thomas De Schryver, Elin Pauwels, Jelle Dhaene, Amélie De Muynck, Marjolein Heyndrickx, and Luc Van Hoorebeke. *Latest technical developments at UGCT: an overview*. In Matthieu Boone and Jan Van den Bulcke, editors, 2nd UGCT seminar : book of abstracts. Ghent University. Centre for X-ray Tomography (UGCT), 2015.

[5] Els Louagie, Isabelle Cambré, Amélie De Muynck, Djoere Gaublomme, Elin Pauwels, Pieter Vanderniepen, Fien Windels, Julie Coudenys, Nadia Schryvers, Eveline Verheugen, Stijn Lambrecht, Peggy Jacques, Luc Van Hoorebeke, and Dirk Elewaut. *Application of μCT in arthritis and osteoporosis research*. In Matthieu Boone and Jan Van den Bulcke, editors, 2nd UGCT seminar : book of abstracts. Ghent University. Centre for X-ray Tomography (UGCT), 2015.

[6] Elin Pauwels, Jelle Dhaene, Amélie De Muynck, Thomas De Schryver, Manuel Dierick, and Luc Van Hoorebeke. *Optimization of scanner parameters for dual energy micro-CT*. In 12th International conference on X-Ray Microscopy : conference program handbook, 2014.

[7] Jelle Dhaene, Elin Pauwels, Thomas De Schryver, Amélie De Muynck, Loes Brabant, Manuel Dierick, and Luc Van Hoorebeke. *Realistic projection simulator for laboratory based X-ray micro-CT*. In Industrial Computed Tomography, 5th Conference, Abstracts, 2014.

[8] Geert Peeters, Charlotte Debbaut, Pieter Cornillie, Elin Pauwels, Diethard Monbaliu, Wim Laleman, and Patrick Segers. *A multi-level computational model to characterize the hepatic circulation in human cirrhosis*. In 11th World Congress on Computational Mechanics, WCCM 2014, 5th European Conference on Computational Mechanics, ECCM 2014 and 6th European Conference on Computational Fluid Dynamics, ECFD 2014, page 2. International Center for Numerical Methods in Engineering, 2014.

[9] Jelle Dhaene, Elin Pauwels, Thomas De Schryver, Amélie De Muynck, Manuel Dierick, and Luc Van Hoorebeke. *Accurate projection simulator for laboratory based X-ray micro-CT*. In 12th International conference on X-Ray Microscopy : conference program handbook, 2014.

[10] Amélie De Muynck, Jelle Dhaene, Elin Pauwels, Thomas De Schryver, Manuel Dierick, and Luc Van Hoorebeke. *A modular approach to generate spectral characteristics of X-ray micro-CT scanner components*. In 12th International conference on X-Ray Microscopy : conference program handbook, pages 107–107, 2014.

[11] Amélie De Muynck, Jelle Dhaene, Elin Pauwels, Manuel Dierick, and Luc Van Hoorebeke. *Modelling scattering contributions in X-ray micro-CT scanners with variable geometry*. In Industrial Computed Tomography, 5th Conference, Abstracts, 2014.

[12] Elin Pauwels, Manuel Dierick, Denis Van Loo, Matthieu Boone, Loes Brabant, and Luc Van Hoorebeke. *Application of generic DECT based on complete CT-setup simulations*. In IEEE 10th International symposium on biomedical imaging: From nano to macro, Proceedings, 2013.

[13] Sam Poppe, Eoghan Holohan, Matthieu Boone, Elin Pauwels, Veerle Cnudde, and Matthieu Kervyn. *Characterizing analogue caldera collapse with computerized X-ray micro-tomography*. In Geophysical Research Abstracts, volume 15. European Geosciences Union (EGU), 2013.

[14] Elin Pauwels, Manuel Dierick, Loes Brabant, and Luc Van Hoorebeke. *Realistic CT image simulation tools for laboratory based X-ray CT at UGCT*. In Veerle Cnudde, editor, Tomography of materials and structures : book of abstracts : posters, pages 39–42, 2013.

[15] Joachim Christiaens, Barbara De Kegel, Emilie Descamps, Alicja Sochacka, Elin Pauwels, and Dominique Adriaens. *Why old school histology still doens't turn pale: histology versus micro-CT of animal tissues*. In Journal of Histotechnology, volume 36, pages 152–152, 2013.

[16] Loes Brabant, Elin Pauwels, Manuel Dierick, Matthieu Boone, and Luc Van Hoorebeke. *Iterative reconstruction algorithms for the reduction of artifacts in high resolution X-ray computed tomography*. In IEEE 10th International symposium on biomedical imaging: From nano to macro, Proceedings, 2013.

[17] Matthieu Boone, Erik LG Wernersson, Manuel Dierick, Loes Brabant, Elin Pauwels, Cris L Luengo Hendriks, and Luc Van Hoorebeke. *Comparison of several phase retrieval and phase correction methods for single-image in-line X-ray phase contrast tomography*. In IEEE 10th International symposium on biomedical imaging: From nano to macro, Proceedings, 2013.

[18] Loes Brabant, Manuel Dierick, Elin Pauwels, Yoni De Witte, and Luc Van Hoorebeke. *Modifications of iterative reconstruction algorithms for the reduction of artefacts in high resolution X-ray computed tomography*. In Veerle Cnudde, editor, Tomography of materials and structures : book of abstracts : posters, pages 111–114, 2013.

[19] Manuel Dierick, Denis Van Loo, Bert Masschaele, Matthieu Boone, Elin Pauwels, Loes Brabant, Veerle Cnudde, and Luc Van Hoorebeke. *HECTOR, a new multifunctional micro-CT scanner at UGCT*. In IEEE 10th International symposium on biomedical imaging: From nano to macro, Proceedings, 2013.

[20] Sam Poppe, Matthieu Boone, Elin Pauwels, Veerle Cnudde, and Matthieu Kervyn de Meerendre. *Characterizing analogue caldera collapse with computerized X-ray tomography*. In Veerle Cnudde, editor, Tomography of materials and structures : book of abstracts : posters, pages 43–46, 2013.

[21] Elin Pauwels, Loes Brabant, Matthieu Boone, Manuel Dierick, Denis Van Loo, and Luc Van Hoorebeke. *The UGCT setup optimizer for developing DECT*. In CT Scan Workshop: Development on non-medical environment, Quebec City, Canada, 2012.

[22] Bert Masschaele, Manuel Dierick, Denis Van Loo, Matthieu Boone, Loes Brabant, Elin Pauwels, Luc Van Hoorebeke, and Veerle Cnudde. *HECTOR: a 240kV micro-CT setup optimized for research*. In X-ray Microscopy, 11th International conference, Abstracts, pages abstract MON–P34:152–abstract MON–P34:152, 2012.

[23] Jan Van den Bulcke, Denis Van Loo, Manuel Dierick, Matthieu Boone, Bert Masschaele, Loes Brabant, Elin Pauwels, Yoni De Witte, Luc Van Hoorebeke, and Joris Van Acker. *State-of-the-art and future prospects of X-ray computed tomography in wood science*. In COST FP0802, Workshop abstracts, 2012.

[24] Manuel Dierick, Denis Van Loo, Bert Masschaele, Jelle Vlassenbroeck, Matthieu Boone, Loes Brabant, Elin Pauwels, Steven Peetermans, Pieter Vanderniepen, and Luc Van Hoorebeke. *Scanner design and construction at UGCT*. In Joris Van Acker, Luc Van Hoorebeke, Patric Jacobs, Veerle Cnudde, and Jan Van den Bulcke, editors, X-ray tomography as a multidisciplinary research tool : exploring new frontiers, pages 13–19. Ghent University. Centre for X-ray Tomography (UGCT), 2010.